2019

Metal-Organic Framework (MOF)-Based Materials: Aerosol Synthesis and Photocatalytic Applications

Xiang He
Virginia Commonwealth University

Metal-Organic Framework (MOF)-Based Materials: Aerosol Synthesis and Photocatalytic Applications

A dissertation submitted in partial fulfillment of the requirements for
the degree of Doctor of Philosophy at Virginia Commonwealth University

By

Xiang He

M.S., Environmental Engineering, Sun Yat-sen University, China, 2015
B.S., Environmental Engineering, Sun Yat-sen University, China, 2013

Advisor: Dr. Wei-Ning Wang
Assistant Professor, Department of Mechanical and Nuclear Engineering

Virginia Commonwealth University
Richmond, Virginia

May 2019

Acknowledgment

Pursuing a Ph.D. in Mechanical and Nuclear Engineering is not an easy task for a man with the education background only in Environmental Engineering. Lucky for me to have a responsible and patient advisor, Prof. Wei-Ning Wang, who not only teaches me the experimental fundaments but also shares with me precious experiences towards a successful academic life. Without his constant support in both research and life, I would've never reached so far. Therefore, I would like to express my greatest appreciation to him.

I would also like to show my gratitude to my dissertation committee members: Prof. Daren Chen, Prof. Reza Mohammadi, Prof. Hani El-Kaderi, Prof. Ram Gupta, and Prof. Puru Jena. I'm grateful for their kind advising of my research work and strong support for my job searching. I would also like to thank Prof. Karla Mossi for her continued support for everything. It is a great treasure for me to have her as my graduate program director.

I also want to thank all the members in Biotech One. It is because of you guys that make the lab full of joy and laugh instead of inactive atmosphere. I would particularly like to thank Prof. Sheng-Chieh Chen for his kind consideration for my future work. I would also like to thank Zan Zhu, Dr. Dawei Wang, Dr. Qijin Huang, and Shihang Li. Talking to you guys really helps to release the pressures off me.

Last but not least, I'm deeply grateful to my beloved family, especially my wife, Xianghua Jin, for being there with me all along.

TABLE OF CONTENTS

List of Figures

List of Schemes

List of Tables

Abstract

METAL-ORGANIC FRAMEWORK (MOF)-BASED MATERIALS: AEROSOL SYNTHESIS AND PHOTOCATALYTIC APPLICATIONS

By Xiang He

A dissertation submitted in partial fulfillment of the requirements for the degree of Doctor of Philosophy at Virginia Commonwealth University

Virginia Commonwealth University, 2019

Advisor: Dr. Wei-Ning Wang
Assistant Professor, Department of Mechanical and Nuclear Engineering

Metal-organic frameworks (MOFs) have been attracting great attention in the past several decades mainly because of their amazing properties, including tunable surface chemistry, flexible structure, large surface area, and huge porosity. Endorsed by those merits, MOFs have been applied in a wide range of applications, such as catalysis, gas separation, drug delivery, and sensing. Typically, MOFs are synthesized via the hydrothermal method, which, however, is difficult to scale up and requires long reaction durations (e.g., from hours to days). To achieve the full potentials of MOFs, the exploration of a novel strategy is necessary for the facile and fast synthesis of MOFs. Here in this dissertation, the aerosol route was presented as a facile route to synthesize MOFs and MOF-based composites. The aerosol route not only enabled fast crystallization of MOFs (i.e., within seconds), but also allowed continuous tuning of MOF's properties by simply adjusting the operating parameters (e.g., temperature, pressure, and precursor conditions). To map out the formation mechanism of MOFs inside the microdroplets, systematic experimental and simulation

work were carried out, which demonstrated that the fast heat and mass transfer during the aerosol route played a vital role in the rapid synthesis of MOFs.

Beyond the synthesis of MOFs, the photocatalytic applications of MOF-based materials for energy and environmental sustainability were also studied in detail. More specifically, several efficient MOF-based composite photocatalysts were designed, including HKUST-1/TiO_2, HKUST-1/TiO_2/Cu_2O, ZIF-8/ZnO, and MIL-100(Fe)/TiO_2. The composite photocatalysts exhibited remarkable efficiencies towards either CO_2 photoreduction or water remediation. In-depth exploration of the photocatalytic mechanism was carried out with the aid of several advanced techniques, such as *in situ* diffuse reflectance infrared Fourier spectroscopy (DRIFTS), photoluminescence spectroscopy, grazing-incidence wide-angle X-ray scattering, and ultrafast transient absorption spectroscopy. Meanwhile, the density functional theory (DFT) calculation was also applied to provide further mechanistic insights. The results demonstrated that MOFs acted as excellent co-catalysts, which not only facilitated molecule adsorption and activation, but also promoted the separation of the photo-induced charge carriers, leading to increased charge carrier densities in the photocatalytic systems for significantly enhanced efficiencies.

The work from this dissertation is expected to broaden the synthesis strategies for the synthesis of MOF-based materials and advance the fundamental understanding of MOFs' roles in photocatalytic applications, which should have a great impact on the rational design of MOF-based composite photocatalysts for energy and environmental sustainability.

Chapter 1. Introduction

1.1 Fundamentals and Applications of Metal-Organic Frameworks (MOFs)

MOFs are a class of highly porous crystals, which are composed of metal/metal clusters and organic ligands connected through coordination bond (**Figure 1.1a**).[1] Because of the abundance of metal and ligand species, massive MOF structures could be designed. Notably, MOFs have drawn great attention in the past several decades and the number of the MOF structures has been increasing dramatically, reaching ~ 70,000 in Cambridge Structural Database (CSD) in 2016.[2] Typical examples of the MOF structures were shown in **Figure 1.1b**.[3]

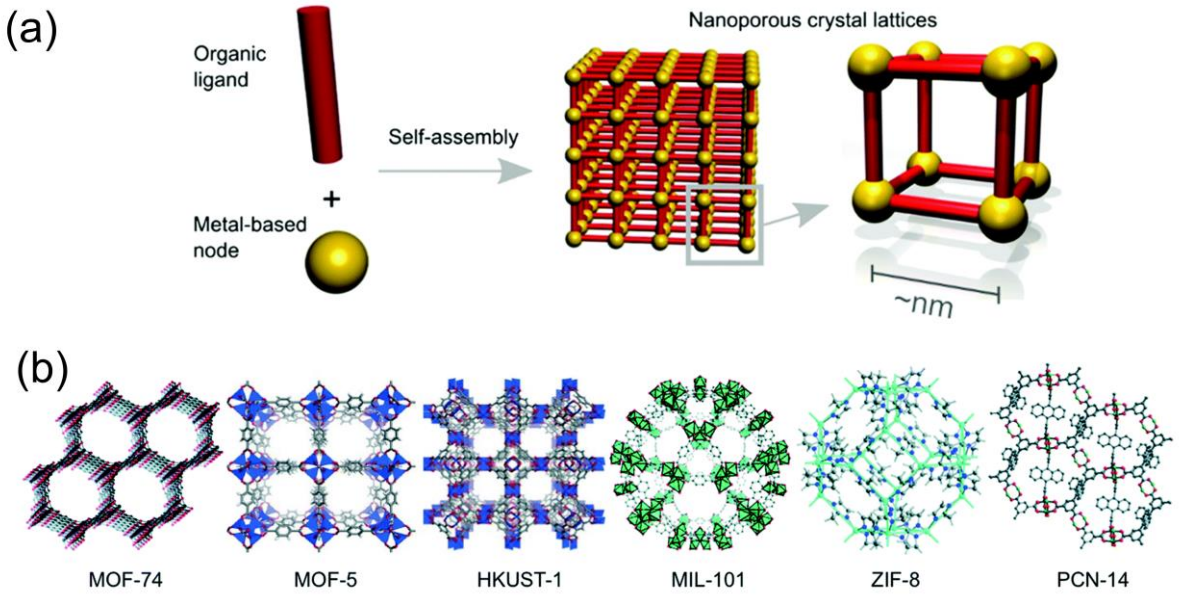

Figure 1.1 (a) MOFs are ordered frameworks built from interconnected organic ligands and metal-based nodes. Reproduced from Ref. [1] with permission form The Royal Society of Chemistry; (b) Crystal structures of common MOFs published in the CSD database. Reproduced form Ref. [3] with permission form The Royal Society of Chemistry.

The reason why MOFs have been attracting such much attention is that they possess many intriguing properties, including huge surface area, tunable surface chemistry, and structural flexibility.[4] All these merits make MOFs promising candidates in a broad range of applications. For instance, MOFs are ideal adsorbents for gas purification and separation via molecular sieving, quantum effect, kinetic separation, and adsorbent-adsorbate interactions.[5] As an example, the capacities of MOF-74(Mg) and MOF-74(Co) for ammonia adsorption were reported to be 6 and 15 times that of conventional activated carbon, respectively.[6] The flexibility of the framework to the external stimuli also offers some MOFs huge potentials in temperature/pressure dependent gas separation.[5, 7-8]

In addition, water stable MOFs have also been showing great potentials in removing industrial, municipal, and agricultural contaminants from aquatic systems.[9-11] Particularly, the fantastic surface area and porosity offer MOFs ability to remove contaminants via adsorption. As summarized in **Figure 1.2**, the adsorption mechanisms are composed of several MOF/adsorbate interactions, such as hydrophobic, electrostatic, and π-π interactions.[12] For example, the PCN-124-stu(Cu) designed by Jin *et al*.[13] exhibited much higher adsorption ability towards antibiotics and dyes compared with conventional porous materials, including activated carbon and zeolite 13X. Two highly stable MOFs, BUT-12 and BUT-13, were designed by Wang *et al*.,[14] which have huge surface areas (i.e., 3387 and 3948 m^2/g, respectively). These two MOFs are not only perfect adsorbent for organic explosives and antibiotics, but also great sensor (ppb level) for these contaminants. Meanwhile, some MOFs possess catalytic abilities with tunable optic properties,[15]

which is beneficial for the photodegradation of pollutants in the water.[16] As an example, NTU-9 was reported to be able to absorb visible light with a very small bandgap (i.e., 1.72 eV).[17] Also, the NTU-9 could serve as a p-type semiconductor to degrade organic pollutants while maintaining structural intact.

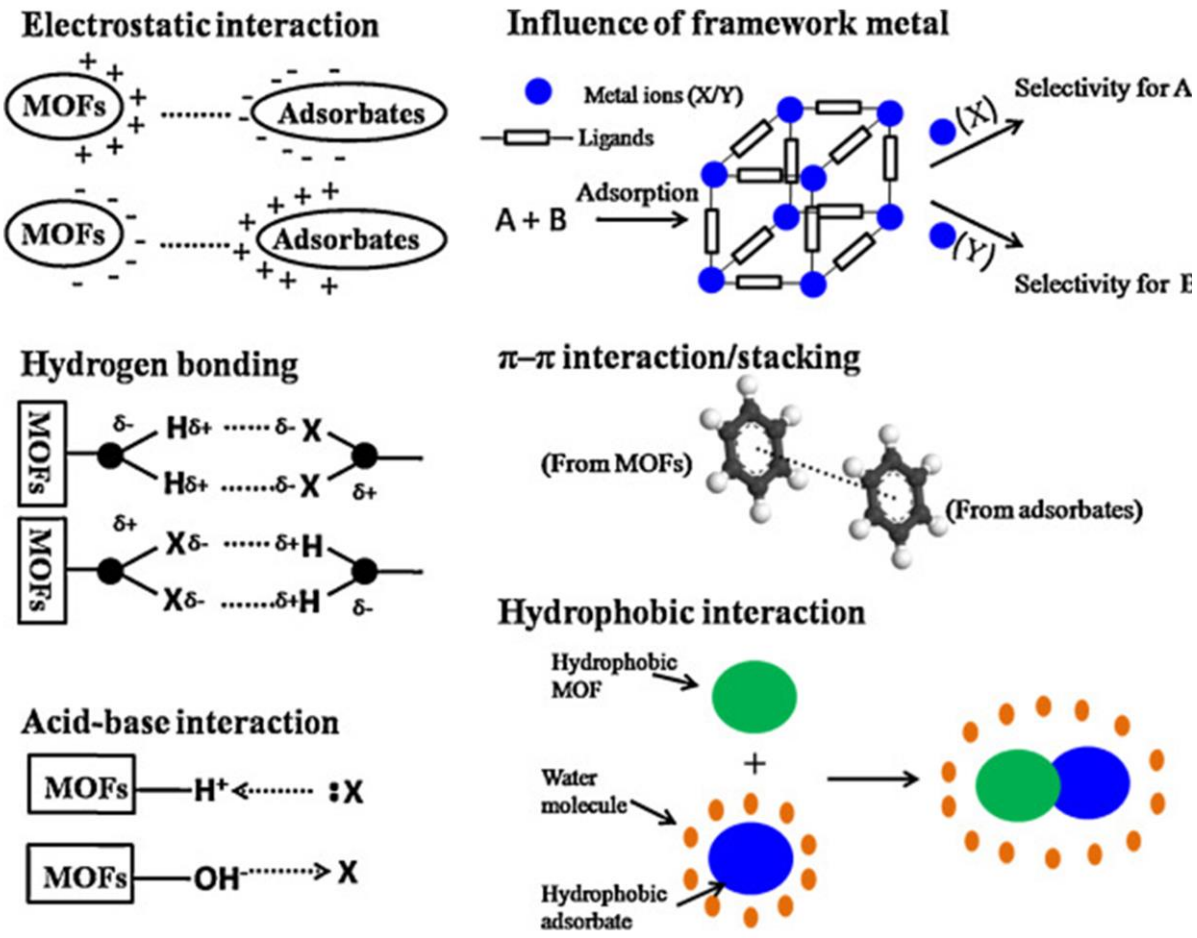

Figure 1.2 Schematic diagram of possible mechanisms for adsorptive removal of hazardous materials over MOFs. Reproduced from Ref. [12] with permission from Elsevier.

In addition, MOFs were also used as electrocatalysts for energy applications in batteries, supercapacitors, and fuel cells,[18] which could significantly reduce the cost of conventional noble metal catalysts. Besides energy and environmental sustainability, MOFs have also been tried for electronic devices because of the appealing properties, such as tunable electronic conductance and dielectric propertis.[1]

1.2 MOFs Based Composites

The functionalities of MOFs can also be improved and extended by the integration with other active materials, including metal and metal oxide nanoparticles.[19-20] For instance, the ability of MOFs for hydrogen storage can be enhanced with the incorporation of metal nanoparticles, which would provide stronger interactions with hydrogen molecules rather than weak van der Waals interactions.[21] As reported by Zlotea *et al.*,[22] the impregnation of Pd in MIL-100(Al) could significantly improve the hydrogen uptake at room temperature even with decreased surface area, which might be attributed to the formation of Pd hydride. Similarly, the integration of Mg nanoparticles with MOFs (**Figure 1.3a**) were also found to have higher isosteric heat of hydrogen physisorption.[23] In addition to H_2 storage, the assembly of metal nanoparticles and MOFs also improves the catalytic efficiency, where metal nanoparticles serve as active sites and MOFs provide porous matrix, preventing metal nanoparticles from aggregation. As an example, Aijaz *et al.*[24] immobilized ultrafine Pt particles (~ 1.8 nm) throughout MIL-101's internal cavities with the aid of special geometry of MIL-101 crystals. The as-prepared Pt@MIL-101 exhibited extraordinary catalytic performance in liquid, gas, and solid phases. Leus *et al.*[25] synthesized an

Au@UiO-66 composite with Au nanoparticles homogeneously distributed inside UiO matrix, which displayed not only excellent oxidation catalytic performance in terms of efficiency and selectivity but also good stability.

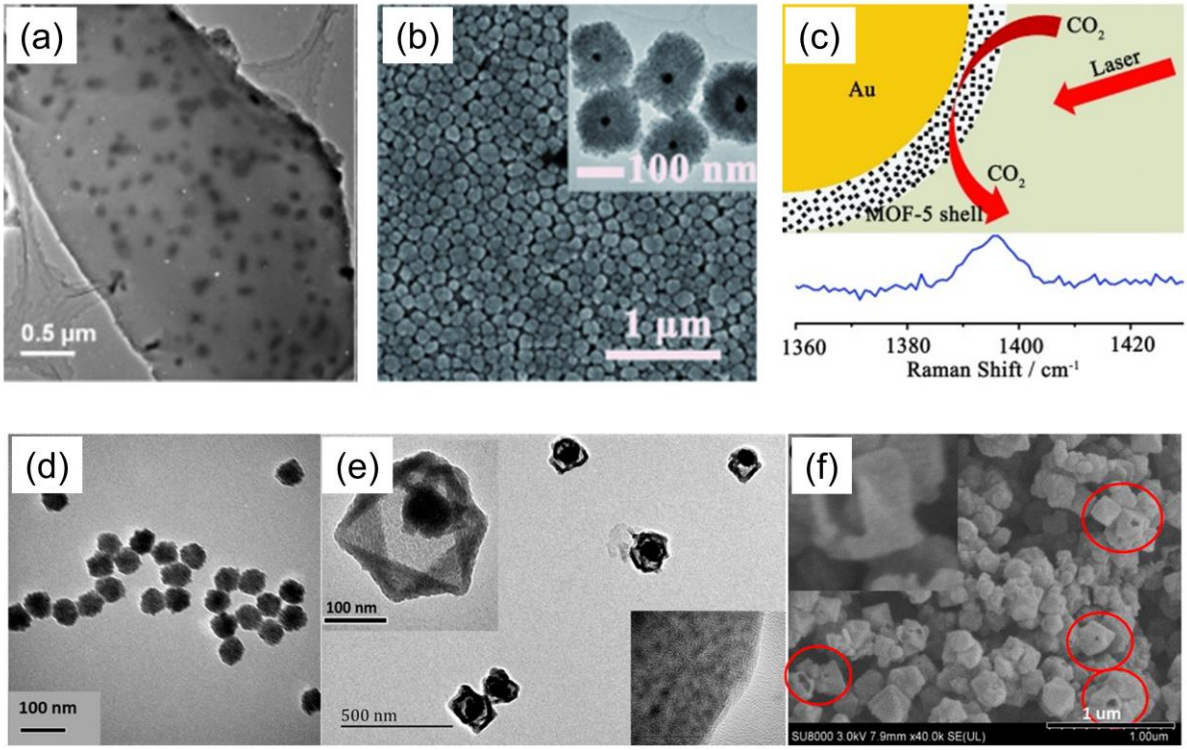

Figure 1.3 (a) High-resolution transmission electron microscopy image of Mg@SNU-90. Reproduced from Ref. [23] with permission from John Wiley and Sons; (b) Scanning electron microscopy (SEM) and transmission electron microscopy (TEM) image of the core-shell Au@MOF-5; (c) Schematic illustration of CO_2 sensing using Au@MOF-5. Reproduced from Ref. [27] with permission from John Wiley and Sons; (d) TEM image of Co_3O_4; TEM image (e) and SEM image (f) of yolk-shell Co_3O_4@MOFs. Reproduced from Ref. [30] with permission from American Chemical Society.

Beyond gas adsorption and catalysis, the metal nanoparticles and MOFs are also complementary to each other in the case of sensing. More specifically, the porous structures of MOFs would function as pre-concentrators and molecular filters, while metal nanoparticles provide physical responses when interacting with target molecules.[19] Taking Pt@UiO-66 for an example, the narrow windows of UiO-66 structure (6 Å) only allow the penetration of small molecules, which gives the composite excellent ability for H_2O_2 detection along with high selectivity.[26] Moreover, the surface chemistry of MOFs also contributes to selective sensing.[27] For instance, the aromatic rings in MOF-5 could selectively and strongly interact with CO_2 through electrostatic attraction.[27-28] Combined with the remarkable optic properties of Au nanoparticles, the Au@MOF-5 composite (**Figures 1.3b and c**) exhibited excellent selective detection of CO_2.[27]

In addition to metal nanoparticles, the integration of metal oxide nanoparticles with MOFs is also of great research interest in various applications.[29-30] For instance, Zeng *et al*.[30] designed a yolk-shell Co_3O_4@MOF composite (**Figures 1.3d-f**) as an efficient catalyst for sulfate radical-based advanced oxidation processes. The as-designed composite structure possesses several benefits compared with conventional Co_3O_4, including the anti-aggregation property of Co_3O_4, protection of Co_3O_4 from bulk solution while preserving accessible active sites, and confinement effect. As a result, the Co_3O_4@MOF composite demonstrated ~ 40% higher efficiency than bare Co_3O_4 toward 4-chlorophenol degradation.[30]

Recently, intensive attention has been drawn in the area of photocatalytic applications by MOF/semiconductor composite catalysts, which combine the merits of both components and have

been showing huge potential for energy and environmental sustainability.[31-34] In particular, bare MOFs are less efficient photocatalysts than semiconductors, mainly because of their unfavorable separation of the photo-induced charge carriers.[33] On the other hand, MOFs possess many merits, such as high surface area, huge porosity, broad light absorption region, and coordinatively unsaturated metal sites, which are usually unattainable with conventional semiconductors. Therefore, efforts have been made to integrate both types of materials and create efficient composite photocatalysts.[35-36] Taking CO_2 photoreduction for an example, the incorporation of MOF-74(Mg) would significantly boost the photocatalytic efficiency of Zn_2GeO_4 via improved CO_2 encapsulation and activation.[35] Similar results were also reported with ZIF-8/Zn_2GeO_4, where the incorporated ZIF-8 could significantly improve the adsorption of dissolved CO_2 in the aqueous medium and enhance the overall photocatalytic efficiency.[36]

In the meantime, the intimate interaction between MOFs and semiconductors would promote the charge transfer between two components, which would inhibit the recombination of charge carriers and thus enhance the overall photocatalytic efficiency.[35, 37-40] For instance, Su *et al*.[37] synthesized a $Cd_{0.2}Zn_{0.8}S$@UiO-66-NH_2 composite photocatalyst, which exhibited better performance in both CO_2 reduction and H_2 evolution than the pristine components. The major reason for the enhancement in photocatalytic efficiency was demonstrated to be the facilitated charge transfer at the interface as evidenced by transient photocurrent responses and photoluminescence measurements.[37]

Despite the great achievement in this area, additional efforts are necessary to improve the mechanistic understanding of photocatalytic pathways of those MOF-based composites. For instance, it is still unclear what the interface structures are like and how these special interface structures affect the charge transfer.

1.3 Synthesis of MOFs Based Materials

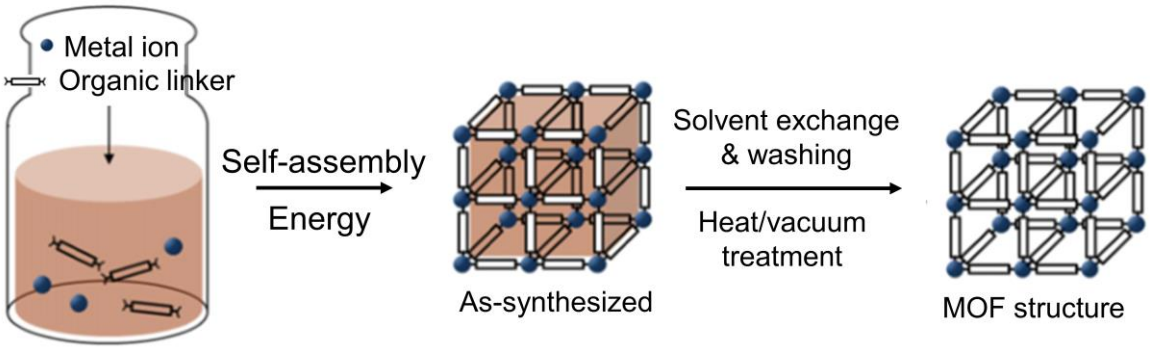

Figure 1.4 Conventional method for the synthesis of MOFs. Reproduced from Ref. [41] with permission from Springer.

The MOFs are generally synthesized via conventional heating method (**Figure 1.4**),[41] where metal ions and organic ligands are dissolved in solvents, which subsequently subject to heating under sealed conditions. Typically, there are two temperature ranges for the synthesis of MOFs. One range is above the boiling point of the solvent, and the other one is below the boiling point, which generally are referred as solvothermal method and nonsolvothermal method, respectively. During the heating process, two steps occur for the framework assembly, including nucleation and crystal growth. With the aid of many *in situ* and *ex situ* characterization tools, systematic exploration of the formation mechanism has been carried out.[4] For example, extended

X-ray absorption fine structure (EXAFS) spectroscopy was applied to monitor the formation pathways of MIL-89.[42] In that study, trimeric iron clusters were used as the starting materials, which remained intact throughout the crystallization process. Moreover, the results also showed the similarity between MIL-89 and classical aluminosilicate zeolite in terms of crystallization. In both cases, amorphous phases were firstly formed and then dissolved to form the final crystalline structure.[42] Recently, Saha *et al*.[43] studied the formation mechanism of ZIF-71 by using light and X-ray scattering techniques. The results also indicated that ZIF-71 was formed from amorphous clusters (mainly by coagulation and monomer addition) to the crystalline structure (i.e., RHO topology). A schematic illustration of the ZIF-71 formation was presented in **Figure 1.5**.

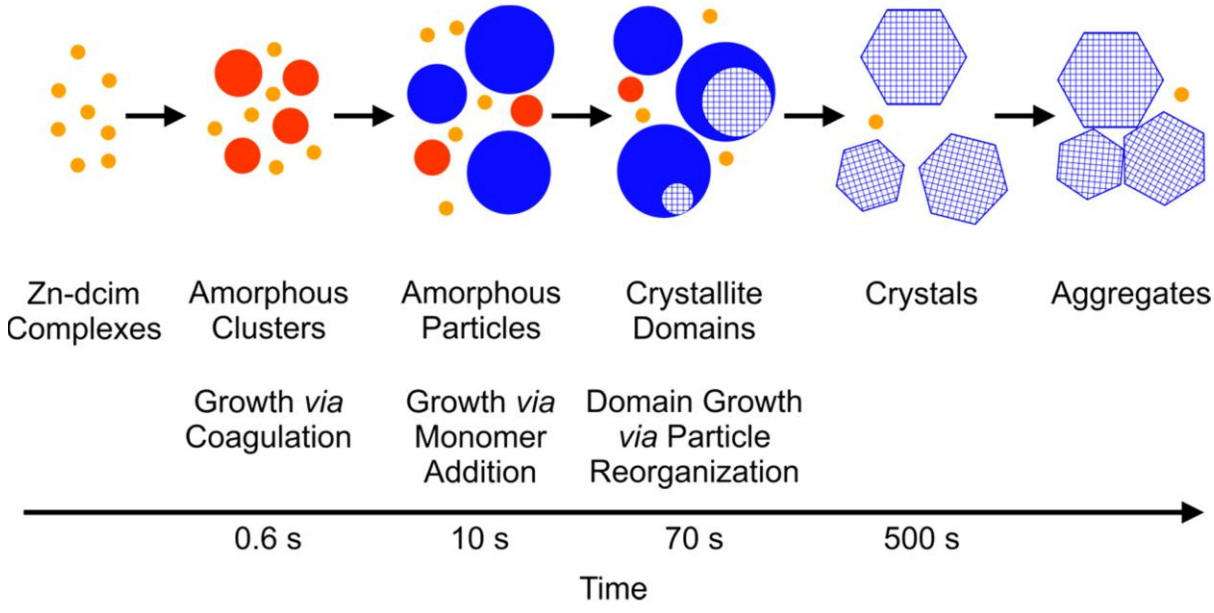

Figure 1.5 A simplistic scheme outlining the proposed steps and intermediates in the formation of ZIF-71. Reproduced from Ref. [43] with permission from American Chemical Society.

Despite the convenience, there are several issues associated with the conventional synthesis method, such as ununiform heating and long reaction duration. Therefore, many other routes have been applied for the MOFs synthesis (**Figure 1.6**), including electrochemistry, atomic layer deposition (ALD), and microwave.[44] With those external energy input (e.g., microwave and ultrasound), several issues existing in the conventional hydrothermal method could be solved. For instance, the microwave irradiation can provide faster and more efficient heating than the conventional method, as the microwaves interact directly with reactants. For the conventional method, thermal energy has to pass through the reactor before getting to the reactants, leading to less efficient heating.[44] As a comparison, for the same production yield of MIL-100(Cr), it only requires 4 hours for the microwave method but 4 days for the conventional heating.[45]

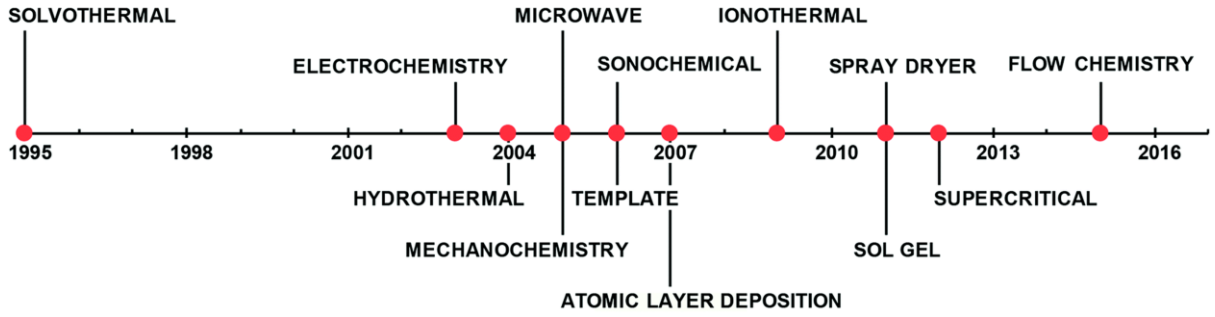

Figure 1.6 Timeline of the most common synthetic approaches patented for the synthesis of MOFs. Reproduced form Ref. [44] with permission form The Royal Society of Chemistry.

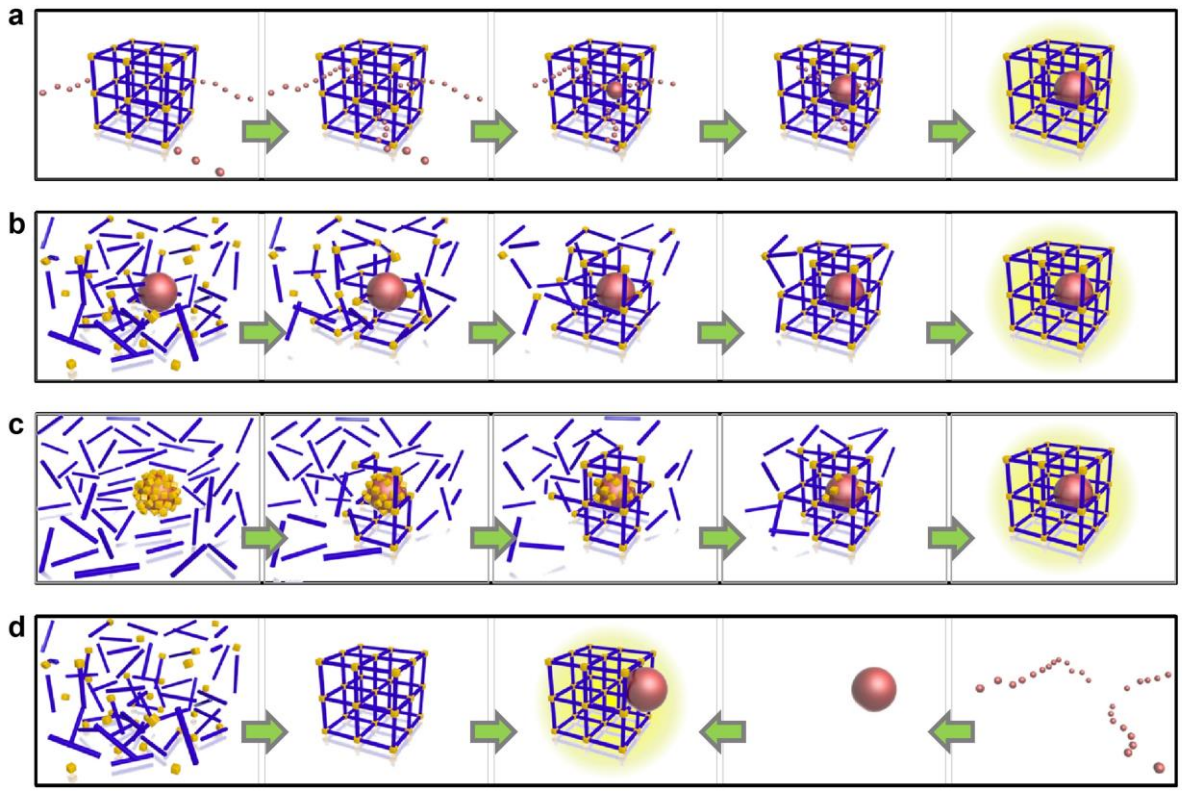

Figure 1.7 Different synthetic approaches for the preparation of nanoparticles@MOF composite: (a) infiltration in preformed MOFs, (b) self-assembly of MOFs encapsulating the nanoparticles, (c) pseudomorphic replication converting a ceramic shell of a core-shell nanoparticle into a MOF, (d) individual preparation of MOFs and nanoparticles and subsequent mixing. Reproduced from Ref. [19] with permission from Elsevier.

Unlike pristine MOFs, the synthesis of MOF-based composites requires more complicated steps to ensure the intimate interaction among MOFs and other components. In general, there are four different routes to prepare the composite materials.[19] As shown in **Figure 1.7a**, the first route is to introduce the starting chemical for the second component into the MOFs' porous structure. With proper treatment (e.g., heating or reduction), the starting chemicals would be converted to

the functional nanoparticles. On the other hand, functional nanoparticles could be synthesized firstly and then put into the precursors of MOFs, followed by the growth of MOFs around the nanoparticles (**Figures 1.7b** and **c**). The last route is to directly combine the pre-synthesized MOFs and nanoparticles to form the composites (**Figure 1.7d**).

It should be noted that, in these methods, many complicated steps are involved, such as mixing and post-treatment, which might cause bath-to-bath errors. Sometimes, harsh chemicals, like HF,[31, 33] are inevitable, which makes the synthesis procedures more complicated. To address the above issues, a novel approach should be developed to simplify the synthesis procedures.

1.4 Objectives and Arrangement of the Dissertation

As mentioned above, the conventional hydrothermal method requires very long reaction times and is difficult to scale up. Despite the development of some new synthesis methods, a novel strategy is still needed to solve the long-standing issues in wet-chemistry methods, like inhomogeneous mixing and complicated procedures. Beyond the synthesis of MOFs and MOF-based composites, the photocatalytic applications of MOF-based composites are also of great interest for energy and environmental sustainability. However, the mechanism of those photocatalytic processes is still vague and requires further exploration. Herein, this dissertation targets these aforementioned issues and it is composed of two major parts: (1) the exploration of a facile strategy to synthesize MOFs via aerosol route (**Chapters 2-3**) and (2) the facile preparation of MOF-based composites (**Chapters 4-5**) and mechanistic insights into their photocatalytic applications (**Chapters 6-8**).

More specifically, **Chapter 2** introduces the modulated synthesis of a typical MOF via the aerosol route by adjusting operating pressures, where systematic experimental and simulation work were carried out to advance the fundamental understanding of MOF synthesis using the aerosol route. **Chapter 3** demonstrates the versatile functions of the aerosol route for the synthesis of MOF-based materials. In particular, mixed-linker MOFs (i.e., Cu-TMA/Cu-BDC) were synthesized via the aerosol route, and the properties of the mixed-linker MOFs (i.e., morphology, crystalline phase, and porous structure) were found to be dependent on the component compositions. The results demonstrate that synthetic parameters can be varied to optimize both the properties and performance of the mixed-linker MOFs via the aerosol route.

In **Chapter 4**, a facile route was developed to prepare the ZnO@ZIF core-shell nanofiber using electrospinning. **Chapter 5** demonstrated the facile preparation of MOF/semiconductor composites using the aerosol route. The roles of synthetic parameters (e.g., temperature and precursor component ratio) on the properties of as-prepared materials were systematically studied. The as-prepared composites exhibited good crystallinity and large surface area, and showed significantly improved photocatalytic efficiency toward CO_2 photoreduction.

In-depth understanding of CO_2 photoreduction by MOF-based composite catalyst was illustrated in **Chapter 6**. Specifically, a ternary $TiO_2/Cu_2O/Cu_3(BTC)_2$ composite photocatalyst was designed and demonstrated as an efficient photocatalyst for CO_2 photoreduction (i.e., higher production rate and preferential formation of CH_4). Systematic measurements and analysis revealed that the coordinatively unsaturated copper sites played a vital role in both charge transfer

and CO_2 activation. Apart from CO_2 photoreduction, the MOF/semiconductor composites are also promising photocatalysts for water remediation. As presented in **Chapter 7**, highly-oriented one-dimensional MOF/semiconductor nanoarrays were prepared for the efficient photodegradation of antibiotics in wastewater. Further exploration was made to get mechanistic insights into the photocatalytic pathways of MOF/semiconductor composites, the results of which were illustrated in **Chapter 8**. It was found that, the combination of MOFs and semiconductors would enhance both photocatalytic reduction and oxidation, which mainly attributed to the fast charge transfer at the interface.

Chapter 2. Pressure-Regulated Synthesis of Cu(TPA)·(DMF) in Microdroplets for Selective CO_2 Adsorption

Dalton Transactions, 48(3): 1006-1016 (2019)
DOI: 10.1039/C8DT03812K

Abstract

The synthesis of metal-organic frameworks (MOFs) by using traditional wet-chemistry methods generally requires very long durations and still suffers from non-uniform heat and mass transfer within the bulk precursor solutions. Towards addressing these issues, a microdroplet-based spray method has been developed. In a typical spray process, the MOF's precursor solution is first atomized into microdroplets. These droplets serve as the microreactors to ensure homogeneous mixing, fast evaporation, and rapid nucleation and crystal growth to form MOF particles. However, the fundamental MOF formation mechanisms by using this strategy have not been fully understood. In this work, the role of the operating pressure in the synthesis of a representative MOF (i.e., Cu(TPA)·(DMF); TPA: terephthalic acid, DMF: dimethylformamide) was systematically investigated. Detailed characterization showed that the pressure variations significantly affected both the morphologies and crystalline structures of Cu(TPA)·(DMF). Numerical simulations revealed that the morphology changes are mainly attributed to the variations in supersaturation ratios, which are caused by different microdroplet evaporation rates due to the regulation of operating pressure. While the crystalline structure variations are closely related to the dissociation of DMF molecules at lower operating pressures. Besides, the dissociation of DMF molecules decreased the surface area of the MOF crystals, but gave rise to massive coordinatively unsaturated metal sites, which greatly enhanced the interaction of CO_2 with the MOF crystal and thus led to improved CO_2 adsorption capacity and selectivity. The outcome of this work would shed new light on the fundamental understanding of MOF synthesis using the microdroplet-based spray method.

2.1 Introduction

Metal-organic frameworks (MOFs), a family of porous polymer materials, are becoming a rising star in material science by virtue of their huge porosity, exceptional surface area, and tunable surface chemistry.[1-3] MOFs are constructed from metal ions/clusters and organic ligands. The abundance of various metal ions and organic linkers grants MOFs considerable diversity. Examples of typical MOF series include ZIFs (zeolitic imidazole frameworks),[4] UIOs (University of Oslo),[5] MILs (Materials of Institute Lavoisier),[6] and CAUs (Christian-Albrechts University).[7] Given the extraordinary properties of MOFs, they have been used in a broad range of applications, including gas separation,[8] gas storage,[9] catalysis,[10-11] water treatment,[12-13] sensing,[14] and biomedical applications.[15] MOFs can also be integrated with other materials (e.g., metals and semiconductors) to enhance their functionalities and efficiencies by boosting molecule adsorption, facilitating charge transfer, and promoting molecule activation.[16-19]

Conventionally, MOFs are synthesized through heating bulk precursor solutions via wet-chemistry processes (e.g., the solvothermal method), where the structure evolution takes place, including deprotonation, coordination, nucleation, and crystal growth.[3] The wet-chemistry methods, however, are usually plagued with long synthesis durations due to inhomogeneous mixing and slow heat transfer within the bulk precursor solutions. For example, in a typical solvothermal process, it generally takes hours even days to obtain well-crystallized ZIF-8 crystals.[20] Various forms of external energies have been used to assist the MOF synthesis, such as microwave irradiation,[21] ultrasound,[22] electric potential,[23] and mechanical force.[24] Recently, a

microdroplet-based spray strategy was developed for the fast and high-throughput synthesis of MOFs.[25, 26] In a typical spray process, the MOF precursor solutions are firstly atomized into droplets with the size ranging from micrometers to millimeters. These droplets serve as microreactors, where uniform mixing and fast heat transfer can be easily achieved to promote efficient deprotonation and coordination. The microdroplets are then subjected to heating for solvent evaporation, nucleation, and crystal growth to form the final MOFs crystals. The whole process only takes about several seconds to complete, making the spray route a rational strategy for the fast synthesis of MOFs. Besides, the spray method can also be used for the postsynthetic modification of MOFs,[27] manufacture of multicomponent MOF superstructures[25] and hierarchical MOFs.[28] It should be noted that, the synthesis of MOFs by using the spray method is still in its early stage. More work needs to be conducted to unravel the formation mechanism of MOFs in this rapid process.

In particular, the evaporation of microdroplets is the first and foremost step of the synthesis of MOFs by using the spray process, because the solvent evaporation of microdroplets directly influences the kinetics of supersaturation of precursors,[29] which will have great effects on the subsequent MOFs formation steps, i.e., nucleation and crystal growth.[3, 30] Fundamentally, the evaporation of microdroplets is a macroscopic phenomenon of microscopic heat and mass transfer,[31] which is generally controlled by several factors, including solvent types, operating temperature, and pressure. In a recent study, we studied the effect of operating temperature on the synthesis of $[Cu_3(TMA)_2(H_2O)_3]_n$ (TMA: trimesic acid) via the microdroplet-based spray

method.[26] The results showed that, the operating temperature affected not only the crystal size but also the accessible open coordination sites. It should be noted that, $[Cu_3(TMA)_2(H_2O)_3]_n$ became amorphous under operating temperatures higher than 300 °C due to the disintegration of organic ligands. Compared with temperature, the adjustment of operating pressure is a milder way to regulate the synthesis of MOFs in microdroplets. Based on the previous studies of inorganic materials formation in microdroplets,[32-33] the regulation of operating pressure would dramatically change the evaporation behaviors of microdroplets,[34] which will alter the supersaturation ratios, nucleation and crystal growth kinetics, and eventually gives rise to different properties of the final products. However, the role of operating pressure in the formation of MOFs in microdroplets has not yet been explored thus far.

Herein, the current work aims to investigate the effect of operating pressure on the formation of MOFs in microdroplets. To be specific, a spray process equipped with a pressure control system was built. A representative MOF, Cu(TPA)·(DMF) (TPA: terephthalic acid, DMF: dimethylformamide), was chosen and synthesized under different operating pressures ranging from 0.2 atm to 1 atm (**Scheme 2.1**). Systematic material characterizations and numerical simulations of microdroplets evaporation were conducted to investigate the changes in MOF's properties brought by the variation in operating pressure. The results showed that, the operating pressure has significant effects on the MOF in terms of morphology, chemical structure, and gas adsorption ability (**Scheme 2.1**). Based on the results, a reasonable mechanism was proposed to

explain the dependence of MOF's properties on operating pressure. The results from this work would advance the understanding of MOFs' synthesis by using the spray strategy.

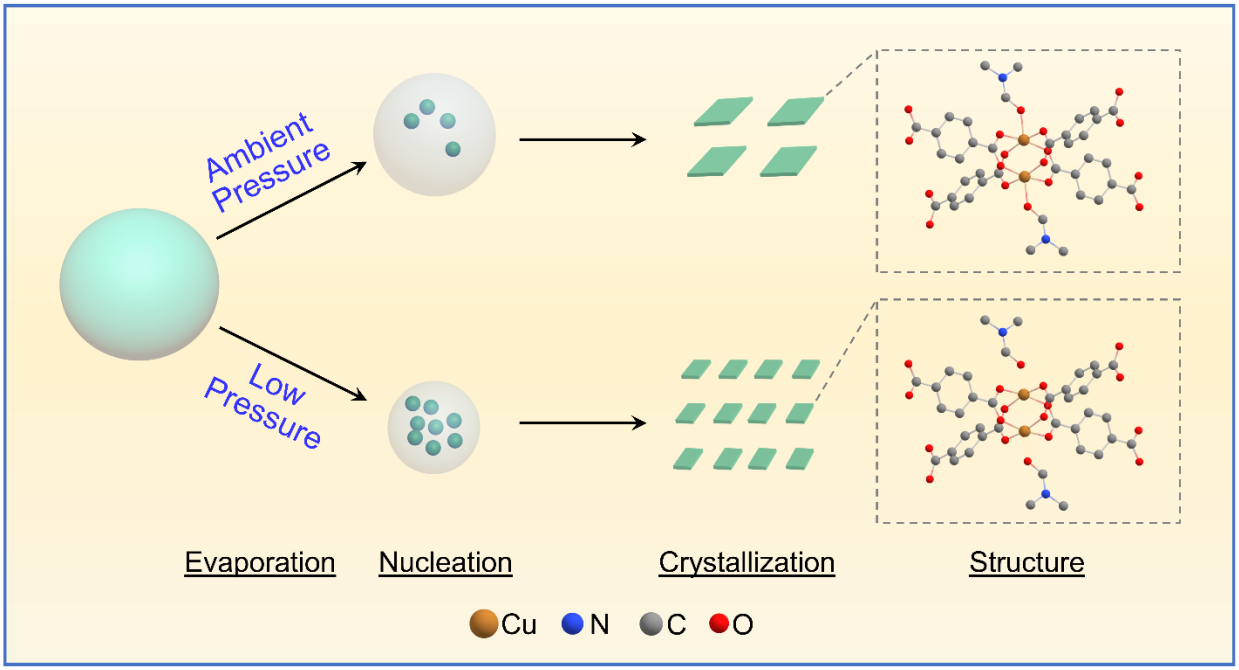

Scheme 2.1 Schematic illustration of the synthesis of Cu(TPA)·(DMF) in microdroplets under various operating pressures.

2.2 Materials and Methods

Synthesis Process. As illustrated in **Scheme 2.2**, the microdroplet-based spray process is composed of several parts, including a Collison nebulizer, a tube furnace, a sample collector (i.e., microfiber filter) and a pressure control system. In a typical synthesis process, the precursor solution was firstly prepared by dissolving 0.2174 g $Cu(NO_3)_2{\cdot}3H_2O$ and 0.0997 g terephthalic acid (TPA) in 15 mL dimethylformamide (DMF). Subsequently, the precursor solution was nebulized into microdroplets, which were carried by an air flow (1.5 L/min) passing through the

tube furnace at a pre-set temperature (200 °C). Flying through the furnace, the microdroplets underwent solvent evaporation, nucleation, and crystallization. The particles were finally collected by using the microfiber filter. During the spray process, the pressure inside the tube was adjusted within the range of 0.2 atm to 1 atm.

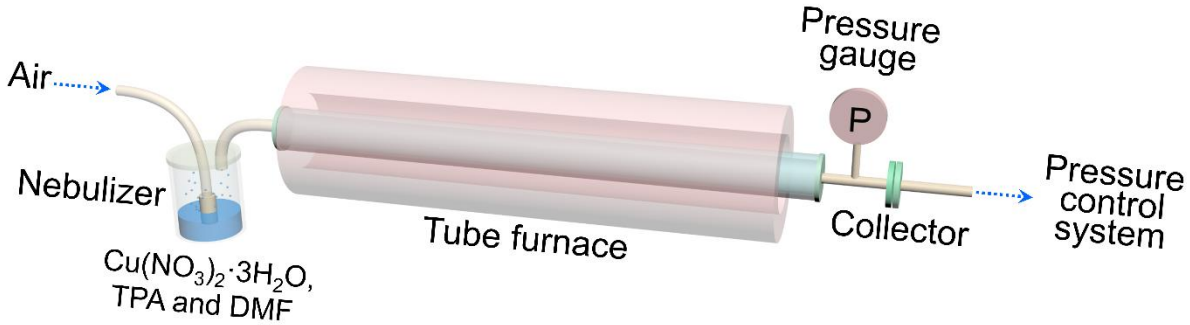

Scheme 2.2 Schematic illustration of the experimental set-up for the microdroplet-based synthesis of MOFs under various operating pressures.

Material Characterization. Detailed characterization of the as-synthesized samples was carried out by using scanning electron microscopy (SEM, Hitachi SU-70), X-ray powder diffraction (XRPD, PANalytical X'Pert Pro Diffractometer: Cu-Kα radiation source (λ = 1.5401Å); reflection mode; step size = 0.026°; time per step: 27.54 s), Fourier-transform infrared spectroscopy (FT-IR, Thermo Scientific Nicolet iS50), Raman spectroscopy (Horiba LABRam Spectrometer), X-ray photoelectron spectroscopy (XPS, Thermofisher ESCALab 250), and surface area and pore structure analysis (Autosorb iQ).

Gas Sorption Analysis. Autosorb iQ was used to obtain the sorption isotherms of N_2 and CO_2 at 273 K and 298 K. After the measurements, the CO_2 adsorption isotherms at these two temperatures

were fitted with the virial equation (**Eq. 2.1**) to calculate the isosteric heats of CO_2 adsorption (Q_{st}) (**Eq. 2.2**).[35-36]

$$ln(p) = ln(n) + \frac{1}{T}\sum_{i=0}^{A} a_i n^i + \sum_{i=0}^{B} b_i n^i \quad (2.1)$$

$$Q_{st} = -R\sum_{i=0}^{A} a_i n^i \quad (2.2)$$

where, p = gas pressure (Torr); n = amount of adsorbed gas molecules (mmol/g); T = temperature (K); a and b = virial coefficients with no dependence in temperature; Q_{st} = isosteric heat of adsorption (J/mol); R = gas constant (8.314 J/(K·mol)).

Analysis of CO_2/N_2 Adsorption Selectivity. The ideal adsorbed solution theory (IAST), which has been demonstrated to be an accurate method to predict gas adsorption selectivity in numerous prior studies,[37-39] was employed here to analyze the CO_2/N_2 adsorption selectivity of various Cu(TPA)·(DMF) samples. To be specific, the pure-component adsorption isotherms of CO_2 and N_2 were firstly fitted by using the dual-site (**Eq. 2.3**) and single-site (**Eq. 2.4**) Langmuir-Freundlich models, respectively.

$$q = q_{A,sat}\frac{c_A p^{\alpha_A}}{1+c_A p^{\alpha_A}} + q_{B,sat}\frac{c_B p^{\alpha_B}}{1+c_B p^{\alpha_B}} \quad (2.3)$$

$$q = q_{A,sat}\frac{c_A p^{\alpha_A}}{1+c_A p^{\alpha_A}} \quad (2.4)$$

where, q = adsorption quantity (mmol/g); $q_{A,sat}$ and $q_{B,sat}$ = saturate adsorption quantities; subscripted A and B indicate various adsorption sites; c_A and c_B = Langmuir-Freundlich coefficients ($bar^{-\alpha}$, temperature-dependent); p = gas phase pressure (bar); α_A and α_B = dimensionless exponents.

Subsequently, the fitting parameters were incorporated into **Eq. 2.5** to calculate the mole fraction of individual component in the adsorbed phase.

$$\int_0^{P\cdot y1/x1} \frac{q_1}{P} dp = \int_0^{P\cdot y2/x2} \frac{q_2}{P} dp \tag{2.5}$$

where, P = total pressure (bar); x and y = mole fraction of gas component in the adsorbed and bulk phase, respectively; q = adsorption quantity (mmol/g); subscripted numbers were used to differentiate the gas components.

Finally, the adsorption selectivity (S_{ads}) was calculated using **Eq. 2.6**.

$$S_{ads} = \frac{x_1/y_1}{x_2/y_2} \tag{2.6}$$

2.3 Results and Discussions

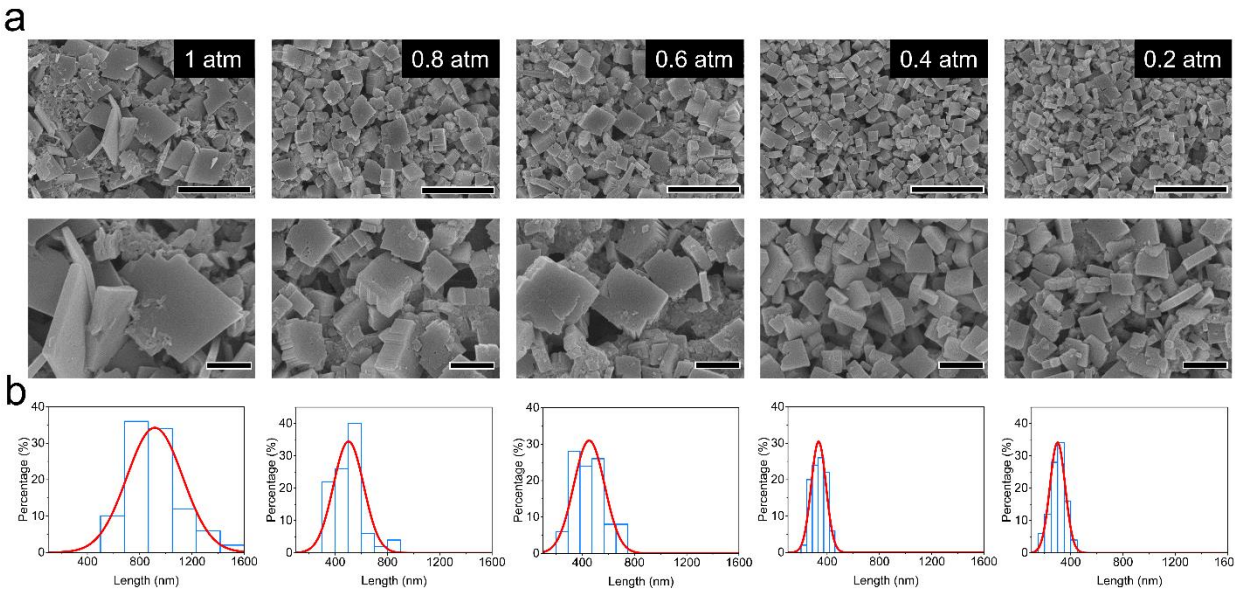

Figure 2.1 (a) SEM images and (b) size distribution histograms of Cu(TPA)·(DMF) synthesized under various pressures. Scale bars in SEM images: 2 μm (up) and 500 nm (down).

Morphology Characterization. The Cu(TPA)·(DMF) samples synthesized under various pressures were subjected to detailed characterization. As exhibited in **Figure 2.1a**, all the Cu(TPA)·(DMF) samples synthesized by the spray process have a sheet morphology, which is consistent with the lamellar crystal structure of Cu(TPA)·(DMF).[40] Notably, the operating pressure affects the size distribution of Cu(TPA)·(DMF) (**Figure 2.1b**). And lower pressures give rise to smaller crystal sizes and more homogeneous size distributions. To be specific, the mean lengths of the Cu(TPA)·(DMF) crystals synthesized under 1, 0.8, 0.6, 0.4 and 0.2 atm were measured to be 915, 502, 453, 334 and 299 nm, respectively. Besides, Cu(TPA)·(DMF) crystals synthesized under ambient pressure (1 atm) have a wide size distribution, ranging from 400 nm to 1600 nm, while the size distribution becomes narrower with decreased pressures. The smaller size and narrow size distribution under lower pressures can be ascribed to faster nucleation rate induced by rapid solvent

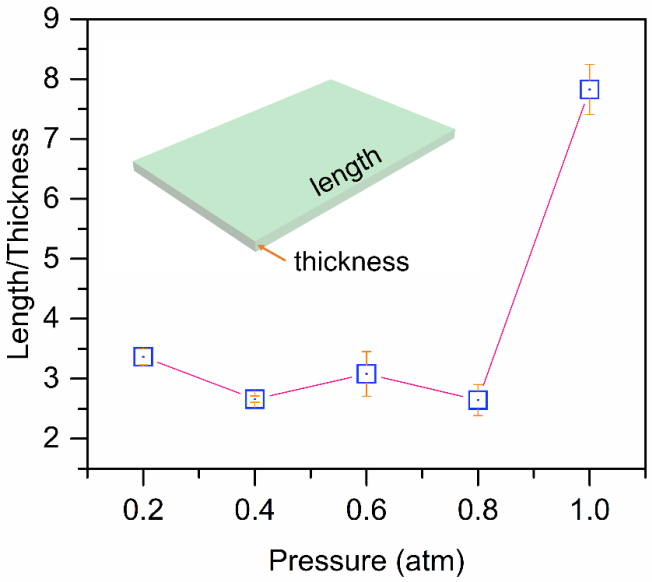

Figure 2.2 Effect of operating pressure on the length/thickness ratio of the samples.

evaporation. In addition, the operating pressure also has a significant effect on the length/thickness ratio of the samples. As shown in **Figure 2.2**, under ambient pressure, the Cu(TPA)·(DMF) exhibits the highest length/thickness ratio (~ 7.8). With the operating pressure smaller than 0.8 atm, the length/thickness ratio stabilizes around 2.6 to 3.4. The variations in crystal size, size distribution, and length/thickness ratio might be related to the pressure-modulated evaporation of the microdroplets during the spray process, as explained in detail in the following section.

Simulation of Microdroplet Evaporation. To better understand the dependence of microdroplet evaporation (i.e., droplet temperature and size) on the operating pressure, numerical simulations were carried out based on the fundamental heat and mass transfer principles.[41] The models are composed of four differential equations (**Eqs 2.7-10**), describing the evolution of droplet diameter (D_d), solvent vapor concentration in air (n), droplet temperature (T_d), and air temperature (T_a) as a function of time, respectively.

$$\frac{dD_d}{dt} = \frac{4D_v m_d (n - n_s)}{\rho_d D_d} \tag{2.7}$$

$$\frac{dn}{dt} = -2\pi D_d D_v N (n - n_s) \tag{2.8}$$

$$\frac{dT_d}{dt} = \frac{3L\frac{dD_d}{dt} + 6\frac{h_d}{\rho_d}(T_a - T_d)}{C_d D_d} \tag{2.9}$$

$$\frac{dT_a}{dt} = \frac{-\pi^2 R^2 {D_d}^2 N h_d (T_a - T_d) + 2\pi R h_t (T_t - T_a)}{F C_a} \times \frac{Q}{\pi R^2} \left(\frac{T_a}{T_a^0}\right)\left(\frac{1 - f_d^0}{1 - f_d}\right) \tag{2.10}$$

where D_d= droplet diameter (m), t = residence time (s), D_v = diffusion coefficient of DMF vapor (m^2/s, derived from **Eq. 2.11**[42]), m_d = molecule mass of DMF (kg), n = number concentration of DMF vapor molecules in air ($1/m^3$), n_s = saturated DMF vapor concentration

($1/m^3$), ρ_d = DMF density (kg/m^3), N = number density of microdroplets in air ($1/m^3$), T_d = temperature of microdroplets (K), K_m = mass transfer coefficient of DMF vapor (m/s), n_t =DMF vapor concentration at tube wall ($1/m^3$), L = latent heat of DMF evaporation (J/kg), h_d = heat transfer coefficient around microdroplets ($W/(m^2 \cdot K)$), T_a = air temperature (K), C_d = heat capacity of DMF ($J/(kg \cdot K)$), R = tube radius (m), h_t = heat transfer coefficient near the tube ($W/(m^2 \cdot K)$), F = mass flow rate of air (kg/s), C_a = heat capacity of air ($J/(kg \cdot K)$), Q = volume flow rate of air (m^3/s), f_d = mole fraction of DMF vapor in air. Superscripted "0" indicates the initial values.

$$D_v = \frac{2.66T_a^{1.5} \times 10^{-7}}{pM_{ad}^{0.5}\sigma_{ad}^2\Omega_D} \tag{2.11}$$

where $M_{ad} = \frac{2}{1/M_a + 1/M_d}$, M_a = molecular weight of air (g/mol), M_d = molecular weight of DMF (g/mol), $\sigma_{ad} = \frac{\sigma_a + \sigma_d}{2}$, σ_a = hard sphere diameter of air (Å), σ_d = hard sphere diameter of DMF (Å), Ω_D is almost unity.

DMF droplets with an initial diameter of 2 μm were selected for simulation. As shown in **Figures 2.3a** and **2.3b**, upon evaporation, the DMF vapor number density in air increased drastically with time, which also leads to the decrease in droplet diameter (**Figures 2.3c** and **2.3d**). Notably, a lower operating pressure would enhance the diffusion coefficient of DMF vapor (**Eq. 2.11**), which would fasten the droplet evaporation and thus give rise to a higher DMF vapor number density and a smaller droplet diameter. To be specific, at the evaporation time of 0.04 ms, the diameter of the microdroplets was calculated to be 1.64 μm under the operating pressure of 1 atm, but decreased to 1.44 μm under 0.2 atm. The rapid decrease in droplet diameter under lower operating pressures would significantly increase the concentration of reactants, and therefore result

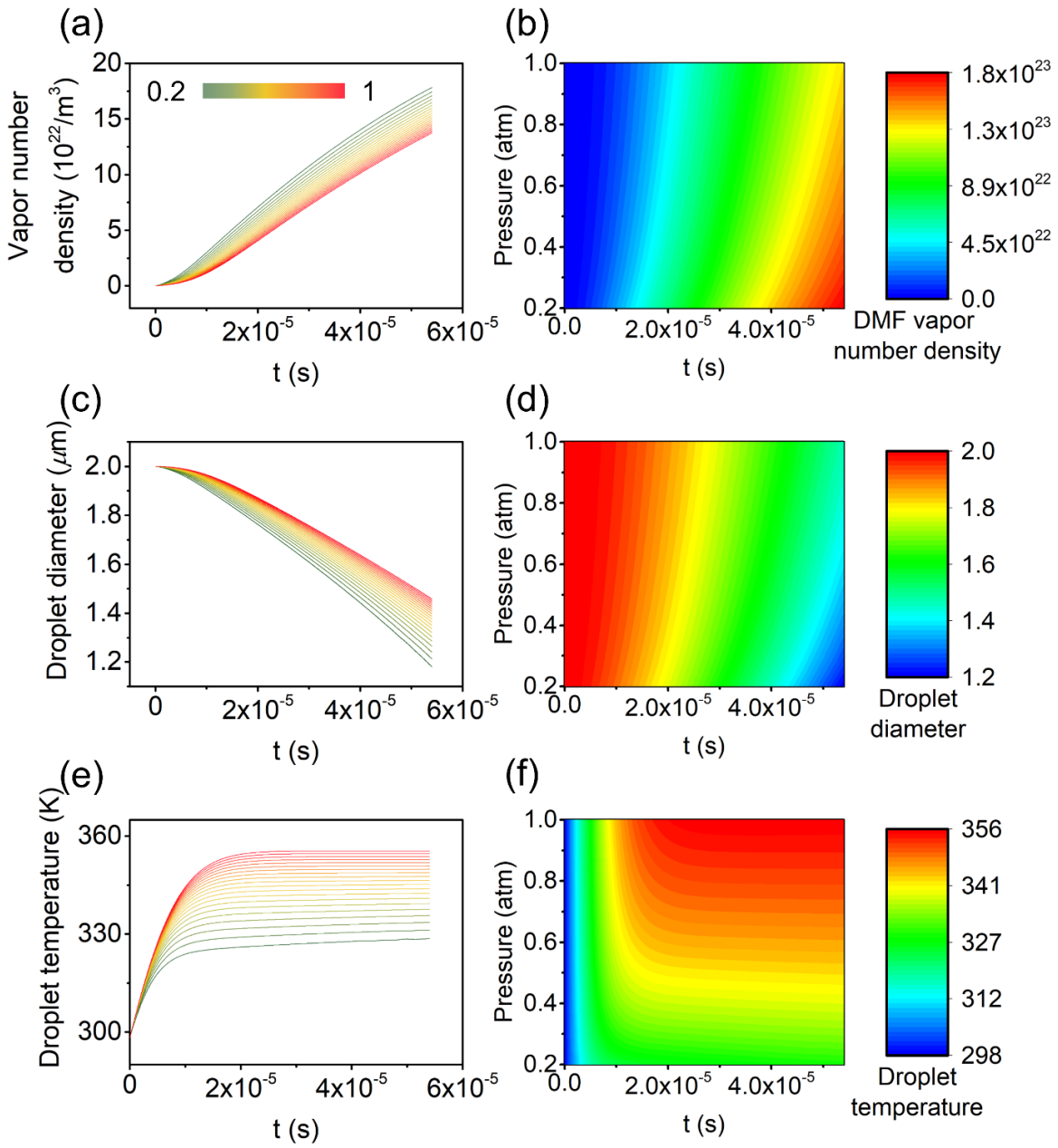

Figure 2.3 Evolution of DMF vapor density (a and b), droplet diameter (c and d), and droplet temperature (e and f) as a function of reaction time under various operating pressures. (a, inset) is the color bar used to indicate various operating pressures (unit: atm) for a, c, and e.

in faster increase in supersaturation ratio. The increase in supersaturation ratio would drastically promote the nucleation process.[26] In particular, more seed nuclei can be obtained under lower operating pressures, which would yield smaller crystals. The simulation results are consistent with the SEM images (**Figure 2.1**). Meanwhile, a lower operating pressure also reduces the equilibrium temperature of the microdroplets (**Figure 2.3e** and **2.3f**). For instance, the equilibrium temperature of the droplet under 1 atm is 355 K, while the equilibrium temperature decreases to 329 K when process is operated under 0.2 atm. The results indicate that the evaporative cooling effect[34] becomes more prominent under lower operating pressures, which will also make partial contributions to the increased supersaturation ratios.

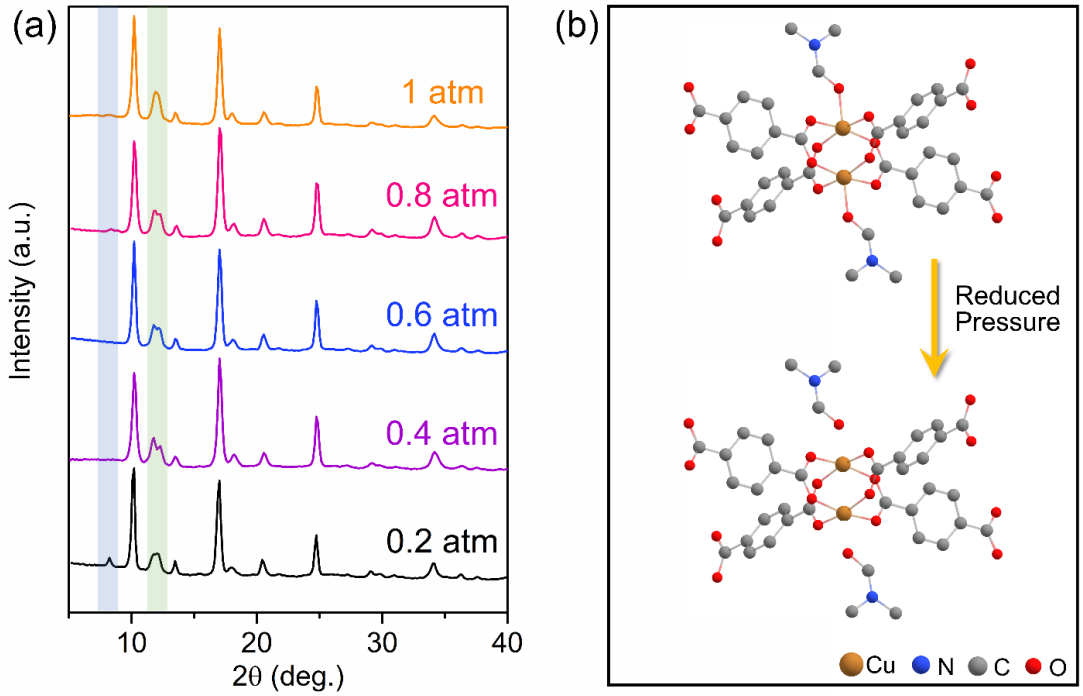

Figure 2.4 (a) XRPD patterns; (b) Schematic illustration of the effect of pressure on the crystal structure of Cu(TPA)·(DMF).

Chemical Properties Analysis. In addition to the morphology variations, the pressure also plays a significant role in the crystallinity of the products. As shown in **Figure 2.4a**, the XRPD patterns of the as-prepared samples agree well with the one reported previously.[40] It is clear from the structure of Cu(TPA)·(DMF) (CCDC-687690)[40] that, the DMF molecules are coordinated with the Cu sites from one end, leaving the other end dangling inside the pores, which become vulnerable upon the variations of temperature and pressure during the synthesis process. Interestingly, with decreasing pressures, the diffraction peak at 12° gradually splits into two peaks. When synthesized at a very low pressure (i.e., 0.2 atm), a new diffraction peak shows up at 8.2°. The variations in crystallinity may be attributed to the loss of DMF coordinated to Cu^{II} sites during the spray process under low-pressure conditions (**Figure 2.4b**), which is analogue to the temperature-modulated changes in crystal structures as reported previously.[40] Despite the various crystal structures, the samples synthesized under various pressures possess similar functional groups as demonstrated from the FT-IR and Raman spectra. All the functional groups stem from the Cu(TPA)·(DMF) crystals.[40, 43] The assignments of the primary IR frequencies and Raman shifts are summarized in **Table 1**. For instance, the IR bands at 676, 1105, 1255, 1386, and 1663 cm^{-1} can be assigned to δ(OCN), $r(CH_3)$, υ_a(C'N), δ(CH) and υ(CO), respectively. All these peaks originate from the DMF molecules existed inside Cu(TPA)·(DMF) crystals. Compared with those of the free DMF molecules, these peaks redshift a little bit to higher wavenumbers. The IR band at 1604 cm^{-1} corresponds to υ_a(COO) of TPA. More information was obtained from the Raman spectra. In particular, the bands at the Raman shifts of 182 and 316 cm^{-1} can be ascribed to ν(Cu-Cu) and ν(Cu-O), respectively.

Table 2.1 The assignments of the representative IR wavenumbers and Raman shifts.

FT-IR		Raman	
Wavenumber (cm^{-1})	Assignment	Raman shift (cm^{-1})	Assignment
676	δ(OCN)	182	ν(Cu-Cu)
882	υ_s(C'N)	316	ν(Cu-O)
1105	r(CH_3)	1430	υ_s(COO)
1255	υ_a(C'N)	1609	ν(C=C)
1386	δ(CH)		
1439	δ_s(CH_3)		
1604	υ_a(COO)		
1663	υ(CO)		

The surface elemental information of Cu(TPA)·(DMF) crystals synthesized under various pressures was examined through XPS measurements. The results show that, all samples exhibit almost identical XPS spectra, including survey scans and high-resolution spectra. Primary elements in Cu(TPA)·(DMF) crystal were identified. In particular, the peaks at 932.5 eV and 952.5 eV can be assigned to Cu 2p3/2 and Cu 2p1/2, respectively.[16] While, the peaks center at 398.3 eV and 529.7 eV correspond to N 1s and O 1s, respectively.[44-45] The minimal differences in FTIR, Raman and XPS results among the samples indicate that, even though the DMF molecules are dissociated from the copper sites at low operating pressures, they might be still trapped inside the pores of the MOF crystals.

The dissociation of DMF from copper sites in Cu(TPA)·(DMF) samples also gives rise to the changes in other properties, including surface area and availability of coordinatively unsaturated copper sites. The surface area and pore size distribution of the samples were analyzed with nitrogen sorption experiments. In particular, the Brunauer–Emmett–Teller (BET) method was used to derive the surface areas. The results show that Cu(TPA)·(DMF) sample synthesized at 1 atm (hereafter Cu(TPA)·(DMF)_1) has a BET surface area of 1187 m^2/g, while the one synthesized at 0.4 atm (hereafter Cu(TPA)·(DMF)_0.4) only has a BET surface area of 57 m^2/g. The nitrogen sorption isotherms of the samples are shown in **Figure 2.5**. For Cu(TPA)·(DMF)_1, the rapid increase in nitrogen uptake observed at low relative pressure ($P/P_0 < 0.01$) indicates the abundance of micropores, while the slight increase at high relative pressure and the existence of hysteresis suggest the presence of mesopores. For Cu(TPA)·(DMF)_0.4, similar nitrogen sorption isotherm was observed but with fewer micropores. The co-existence of mircopores and mesopores is also confirmed by the pore size distribution results. As shown in **Figures 2.5b** and **2.5d**, Cu(TPA)·(DMF)_1 and Cu(TPA)·(DMF)_0.4 exhibit similar pore size distributions. Fewer micropores are observed in the case of Cu(TPA)·(DMF)_0.4, which is consistent with the nitrogen sorption isotherms. The change in the porous structures becomes more apparent when a lower pressure (0.2 atm) was used, where the sample was designated as Cu(TPA)·(DMF)_0.2. In particular, Cu(TPA)·(DMF)_0.2 has a BET surface area of 49 m^2/g, with a dominated pore diameter of 27.7 Å.

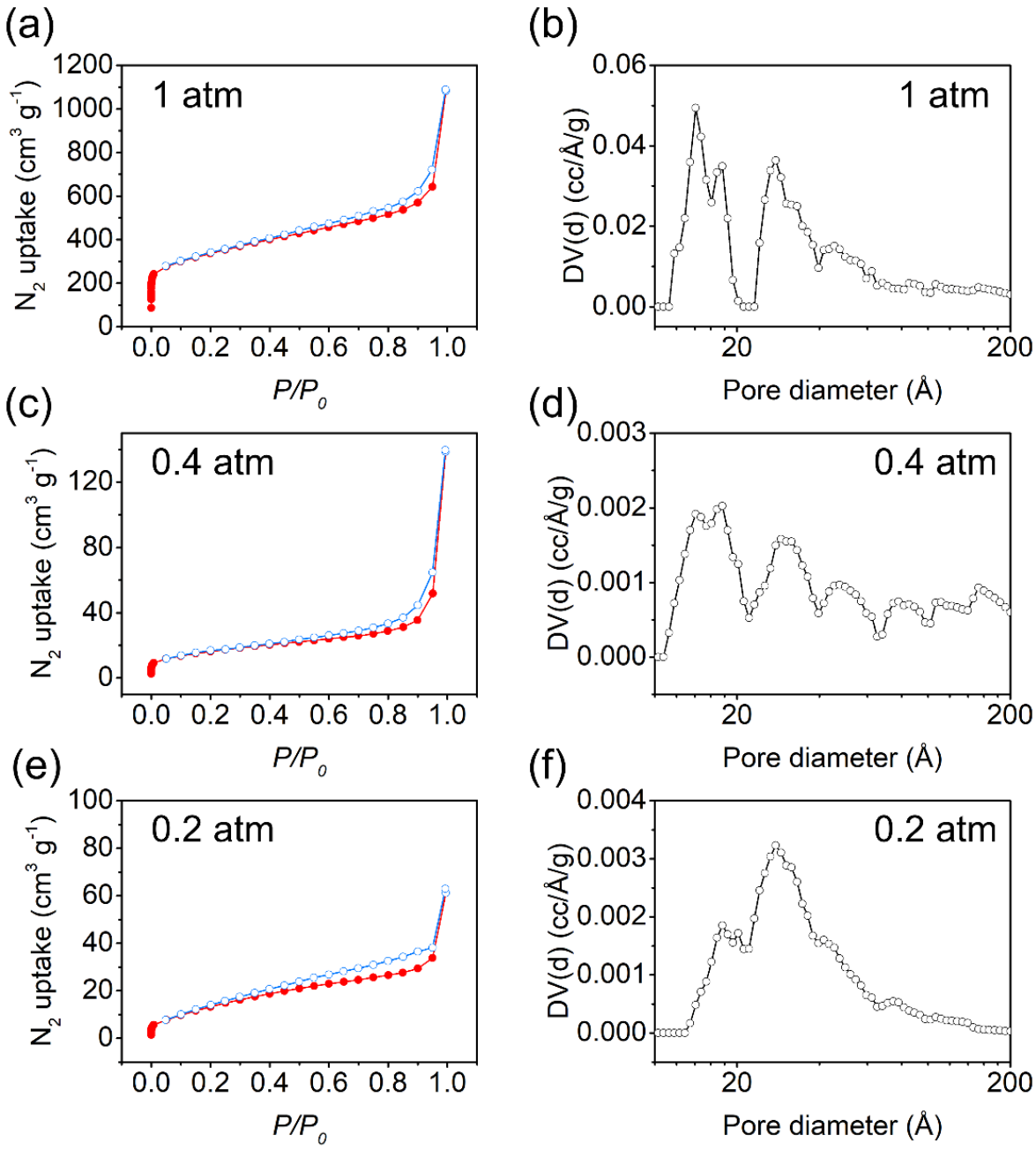

Figure 2.5 Nitrogen sorption isotherms and Density Functional Theory (DFT) pore size distributions of Cu(TPA)·(DMF) synthesized under various pressures (NLDFT-N_2-carbon equilibrium transition kernel at 77 K based on a slit-pore model).

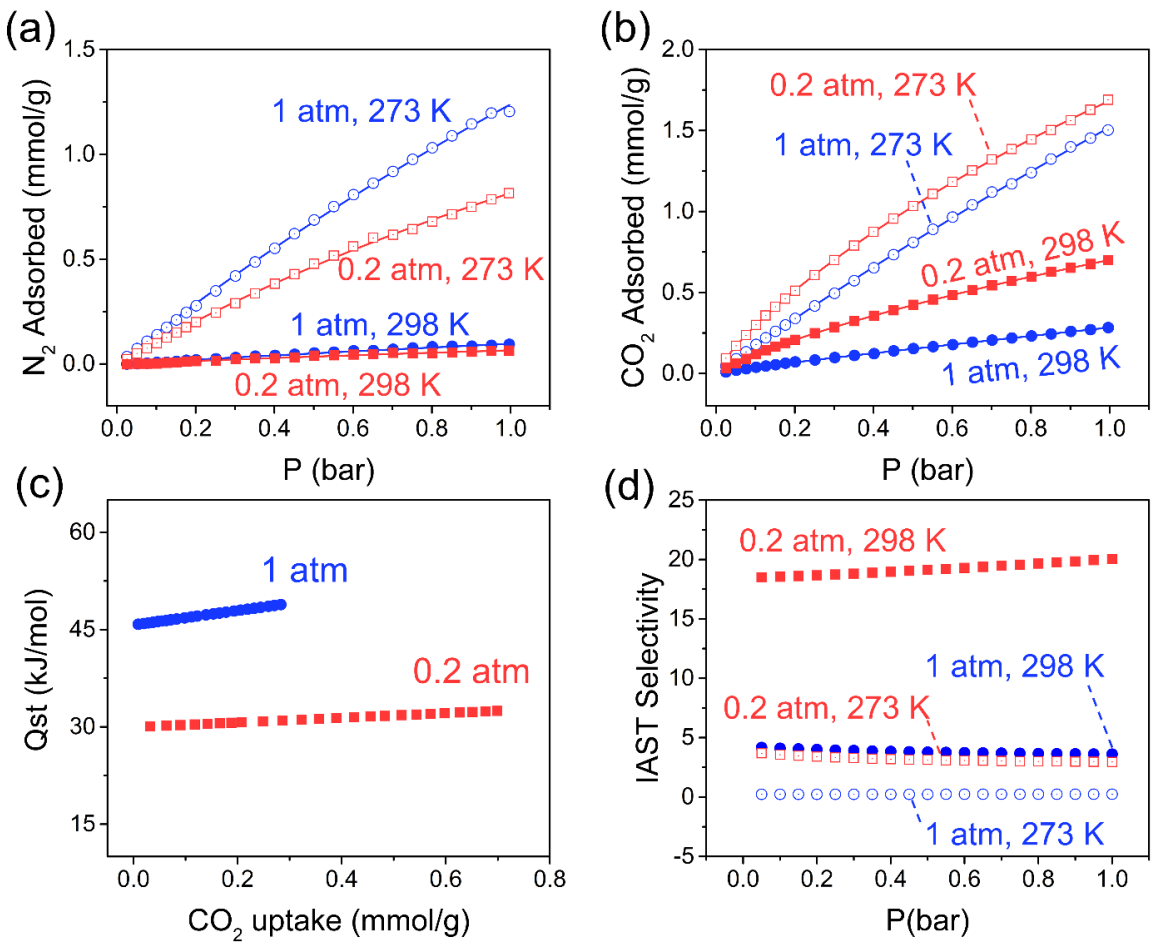

Figure 2.6 (a) N_2 adsorption isotherms; (b) CO_2 adsorption isotherms; (c) Isosteric heats of CO_2 adsorption; (d) Adsorption selectivity for CO_2/N_2 mixtures estimated using IAST. Note: the pressure values indicate the operating pressures used during the synthesis process; the temperature values indicate the temperatures used for gas adsorption tests.

The variations in porosity and crystal structures of Cu(TPA)·(DMF) lead to different performances in gas adsorption as demonstrated with N_2 and CO_2 adsorption experiments (**Figure 2.6**). The analysis of pure gas adsorption was performed at 273 K and 298 K, after which, in-depth

modelling was conducted to analyze the isosteric heats and adsorption selectivity. Specifically, at 273 K, Cu(TPA)·(DMF)_1 has a N_2 uptake of 1.23 mmol/g at 1.0 bar, which is 52% higher than that of Cu(TPA)·(DMF)_0.2 (**Figure 2.6a**). While, at a higher temperature (298 K), these two samples possess similar N_2 adsorption capacity (~ 0.10 mmol/g at 1.0 bar). Interestingly, Cu(TPA)·(DMF)_0.2 shows much higher capacity for CO_2 uptake at both 273 K and 298 K (**Figure 2.6b**), even though the surface area of Cu(TPA)·(DMF)_0.2 is much smaller than that of Cu(TPA)·(DMF)_1. To get further understanding of the CO_2 adsorption with these two samples, the isosteric heats of CO_2 adsorption were calculated using the Clausius-Clapeyron equation (**Eq. 2.2**). In the case of Cu(TPA)·(DMF)_1, the isosteric heats of CO_2 adsorption gradually increased with higher loading of CO_2, which might arise from the enhanced CO_2-CO_2 interaction.[37] Compared with isosteric heats of CO_2 adsorption for Cu(TPA)·(DMF)_0.2 (~ 30 kJ/mol), higher values were observed with Cu(TPA)·(DMF)_1 (46 to 49 kJ/mol), which indicates that the interaction between CO_2 molecules and Cu(TPA)·(DMF)_1 was stronger than that with Cu(TPA)·(DMF)_0.2. Besides, it also suggests tunability of isosteric heats of CO_2 adsorption through pressure-regulated synthesis of Cu(TPA)·(DMF) samples, offering huge potentials to optimize sorption profiles of CO_2. As shown in **Table 2.2**, the isosteric heats of CO_2 adsorption of the Cu(TPA)·(DMF) are comparable with other porous materials, such as $Cu_3(BTC)_2$ (29.8 ± 0.2 kJ/mol), Mg-MOF-74 (22 to 42 kJ/mol)), and zeolites (20 to 50 kJ/mol). It should be noted that the isosteric heats of CO_2 adsorption of Cu(TPA)·(DMF) samples can be further improved by modifying binding functionalities, just like the examples exhibited in **Table 2.2** (i.e., cation-exchanged MCM-22 zeolite and modified SBA-15 mesoporous silica). In addition, the IAST

model was used to analyze the adsorption selectivity for CO_2 from flue gas (75% N_2, 15% CO_2 and 10% other gases) based on the isotherms. As shown in **Figure 2.6d**, the IAST selectivities of Cu(TPA)·(DMF)_0.2 at 273 K and 298 K are calculated to be ~ 3 and ~ 20, respectively, which are much larger than those of Cu(TPA)·(DMF)_1, indicating that Cu(TPA)·(DMF)_0.2 has a better ability to selectively adsorb CO_2 over N_2.

Table 2.2 Comparison of the isosteric heats of adsorption

Adsorbate	Adsorbent	Q_{st} (kJ/mol)	Reference
CO_2	Cu(TPA)·(DMF)_0.2	~ 30	this work
CO_2	Cu(TPA)·(DMF)_1	46 to 49	this work
CO_2	$Cu_3(BTC)_2$	29.8 ± 0.2	Dalton Trans., 2012, 41, 7931–7938
CO_2	Mg-MOF-74	22 to 42	Energy Environ. Sci., 2012, 5, 6465–6473
CO_2	CMP-1	24 to 26	Chem. Sci., 2011, 2, 1173–1177
CO_2	ZK-5	25 to 50	ChemSusChem, 2012, 5, 2237–2242
CO_2	Cation-exchanged MCM-22 zeolite	20 to 40	Adsorption, 2009, 15, 264–270
CO_2	Modified SBA-15 mesoporous silica	10 to 70	Chem. Eng. J., 2018, 348, 327–337

Note: BTC: Benzene-1,3,5-tricarboxylic acid; CMP: conjugated microporous polymer; ZK-5: an 8-membered-ring zeolite (Framework Type Code: KFI).

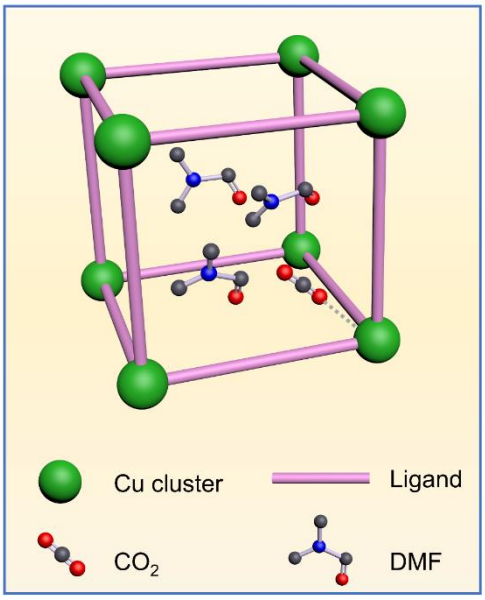

Scheme 2.3 Schematic illustration of CO_2 adsorption inside the framework of Cu(TPA)·(DMF) synthesized under low pressures. H atoms are omitted for simplicity.

On the basis of the above results, a plausible mechanism for the enhanced CO_2 uptake and selectivity with Cu(TPA)·(DMF)_0.2 was schematically illustrated in **Scheme 2.3**. With lower operating pressures, DMF molecules tend to dissociate from the crystal structure due to the increased diffusivity of DMF molecules (**Eq. 2.11**). Instead of leaving away from the framework, these dissociated DMF molecules are trapped inside the pores as suggested by the systematic characterization results. The dissociated but trapped DMF molecules led to decreased surface area but created massive coordinatively unsaturated copper sites. As demonstrated in many prior studies,[46-47] the coordinatively unsaturated metal sites would produce strong electric fields to bind polar molecules (e.g., CO_2),[48] which would subsequently improve the CO_2 adsorption capacity. Generally, the open metal sites would also increase the isosteric heat (Qst). However, smaller Qst

values were observed for Cu(TPA)·(DMF)_0.2 compared with that for Cu(TPA)·(DMF)_1. This might be due to the fact that, Cu(TPA)·(DMF)_0.2 has lots of dissociated DMF molecules trapped inside the pores (**Scheme 2.3**), which would cause steric hindrance and thus decrease the isosteric heat.

2.4 Conclusions

A pressure-regulated microdroplet-based spray route has been developed for the synthesis of MOFs. Systematic experimental and modelling studies have been conducted to investigate the dependence of the properties of Cu(TPA)·(DMF) on the pressures of the spray process. Apparent variations in morphology and crystal structure were observed with different synthesis pressures, which could be attributed to the different evaporation rates of microdroplets and the dissociation of coordinated DMF under low pressures, respectively. The dissociation of DMF molecules would generate large numbers of coordinatively unsaturated metal sites, which leads to higher CO_2 adsorption capacity and selectivity. The outcome of this work would contribute to the fundamental understanding of pressure-regulated synthesis of MOFs using spray process.

Chapter 3. Synthesis of Cu-TMA/Cu-BDC via Microdroplets: Roles of Component Compositions

Abstract

Mixed-linker metal-organic frameworks (MOFs) offer great tunability in both pore structures and surface chemistry. This study reports the synthesis and characterization of model mixed-linker MOFs (i.e., Cu-TMA/Cu-BDC) via a microdroplet-based spray process, to unravel the relationship between the properties of mixed-linker MOFs and the component compositions. The as-prepared mixed-linker MOFs exhibited distinct properties in terms of morphology, crystalline phase, surface chemistry, and pore structure. In particular, two-dimensional correlation spectroscopy (2D-COS) analysis was conducted to analyze the correlational features among surface functional groups, which are unattainable from traditional infrared (IR) and Raman spectra. The results from the 2D-COS analysis also suggest that the surface chemistry of the mixed-linker MOFs is adjustable by controlling the precursor conditions. Measurements of CO_2 adsorption on the mixed-linker MOFs demonstrated the tunability of the preferential adsorption sites and adsorption kinetics. All the above-mentioned information implies that synthetic parameters can be varied to optimize the performance of the mixed-linker MOFs. The outcome of this study offers new insights into the synthetic chemistry of mixed-linker MOFs in a microdroplet-based spray process.

3.1 Introduction

Metal-organic frameworks (MOFs) have been attracting extensive attention during the past decades due to their unique properties (e.g., high surface area and extraordinary porosity) and great potentials in numerous applications (e.g., gas adsorption, catalysis, and sensing).[46-47] Recently, considerable interest has been directed towards synthesizing mixed-component MOFs,[48-52] which provides opportunities to grant the frameworks with more remarkable properties, such as pore heterogeneity,[53-54] framework flexibility,[55] and enhanced selectivity towards gas molecules.[56] The mixed-component MOFs could be multiple-linker MOFs or multiple-metal MOFs, consisting of components either with identical structure or distinct structures.[53]

Notable examples include hybrid zeolitic imidazolate framework (ZIF) systems, which have been intensively explored for controllable textual properties and sorbate diffusion properties.[55, 57-58] For instance, Guo et al. studied the kinetic-controlled formation of Zn(2-mIM)$_2$/Co(2-mIM)$_2$ (2-mIM = 2-methylimidazole),[57] where sophisticated heterogeneous structures were obtained by manipulating the Co/Zn ratios. Nair and co-workers studied the hybrid ZIF materials (e.g., ZIF-7-8, ZIF-7-90 and ZIF-8-90) synthesized with mixed imidazole linkers (e.g., benzimidazole, 2-mIM and 2-carboxyimidazole) in the precursor solutions.[55, 59-61] With controlled synthesis, they were able to achieve distinct crystalline phases, flexible framework, and tunable pore structures. In addition to the hybrid ZIF systems, other mixed-component MOF systems have also been studied, such as IRMOF systems containing various functionalized linkers,[62] and MIL systems with mixed metals.[63]

Generally, these mixed-component MOFs can be constructed either with one-pot reaction of multiple components or post-synthetic modification of a single-component MOF.[57] Recently, a microdroplet-based spray process has been developed for the synthesis of MOFs, which has shown several advantages over the conventional methods, such as fast reaction rate and homogeneous distribution of the reactants.[64-65] The attempt to synthesize multicomponent MOFs using the spray process was reported in a prior study,[66] where Zn-MOF-74/Ni-MOF-74 and HKUST-1/NOTT-100 superstructures were fabricated. With multiple components in the precursor microdroplets, the formation mechanism of MOFs would become much more complicated. For instance, it is still unclear, when the microdroplet-based spray process is used, whether the formation of one MOF component would affect the other one, and how would the properties of the mixed-component MOFs change with different ratios of individual components.

To make the spray process a better platform for the synthesis of mixed-component MOFs, it is crucial to answer the above-mentioned questions. Therefore, in this article, we carried out a systematic study on the synthesis of a series of mixed-component MOFs with two distinct linkers by using the microdroplet-based spray process. To be specific, two prototypical MOFs, i.e., Cu-TMA (TMA: trimesic acid) and Cu-BDC (BDC: 1,4-benzenedioic acid), were chosen as the components for the mixed-component MOFs. The results show that the Cu-TMA/Cu-BDC mixed-linker MOFs can be successfully fabricated in a range of compositions as verified by the corresponding X-ray diffraction (XRD) analysis. A variety of other characterizations of the MOFs were also conducted. Especially, the two-dimensional correlation spectroscopy (2D-COS) was

used to achieve a better spectral resolution and unravel the correlation between the linkers and the properties of the mixed-component MOF over a wide range of compositions, which is unreachable from traditional one-dimensional (1D) infrared (IR) or Raman spectra. The current study also demonstrates that the ratios of the organic linkers could be adjusted to tune the morphologies, surface chemistry, CO_2 adsorption capacity and preferential adsorption site, and achieve hierarchical pore structures. The outcome of this study would constitute a fundamental advance towards the synthetic chemistry of mixed-linker MOFs in the microdroplet-based spray processes.

3.2 Materials and Methods

Synthesis Process. The synthesis of mixed-linker MOFs by using the microdroplet-based spray process is illustrated in **Scheme 3.1A**. To be specific, the precursor solution was prepared by dissolving 0.2174 g copper nitrate trihydrate, 0.0997 g 1,4-benzenedioic acid (BDC), and certain amount of trimesic acid (TMA) in 30 mL dimethylformamide (DMF). The precursor solution was then atomized to microdroplets, which were subsequently carried by air flow (5 L/min) through an electric furnace at 300 °C, where the solvent evaporates, and the chemicals converted to final products. A filter was used to collect the sample powders downstream of the furnace. The as-collected samples were dispersed in 10 mL methanol and precipitated by centrifuging at 6000 rpm for 5 min. This dispersion-centrifugation process was repeated three times in order to remove all the chemical residuals. Finally, the samples were dried in a vacuum oven at 50 °C. Based on the amount of the chemicals used in the precursor solution, the as-prepared samples were termed

hereafter Cu-TMA (**Scheme 3.1B**), Cu-BDC (**Scheme 3.1C**), and Cu-$(BDC)_2(TMA)_x$, where the subscripts were used to indicate the mole ratio of the components.

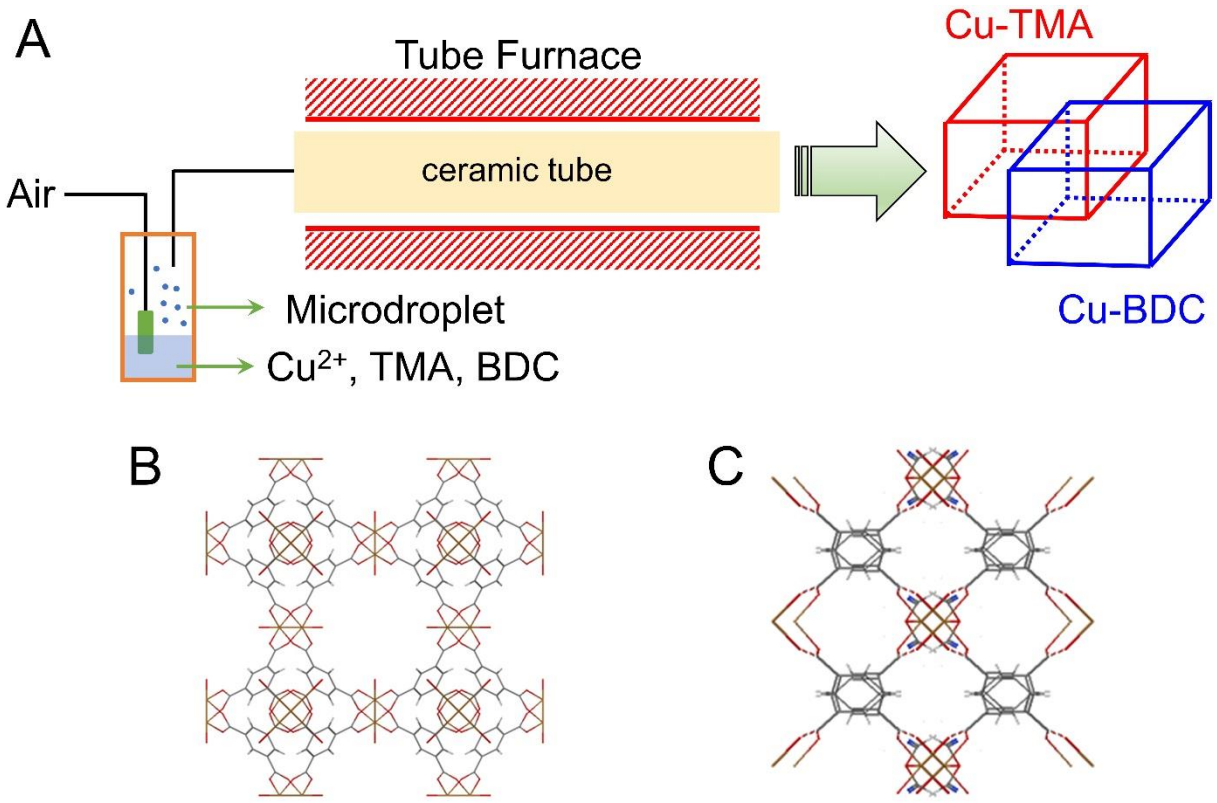

Scheme 3.1 Schematic illustrations of (A) the synthesis procedure, (B) the structure of Cu-TMA and (C) the structure of Cu-BDC.

Material Characterization. The morphology and crystallinity of the materials were analyzed by scanning electron microscopy (SEM, SU-70, Hitachi) and powder X-ray diffraction (XRD, X'Pert PRO, PANalytical), respectively. The Fourier-transform infrared (FT-IR) and Raman spectra were obtained by using Nicolet iS50 (Thermo Scientific) and LabRAM HR Evolution (HORIBA),

respectively. The surface area and pore size distribution were measured by using Autosorb iQ (Quantachrome Instruments). The elemental composition was determined by using X-ray photoelectron spectroscopy (XPS, ESCALab 250, ThermoFisher). Diffuse reflectance infrared Fourier transform spectroscopy (DRIFTS) was applied to analyze CO_2 adsorption behaviors on the as-prepared samples, the procedures of which have been detailed elsewhere.[67]

Two-Dimensional Correlation Spectroscopy (2D-COS). 2D-COS method[68] was used to (1) get a better resolution of the spectroscopic peaks and (2) analyze correlational features among chemical groups. The fundamentals and computation procedures of the 2D-COS have been detailed elsewhere.[68] In this work, the 2Dshige software developed by Kwansei-Gakuin University was used to generate two 2D correlation spectra (i.e., the synchronous spectrum and the asynchronous spectrum).

3.3 Results and Discussions

Material Characterization. The morphologies of Cu-BDC, Cu-TMA, and Cu-$(BDC)_2(TMA)_x$ were examined by SEM. As shown in **Figure 3.1A**, the pure Cu-TMA sample has a spherical shape, which can be attributed to the typical formation mechanism in the spray process.[64, 69] While with increasing amount of BDC, the spherical shape of the samples became less intact (**Figures 3.1B-E**). The crystal structures of the samples were analyzed with XRD measurements. As shown in **Figure 3.1F**, the diffraction patterns of both Cu-BDC and Cu-TMA agree well with the previously reported ones.[64, 70] For Cu-$(BDC)_2(TMA)_x$, the characteristic diffraction peaks of

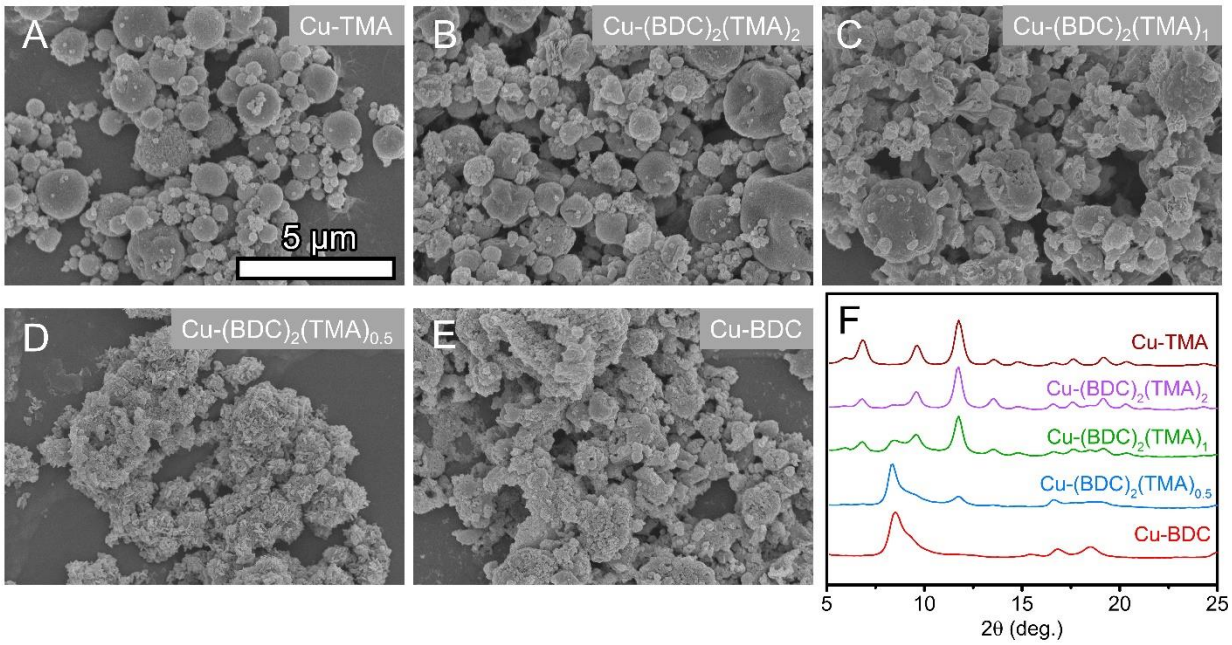

Figure 3.1 SEM images of the samples: (A) Cu-TMA; (B) Cu-$(BDC)_2(TMA)_2$; (C) Cu-$(BDC)_2(TMA)_1$; (D) Cu-$(BDC)_2(TMA)_{0.5}$; (E) Cu-BDC. (F) XRD patterns of the samples.

both MOF components (i.e., Cu-BDC and Cu-TMA) can be clearly identified, indicating the co-existence of both MOFs. The intensity ratios of these characteristic peaks were found to be dependent on the relative amount of the MOF components. Based on the XRD patterns, the weight percentages of the MOF components in Cu-$(BDC)_2(TMA)_x$ were analyzed with the Rietveld confinement using the MAUD program (MAUD: Materials Analysis Using Diffraction). After the confinement, the weight percentages of Cu-TMA in Cu-$(BDC)_2(TMA)_2$, Cu-$(BDC)_2(TMA)_1$ and Cu-$(BDC)_2(TMA)_{0.5}$ were calculated to be 78.9 wt%, 54.5 wt% and 5.4 wt%, respectively. Notably, the actual ratios of the components in the products slightly deviated from those of the precursors, which might be related to the variations in crystallization rates between Cu-TMA and Cu-BDC.

The surface functional groups of the Cu-$(BDC)_2(TMA)_x$ samples were analyzed by FT-IR (**Figure 3.2A**), where the characteristic peaks of individual MOF can be clearly observed. For instance, Cu-TMA has several characteristic peaks at 760 and 1446 cm^{-1}, corresponding to Cu-O[71] and C=O[72], respectively. In addition, both peaks at 1615 and 1642 cm^{-1} can be ascribed to C=O,[64, 73-74] originating from the carboxyl group in TMA coordinated with the Cu sites. On the other hand, Cu-BDC has several characteristic peaks at 566, 1022, and 1288 cm^{-1}, which can be assigned to Cu-O,[75] C-H,[76-77] C-C,[78] respectively. The peaks at 1503, 1567 and 1689 cm^{-1} are related to C=O in BDC.[73, 79-80] It is interesting to note that the relative intensities of these characteristic IR peaks change with different ratios of Cu-BDC to Cu-TMA. Unfortunately, little information regarding correlational features of these IR peaks can be obtained from the conventional 1D FT-IR spectra.

Table 3.1 Guidelines of 2D-COS analysis

2D COS analysis		
	Synchronous	**Asynchronous**
Autopeaks (i.e., peaks on the diagonal line)	Extent of the spectral fluctuations[a]	N/A
Cross Peaks (i.e., peaks off the diagonal line)	Trends of the fluctuations[b]	Sequential orders of the spectral variations[c]

Notes: (a) Stronger color indicates a higher extent of the spectral fluctuation.

(b) Red cross peak (X, Y) indicates that the bands at X cm^{-1} and Y cm^{-1} change in the same direction. Otherwise (i.e., blue cross peak), these bands change in the opposite direction.

(c) If a cross peak (X, Y) shows the same color in both synchronous and asynchronous spectra, this implies that the band at X cm^{-1} changes before that at Y cm^{-1}. Otherwise, the band at X cm^{-1}

changes after that at Y cm^{-1}. Special case: cross peak (X, Y) in either spectrum has no color: bands at X and Y cm^{-1} change simultaneously.

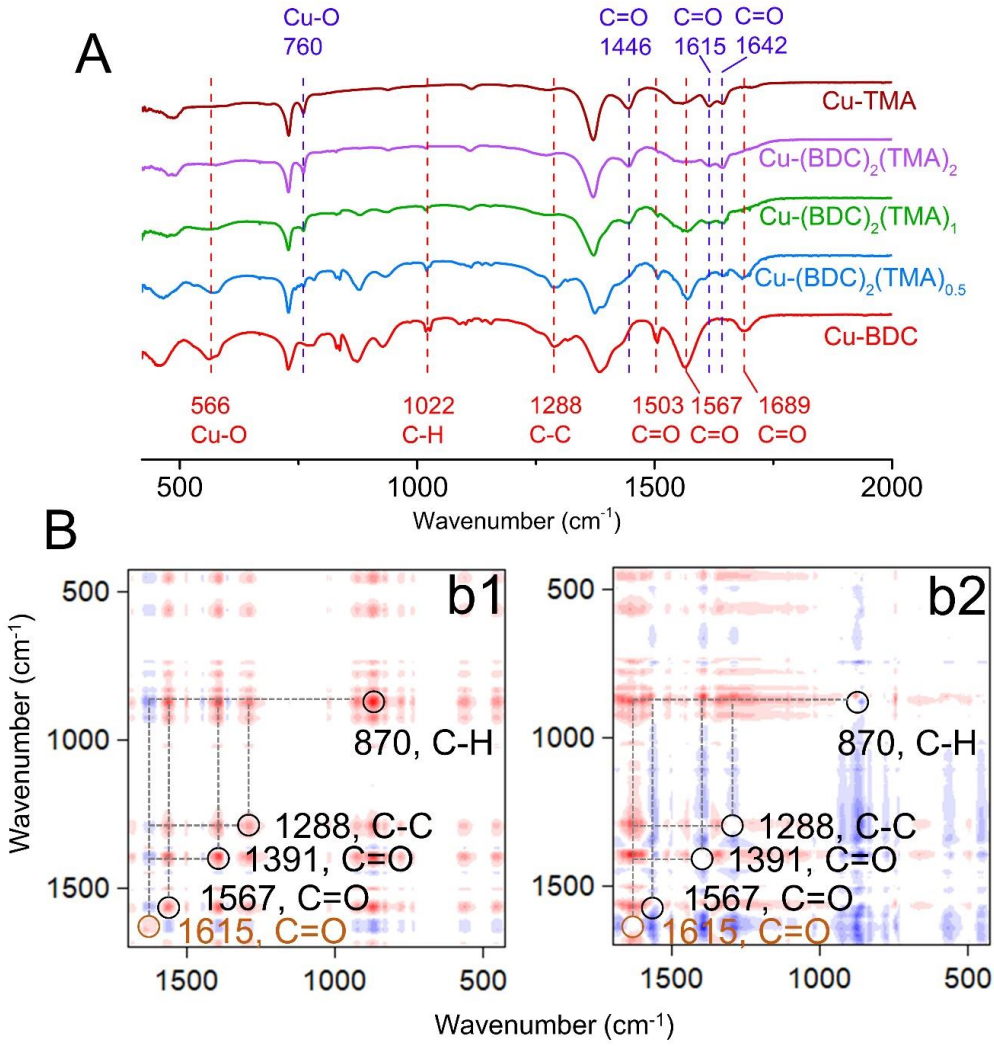

Figure 3.2 (A) Traditional 1D FT-IR spectra of the samples (Top: functional groups in Cu-TMA, Bottom: functional groups in Cu-BDC); (B) 2D FT-IR correlation spectra with decreasing amount of TMA in precursors as the perturbation: (b1) synchronous and (b2) asynchronous.

To get better resolved peaks and correlational features of the IR peaks, the 2D-COS method was used to generate 2D FT-IR correlation spectra with decreasing amount of TMA in precursors as the perturbation. The 2D FT-IR correlation spectra consist of a synchronous spectrum (**Figure 3.2b1**) and an asynchronous spectrum (**Figure 3.2b2**), which can be used to analyze the dynamic spectral fluctuations (e.g., increase or decrease of peak intensity) and sequential orders of the variations of the IR peaks, respectively (See **Table 3.1** for details).[81] In particular, the synchronous spectrum is symmetrical with respect to the diagonal line, where several peaks are located (**Figure 3.2b1**). These peaks are called autopeaks, the intensity of which indicates the extent of the fluctuations of a peak at a specific wavenumber. As shown in **Figure 3.2b1**, five dominant autopeaks, indicated by red color, are observed at 870 cm^{-1} (C-H), 1288 cm^{-1} (C-C), 1391 cm^{-1} (C=O), 1567 cm^{-1} (C=O), and 1615 cm^{-1} (C=O), suggesting that the intensity changes of these peaks were much greater than others (e.g., 566 cm^{-1} (Cu-O)) and the variations in the precursor linkers would mainly lead to the changes in surface chemistry of the mixed-component MOFs. The peaks off the diagonal line are referred to as cross peaks, the color of which represents the trends of the fluctuations (**Table 3.1**). Notably, the cross peaks at (1615, Y) (Y = 870, 1288, 1391, 1567 cm^{-1}) exhibit blue color, which means that the intensity of the band at 1615 cm^{-1} (i.e., C=O in TMA) changes in the opposite direction of the other bands (i.e., 870, 1288, 1391, 1567 cm^{-1}, corresponding to functional groups in BDC).

Unlike the synchronous spectrum, the asynchronous spectrum has no peaks on the diagonal line (i.e., no autopeaks). While, the asynchronous spectrum contains similar cross peaks off the

diagonal line as the synchronous one. By comparing the colors of the same cross peaks in both synchronous and asynchronous spectra, the sequential orders of the spectral variations can be obtained.[81] To be specific, if the cross peak (X, Y) shows the same color in synchronous and asynchronous spectra, then the IR band at X cm^{-1} changes before that at Y cm^{-1}. Otherwise, the IR band at X cm^{-1} changes after that at Y cm^{-1}. One special case is that, if the cross peak (X, Y) in either spectrum has no color, the IR bands at X and Y cm^{-1} change simultaneously.[82] With decreasing amount of TMA in precursors, the changes of the spectral peaks occurred in the following sequence: 1288 cm^{-1} (C-C in BDC) = 1391 cm^{-1} (C=O in BDC) > 1567 cm^{-1} (C=O in BDC) > 870 cm^{-1} (C-H in BDC) > 1615 cm^{-1} (C=O in TMA). Interestingly, some peaks originate from BDC, but they don't change synchronously. This implies that mutual effects exist during the simultaneous synthesis of multiple MOFs in microdroplets, and the surface chemistry of individual MOF component could be finely tuned by changing the precursor composition.

The vibration properties of the samples were further analyzed with the aid of Raman spectroscopy, which is complementary to the IR spectroscopy, aiming to uncover a complete picture of surface chemistry of the samples. As shown in **Figure 3.3A**, both Cu-TMA and Cu-BDC have several characteristic peaks. For Cu-TMA, several peaks were observed at 496 cm^{-1}, 741 cm^{-1}, 824 cm^{-1}, 1003 cm^{-1}, 1539 cm^{-1} and 1610 cm^{-1}. In particular, the peak at 496 cm^{-1} originates from Cu(II) species.[83] The peaks at 741 cm^{-1} and 824 cm^{-1} can be attributed to the vibration of C-H group,[84] while the peaks at 1003 cm^{-1} and 1610 cm^{-1} are related to the vibration of C=C group.[84] The band at 1539 cm^{-1} is due to the vibration of COO^-.[85] In the case of Cu-BDC, the

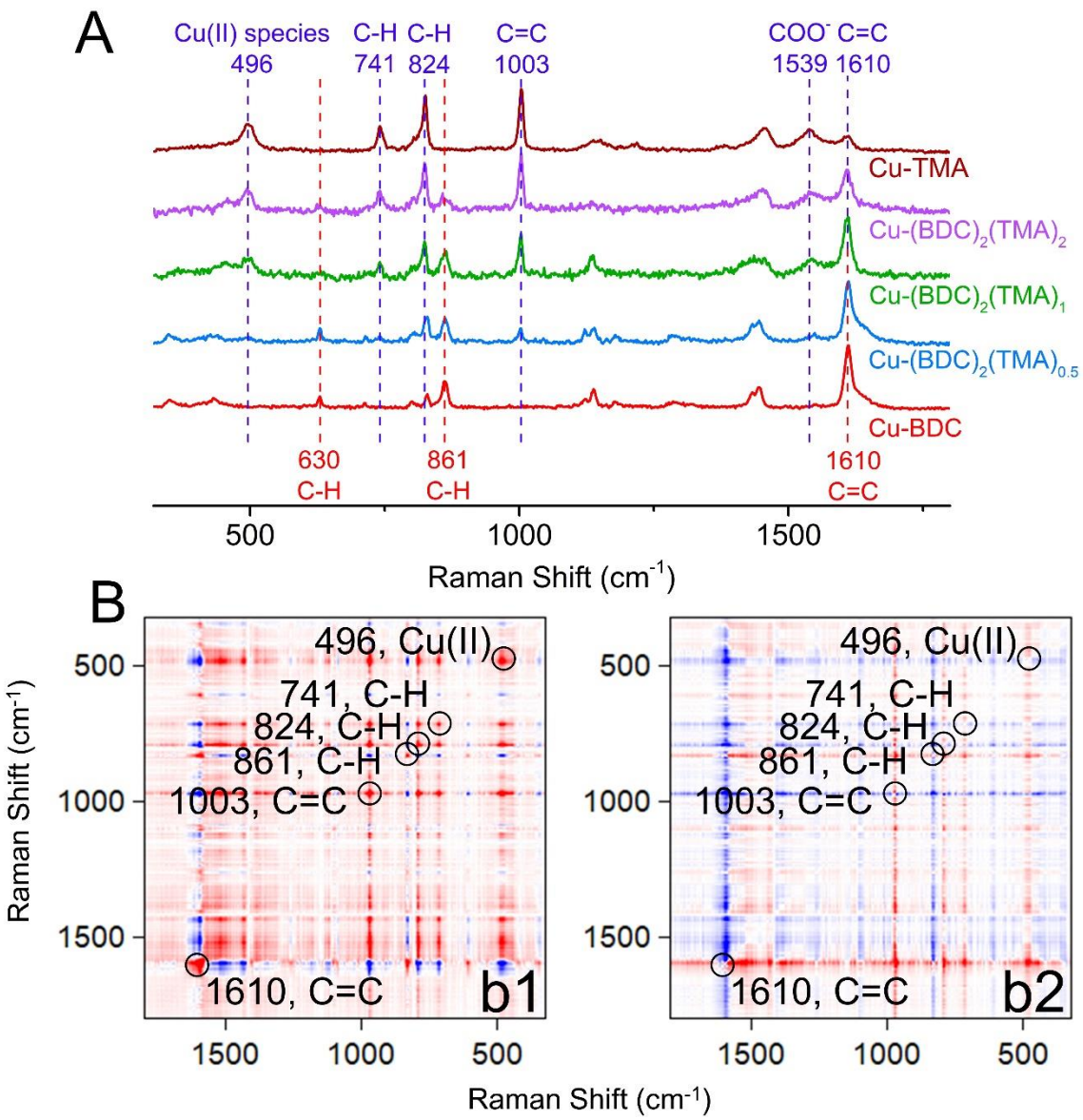

Figure 3.3 (A) Traditional 1D Raman spectra of the samples (Top: functional groups in Cu-TMA, Bottom: functional groups in Cu-BDC); (B) 2D Raman correlation spectra with decreasing amount of TMA in precursors as the perturbation: (b1) synchronous and (b2) asynchronous.

peaks at 630 cm^{-1} and 861 cm^{-1} can be assigned to C-H in BDC.[86] Additionally, the peak at 1610 cm^{-1} is also observed but with much higher intensity for the case of Cu-BDC, which is associated with the C=C in BDC.[87] Similar to the FTIR results, the intensities of these Raman peaks also varied with the composition of the MOF mixtures.

To get further information regarding the mutual effects of MOFs mixtures during the synthesis process, the same 2D-COS approach was employed to de-convolute the 1D Raman spectra into 2D correlation ones with decreasing amount of TMA in precursors as the perturbation. The guidelines (**Table 3.1**) used to analyze 2D FT-IR spectra also apply here. As shown in **Figure 3.3A**, six autopeaks were observed in the synchronous spectrum, including 496 cm^{-1} (Cu(II) species), 741 cm^{-1} (C-H), 824 cm^{-1} (C-H), 861 cm^{-1} (C-H), 1003 cm^{-1} (C=C) and 1610 cm^{-1} (C=C). As shown from the color of the cross peaks, with decreasing amount of TMA in the precursor, the intensities of Raman peaks at 861 cm^{-1} (C-H in BDC) and 1610 cm^{-1} (C=C in TMA/BDC) change in the opposite direction of the rest peaks (i.e., functional groups in TMA). From the information of the cross peaks in both synchronous spectrum and asynchronous spectrum, the sequence of the spectral variations was derived as follows: 824 cm^{-1} (C-H in TMA) > 741 cm^{-1} (C-H in TMA) = 496 cm^{-1} (Cu(II) species in Cu-TMA) > 1003 cm^{-1} (C=C in TMA) > 1610 cm^{-1} (C=C in TMA/BDC) > 861 cm^{-1} (C-H in BDC). As shown, the spectral fluctuations occurred with different sequential orders even for functional groups from the same component, which agrees with the FT-IR results, once again demonstrating the tunability of the surface chemistry of individual MOF component with various linker compositions. Besides, the information of the sequential orders

offers clues for the interactions between the mixed components and provides evidence for the framework interpenetration. It would also be of great importance to guide us in designing mixed-component MOFs with specified surface chemistries for future applications.

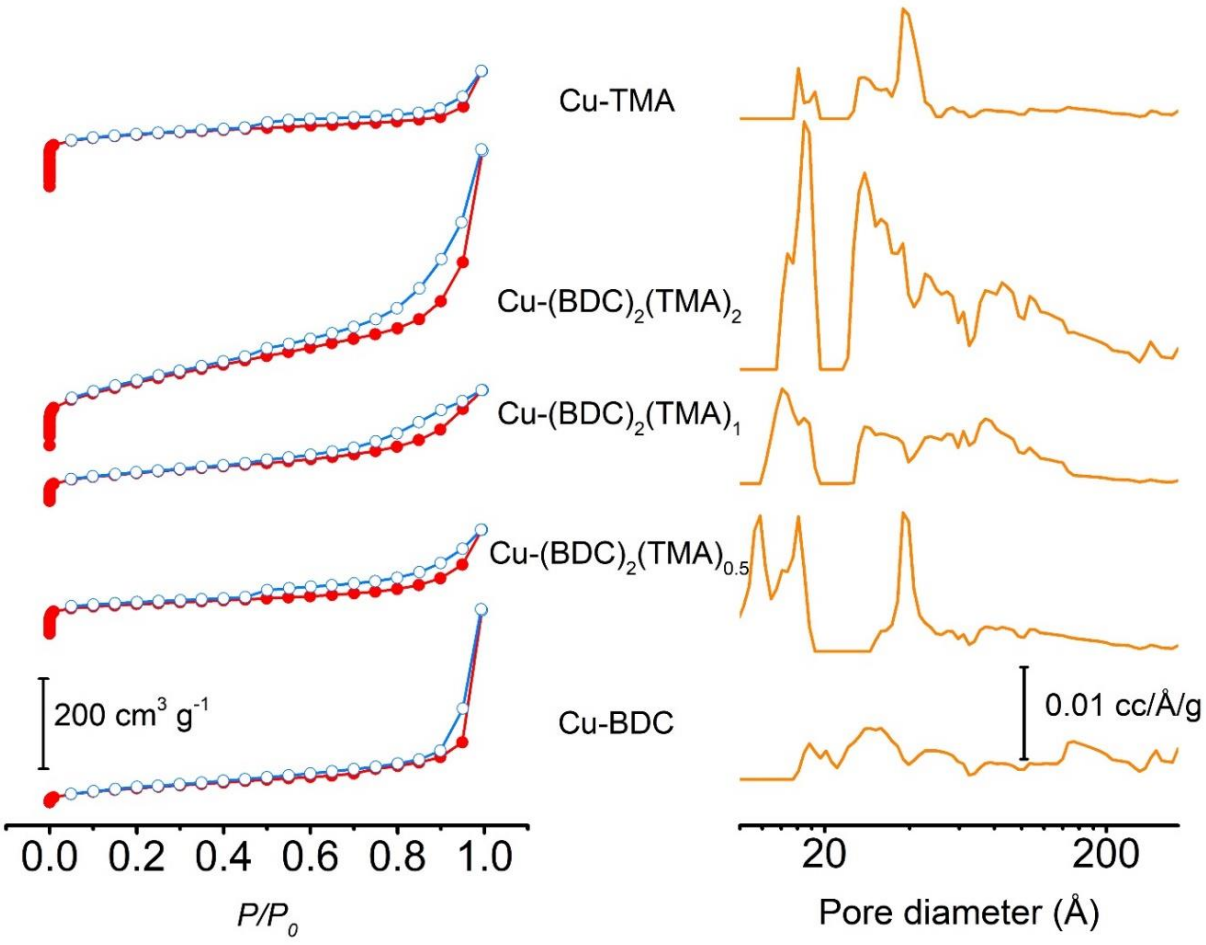

Figure 3.4 Left: nitrogen sorption isotherms; Right: pore size distribution calculated using density functional theory (DFT).

Table 3.2 Summary of BET surface areas and pore volumes

Samples	BET surface area (m^2/g)	Pore volume (cm^3/g)
Cu-TMA	763	0.43
Cu-$(BDC)_2(TMA)_2$	657	0.88
Cu-$(BDC)_2(TMA)_1$	300	0.37
Cu-$(BDC)_2(TMA)_{0.5}$	348	0.33
Cu-BDC	121	0.40

The porosities and surface areas of the as-prepared samples were analyzed by nitrogen sorption measurements. The nitrogen sorption isotherms and pore size distributions are shown in **Figure 3.4**, and the deduced values were summarized in **Table 3.2**. As shown in **Figure 3.4**, Cu-BDC demonstrates type IV nitrogen sorption isotherm, indicating the dominance of mesopores, which is in line with the corresponding pore size distribution. The Brunauer–Emmett–Teller (BET) surface area and pore volume of Cu-BDC were found to be 121 m^2/g and 0.40 cm^3/g, respectively. On the other hand, Cu-TMA exhibits type I isotherm with massive micropores. The slight rise and the hysteresis loop observed at high relative pressure implies the existence of mesopores, which is attributed to the interparticle voids.[88] The as-synthesized Cu-TMA has a BET surface area of 763 m^2/g and a pore volume of 0.43 cm^3/g. Notably, hierarchical pore structures (i.e., micro-mesopores)

were found in the cases of Cu-$(BDC)_2(TMA)_x$ samples. To be specific, the nitrogen sorption isotherms of Cu-$(BDC)_2(TMA)_x$ samples feature sharp nitrogen uptake at low relative pressure ($P/P_0 < 0.01$), and an obvious rise and a hysteresis loop at high relative pressures ($P/P_0 > 0.5$), suggesting the co-existence of abundant micropores and mesopores. This hierarchical pore structures can accelerate mass transfer rates and thus facilitates the overall efficiency of practical applications, such as catalysis.[89] Moreover, the BET surface areas and pore volumes of the Cu-$(BDC)_2(TMA)_x$ samples also have a great dependence on the ratio of BDC to TMA used in the precursor solution. Overall, the BET surface area decreases with decreasing amount of TMA in the mixed-component MOFs. Interestingly, the highest pore volume was found with Cu-$(BDC)_2(TMA)_2$ (i.e., 0.88 cm^3/g), which might be attributed to formation of additional pores due to the framework interpenetration.[90]

The variations in surface elemental composition among these samples were analyzed by using XPS, which can provide further information regarding synthetic chemistry of mixed-linker MOFs in microdroplets. As shown in **Figure 3.5A**, analogous survey scans were observed for these samples, where the main elements could be clearly identified, including Cu, N, and O. High-resolution spectra of these elements are shown in **Figures 3.5B-D**. The presence of N is due to the existence of DMF residues in the pore channels or coordinated DMF at the Cu sites (**Figure 3.5B**). For Cu-TMA, small amount of N was observed, indicating the limited ability of methanol to exchange DMF from the framework, which might be ascribed to the limitation from the micropore structures. In contrast, no peak was observed at 398.2 eV in the case of Cu-BDC (**Figure 3.5B**),

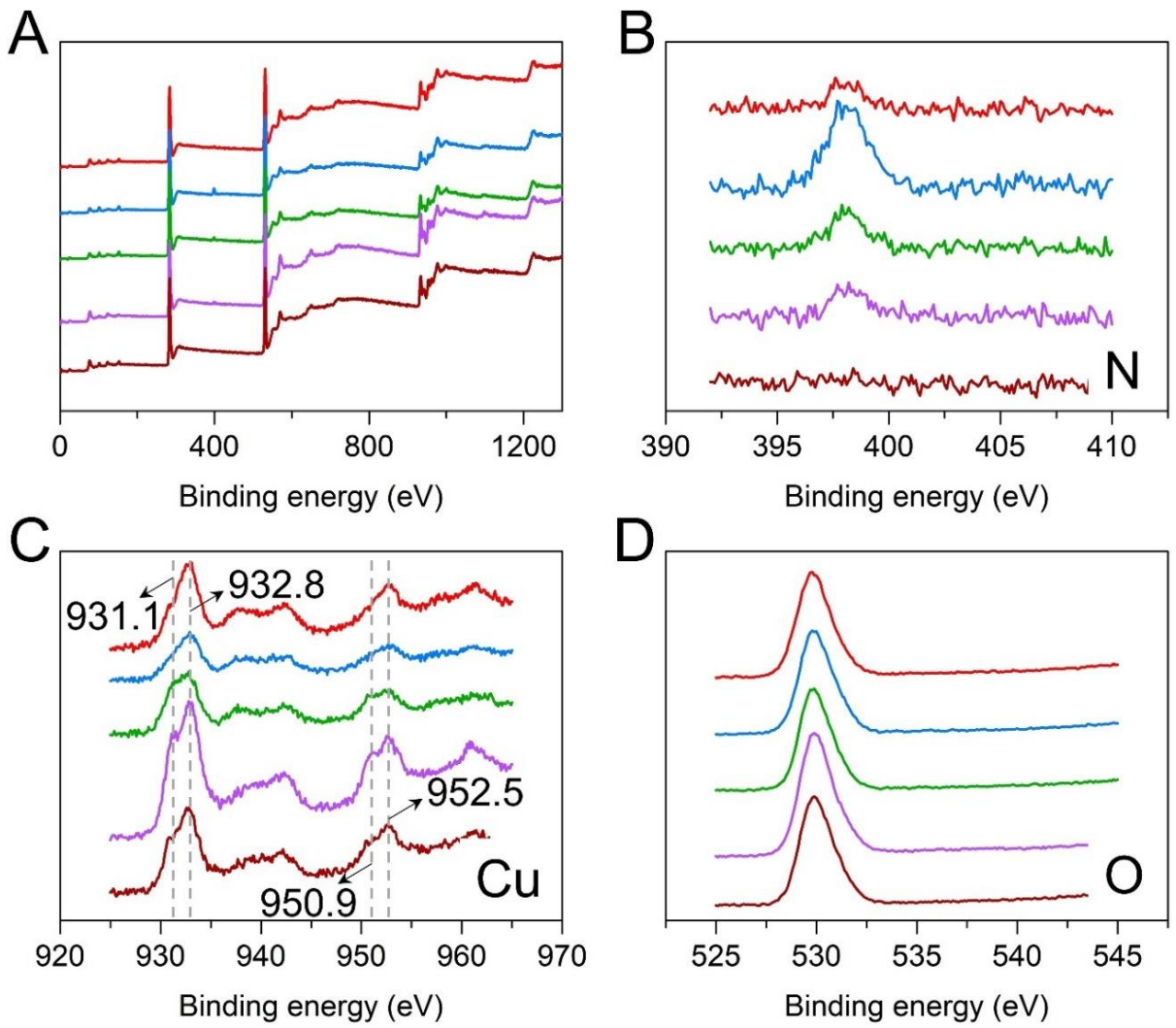

Figure 3.5 XPS spectra: (A) survey scan; (B) N 1s; (C) Cu 2p; (D) O 1s. (From top to bottom: Cu-TMA, Cu-$(BDC)_2(TMA)_2$, Cu-$(BDC)_2(TMA)_1$, Cu-$(BDC)_2(TMA)_{0.5}$ and Cu-BDC)

suggesting the absence of DMF in the as-prepared Cu-BDC crystals. Interestingly, higher N peaks were observed in the case of mixed-linker MOFs, which implies higher amount of DMF existing in the mixed-linker MOFs, which might be owing to the interpenetrating framework preventing the release of DMF molecules.[91] Typically, DMF molecules exist inside the framework through

the coordination with metal sites. The release of DMF molecules from the framework would give rise to coordinatively unsaturated metal sites and enhanced porosity, which are beneficial for several applications, including catalysis and gas storage.[92] On the other hand, the coordination of DMF molecules with Cu sites is necessary to maintain the structural integrity of some MOFs, like Cu-BDC.[70] Therefore, as a trade-off between functionality and structural integrity, careful consideration is always required about the presence of DMF inside the framework. In addition, the samples also exhibit variations in the valence states of Cu due to the coordination with distinct linkers and different amount of DMF molecules. As shown in the high-resolution XPS spectra of Cu 2p (**Figure 3.5C**), both Cu-TMA and Cu-BDC display peaks at 932.8 eV and 952.5 eV, corresponding to Cu $2p_{3/2}$ and Cu $2p_{1/2}$, respectively.[93-94] In addition, for Cu-BDC, satellite peaks were observed at 931.1 eV and 950.9 eV. The peak intensities of Cu 2p vary with different component compositions. Interestingly, the intensity changes of Cu 2p peak followed the opposite trend of those of N 1s (**Figure 3.5B**), suggesting peak intensity of Cu 2p was closely related to the amount of DMF remaining in the framework. In other words, with more DMF molecules remaining in the framework, less signal from Cu 2p would be detected during the XPS measurements. This is reasonable, as XPS only detects photo-emitted electrons escaped from the samples, while the presence of DMF molecules could block electrons emitted from Cu 2p from escaping and reaching the XPS detector. On the other hand, no apparent differences were observed in the high-resolution XPS spectra of O 1s (**Figure 3.5D**).

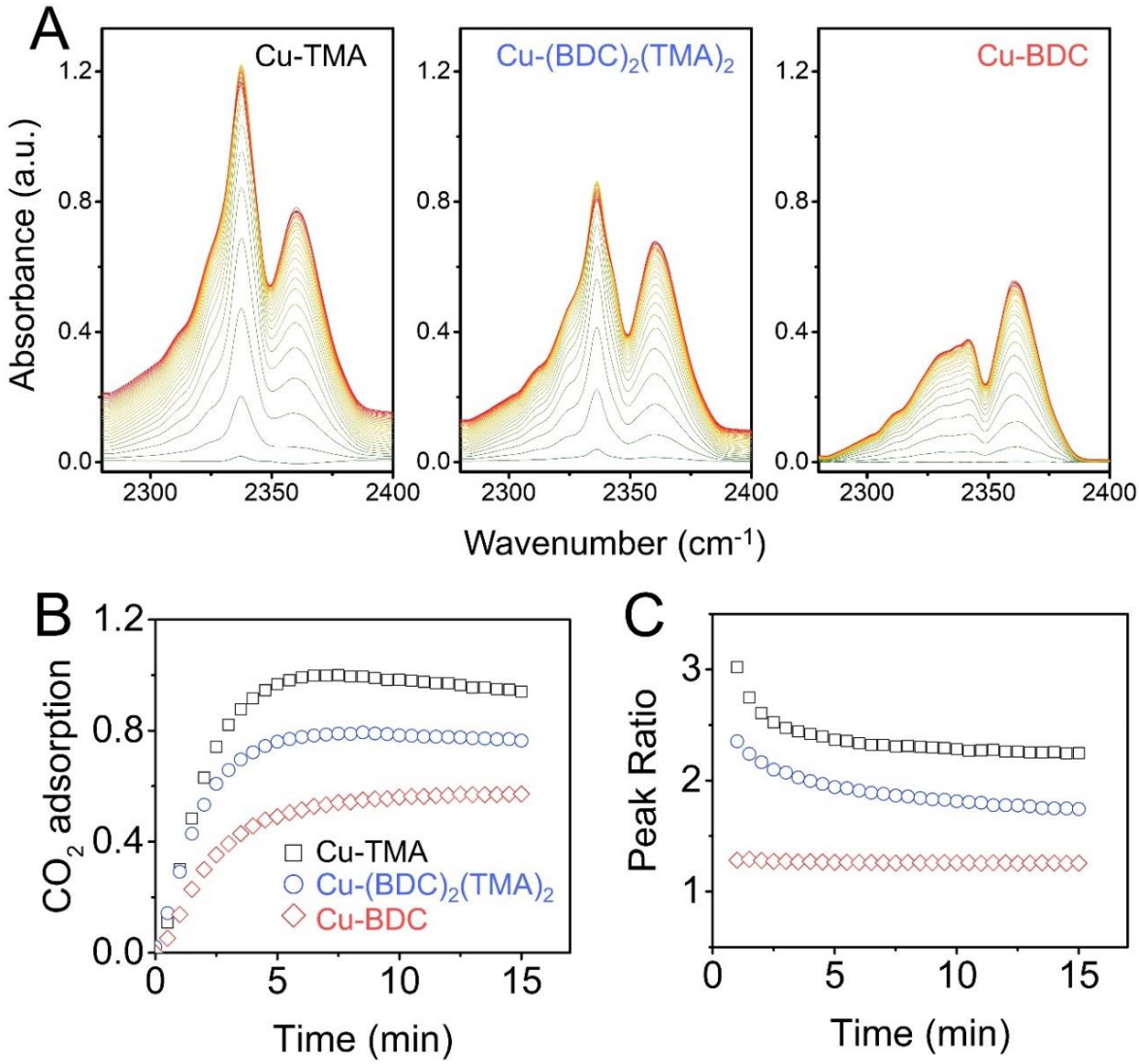

Figure 3.6 (A) *In situ* IR spectra collected during the 15-min CO_2 adsorption process; (B) CO_2 adsorption kinetics; (C) Area ratios of Peak (2337 cm^{-1}) to Peak (2360 cm^{-1}) as a function of adsorption time.

In addition to property characterization, the gas adsorption performance of the as-prepared MOFs was also evaluated. In particular, DRIFTS was used to analyze the CO_2 adsorption behaviors of these samples. As shown in **Figure 3.6A**, the characteristic IR peaks of adsorbed CO_2

on three representative samples have different areas and shapes, indicating the various CO_2 adsorption capacity and preferential sites. Specifically, the IR peak area is closely related to the amount of adsorbed CO_2 molecules. Therefore, the peak areas in the wavenumber range from 2220 cm^{-1} to 2450 cm^{-1} were measured as a function of time and then used to obtain the CO_2 adsorption kinetics (**Figure 3.6B**). As exhibited in **Figure 3.6B**, Cu-TMA shows the highest CO_2 adsorption rate and capacity, followed by Cu-$(BDC)_2(TMA)_2$ and then Cu-BDC. Moreover, the adsorbed CO_2 exhibits two IR bands at 2337 cm^{-1} and 2360 cm^{-1} (**Figure 3.6A**), corresponding to the interaction of CO_2 molecules with metal sites and functional groups, respectively.[64] Interestingly, with more Cu-TMA, the intensity of Peak (2337 cm^{-1}) becomes larger while the intensity of Peak (2360 cm^{-1}) becomes smaller, inferring the changes in the preferential adsorption of CO_2 molecules on the sites of copper ions over functional groups. To quantify the preferential adsorption, the area ratios of the IR Peak (2337 cm^{-1}) to Peak (2360 cm^{-1}) were calculated and presented in **Figure 3.6C**. For the case of pure Cu-TMA, the peak ratio has the highest value (i.e., 3.02) in the beginning of the adsorption process, and then gradually decreased and stabilized at 2.25, indicating that CO_2 molecules prefer to be adsorbed with the interaction with metal sites, and then on the functional groups. While, in the case of Cu-BDC, the values of the peak ratios were the lowest but also the most stable ones, suggesting that there is no variation in preferential adsorption site during the evolution process. The above results imply that both preferential adsorption site and adsorption capacity of CO_2 molecules are tunable by adjusting the component ratios in the mixed-linker MOFs.

3.4 Conclusions

In summary, Cu-TMA/Cu-BDC mixed-linker MOFs with a range of component ratios have been successfully fabricated via the microdroplet-based spray process. Results show that, the adjustment of the mole ratio of TMA to BDC in the precursor solution would allow continuous tuning of the properties of mixed-linker MOFs, including crystalline phases, surface chemistry, and textual properties. In particular, the mixed-linker MOFs possess interpenetrating framework, which leads to the formation of additional pores and thus increased pore volume. Moreover, DRIFTS was also used to study the CO_2 preferential adsorption sites and adsorption kinetics, which have also been proven to have significant dependence on the component ratios of mixed-linker MOFs. This is the first systematic study of the synthetic chemistry of mixed-linker MOFs in the microdroplet-based spray process. It is expected that, through rational control of the synthetic parameters, the microdroplet-based spray process can be applied to produce a variety of mixed-component MOFs with specifically desired properties.

Chapter 4. Facile synthesis of ZnO@ZIF core–shell nanofibers: crystal growth and gas adsorption

CrystEngComm, 19(18): 2445-2450 (2017)
DOI: 10.1039/C7CE00368D

Abstract

ZnO@ZIF-8 core-shell nanofibers were manufactured via direct growth of ZIF-8 on eletrospun ZnO nanofibers for the first time. The versatility of this synthesis strategy for other ZnO@ZIF nanofibers was also demonstrated. The as-synthesized ZnO@ZIF-8 nanofibers exhibit enhanced CO_2 adsorption ability and unique adsorption preference as compared to pristine ZnO nanofibers.

4.1 Introduction

In the past several decades, metal organic frameworks (MOFs) have been attracting tremendous attention for various applications, such as gas storage, separation and catalysis,[4] due to their high surface areas, tunable pore sizes and tailorable surface chemistry.[95] In addition to pure MOFs, profound attention has also been directed toward the incorporation of MOFs with metals/metal oxides aiming to integrate the functionalities of both materials.[96-97] These kinds of composites can be produced with several different morphologies, such as films,[98] hollow spheres[99], nanowires[100] and nanorods.[101-102] On the other hand, the nanofiber structure is also of great interest, considering its high aspect ratio and ability to avoid aggregation, which is important for many applications, including gas adsorption and catalysis. However, only a few papers have reported the synthesis of metal oxide@MOF composites in the form of nanofibers thus far (e.g., Al_2O_3@MIL-53-NH_2 and TiO_2@UiO-66).[103-108] The procedures for the fabrication of these metal oxide@MOF nanofibers in the reported papers are similar.[103-108] In brief, atomic layer deposition (ALD) was employed to deposit metal oxide layers onto the polymer nanofibers. These metal oxide layers served as the

template for the MOFs growth via the solvothermal method. However, the ALD deposition of metal oxide layers involves complicated and multi-step processes, which may limit the further exploration of this strategy.

In order to simplify the synthesis procedure and avoid the use of costly equipment (e.g., ALD), a new strategy was developed in this study for the facile synthesis of metal oxide@MOF nanofibers. Briefly, an electrospinning technique was used to produce polymer nanofibers containing zinc nitrate, which were then calcinated to obtain the zinc oxide (ZnO) nanofibers. These nanofibers subsequently acted as a sacrificial metal source and template for ZIF (zeolitic imidazolate framework) growth to form the ZnO@ZIF core-shell structure. To the best of our knowledge, this is the first demonstration of the facile manufacturing of ZnO@ZIF core-shell nanofibers by using this method. The core-shell nanofibers combine the functionalities of both ZnO and ZIF. In particular, ZnO has been widely used in gas sensing and catalytic processes.[109] Meanwhile, the ZIF shell, with an excellent gas capture ability, can supply more gas molecules to the ZnO surface, which can help ZnO to achieve better performance.

4.2 Materials and Methods

Materials. PVP (MW: 1, 300, 000), $Zn(NO_3)_2 \cdot 6H_2O$ were purchased from the Sigma-Aldrich Chemicals company. *N, N*-dimethylformamaide (DMF) was obtained from VWR Corporation. 2-methylimidazole and 4-methyl-5-imidazolecarboxaldehyde were purchased from Acros Organics. All the chemicals were used without further treatment

Fabrication of ZnO and ZnO@ZIF nanofiber. In a typical procedure, 3 g of PVP was dissolved in 38 mL ethanol, and then mixed with 10 mL DI water containing 4 g of $Zn(NO_3)_2 \cdot 6H_2O$. The mixture was subjected to magnetic stirring for ca. 1 hour to obtain a transparent solution. Subsequently, the solution was loaded into a glass syringe equipped with a stainless steel needle (Inner diameter: 250 μm), which was connected to high voltage supply. The feeding rate was controlled by the syringe pump. The PVP-$Zn(NO_3)_2$ nanofibers were obtained by electrospinning at a voltage of 15 kV, an electrospinning distance of 10 cm and a feeding rate of 1.0 mL/h. A piece of alumina foil was used to collect the electrospun nanofibers. The temperature and humidity during the electrospinning process were controlled at 25 °C and 30%, respectively. The as-spun nanofibers were then subjected to calcination in a muffle furnace at 500 ºC (ramping rate: 2 ºC/min) in air for 1 hour to remove the PVP and decompose $Zn(NO_3)_2$ to synthesize ZnO nanofibers. The as-prepared ZnO nanofibers were placed in a glass bottle, in which 2-methylimidazole was dissolved in DMF with a concentration of 0.08 mol/L. The molar ratio of ZnO nanfiber to the ligands was controlled at 0.03. After the mixture was heated in the oven at 70 ºC for 3 h, the nanofibers were taken out and immersed in methanol for 1 hour to remove the residuals. After that, ZnO@ZIF-8 core-shell nanofibers were obtained. The same procedures were carried out for the synthesis of ZnO@ZIF-93, except that 4-methyl-5-imidazolecarboxaldehyde was used as a ligand instead of 2-methylimidazole.

Synthesis of pure ZIF-8 particles. The following procedure was slightly modified from a previous report.[110] A solution of 1.4622 g $Zn(NO_3)_2 \cdot 6H_2O$ (4.92 mmol) in 100 mL methanol was

rapidly added to a solution of 1.6248 g 2-methylimidazole (19.8 mmol) and 0.1676 g sodium formate (2.46 mmol) in 100 mL methanol under stirring with a magnetic bar. The stirring was turned off after one minute and the solution slowly turned turbid. After 24 hours, the ZIF-8 particles were collected by centrifugation at 7000 rpm for 10 minutes, and then washed with fresh methanol three times.

Sample Characterization. The morphology and diameter distribution of the nanofibers were observed by SEM (Su-70, Hitachi) and TEM (Libra 120, Zeiss). The phase identification was obtained using a PANalytical X'Pert Pro MPD X-ray diffractometer equipped with a Cu-Kα radiation source (λ=1.5401 Å). Fourier Transform Infrared (FTIR) spectrometer (Nicolet iS50, Thermos Scientific), which is equipped with an attenuated total reflectance (ATR) accessory, was used to analyze the vibrational properties of the samples. The Micromeritics ASAP 2020 Plus Physisorption system was used to determine the N_2 physisorption isotherms and BET surface areas of the samples.

***In-situ* DRIFTS Analysis (CO_2 adsorption).** This analysis was conducted in a DRIFTS chamber. Firstly, the chamber loaded with nanofibers was purged with ultrapure helium gas (purity > 99.995 %, Praxair) with a flow rate of 30 mL/min at 150 °C for 30 min. Subsequently, the heater was turned off to allow the temperature to cool down to room temperature and an IR background spectrum was collected. Then, CO_2 gas (10%, helium as balance gas, Praxair) was continuously introduced to the chamber with a flow rate of 4 mL/min. Meanwhile, the IR spectra were collected to record the CO_2 adsorption as a function of time.

4.3 Results and discussions

The synthesis procedures are illustrated in **Figure 4.1A** and detailed in the experimental section. In brief, a mixture of PVP (polyvinylpyrrolidone)/$Zn(NO_3)_2 \cdot 6H_2O$/water/ethanol was electrospun to obtain PVP/$Zn(NO_3)_2$ nanofibers. The as-prepared nanofibers were then calcined at 500 °C in air for 1 hour with a heating rate of 2 °C/min to remove PVP and obtain ZnO nanofibers. Subsequently, the ZnO nanofibers were immersed in a solution containing 2-methylimidazole (MIM, linker) and N, N-dimethylformamaide (DMF, solvent), heated at 70 °C for ZIF-8 growth.

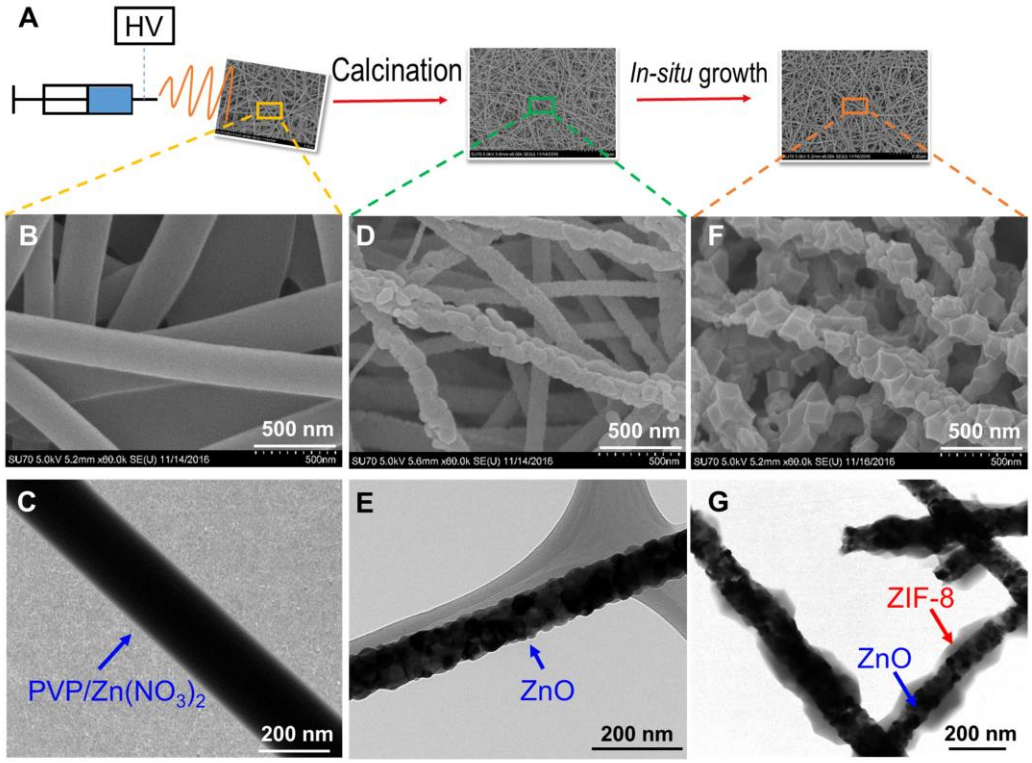

Figure 4.1 (A) Schematic illustration of the synthesis procedures; SEM images of (B) electrospun PVP/$Zn(NO_3)_2$ nanofibers, (D) ZnO nanofibers and (F) ZnO@ZIF-8 nanofibers; TEM images of (C) electrospun PVP/$Zn(NO_3)_2$ nanofibers, (E) ZnO nanofibers and (G) ZnO@ZIF-8 nanofibers.

As shown in **Figure 4.1B** and **4.1C**, the PVP/$Zn(NO_3)_2$ nanofibers exhibit smooth surface and have a geometric mean diameter of 262 nm with narrow diameter distribution with a standard deviation of around 1.2. After calcination, the PVP was removed and $Zn(NO_3)_2$ was converted into ZnO as a result of thermal decomposition: $2Zn(NO_3)_2 \rightarrow 2ZnO + 4NO_2\uparrow + O_2\uparrow$.[111] The surfaces of the ZnO nanofibers turned out to be relatively rough as revealed from the SEM (scanning electron microscopy, **Figure 4.1D**) and TEM (transmission electron microscopy, **Figure 4.1E**) images, where primary ZnO nanocrystals are clearly observed. The size and crystallinity of the ZnO nanocrystals can be controlled by adjusting the calcination temperature and time.[112] Compared with the PVP/$Zn(NO_3)_2$ nanofibers, the ZnO nanofibers have a smaller geometric mean diameter (144 nm), owing to the removal of PVP and pyrolysis of $Zn(NO_3)_2$. After immersing the ZnO nanofiber in a 2-methylimidazole ligand solution for 3 hours, ZIF-8 crystals were successfully grown on the surfaces of ZnO nanofibers with rhombic dodecahedron morphology (**Figure 4.1F and 4.1G**). The coating of the ZIF-8 shell increased the geometric mean diameter of the nanofiber to 258 nm. The geometric mean diameter of the ZnO core was calculated to be 97 nm from the TEM images. Based on the changes in diameters of ZnO nanofibers before and after the ZIF growth, the molar ratio of the ZIF-8 shell to the ZnO core was calculated to be 1.2. This molar ratio can be tuned by changing the growth conditions for ZIF-8, such as temperature, time, and MIM concentration to achieve optimal performance as needed.

After synthesis, the samples were subjected to detailed characterization. First, X-ray diffraction (XRD) analysis (**Figure 4.2A**) confirms the crystal structures of ZnO and ZIF-8, in line with those reported in literature.[113-114] Specifically, the diffraction peaks at 31.8°, 34.5° and 36.7° are associated with the (100), (002) and (101) planes of wurtzite hexagonal structure of ZnO crystals (PDF 36-1451), respectively, which is the most thermodynamically stable crystal structure of ZnO at room temperature.[115] The diffraction peaks at 7.4°, 10.5° and 12.8° correspond to the (011), (002) and (112) planes of ZIF-8 crystals, respectively.

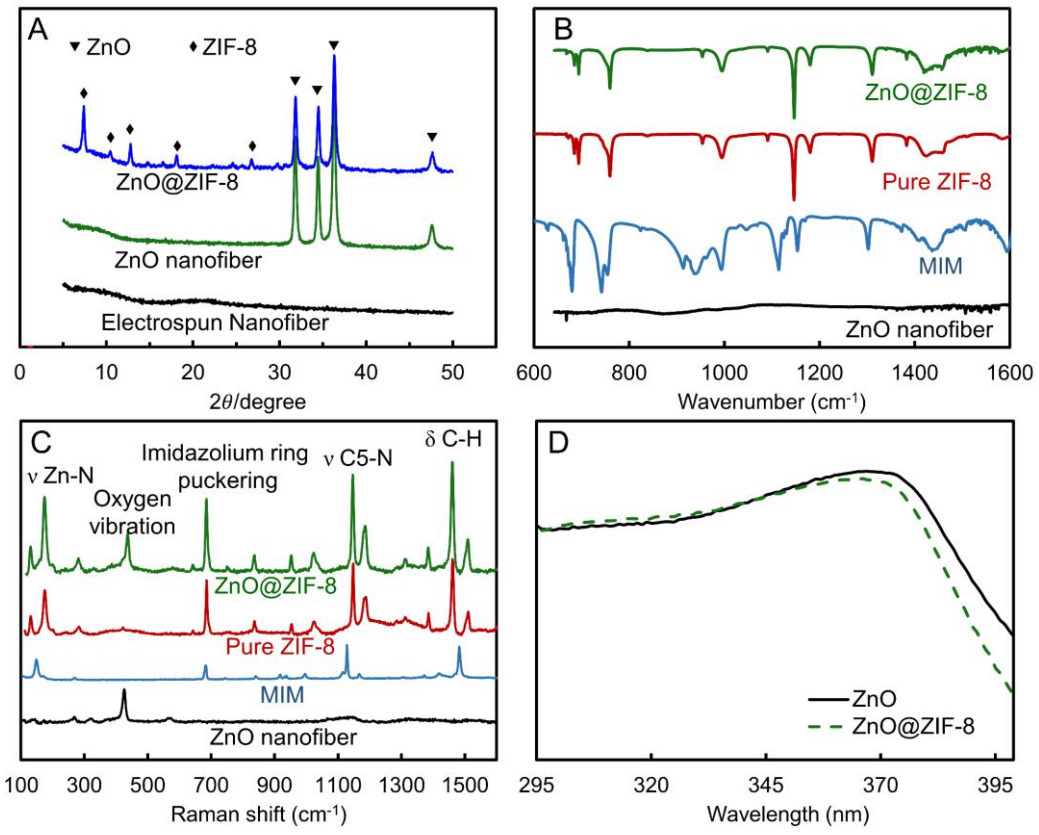

Figure 4.2 Characterization of the samples: (A) XRD patterns, (B) FTIR, (C) Raman Spectra, and (D) UV-vis spectra.

The introduction of surface functional groups was revealed from Fourier transform infrared (FT-IR) analysis. As shown in **Figure 4.2B**, no appreciable peak was observed on the ZnO nanofibers, while intense IR peaks were found for ZnO@ZIF-8 nanofibers, which differ from the MIM's IR peaks but perfectly match with those belonging to pure ZIF-8 particles, demonstrating the formation of ZIF-8 crystals on the ZnO nanofibers. Specifically, the observed IR peaks on ZnO@ZIF-8 nanofibers originate from the vibrations of imidazole units, with bending and stretching modes in the spectral region of 600-1350 cm^{-1} and 1350-1500 cm^{-1}, respectively.[116-117]

Raman spectroscopy was utilized to understand the vibrational properties of ZnO and ZnO@ZIF-8 nanofibers (**Figure 4.2C**). For ZnO nanofibers, the peak at 436 cm^{-1} is related to E_{2H} mode, and its strong intensity suggests the long-range crystalline order of ZnO.[118] Peaks at 280, 333, 580 cm^{-1} correspond to $B_1^{high} - B_1^{low}$, $E_2^{high} - E_2^{low}$, and E_1(LO) modes, respectively.[119] All of the peaks in the Raman spectra for ZnO nanofibers correspond to the various phonon modes of wurtzite ZnO, consistent with the XRD data. The aforementioned information demonstrates that the obtained ZnO nanofiber is stable and well crystallized. For ZnO@ZIF-8 nanofibers, four new strong peaks appear at 175, 685, 1147, and 1460 cm^{-1}, corresponding to Zn-N stretching, imidazolium ring puckering, C5-N stretching, and C-H bending, respectively.[120-121] Other small peaks, excluding the ones belonged to ZnO (280, 436 and 580 cm^{-1}), are all associated with the vibrational properties of ZIF-8. The new bands once again confirm the successful growth of ZIF-8 on the ZnO nanofibers.

The UV-vis absorption spectra are displayed in **Figure 4.2D**, demonstrating the variation in the light absorption properties between ZnO@ZIF-8 and ZnO nanofibers, which is attributed to the larger band gap of the core-shell structure as compared that of the pristine ZnO nanofiber. This result is consistent with the fact that ZIF-8 (~ 4.9 eV[122]) has a much larger band gap than that of ZnO (~ 3.15 eV[123]).

Understanding the mechanism and key parameters (i.e., solvent species[101] and MIM concentration[124]) governing *in-situ* ZIF-8 formation on ZnO surface is of significant importance. Initially, 2-methylimidazole acts as an etching reagent to dissolve ZnO and release Zn^{2+} ions, which subsequently coordinate with the MIM ligands to form nuclei and then ZIF-8 crystals.[101] The ZIF-8 crystals can be generated either in the solution as free particles or *in situ* on the ZnO surface as a shell, determined by the rates of dissolution and coordination.[101] Specifically, if the dissolution rate is much faster than the coordination rate, the released but uncoordinated Zn^{2+} will diffuse into the solution, thus forming free crystals.[125] Several parameters can be adjusted in order to control the dissolution rate, including the solvent species and concentration of MIM. As reported by Zhan et al.,[101] the solvent plays a significant role in determining the Zn^{2+} dissolution rate. As compared to water, DMF has the capability to reduce the etching rate of the ligand and thus the dissolution rate of Zn^{2+}. To minimize the possibility of free crystals and assure the formation of a well-defined ZnO@ZIF-8 core-shell structure, pure DMF was used in the current study. In addition to solvent species, MIM concentration also affects the dissolution rate. In particular, high MIM concentration causes rapid Zn^{2+} releasing rate and thus the formation of free ZIF-8 crystals, while

low MIM concentration significantly decrease the reaction rate. In this study, an optimized MIM concentration was chosen to ensure the absence of free ZIF-8 crystals while maintaining a reasonable reaction rate.

The growth of ZIF-8 crystals on ZnO nanofibers was monitored with the evolution of morphology (**Figure 4.3**) and crystallinity (**Figure 4.4**) as a function of reaction time. At the initial stage of reaction (i.e., 1 hour), small amount of sphere-like particles appeared on the surface of ZnO nanofibers (**Figure 4.3A**). These particles have a diameter of 74 nm and poor crystallinity (**Figure 4.4**, black line). Prolonged reaction time (i.e. 2 hours and 3 hours) not only increased the crystal size (106 nm after 2-hour reaction) and amount **(Figure 4.3B and C)**, but also enhanced the crystallinity (**Figure 4.4**, green and blue line) and shapes the particles into rhombic

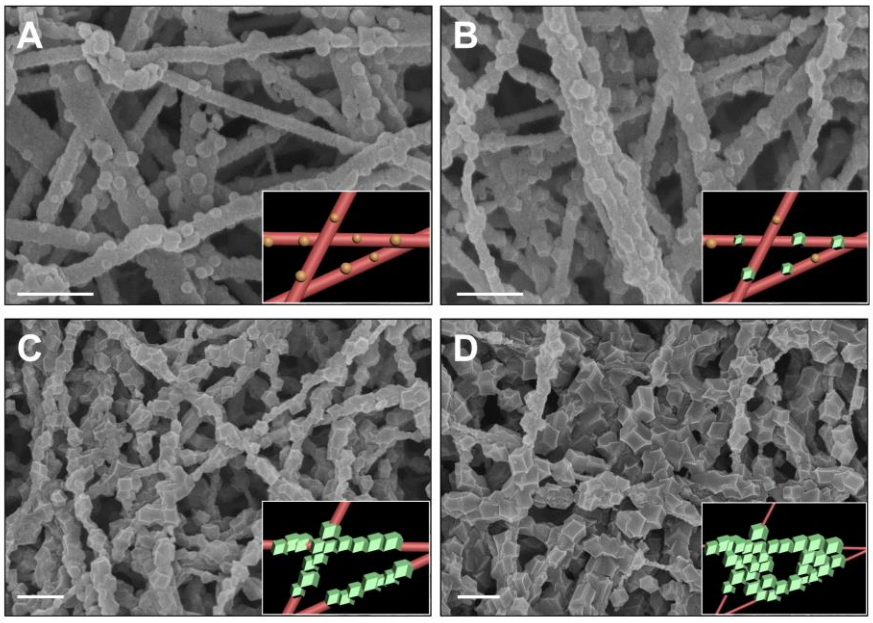

Figure 4.3 Time-dependent morphology evolution ZIF-8 on ZnO nanofibers: (A) 1 h, (B) 2 h, (C) 3 h and (D) 6 h. Scale bar: 500 nm.

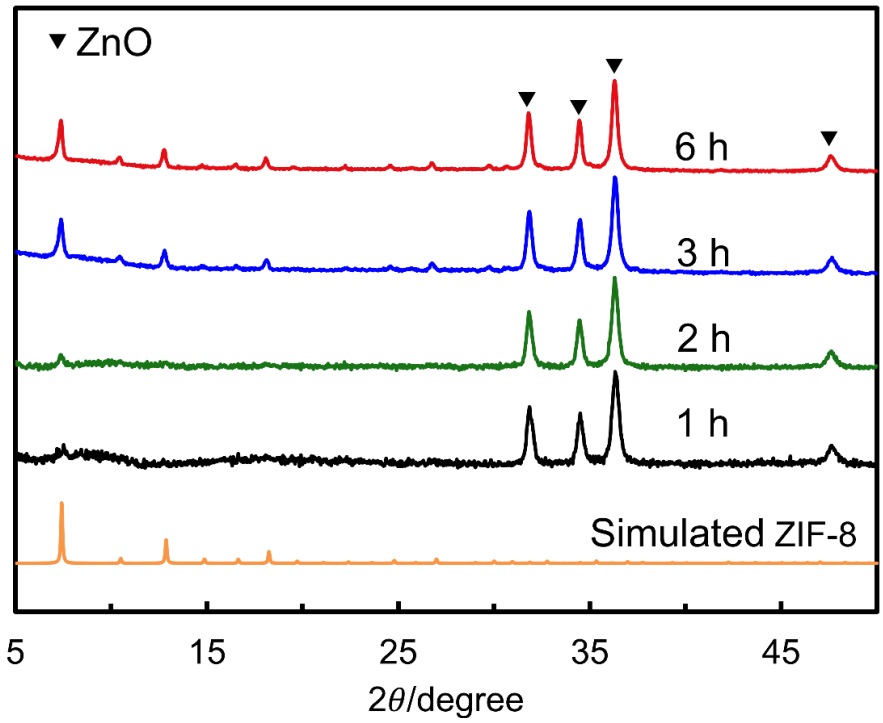

Figure 4.4 Time-dependent crystallinity evolution of ZnO@ZIF-8 nanofibers.

dodecahedron **(Figure 4.3B and C)**. As the growth proceeds to 6 hours, the ZIF-8 crystals started to integrate and form a uniform shell (**Figure 4.3D**).

ZIF-8 has been widely used for CO_2 capture.[126] With the incorporation of ZIF-8, the CO_2 uptake of the nanofibers is expected to be improved. Herein, the *in situ* diffuse reflectance infrared Fourier transform spectroscopy (DRIFTS) analysis was conducted in order to assess the CO_2 adsorption capabilities of the core-shell nanofibers. As revealed in **Figure 4.5A** and **Figure 4.5B**, the adsorbed CO_2 gases show two characteristic peaks at 2340 and 2360 cm^{-1}, associated with the antisymmetric stretching modes of CO_2 gas adsorbed on metal sites ($Zn^{2+}\cdots O=C=O$)[127] and on functional groups ($OH\cdots O=C=O$),[128] respectively. By comparing the spectra in **Figure 4.5A** and

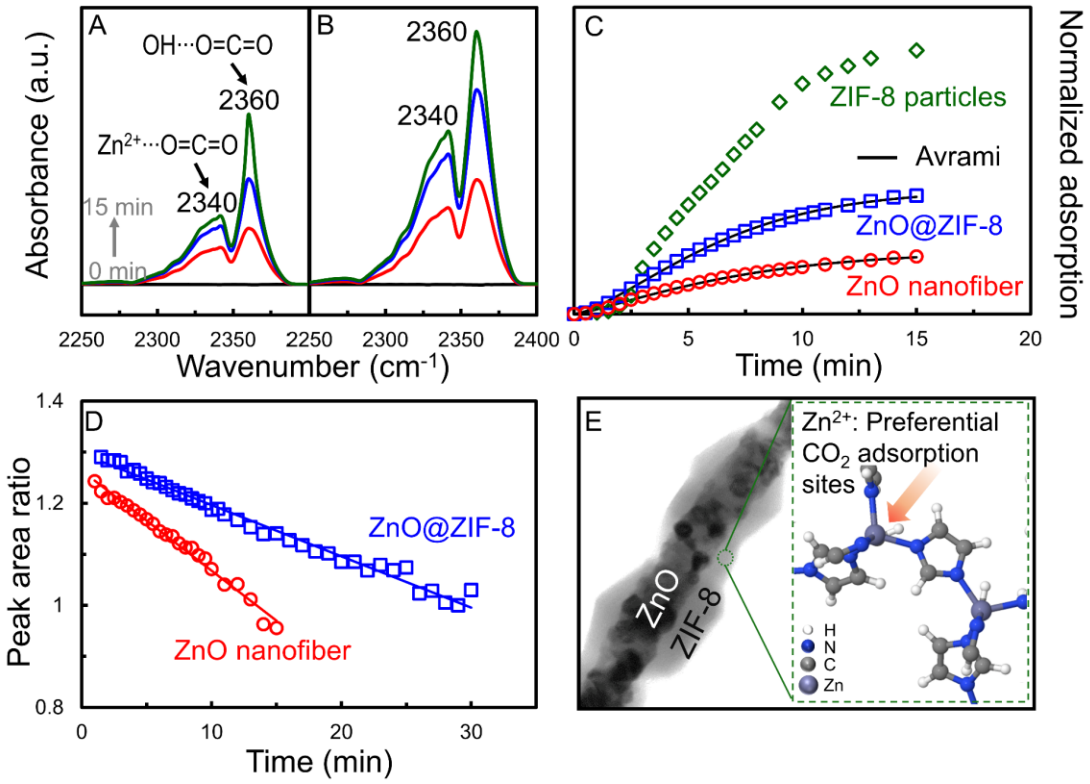

Figure 4.5 DRIFTS spectra of adsorbed CO_2: (A) ZnO nanofiber and (B) ZnO@ZIF-8 nanofiber; (C) CO_2 adsorption kinetics; (D) Changes of the peak area ratio ($Peak_{2340}/Peak_{2360}$) as a function of time; (E) Illustration of the preferential CO_2 adsorption sites of ZnO@ZIF-8.

4.5B, higher peaks were observed in the case of ZnO@ZIF-8 nanofibers, intuitively indicating that more CO_2 gases were adsorbed on ZnO@ZIF-8 nanofibers than those on ZnO nanofibers. In addition, the adsorption kinetics were also obtained by recording the IR peak areas as a function of time. As shown in **Figure 4.5C**, ZnO@ZIF-8 core-shell nanofibers show a larger adsorption capacity and faster adsorption rate compared with ZnO nanofibers. CO_2 adsorption experiments were also conducted on the surface of pure ZIF-8 particles. As shown in **Figure 4.5C**, pure ZIF-8 was found to have the best CO_2 adsorption ability. The varying CO_2 adsorption abilities mainly

results from the differences in the surface areas. Specifically, pure ZIF-8 has the largest surface area (1061 ± 17.7 m^2/g), while ZnO nanofibers have the lowest surface area (20 ± 1.2 m^2/g). With the incorporation of ZIF-8 shell, the surface area of ZnO@ZIF-8 nanofibers is improved to 253 ± 4.2 m^2/g, but still lower than that of pure ZIF-8, due to the large portion of ZnO in the composite nanofibers. It should be noted that it is desirable to keep ZnO as the core so that its functionalities (e.g., gas sensing and catalytic ability) can be maintained. The ZIF-8 shell is mainly used to capture CO_2 or other gases and supply more gas molecules to the ZnO core for better performance.

Table 4.1 Adsorption kinetic constants and error calculated from the fitting of Avrami model.

Sample	Avrami model $q_t = q_e(1 - \exp(-(k_A t)^{n_A}))$			
	k_A	q_e	n_A	Error (%)
ZnO	0.135	32687	1.24	2.9
ZnO@ZIF-8	0.144	64571	1.41	2.2

q_t and q_e (IR peak area/g) are the adsorbed amount at given time (t, min) and equilibrium, respectively; k_A (min^{-1}) is the Avrami kinetic constant; n_A is the Avrami exponent.

The kinetics of CO_2 adsorption on the nanofibers were further simulated by using the least square method with three different models, including pseudo-first order, pseudo-second order and the Avrami model. To compare the divergence between the experimental and fitting data, an error function was used as shown below,[129]

$$\text{Error (\%)} = \sqrt{\frac{\Sigma(\frac{q_{t(exp)} - q_{t(mod)}}{q_{t(exp)}})^2}{N-1}} \times 100 \quad (4.1)$$

where, $q_{t(exp)}$ and $q_{t(mod)}$ are the experimental and modelling adsorbed CO_2 amount (IR peak area/g) at a given time, t (min); N is the number of the data points.

The results show that, the Avrami model provides the best fit to the adsorption data with the least error values (< 3%). The best fit of the Avrami model to the adsorption data reflects the complexity of CO_2 adsorption on the nanofibers.[130-131] In addition, a larger Avrami exponent (n_A) was achieved when the ZnO@ZIF-8 core-shell nanofibers were used as the adsorbents, indicating that CO_2 adsorption on the core-shell nanofibers were more contact time dependent.[132]

In addition to the large surface area of ZIF-8, facilitated interaction of CO_2 with the metal sites in ZIF-8 also contributed to the enhanced CO_2 adsorption on the ZnO@ZIF-8 core-shell nanofibers, which can be evaluated by monitoring the area ratios of $Peak_{2340}$ to $Peak_{2360}$. As shown in **Figure 4.5D**, a higher $Peak_{2340}/Peak_{2360}$ ratio was observed in the case ZnO@ZIF-8 nanofibers, indicating that a larger fraction of CO_2 molecules was adsorbed on metal sites in the presence of ZIF-8, the schematic illustration of which was displayed in **Figure 4.5E**. This preferential interaction of CO_2 with the surface metal sites is caused by the existence of low-coordinated zinc ions at the external surface of ZIF-8. According to the studies of Chizallet and co-workers,[133-134] due to the crystal cleaving (i.e., linker loss), ZIF-8's external surface is dominated by low-coordinated Zn sites, which act as potential Lewis acid sites and thus facilitate the adsorption of CO_2 molecules. Besides, the interaction of CO_2 with Zn sites could cause greater distortion of CO_2 bond angle and lead to CO_2 bond activation,[135] which is of great importance for CO_2 photo-conversion process.[64, 136]

4.4 Conclusions

A novel strategy was developed to synthesize the ZnO@ZIF core-shell nanofibers. The growth mechanism of ZIF-8 on ZnO nanofibers was explored by monitoring the morphology and crystallinity evolution as a function of reaction time. This core-shell structure has a high CO_2 adsorption ability, mainly due to the large surface area of ZIF-8 and the unique interaction of CO_2 with the metal sites, and shows great potential for future applications, such as CO_2 photoreduction into hydrocarbon fuels.

Chapter 5. Rapid Formation of Metal–Organic Frameworks (MOFs) Based Nanocomposites in Microdroplets and Their Applications for CO_2 Photoreduction

Abstract

A copper-based metal–organic framework (MOF), $[Cu_3(TMA)_2(H_2O)_3]_n$ (also known as HKUST-1, where TMA stands for trimesic acid), and its TiO_2 nanocomposites were directly synthesized in micrometer-sized droplets via a rapid aerosol route for the first time. The effects of synthesis temperature and precursor component ratio on the physicochemical properties of the materials were systematically investigated. Theoretical calculations on the mass and heat transfer within the microdroplets revealed that the fast solvent evaporation and high heat transfer rates are the major driving forces. The fast droplet shrinkage because of evaporation induces the drastic increase in the supersaturation ratio of the precursor, and subsequently promotes the rapid nucleation and crystal growth of the materials. The HKUST-1-based nanomaterials synthesized via the aerosol route demonstrated good crystallinity, large surface area, and great photostability, comparable with those fabricated by wet-chemistry methods. With TiO_2 embedded in the HKUST-1 matrix, the surface area of the composite is largely maintained, which enables significant improvement in the CO_2 photoreduction efficiency, as compared with pristine TiO_2. In situ diffuse reflectance infrared Fourier transform spectroscopy analysis suggests that the performance enhancement was due to the stable and high-capacity reactant adsorption by HKUST-1. The current work shows great promise in the aerosol route's capability to address the mass and heat transfer issues of MOFs formation at the microscale level, and ability to synthesize a series of MOFs-based nanomaterials in a rapid and scalable manner for energy and environmental applications.

5.1 Introduction

The growing concerns about global warming, caused by the continuous increase of atmospheric carbon dioxide (CO_2) concentrations, have driven considerable research interests in CO_2 capture and conversion.[137-138] Among various technologies, CO_2 photoreduction appears to be a promising approach, which not only addresses global warming issues by decreasing CO_2 levels, but also converts CO_2 into valuable chemicals.[139-145] In particular, the development of efficient photocatalysts for CO_2 photoreduction has been an active field of research.

During the past few decades, a myriad of semiconductors have been employed for CO_2 photoreduction, such as titanium dioxide (TiO_2), zinc oxide (ZnO), and cadmium sulfide (CdS).[145] However, the CO_2 photoreduction efficiencies of these semiconductor-based photocatalysts remain unsatisfactory. One of the crucial reasons is that CO_2 molecules usually have a low affinity for the semiconductor surface and thereby resulting in low CO_2 supply during the photoreduction process.[146] Progress has been achieved in enhancing the CO_2 capture efficiencies by incorporating inorganic porous media (e.g., zeolites and silica[145]) and layered double hydroxides.[147]

On the other hand, metal organic frameworks (MOFs), a type of emerging porous polymer materials, have attracted extensive attention in the past few decades due to their extremely large surface areas, tunable nanoscale cavities, ultralow densities, and high chemical tailorability.[95] In particular, MOFs have been widely conceived as excellent candidates for CO_2 capture, separation, and storage.[148] The development of MOFs-based photocatalysts, such as light-harvesting MOFs[149] for simultaneous CO_2 capture and photoreduction, however, is still in its infancy.[145] Several MOFs

have been synthesized for CO_2 photoreduction, such as UiOs,[150] MILs,[151] and porphyrin-MOFs.[146, 152] However, these pristine MOFs generally exhibited lower CO_2 photoreduction efficiencies than their semiconductor counterparts.

The integration of semiconductors and MOFs could be a rational strategy to improve the CO_2 photoreduction efficiency, as the hybrid system combines the advantages of the high adsorption capacity of MOFs with the high stability, low cost, and good photocatalytic ability of semiconductors.[153-155] For instance, Liu et al. synthesized zeolitic imidazolate framework (ZIF)-semiconductor composites by growing ZIF-8 crystals on Zn_2GeO_4 nanorods via a hydrothermal method, the CO_2 photoreduction efficiency of which was 62% higher than that of bare Zn_2GeO_4 due to the enhancement in CO_2 adsorption capacity.[153] Wang et al. demonstrated the promotional effect of cobalt-containing ZIF (Co-ZIF-9) on the electron transfer when the CdS is used as the co-catalyst, leading to a high apparent quantum yield and CO_2 photoreduction efficiency.[154] Li et al. recently reported a MOF@TiO_2 core-shell structure, where the MOF not only enhanced the CO_2 capture efficiency, but also facilitated the charge separation in TiO_2.[155]

The aforementioned pioneering studies have demonstrated the significant potentials for CO_2 photoreduction efficiency improvement by the integration of MOFs and semiconductors. However, the rational design and synthesis of MOFs-semiconductor composites still need to be further explored. For example, coating of semiconductors on MOFs surfaces may be undesirable since the semiconductor may limit the gas adsorption capability of the MOFs by blocking the gas adsorption sites and transport channels. In order to maximize the usage of MOFs' high surface

area, tunable porosity, and rich surface functionality, embedding semiconductors within the MOFs porous matrix may be preferred toward better CO_2 photoreduction efficiencies. It is also worth noting that all the above MOFs and MOFs-semiconductor composites were synthesized by conventional bulk solution or wet-chemistry methods,[4] where multi-step procedures and long reaction time (hours to days) are usually required. Furthermore, homogenous growth of MOFs crystals and smooth integration of semiconductors and MOFs in bulk solution processes still face challenges of slow nucleation and crystal growth, non-uniform heating, and inhomogeneous mixing.[4] In this sense, synthesis of MOFs-based nanocomposites inside micrometer-sized droplets (microdroplets, hereafter) via gas phase routes, such as aerosol methods,[156] may be a promising approach to address the heat and mass transfer issues in the microscale.

Herein, we report a strategy for the direct synthesis of a copper-containing MOF, $[Cu_3(TMA)_2(H_2O)_3]_n$ (known as HKUST-1,[157] where TMA stands for trimesic acid), and HKUST-1/TiO_2 nanocomposites in microdroplets via a single-step aerosol route in a rapid manner, i.e., within several seconds (**Scheme 5.1**). The aerosol routes have been widely recognized as being capable of producing a variety of functional materials with controlled sizes, morphologies, and functionality in a continuous and scalable manner.[158-159] HKUST-1 was employed due to its porous structure, which offers a highly accessible porosity (~ 40.7%) and a high surface area (over 600 m^2/g).[157] In addition, the hydrophilicity of HKUST-1 guarantees simultaneous adsorption of water (H_2O), which is a key co-reactant in many CO_2 photoreduction processes.[145] With TiO_2 embedded within the HKUST-1 matrix, its surface area was largely maintained and a higher CO_2

photoreduction efficiency was achieved. Detailed materials characterization, systematic tuning of process and precursor parameters, and numerical simulations on the mass and heat transfer within the microdroplets disclosed the formation mechanism of HKUST-1 and HKUST-1/TiO_2 in the aerosol route. Possible reaction pathways were also proposed to describe the enhancement of the CO_2 photoreduction efficiency based on the *in-situ* analysis of reactants adsorption, intermediates formation and consumption, and overall CO_2 photoreduction performance. We expect that the aerosol route will enable us to fabricate a wide range of MOFs-semiconductor nanocomposites in a rapid, scalable, and pre- and post-treatment avoided manner, which can find a variety of energy and environmental applications.

5.2 Materials and Methods

Precursor Solution Preparation. The HKUST-1 precursor solution was prepared by dissolving copper nitrate trihydrate ($Cu(NO_3)_2 \cdot 3H_2O$, 98%, Sigma-Aldrich) and trimesic acid (98% Sigma-Aldrich, hereafter TMA) in dimethylformamide (hereafter DMF). The TMA amount was fixed, while the copper nitrate amount was varied with the molar ratio of Cu^{2+}/TMA ranging from 0.33 to 3.5. All precursor solutions were prepared at room temperature and stable for at least 5 hours. The precursor of the nanocomposites was prepared by adding TiO_2 nanocolloids (AERODISP® W740X, Evonik Industries) into the HKUST-1 precursor solution with the molar ratio of HKUST-1/TiO_2 varying from 0.67 to 33.3, based on which the composites were indicated as 0.67 HKUST-1/TiO_2, 1.11 HKUST-1/TiO_2, 3.33 HKUST-1/TiO_2, and 33.3 HKUST-1/TiO_2, respectively.

Materials Synthesis. HKUST-1 and HKUST-1/TiO_2 composites were synthesized by using an aerosol method, as schematically shown in **Figure 5.1A**. The process consisted of a carrier gas feeding system, a Collison nebulizer, an electric furnace, an activated carbon (AC) dryer and a microfiber filter. The precursor solution was atomized by the nebulizer into microdroplets (R_d = ~ 1 μm[160]), and carried by the carrier gas (Q = 4.5 L/min) through the furnace at a predetermined temperature (e.g., 100 to 500 °C), where the microdroplets underwent solvent evaporation, nucleation, evaporation-driven self-assembly of HKUST-1(/TiO_2 composites) and further drying to form final particles (**Figure 5.1B**). The residence time of the process was calculated to be 3.8 s

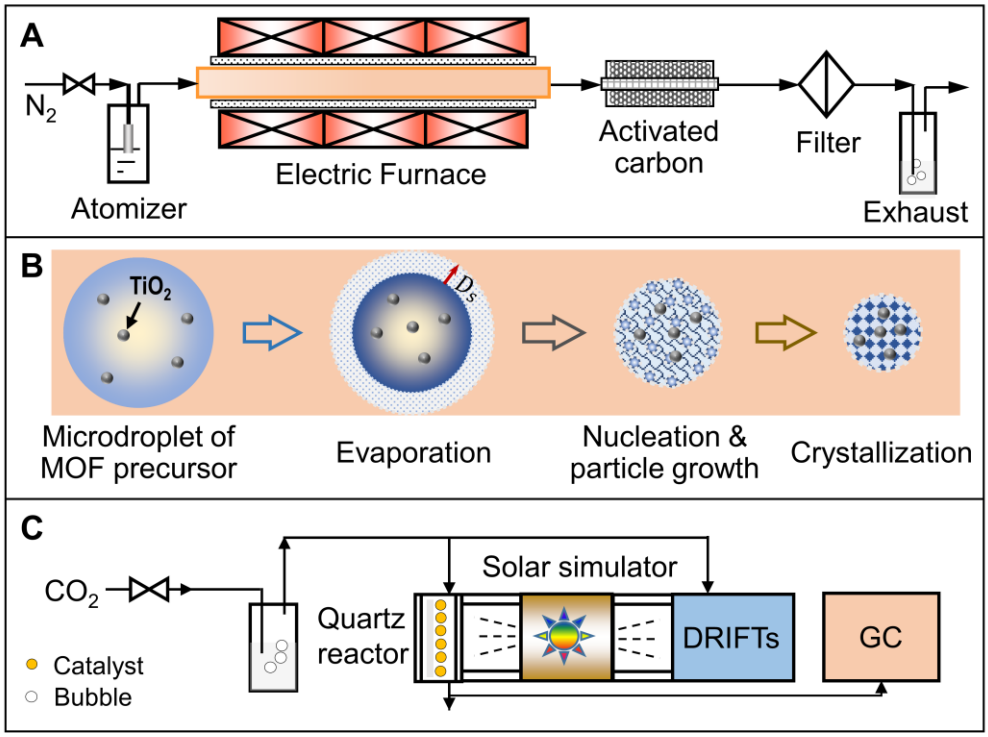

Figure 5.1 Schematic illustration of (A) the furnace aerosol reactor, (B) proposed HKUST-1 and HKUST-1/TiO_2 formation steps inside a microdroplet, and (C) photoreduction measurements.

at 300 °C. The residual solvent/linkers were extracted from the particles by the AC dryer. Finally, the synthesized particles were collected by the microfiber filter.

Materials Characterization. The X-ray diffraction (XRD) patterns of the synthesized samples were obtained from a PANalytical X'Pert Pro MPD X-ray diffractometer using Cu-Kα radiation and the primary crystal sizes were calculated by the Scherrer equation.[161] The characterization of surface chemistry was carried out by using a Fourier transform infrared (FT-IR) spectrometer (Nicolet iS50, Thermo Scientific) equipped with an attenuated total reflectance (ATR) accessory. A transmission electron microscope (TEM, JEM 1230, JEOL) was used to determine the inner structures of the samples. The morphology and size of the samples were analyzed with a Hitachi Su-70 field emission scanning electron microscope (FE-SEM). The porous structures of the samples were analyzed by a gas sorption analyzer (Autosorb iQ, Quantachrome Instruments), where the surface area was obtained by using the Brunauer-Emmett-Teller (BET) method and the pore volume and width were calculated based on the density functional theory. The static contact angles were measured by an OCA 15 goniometer (DataPhysics Instruments).

CO_2 Photoreduction Analysis. The system is illustrated in **Figure 5.1C**, consisting of a home-made flow photoreactor, a 450W Xe lamp (Newport) with an AM 1.5G filter, a gas chromatograph (GC, 7890B, Agilent), and a diffuse reflectance infrared Fourier transform spectrometer (DRIFTS).

(1) GC measurements. The procedures were detailed previously.[162-163] In brief, the compressed CO_2 gas (purity ≥ 99.99 %, Airgas) was introduced into a water bubbler to generate a mixture of CO_2/H_2O vapor, which then passed through the photoreactor under irradiation by the lamp. The

concentrations of effluent gases were recorded by the GC equipped with a CarboPLOT P7 (25 m × 0.53 mm × 25 μm) column and a thermal conductivity detector (TCD). Before each photoreduction test, the photoreactor loaded with the catalysts was purged with the CO_2/H_2O vapor mixture at a flow rate of 30 mL/min for 30 min, and 4 mL/min afterwards. **(2) *In-Situ* DRIFTS analysis.** The analysis (**Figure 5.1C**) was carried out using the FT-IR spectrometer equipped with a Praying Mantis™ diffuse reflection accessory and a reaction chamber (Harrick Scientific). The chamber has two ZnSe windows for IR transmission and one quartz window for irradiation. All DRIFTS tests were performed at 25 °C using a liquid nitrogen cooled HgCdTe (MCT) detector in the range of 720 to 4000 cm^{-1}. Before each DRIFTS test, the reaction chamber loaded with the catalyst was heated at 150 °C and purged with helium (He) gas (purity > 99.995 %, Praxair) at 30 mL/min for 60 min to remove any adsorbed impurities, and then cooled down to 25 °C. After that, a spectrum background was collected. Subsequently, 10% CO_2/He gas mixture (purity > 99.999%, Praxair) or H_2O vapor was fed into the chamber at 4 mL/min for 60 min, during which adsorption spectra were recorded as a function of time. The obtained IR spectra were used to determine CO_2 and H_2O adsorption kinetics, and the generation/consumption of intermediates during CO_2 photoreduction.

Detection of Hydroxyl Radicals ($OH^{\cdot}$). The experimental procedures were analogous to the CO_2 photoreduction except that the catalysts were mixed with terephthalic acid (TA) (mass ratio = 1:5). TA reacts with photogenerated $OH^{\cdot}$ to form 2-hydroxyterephthalic acid (TAOH), which is a perfect probe molecule of $OH^{\cdot}$ and has a characteristic fluorescent peak at ca. 425 nm when excited at 315

nm.[164] All catalysts were kept at the same weight. After illumination, they were dispersed in deionized water, and underwent mixing and centrifuging to obtain a suspension for fluorescence measurements (QuantaMaster™ 400, Photon Technology International).

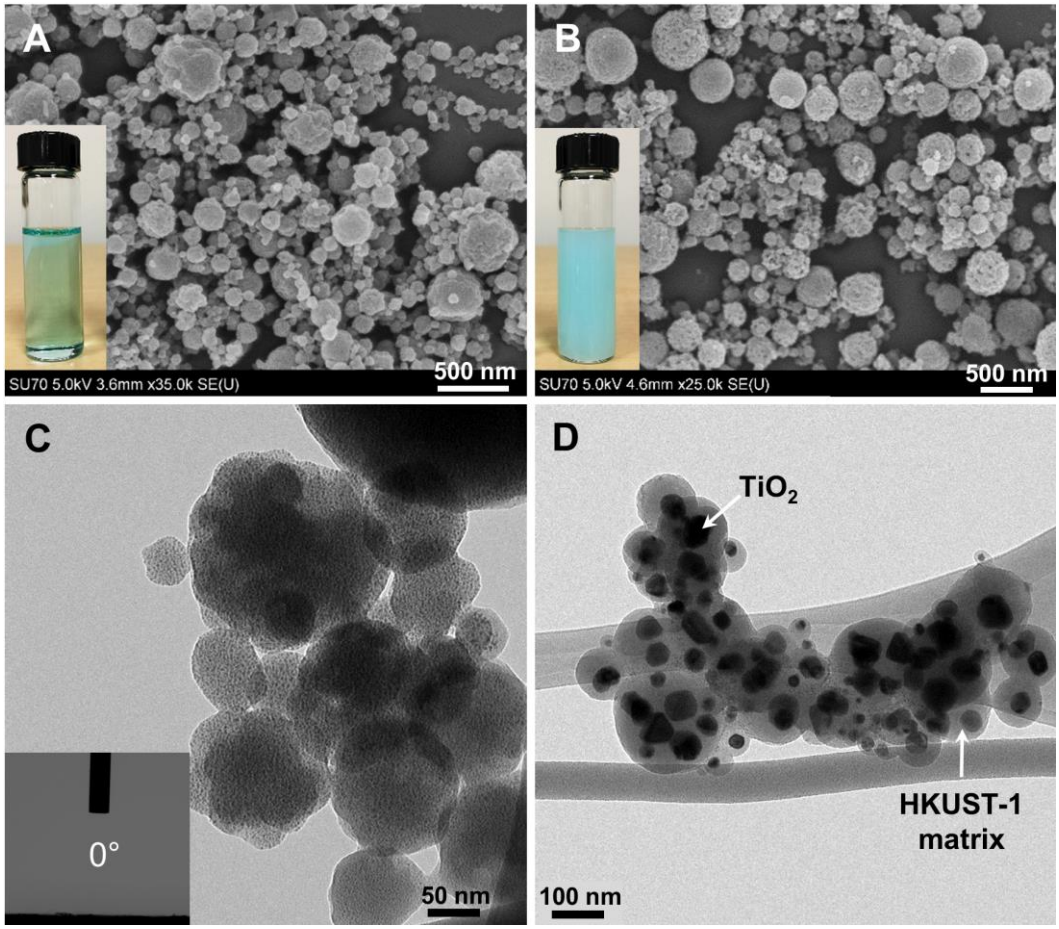

Figure 5.2 SEM images of (A) as-synthesized HKUST-1 and (B) 0.67 HKUST-1/TiO_2 at 300 °C; TEM images of (C) as-synthesized HKUST-1 and (D) 33.3 HKUST-1/TiO_2 at 300 °C. (A, inset) and (B, inset) are the images of precursor solutions of HKUST-1 and 0.67 HKUST-1/TiO_2, respectively. (C, inset) is the image of the contact angle measurement of HKUST-1 surface.

5.3 Results and Discussions

Morphology and Structure Characterization. Two representative samples, i.e., HKUST-1 and HKUST-1/TiO_2 composites, were chosen. HKUST-1 was synthesized at 300 °C from a transparent DMF solution containing $Cu(NO_3)_2$ and TMA (see inset in **Figure 5.2A**). The as-prepared HKUST-1 particles are spherical in shape (**Figure 5.2A**), and have a geometric mean diameter of 94.91 nm with a standard deviation of 1.49, indicating a relatively narrow size distribution. The HKUST-1 particles exhibit highly porous structure as verified by the TEM image in **Figure 5.2C**. Its surface is superhydrophilic with a static contact angle of 0° (**Figure 5.2C**, inset), which is highly favorable for water adsorption during CO_2 photoreduction. The HKUST-1/TiO_2 composite was obtained by spraying the suspension containing TiO_2 nanocolloids and HKUST-1 precursor (**Figure 5.2B**, inset). The composite shows an analogous morphology (**Figure 5.2B**) to that of pristine HKUST-1. In addition, the surface chemistry of the HKUST-1/TiO_2 composites is almost identical to that of pristine HKUST-1. These phenomena are attributed to the homogenous distribution of the precursor components within the microdroplets due to well-mixing in the microscale during liquid atomization.[158] As shown in the TEM image in **Figure 5.2D**, all the TiO_2 nanocolloids were well encapsulated within the HKUST-1 matrix with the outer surface terminated by HKUST-1, which explains the similar morphologies and FT-IR results between HKUST-1 and HKUST-1/TiO_2 composites.

Crystallinity, Surface Chemistry and Pore Structure Characterization. To verify the formation of HKUST-1, the crystallinity should be identified first. As shown in **Figure 5.3A**,

crystallized HKUST-1 was obtained at a temperature as low as 100 °C, demonstrating the feasibility of rapid formation of HKUST-1 by the aerosol route. All XRD peaks of the sample are coincident well with the simulated pattern of HKUST-1.[165] The crystallinity of the HKUST-1 samples is maintained at synthesis temperature up to 300 °C, indicating their relatively high thermal stability. Amorphous samples were obtained at 400 °C and higher, which can be ascribed to the disintegration of metal-organic frameworks owing to thermal instability. This is intuitively seen from the changes in sample colors (**Figure 5.3A**, inset): light to dark blue is observed for samples prepared at 100 to 300 °C; while black is present at higher temperatures, indicating the decomposition of organic ligands into amorphous carbon.[166]

Quantitative analysis of the XRD patterns shows that the increased temperature led to a decrease in the crystal size from 44.6 nm at 100 °C to 26 nm at 300 °C (**Table 5.1**). This is because the nucleation is favored over crystal growth at high temperatures.[167] Specifically, high temperatures increase the population of supersaturated region and thus leads to increased number of seed nuclei of HKUST-1, resulting in decreased crystal sizes.[168] Moreover, the HKUST-1 particles also exhibit varying hydration degree with synthesis temperature, as indicated by the deviations in I_{200}/I_{220} ratios.[169] The smaller hydration degree indicates that more copper coordination sites are accessible for other molecules,[169] such as CO_2. The least hydration degree was obtained at 300 °C, resulting from the competition between hydration and dehydration at elevated temperatures (see **Table 5.1**).

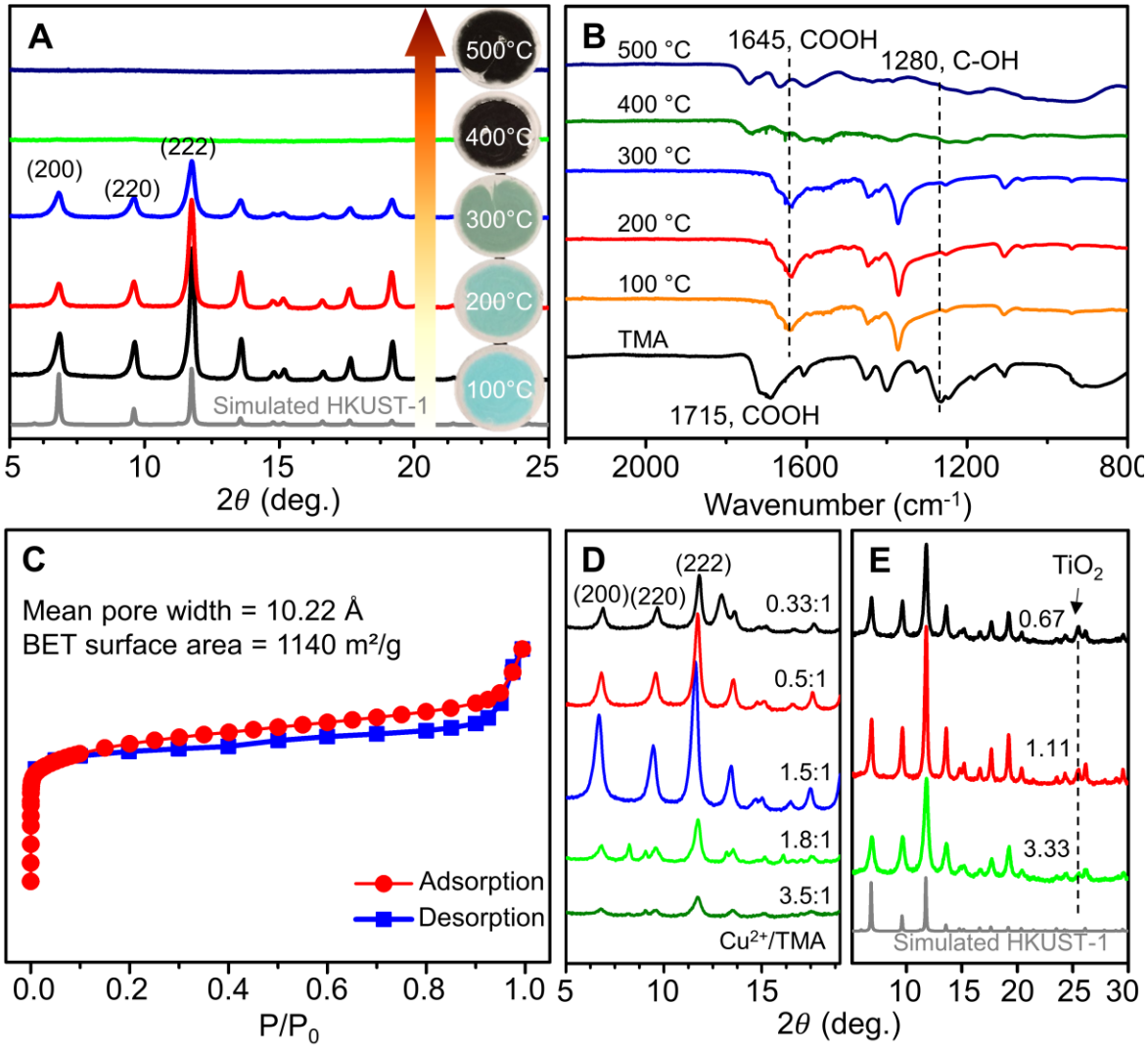

Figure 5.3 (A) XRD patterns and (B) FT-IR spectra of the HKUST-1 samples synthesized at different temperatures; (C) gas sorption isotherms, pore size and surface area of HKUST-1; XRD patterns of (D) HKUST-1 synthesized with various Cu^{2+}/TMA ratios and (E) HKUST-1/TiO2 composites with different HKUST-1/TiO_2 molar ratios. The synthesis temperature was kept at 300 °C in panels C−E.

Table 5.1 Quantified crystal sizes* and peak ratios from XRD measurements

Cu:TMA	T (°C)	Crystal size (nm)	I_{200}/I_{220} (-)
0.33:1	300	39	0.975
0.5:1	300	31.2	1.009
1.5:1	300	26	1.586
1.5:1	200	39	0.898
1.5:1	100	44.6	1.255

* Crystal sizes were calculated by the Scherrer equation.

In addition to the crystallinity, the surface chemistry of the HKUST-1 particles were also analyzed by FT-IR. As seen from **Figure 5.3B**, the spectra of HKUST-1 synthesized at low temperatures (100 - 300 °C) showed a close resemblance to that of free TMA. The major band at 1715 cm^{-1} in the free TMA spectrum is assigned to acidic COOH stretching vibration. After coordination with Cu^{2+}, this peak shifts to 1645 cm^{-1} as a result of deprotonation of COOH group.[170] In addition, the absorption band around 1280 cm^{-1} originates from the C-OH group, which virtually disappeared after the complexation with Cu^{2+}, inferring the sufficient deprotonation of C-OH after crystallization.[171] These adsorption bands were gradually weakened when the temperature reaches 400 °C and higher, which is attributed to the collapse of the framework structure. The FT-IR results are in a good agreement with the XRD data in **Figure 5.3A**.

The above results demonstrate the significant role of temperature in the synthesis of HKUST-1 via the aerosol route. In the subsequent experiments, 300 °C was used since the least hydration degree can be achieved at this temperature. To further analyze the surface area and porous structure, the representative 300 °C sample was analyzed by gas sorption. **Figure 5.3C** exhibits typical Type I adsorption/desorption hysteresis, indicating the microporous nature of HKUST-1. The mean pore width of the sample is 10.22 Å and the BET surface area is as high as 1140 ± 3.4 m^2/g, comparable with those prepared by wet-chemistry methods.[157, 172] By adding TiO_2 into HKUST-1, the pore width was kept at the same and the surface area was largely maintained (i.e., 773 ± 2.5 m^2/g for 1.11 HKUST-1/TiO_2). The surface area of HKUST-1 component in 1.11 HKUST-1/TiO_2 was calculated to be 865 m^2/g by neglecting the contributions from TiO_2 given its much smaller surface area. The decrease in the surface area of HKUST-1 component might be attributed to the pore blocking caused by its internal interaction with TiO_2.

In addition, the effect of Cu^{2+}/TMA ratio on the crystallinity of HKUST-1 particles was also explored. As shown in **Figure 5.3D**, when the ratio was increased from 0.33:1 to 1.5:1, the crystallinity of HKUST-1 was enhanced while the crystal size decreased from 39 nm to 26 nm (**Table 5.1**). The decreased crystal size is related to the promoted deprotonation of TMA driven by the coordination with Cu^{2+}. With a higher Cu^{2+}/TMA ratio, more deprotonated TMA is available, resulting in accelerated nucleation and crystallization rates, thereby decreasing the crystal size.[171] The enhanced deprotonation of TMA also decreased the hydration degree (see **Table 5.1** for details), due to decreased availability of residual coordination sites of Cu^{2+} for water molecules.[169]

When the Cu^{2+}/TMA ratio was further increased, the crystallinity deteriorated as a result of the insufficient amount of TMA. In addition to pristine HKUST-1, the XRD patterns of several HKUST-1/TiO_2 composites were also taken as shown in **Figure 5.3E**, where all the diffraction peaks can be indexed to HKUST-1 and TiO_2, indicating that the crystallinity of HKUST-1 is not affected by the incorporation of TiO_2 nanoparticles. This is reasonable, because the TiO_2 crystals are very stable in the reaction system and have no participation in nor interference to the HKUST-1 synthesis process. This explanation also applies to the minimal effect of TiO_2 on the hydration degree. Moreover, with decreased molar ratio of HKUST-1 to TiO_2, the XRD data (**Figure 5.3E**) shows increased intensity ratio of the peak at 25.3 ° (TiO_2 (101) plane) to that at 11.7 ° (HKUST-1 (222) plane), indicating increased amount of TiO_2 in the HKUST-1 matrix.

Finally, to further confirm the quality of HKUST-1 synthesized directly by the aerosol route, FT-IR was used to compare its surface chemistry to that of the sample subjected to two sequential post-treatments (i.e., washing and drying). These post-treatment steps are commonly used in wet-chemistry methods to remove residuals (also known as MOFs activation).[173] The results show that, the as-prepared HKUST-1 via the aerosol route exhibits almost identical FT-IR spectrum as that of the post-treated sample, indicating the aerosol process may be used to directly synthesize highly-quality HKUST-1 in a rapid and continuous manner without any post-treatments.

Possible HKUST-1 Formation Mechanism in Microdroplets. It is worth mentioning that the HKUST-1 single crystals are generally octahedral when synthesized by wet-chemistry methods.[155, 157, 166] The unique spherical HKUST-1 particles synthesized in this work is attributed to the typical

particle formation mechanism in the aerosol process, i.e., one droplet to one particle (ODOP) conversion.[158] Specifically, the microdroplet serves as a microreactor, where solvent evaporation, nucleation, particle growth, and crystallization occur, meanwhile assembling individual HKUST-1 primary crystals to form a spherical particle (**Figure 5.1B**). At 300 °C with 4.5 L/min carrier gas flow, the whole process completes within 4 s, which is much faster than wet-chemistry methods where longer reaction times (e.g., hours to days) are required.[4] The rapid formation of HKUST-1 in the aerosol route is driven by fast solvent evaporation and heat transfer rates within the microdroplets, which cause the decrease in droplet size, the increase of the supersaturation ratio (S) of precursor, and finally the promotion of nucleation and crystal growth.

Theoretically, the change in droplet radius (R_d) with time (t) due to the solvent evaporation (i.e., mass transfer) within a microdroplet in the continuum regime is governed by the following equation based on the mass conservation law:[174-175]

$$\frac{dR_d}{dt} = \frac{D_v \cdot m}{R_d \cdot \rho}(n_\infty - n_s) \tag{5.1}$$

where D_v is the diffusion coefficient of DMF vapor in air at atmospheric pressure ($D_v \propto T^{1.75}$),[176] m is the mass of DMF molecule, ρ is the density of DMF, and n_s and n_∞ are the number densities of DMF molecules at the droplet surface and infinite region, respectively.

Taking a DMF droplet with an initial radius (R_{d0}) of 1 μm as an example, as shown in **Figure 5.4A**, the droplet radius generally decreases with time due to evaporation. Faster droplet shrinkage is observed at higher furnace temperatures since higher evaporation rates are expected based on **Eq. 5.1**. For instance, when heating at 300 °C, it takes merely 0.03 ms to reduce the

radius to its half (i.e., 0.5 μm); while at 100 °C, only 3.4% decrease in radius (i.e., 0.966 μm) is observed over the same time period. In addition to the temperature, the droplet size also plays an important role. As from **Figure 5.4B**, microdroplets ($R_d \leq 5\ \mu m$) have much shorter evaporation times (typically within ms) as compared to the larger. The fast decrease in droplet size leads to an increased precursor concentration in the droplet and subsequently an enhancement in its supersaturation ratio. For instance, for $R_{d0} = 1\ \mu m$ at 300 °C, the supersaturation ratio of the precursor at 0.038 ms is 156 times that of its initial state at 25 °C. The drastically enhanced supersaturation ratio subsequently promotes nucleation and crystal growth, which aligns well with the XRD data (**Figure 5.3A**), which shows that smaller crystal sizes were obtained at higher temperatures due to increased number of seed nuclei.[168]

In addition to the size change, the temperature variation within the microdroplets due to evaporation was also quantified to better understand the heat transfer in the microscale:[175]

$$\frac{dT_d}{dt} = \frac{3}{c_p R_d}\left[H_{vap}\frac{dR_d}{dt} + \frac{k_a}{\rho R_d}(T_f - T_d)\right] \tag{5.2}$$

where c_p is the specific heat capacity of DMF, H_{vap} is the specific latent heat of vaporization of DMF, k_a is the heat conductivity of air, and T_f is the furnace temperature. The time to reach the thermal equilibrium within the microdroplets depends on the furnace temperature (**Figure 5.4C**) and droplet size (**Figure 5.4D**). For the microdroplets ($R_d \leq 5\ \mu m$) being considered in this work, T_d can reach the thermal equilibrium within extremely short time (i.e., milliseconds). Faster thermal equilibrium can be achieved in smaller droplets and at higher furnace temperatures. The fast heat transfer rate is desirable for the homogeneous synthesis of MOFs

crystals, but can hardly be achieved in the bulk solutions. It should be noted that there are certain discrepancies between equilibrium droplet temperature and the furnace temperature, which are due to the evaporative cooling effect of the microdroplets.[177]

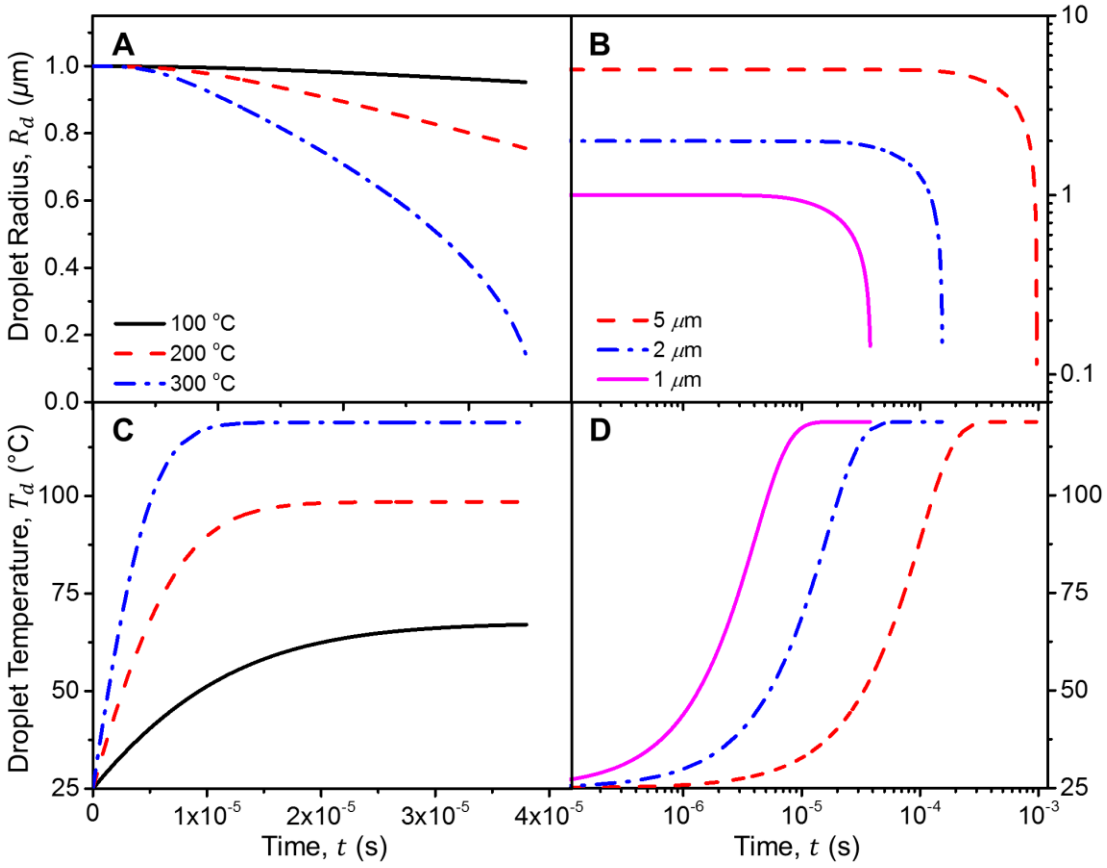

Figure 5.4 Changes of droplet radius: (A) and (B), and droplet temperature: (C) and (D). Conditions for (A) and (C): R_{d0} = 1 μm, T_f = 100, 200, and 300 °C; for (B) and (D): T_f = 300 °C, R_{d0} = 1, 2 and 5 μm. All calculations were performed in the continuum regime ($Kn \ll 1$). The initial droplet temperature (T_{d0}) was fixed at 25 °C, and the temperature is assumed to be uniform within the microdroplets.

Similar particle formation pathways are expected for HKUST-1/TiO_2 nanocomposites, where the uniform distribution of TiO_2 nanocolloids inside the HKUST-1 matrix was achieved via evaporation-induced self-assembly.[158] These TiO_2 nanocolloids did not interfere the crystallinity nor the surface chemistry of HKUST-1 (see **Figures 5.2B and 5.2D**).

Performance Evaluation for CO_2 Photoreduction. The as-synthesized HKUST-1-based photocatalysts were then subjected to CO_2 photoreduction analysis. Prior to the analysis, a series of control experiments were performed to address concerns about HKUST-1 regarding photostability, possibility of carbon contamination, photodegradation caused by TiO_2 and its specific role in CO_2 photoreduction. The as-prepared HKUST-1 was found to be stable in terms of both surface chemistry and crystallinity even under intense light illumination for at least 7 hours. In addition, the HKUST-1 synthesized at 300 °C does not contain nor introduce any carbon contamination during illumination, as shown in **Figure 5.5A** where only trace amount of background air was observed. Similar results were obtained with the 1.11 HKUST-1/TiO_2 composite (**Figure 5.5B**), indicating no observable photodegradation of HKUST-1 in the presence of TiO_2. Pristine HKUST-1 is also not an active photocatalyst for CO_2 photoreduction as no discernible product peaks (e.g., CO, H_2, or CH_4) were identified when pristine HKUST-1 was illuminated under CO_2 atmosphere with water vapor (**Figure 5.5C**), which might be attributed to that the unique conjugated structure of HKUST-1 is not favorable for charge separation.[155] When 1.11 HKUST-1/TiO_2 composite was used as the catalyst, an appreciable CO peak was observed in the GC chromatogram (**Figure 5.5D**).

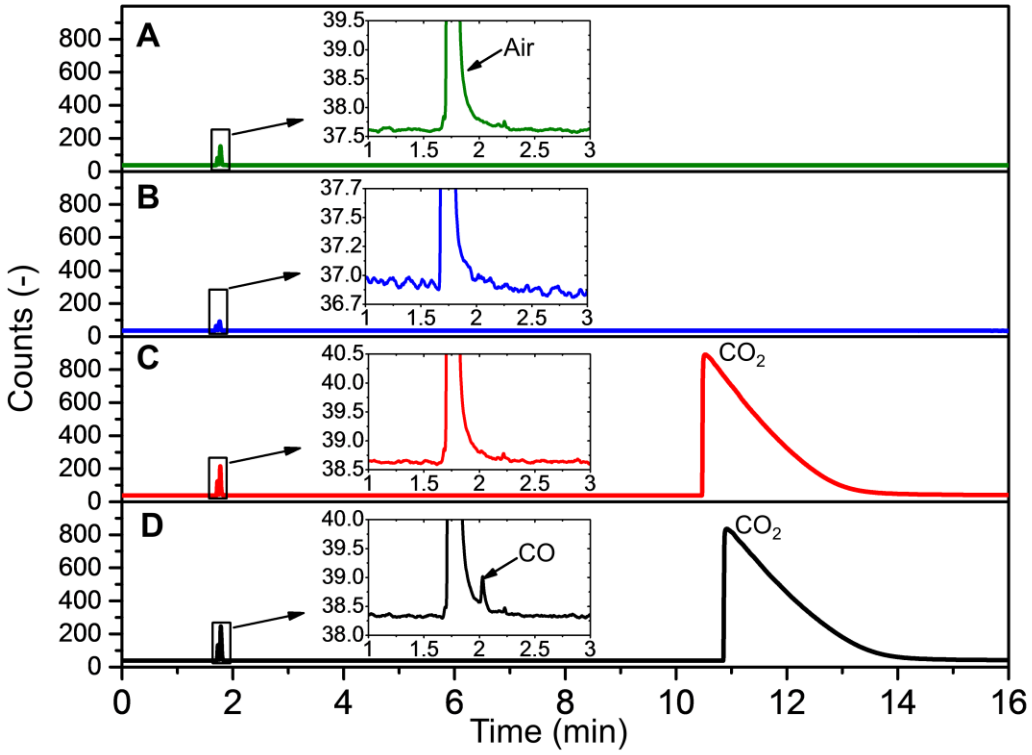

Figure 5.5 GC chromatograms obtained in a typical cycle under different experimental conditions: (A) and (B) were obtained with pure HKUST-1 and 1.11 HKUST-1/TiO_2 composite, respectively, under illumination at helium atmosphere with moisture; (C) and (D) were obtained with pure HKUST-1 and 1.11 HKUST-1/TiO_2 composite, respectively, under illumination at CO_2 atmosphere with moisture. Both particles were synthesized at 300 °C.

Detailed CO_2 photoreduction analysis of TiO_2 and HKUST-1/TiO_2 composites was conducted and the results are shown in **Figure 5.6**, where the pure TiO_2 can only generate a peak CO yield of 11.48 μmol/(g-TiO_2·h) after being irradiated for 2.53 h. With the incorporation of HKUST-1, both the photoreaction rate and the CO yield were promoted. This promotion is

amplified with increased amount of HKUST-1 in the composite. Specifically, with the ratio of HKUST-1/TiO_2 increasing from 0 to 3.33, the peak time decreased from 2.53 h to 0.78 h and the CO yield increased from 11.48 to 256.35 μmol/(g-TiO_2·h), demonstrating more than 20-fold enhancement in CO_2 photoreduction efficiency. The enhancement is superior compared with the composite of TiO_2 and inorganic porous media (e.g., silica), where the photocatalytic efficiency was only increased by 1.14[178] or 2.80[179] times. The improved photoreduction performance of the HKUST-1/TiO_2 nanocomposites could be attributed to the enhanced reactants adsorption on the catalyst, which was verified by the subsequent *in-situ* DRIFTS analysis.

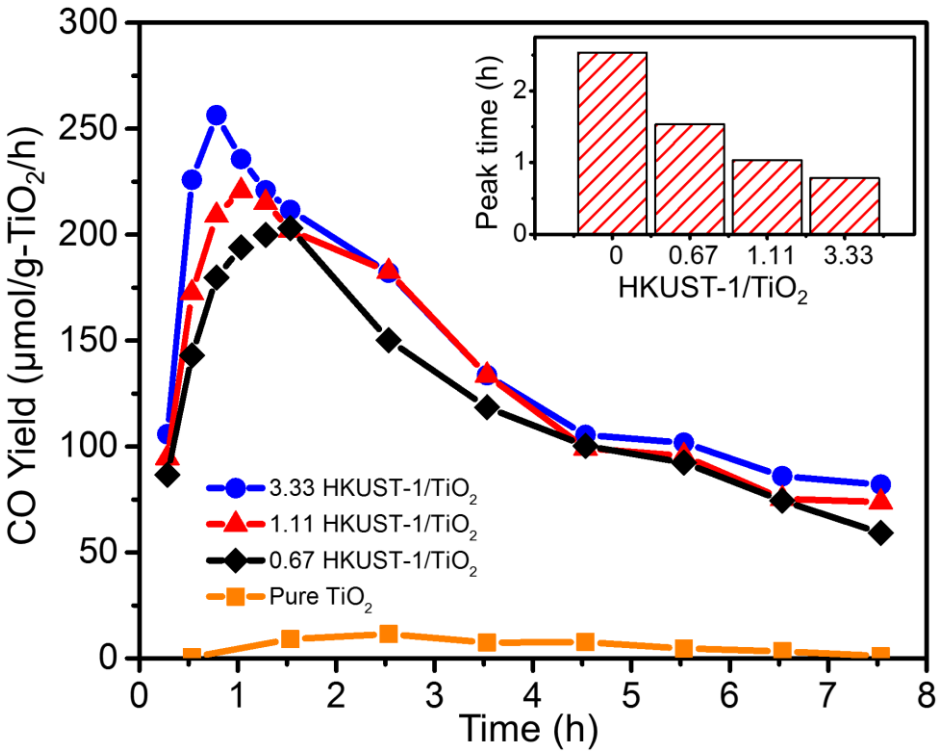

Figure 5.6 CO_2 photoreduction analysis of TiO_2 and HKUST-1/TiO_2 composites.

CO_2 and H_2O Adsorption Analysis. The adsorption abilities of CO_2 and H_2O on HKUST-1 are 8.8 and 13.1 times higher than those on TiO_2, respectively, as shown by the DRIFTS results in **Figures 5.7A** and **D**. The adsorption kinetics fit well with Avrami's kinetic model,[180] a powerful tool to simulate complex gas adsorption on porous materials:

$$C_t = C_e[1 - \exp(-(kt)^n)] \tag{5.3}$$

where, C_t and C_e are the normalized concentration of adsorbed molecules at a given time (t) and at equilibrium, respectively; k is the kinetic constant (s^{-1}); n is the fractional order. As shown in **Figures 5.7A** and **D**, all the adsorption results agree well with the model with a minimal R^2 value of 0.9882. The excellent fit of the experimental data with the Avrami's kinetic model indicates the existence of multiple adsorption pathways,[180] which is confirmed by the multiple adsorption peaks in the DRIFTS spectra (**Figures 5.7B, C, E and F**).

For example, gaseous CO_2 can be adsorbed on the catalyst surface via the interactions with the metal sites and/or functional groups. In **Figures 5.7B and C**, two major CO_2 absorption peaks were observed at 2360 cm^{-1} and ~2340 cm^{-1}, which can be assigned to the antisymmetric stretching mode of CO_2 gases adsorbed on hydroxyl groups forming weakly bonded OH···O=C=O adducts[181] and those adsorbed on the metal sites forming Ti^{2+}(/Cu^{2+})···O=C=O adducts,[127] respectively. Moreover, the 2340 cm^{-1} peak is slightly red shifted on HKUST-1 as compared to that at 2342 cm^{-1} on TiO_2, suggesting that Cu ions have stronger interaction with CO_2 as compared to Ti ions.[182] The stable CO_2 adsorption on HKUST-1 is helpful for the enhancement in CO_2 photoreduction performance.

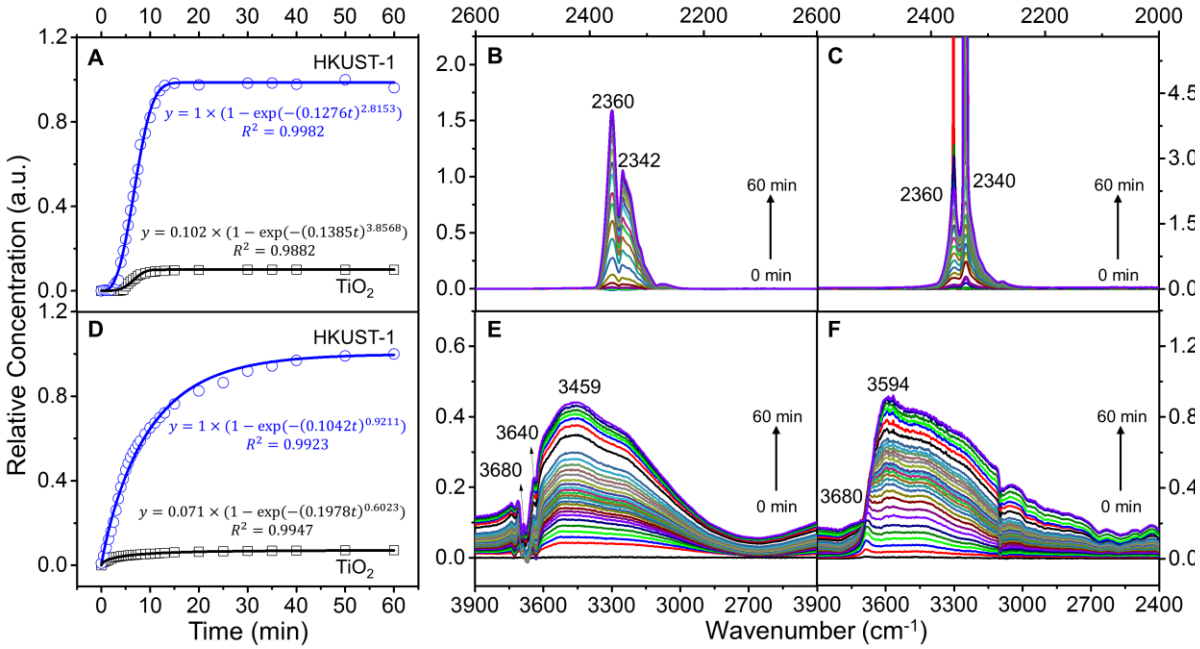

Figure 5.7 CO_2 and H_2O adsorption spectra and kinetics. (A) and (D) are adsorption kinetics of CO_2 and H_2O, respectively; (B) and (C) are CO_2 adsorption on TiO_2 and HKUST-1, respectively; (E) and (F) are water adsorption on TiO_2 and HKUST-1, respectively.

Likewise, H_2O also has multiple adsorption pathways on the catalyst surfaces either dissociatively (2500 – 3900 cm^{-1})[183] or molecularly (1620 – 1665 cm^{-1}).[184] Due to surface defects, dissociation of water is kinetically favored on the catalyst surface, which results in –OH stretching mode.[185] This is clearly observed in the IR spectra of H_2O adsorption on both TiO_2 and HKUST-1 surfaces. For instance, **Figure 5.7E** shows a broad band centered 3460 cm^{-1} and sharp bands at 3640 cm^{-1} and 3680 cm^{-1}, assigned to bridged[186] and linear OH groups,[187] respectively. The

intensities of all these bands increase with the increasing adsorption time. While for HKUST-1 (**Figure 5.7F**), the 3680 cm^{-1} peak is observed initially and goes off with prolonged time. Meanwhile, a broad band appears and grows at 3594 cm^{-1}, suggesting the formation of multilayer adsorption of water via H-bonding over the metal sites.[188] This significantly contributes to the high adsorption capacity of HKUST-1 and was not observed when TiO_2 was used as the adsorbent. Molecular water adsorption hinders CO_2 diffusion and thus is considered unfavorable for CO_2 photoreduction. This type of adsorption was only observed on pristine TiO_2 surface, but not on HKUST-1 surface. Therefore, HKUST-1 serves as the predominant adsorbent in the composites, providing more reactants (H_2O and CO_2) and resulting in the promoted photoreduction performance.

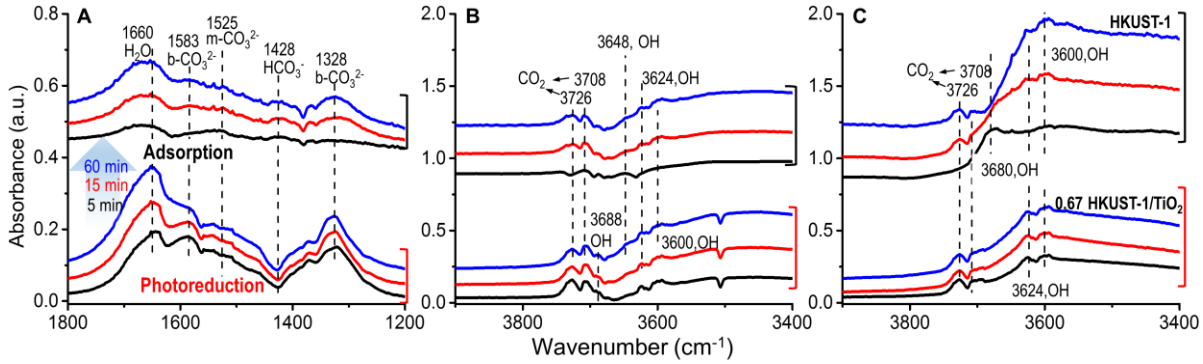

Figure 5.8 Intermediates generated during the adsorption and photoreduction processes on the surface of: (A) and (B) TiO_2; (C) HKUST-1 and 0.67 HKUST-1/TiO_2 composite.

Intermediates Analysis. *In-situ* DRIFTS was also used to analyze intermediates during the adsorption and photoreduction processes. As shown in **Figure 5.8A**, exposure of TiO_2 to the CO_2/H_2O vapor mixture without light illumination led to the formation of several intermediate

species, including monodentate carbonate (m-CO_3^{2-}, 1525 cm^{-1}),[189] bidentate carbonate (b-CO_3^{2-}, symmetric stretching at 1328 cm^{-1} and asymmetric stretching at 1583 cm^{-1}),[190-192] and bicarbonate (HCO_3^-, 1428 cm^{-1}).[190] The peak intensity of molecular H_2O (1660 cm^{-1}) and b-CO_3^{2-} increased with prolonged exposure time. HCO_3^- is formed by the interaction of coordinated CO_2 with surface OH groups,[193] and the peak intensity was constant with prolonged adsorption process, suggesting a limited amount of OH groups on the catalyst surface. Upon illumination, the peak intensity of b-CO_3^- (asymmetric stretching at 1583 cm^{-1}) decreased, and the peaks of HCO_3^- and m-CO_3^{2-} disappeared, mainly due to their desorption and transformation into products (e.g., CO).[194] It's worth noting that, the peak intensity of b-CO_3^- at 1328 cm^{-1} were relatively stable during the illumination process, which might be associated with the fact that the symmetric stretching mode is more stable than the asymmetric stretching mode.[195] On the other hand, the IR spectrum (1200 – 1800 cm^{-1}) of HKUST-1 during the adsorption process and 0.67 HKUST-1/TiO_2 during the illumination process were very noisy, indicating no such intermediates were present on the HKUST-1 surface.

In addition to the (bi-)carbonate species, a number of hydroxyl species (3600,[196] 3624,[186] 3648, 3688 cm^{-1}) have also been identified on the TiO_2 surface upon CO_2/H_2O adsorption. And the peak intensities of all these hydroxyl species only slightly increased with prolonged adsorption process, confirming the limited amount of OH groups on TiO_2 surface. Few changes were observed in the peak intensities of these hydroxyl groups on TiO_2 surface upon illumination (**Figure 5.8B**). Similarly, several OH species (3600 and 3624 cm^{-1}) were also observed on HKUST-1 or the

HKUST-1/TiO_2 samples (**Figure 5.8C**) with comparable intensities with that on TiO_2 samples. Besides, similar to the adsorption of sole water vapor on HKUST-1, the OH at 3680 cm^{-1} appeared with a much stronger intensity after 5-min exposure of HKUST-1 to CO_2/H_2O vapor mixture while disappeared after prolonged adsorption time (15 and 60 min). The absorption bands at 3708 and 3726 cm^{-1} were observed on all catalysts, and they are attributed to the fermi resonance of linearly adsorbed CO_2.[197] The intensities of both peaks increased with prolonged adsorption time, indicating the increased amount of adsorbed CO_2. During the illumination process, these two bands decreased with elapsed illumination time which can be attributed to the consumption of CO_2 during the photoreduction process.

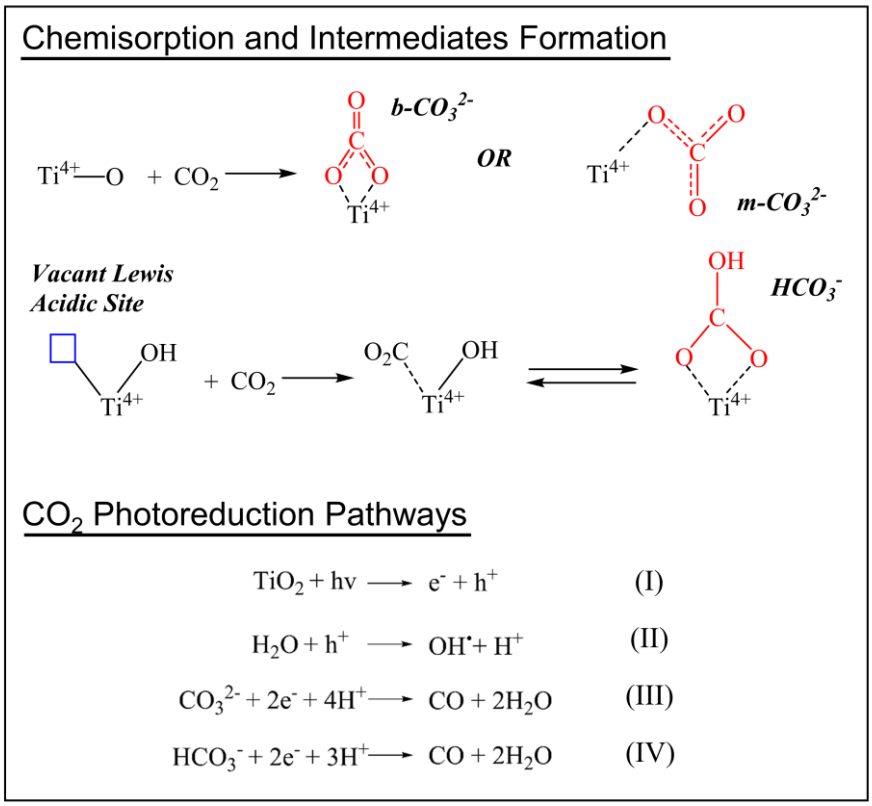

Figure 5.9 Possible CO_2 chemisorption and photoreduction pathways.

Possible CO_2 Photoreduction Mechanism. Based on the GC and DRIFTS results, a possible pathway of CO_2 photoreduction by HKUST-1/TiO_2 composites was proposed and illustrated in **Figure 5.9**. In this composite system, HKUST-1 is mainly acting as an efficient adsorbent to capture the H_2O and CO_2 molecules, which subsequently diffuse to the TiO_2 surface due to the high transport diffusion coefficient of gas molecules in HKUST-1.[198] Then, several intermediates were generated during the chemisorption of CO_2 on the TiO_2 surface. The species of the intermediates depend on the sites that interacted with CO_2. In particular, the interaction of CO_2 and Ti^{4+} produced b-CO_3^- or m-CO_3^{2-}. While, HCO_3^- can be formed in the simultaneous presence of OH group and vacant Lewis acidic site.[193] Upon illumination, TiO_2, serving as the catalyst, generates electrons and holes. The adsorbed water then reacts with the holes to produce protons and $OH^{\cdot}$, and this process was confirmed by the detection of $OH^{\cdot}$.[199] Subsequently, the carbonate and bicarbonate intermediates reacted with the generated electrons and protons, and were consumed as indicated by the decreased IR peak to form the final products.

5.4 Conclusions

In summary, HKUST-1 and HKUST-1/TiO_2 composites were successfully synthesized in microdroplets via a rapid, continuous, and scalable aerosol route. The rapid formation of the MOFs crystals in the microdroplets is attributed to the rapid evaporation and heat transfer rates, the subsequent promotion of supersaturation ratio of precursors, and finally the fast nucleation and crystal growth rates. The aerosol route shows great promise in addressing the fundamental issues of heat and mass transfer at the microscale, such as non-uniform mixing, slow heat transfer,

sluggish nucleation, and crystal growth rates, which are normally present in bulk liquid methods. The HKUST-1 and its TiO_2 nanocomposites demonstrated good crystallinity, high photostability, and enhanced CO_2 photoreduction performance. Detailed DRIFTS analysis suggests that the enhancement was due to the promoted reactant adsorption by HKUST-1. It should be noted that the current work is the first demonstration of the feasibility of aerosol processing of MOFs-based materials in a rapid manner. Further investigations of the quantitative formation mechanisms of MOFs in the aerosol routes, the expansion of synthesizing different kinds of MOFs, and the incorporation of various guest components will be carried out in the near future.

Chapter 6. MOF-based Ternary Nanocomposites for Better CO_2 Photoreduction: Roles of Heterojunctions and Coordinatively Unsaturated Metal Sites

Journal of Materials Chemistry A, 6(3): 932-940 (2018)
DOI: 10.1039/C7TA09192C

Abstract

Semiconductors are the most widely used catalysts for CO_2 photoreduction. However, their efficiencies are limited by low charge carrier density and poor CO_2 activation. Towards solving these issues, a metal–organic framework (MOF)-based ternary nanocomposite was synthesized through self-assembly of TiO_2/Cu_2O heterojunctions *via* a microdroplet-based approach followed by *in situ* growth of $Cu_3(BTC)_2$ (BTC = 1,3,5-benzenetricarboxylate). With increased charge carrier density and efficient CO_2 activation, the hybrid ternary nanocomposite exhibits a high CO_2 conversion efficiency and preferential formation of CH_4. Systematic measurements by using gas chromatography, photoluminescence spectroscopy, X-ray photoelectron spectroscopy, and time-resolved *in situ* diffuse reflectance infrared Fourier transform spectroscopy reveal that the semiconductor heterojunction and the coordinatively unsaturated copper sites within the hybrid nanostructure are attributable to the performance enhancements.

6.1 Introduction

Carbon dioxide (CO_2) photoreduction is a promising engineering approach to reduce atmospheric CO_2 levels and simultaneously convert CO_2 into hydrocarbon fuels.[139-145, 200-201] Among the numerous catalysts for CO_2 photoreduction, semiconductors have been studied intensively because of their low cost, easy availability, nontoxicity, and exceptional chemical stability.[140, 202] However, the semiconductor-based CO_2 photoreduction still suffers from low efficiency and poor selectivity, mainly due to low charge carrier density and weak ability to activate the adsorbed CO_2 molecules.

The low charge carrier density is mainly caused by inherent fast electron-hole recombination. This issue may be remediated by surface metalation,[203] where the metals serve as electron sinks to separate electron-hole pairs. Creating heterojunctions of semiconductors with proper band alignments,[204] such as TiO_2/Cu_2O,[202] Fe_2O_3/Cu_2O,[205] C_3N_4/Bi_2WO_6[206] and ZnO/CuO,[207] is another effective approach to boost the transfer of photoexcited charge carriers between the metal oxides in the heterojunction.[202, 204] An added benefit of this type of heterojunctions is that the enhanced solar energy utilization can be achieved due to the coupled narrow bandgap semiconductors, such as Cu_2O.[208]

Extensive efforts have been directed to creating semiconductor heterojunctions, many of which, however, require complicated processes.[202, 209] In addition, many heterojunctions are fabricated in the form of “core-shell” structure, that is, one semiconductor layer is uniformly coated on the other.[202] This significantly limits the use of

heterojunctions, since in many cases, the surfaces of both semiconductors are required to participate in the redox reactions.[204] Moreover, despite the promise of enhanced charge transfer, the semiconductor heterojunctions still suffer from poor CO_2 adsorption and activation due to the low affinity of CO_2 molecules for the semiconductor surface.[146] Rational design of photocatalysts for efficient CO_2 photoreduction is thus highly desirable.

On the other hand, metal-organic frameworks (MOFs), as an emerging class of highly porous materials, have received increasing attention in CO_2 photoreduction,[33, 40, 64, 210-211] mainly due to their high surface area, tunable pore size, and rich surface functionality. Given the exceptional gas adsorption ability of MOFs, many current studies are focusing on designing MOFs/semiconductor hybrids to enhance the gas uptake during CO_2 photoreduction.[210, 212] For example, the hybrid nanorods of Zn_2GeO_4/zeolitic imidazolate framework (ZIF)-8 exhibited 1.62 times higher CO_2 photoreduction efficiency than that of bare Zn_2GeO_4,[36] attributed to the enhancement in the CO_2 adsorption capacity after the incorporation of ZIF-8. Similarly, C_3N_4/ZIF-8 composite nanotubes were reported to have a better CO_2 photoreduction performance than the pristine C_3N_4, where the enhanced CO_2 adsorption capacity due to ZIF-8 was the main reason.[212] Besides ZIF-8, other MOFs were also used to increase the CO_2 adsorption ability of the catalysts.[213]

It should be noted that, adsorption is the first step in CO_2 photoreduction. Whether and how the adsorbed CO_2 molecules are activated and then reduced within the MOF structure are also of great importance to study. In particular, some MOFs (e.g., $Cu_3(BTC)_2$,

BTC = 1,3,5-benzenetricarboxylate) have coordinatively unsaturated metal sites, which could act as electron donors to activate the adsorbed gas molecules.[214] However, little attention has been directed into this area.

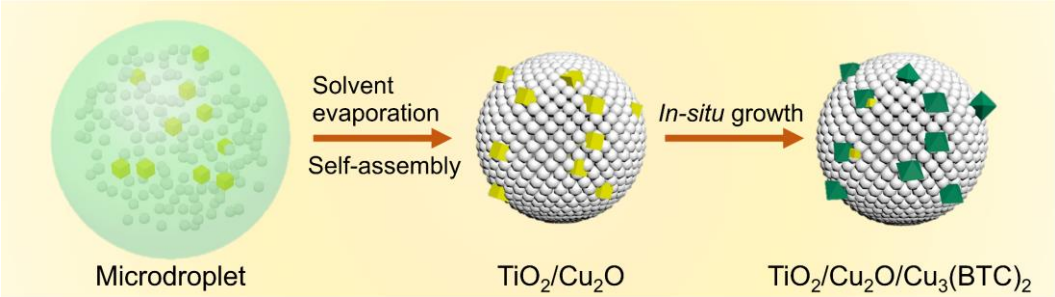

Scheme 6.1 Schematic illustration of the experimental procedure to synthesize $TiO_2/Cu_2O/Cu_3(BTC)_2$ ternary nanocomposites (white spheres: TiO_2; yellow cubes: Cu_2O; green octahedrons: $Cu_3(BTC)_2$).

Towards addressing the aforementioned long-standing issues in CO_2 photoreduction (i.e., low charge carrier density and inefficient CO_2 activation), we herein report a rational development of MOF-based ternary nanocomposites composed of TiO_2/Cu_2O heterojunctions and $Cu_3(BTC)_2$, where the roles of the heterojunctions and MOF in charge transfer and CO_2 activation are systematically explored. Specifically, the nanocomposites were synthesized via rapid self-assembly of TiO_2/Cu_2O nanoparticles within microdroplets,[215-216] followed by *in-situ* growth of $Cu_3(BTC)_2$ on the TiO_2/Cu_2O surface, where part of Cu_2O serves as the sacrificial copper source. The overall synthetic procedure of the $TiO_2/Cu_2O/Cu_3(BTC)_2$ ternary nanocomposites is illustrated in **Scheme 6.1** and

detailed in **Experimental** section. The unique ternary $TiO_2/Cu_2O/Cu_3(BTC)_2$ composite possesses heterojunctions and abundant coordinatively unsaturated copper sites, which results in not only increased charge carrier density but also efficient activation of CO_2 molecules, therefore leading to high CO_2 conversion efficiency and preferential formation of CH_4. With systematic measurements and analyses, a plausible pathway of CO_2 activation and subsequent reduction in this ternary system was proposed. The outcome of this work provides new insights in rational design of MOFs-based hybrid nanomaterials for efficient CO_2 photoreduction.

6.2 Materials and Methods

Synthetic Procedures. All chemicals were purchased from commercial suppliers (Sigma-Aldrich, VWR, Acros Organics) and used as received without further purification. **(1) Synthesis of Cu_2O nanocubes.** The Cu_2O nanocubes were synthesized as previously published:[217] 1 mL $CuSO_4$ solution (1.2 mol/L) was firstly added into 400 mL deionized (DI) water. Then, NaOH (1 mL, 4.8 mol/L) and ascorbic acid (1 mL, 1.2 mol/L) were injected into the solution after 5 min and 10 min, respectively. The solution was then aged for 30 min. All the above processes were done with vigorous stirring at room temperature. After that, the Cu_2O nanocubes were collected and washed four times with DI water via centrifugation and redispersion to ensure the complete removal of residues. **(2) Aerosol-assisted synthesis of TiO_2/Cu_2O composites.** TiO_2/Cu_2O composites were assembled via the aerosol process as detailed in our previous studies.[215] Briefly, aqueous solution

containing TiO_2 nanoparticles (0.05 mol/L, Degussa (Evonik) P25) and Cu_2O nanocubes (0.0025 mol/L) was used as the precursor, from which microdroplets were generated using a Collison nebulizer. The droplets were then carried through a furnace (400 °C) carried by air (10 L/min). During the flying process, the droplets underwent solvent evaporation and self-assembly of Cu_2O and TiO_2 nanoparticles. The TiO_2/Cu_2O composites were collected in the downstream of the furnace by a micro-filter. **(3) *In situ* growth of MOF.** The as-prepared TiO_2/Cu_2O composite was then put into the BTC solution (0.04 mol/L, V_{EtOH}/V_{H2O} = 9/1), which was then subjected to vortex mixing for 0.5 min to partially convert Cu_2O to $Cu_3(BTC)_2$ and obtain $TiO_2/Cu_2O/Cu_3(BTC)_2$ composites. After that, the final product was immediately collected and washed with ethanol four times to remove the residuals via centrifugation/redispersion and then dried in the vacuum at 50 °C.

Materials Characterization. The morphologies and inner structures of the samples were characterized by scanning electron microscope (SEM, Su-70, Hitachi) and transmission electron microscope (TEM, JEM 1230, JEOL), respectively. A PANalytical X'Pert Pro MPD X-ray diffractometer equipped with a Cu-Kα radiation source (λ = 1.5401 Å) was used for the crystallinity determination. The surface functional groups were analyzed by using a Fourier transform infrared (FT-IR) spectrometer (Nicolet iS50, Thermo Scientific). X-ray photoelectron spectroscopy (XPS) measurements were carried out by using the Thermofisher ESCALab 250. A UV-Visible spectrophotometer (Evolution 220, ThermoFisher) was used to obtain the optical properties of the samples.

CO_2 Photoreduction Analysis. The CO_2 photoreduction was carried out in a continuous-flow mode and the analysis procedures were detailed in our previous studies.[64] In brief, CO_2/H_2O mixture was generated by passing CO_2 gas (purity > 99.99%, Praxair) through a water bubbler. The gas mixture, serving as the reactants, was then introduced into a home-made photoreactor loaded with catalysts. The photoreactor consists of a cylindrical cavity made of stainless steel (60 mm in diameter and 25 mm in depth) and a quartz glass for the light to pass. The light illumination was provided by a Xe lamp (450W, Newport). The reactor was first purged with the gas mixture with a flow rate of 50 mL/min for 30 min. The flow rate of the gas mixture was then reduced to 3 mL/min and the lamp was turned on for the photoreduction process. The effluent gases were analyzed by a gas chromatograph (GC, Agilent 7890B) equipped with a CarboPLOT P7 column and a thermal conductivity detector (TCD). For each sample, the analysis was conducted three times to obtain the average production yield. A liquid filter (6123NS, Newport) was used to minimize the thermal effects. As reported in our previous work where same apparatus was used,[162] the reactor temperature can be controlled within 32 °C with the aid of the filter, limiting the thermal contributions to CO_2 photoreduction. In order to rule out any possibilities of carbon contamination, control experiments were conducted with the same procedures using helium gas (purity > 99.995%, Praxair) instead of CO_2.

Hydroxyl Radicals (·OH) Analysis. The detection of ·OH was conducted using the same procedure as the CO_2 photoreduction but with the mixtures of catalysts (1 mg) and

coumarin (10 mg). During the illumination process, ·OH radicals form through the reaction of holes with water molecules adsorbed on the catalyst surfaces. These radicals then react with coumarin, producing 7-hydroxycoumarin, which has a characteristic florescence peak around 455 nm when excited at 350 nm. After the completion of photocatalysis process, the powder mixtures were dispersed in 4 mL DI water to extract 7-hydroxycoumarin. The powders were then removed by centrifugation. And the suspension was analyzed by a fluorescence spectrofluorometer (QuantaMaster 400, Photon Technology International).

Time-resolved In Situ Diffuse Reflectance Infrared Fourier Transform Spectroscopy (DRIFTS) Analysis. The DRIFTS analysis was conducted in a reaction chamber assembled in a Praying Mantis diffuse reflection accessory of the FT-IR spectrometer (i50, Thermo Scientific). The experimental procedure involves two steps, i.e., purging and CO_2 adsorption. In brief, photocatalysts were firstly loaded in the reaction chamber and then subjected to purging under helium gas flow (30 mL/min) at 150 °C for 30 min in order to further remove any residual hydrocarbons. After that, the heater was turned off and the chamber was cooled down to room temperature. Helium gas flow was stopped and CO_2 gas flow (10%, helium as the balance gas) was introduced into the reaction chamber at a flow rate of 4 mL/min after passing through the water bubbler. The IR spectra were recorded as a function of adsorption time.

6.3 Results and Discussions

Materials Characterization. The representative samples, i.e., as-sprayed TiO_2, TiO_2/Cu_2O, and $TiO_2/Cu_2O/Cu_3(BTC)_2$, were first subjected to detailed characterization. As shown in the digital images (**Figures 6.1A-C**), the color change of the samples is apparent. The white color of TiO_2 (**Figure 6.1A**) turned yellow with the incorporation of Cu_2O (**Figure 6.1B**) due to its broad light absorption between 350 nm and 500 nm. After partial conversion of Cu_2O to $Cu_3(BTC)_2$, the color of the nanocomposite changed to gray (**Figure 6. 1C**). The high-magnification SEM analysis reveals that the as-sprayed TiO_2 and TiO_2/Cu_2O particles have a spherical shape (**Figures 6.1D** and **6.1E**), resulting from the one droplet to one particle conversion principle.[215] The existence of Cu element in the TiO_2/Cu_2O composite was confirmed by energy dispersive X-ray (EDX) analysis (**Figures 6.1G-I**). Cu_2O nanocubes are also found in **Figure 6.1J**, where free surfaces are available for the subsequent growth of $Cu_3(BTC)_2$. After the growth of $Cu_3(BTC)_2$, the spherical shape was largely maintained (**Figure 6.1F**). The octahedral $Cu_3(BTC)_2$ crystals are clearly observed from both SEM (**Figure 6.1F**) and transmission electron microscopy (TEM) images (**Figure 6.1K**). The existence of Cu_2O and $Cu_3(BTC)_2$ in the composite was further identified by X-ray diffraction (XRD) analysis (**Figure 6.1L**). For example, Cu_2O in the TiO_2/Cu_2O composite was confirmed by the peak of (111) plane at 36.5°, the intensity of which decreased after the growth of $Cu_3(BTC)_2$. The presence of $Cu_3(BTC)_2$ in the ternary composite is evidenced by its main XRD peak at $2\theta = \sim 11.6°$, corresponding to its (222)

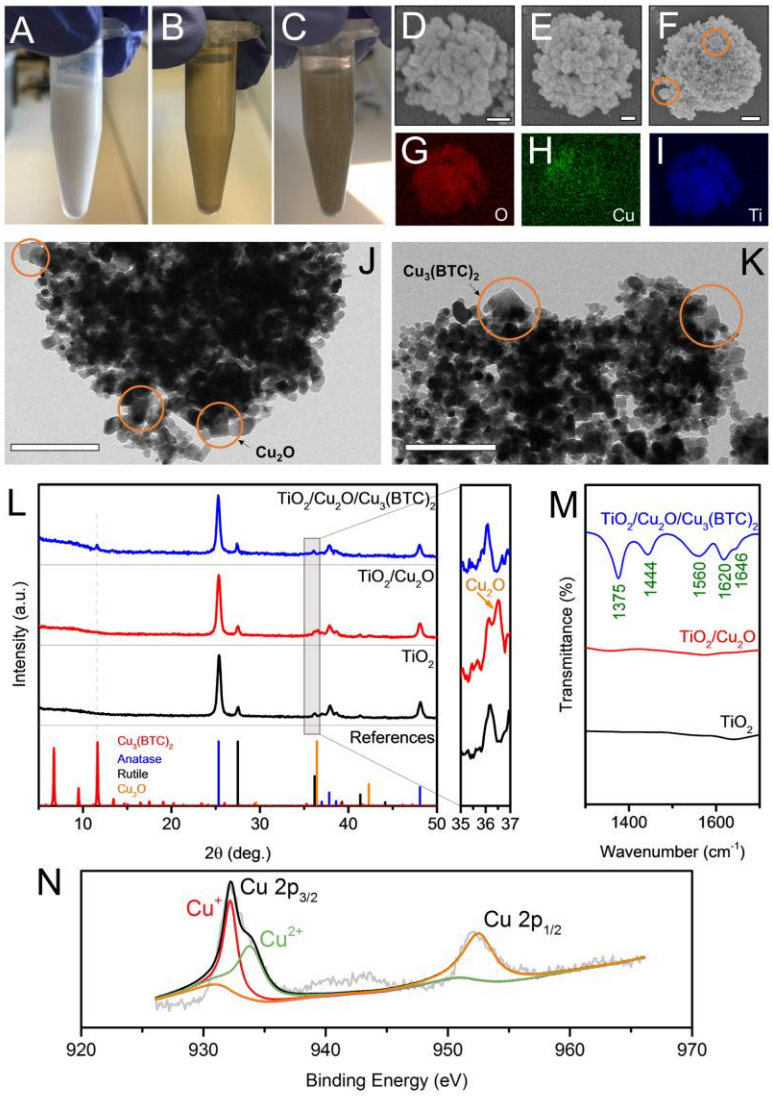

Figure 6.1 Digital images of aqueous suspensions containing (A) as-sprayed TiO_2, (B) TiO_2/Cu_2O, and (C) $TiO_2/Cu_2O/Cu_3(BTC)_2$; SEM images of (D) as-sprayed TiO_2, (E) TiO_2/Cu_2O and (F) $TiO_2/Cu_2O/Cu_3(BTC)_2$ samples; (G), (H) and (I): EDX mapping images of TiO_2/Cu_2O particle; TEM images of (J) TiO_2/Cu_2O and (K) $TiO_2/Cu_2O/Cu_3(BTC)_2$; XRD patterns (L) and FT-IR spectra (M); (N) Cu2p XPS spectra of as-prepared $TiO_2/Cu_2O/Cu_3(BTC)_2$ composite. (Scale bars: D and E: 100 nm; F: 300 nm; J-K: 200 nm)

plane.[64, 218] Besides, the Fourier transform infrared (FT-IR) spectra also confirm the successful growth of $Cu_3(BTC)_2$, where intense peaks were observed at 1375, 1444, 1560, 1620 and 1646 cm^{-1}, assigned to carboxylate groups of $Cu_3(BTC)_2$.[219-220] It should be noted that both XRD peaks of Cu_2O and $Cu_3(BTC)_2$ are relatively weak due to their low molar ratios. These were intentionally set to minimize the influence of adsorption variation, in order to better understand the roles of TiO_2/Cu_2O heterojunction and $Cu_3(BTC)_2$ in the enhancements of charge carrier density and CO_2 molecule activation during CO_2 photoreduction. In addition, the valence states of Cu in the ternary composite analyzed by X-ray photoelectron spectroscopy (XPS) further confirms the coexistence of Cu_2O and $Cu_3(BTC)_2$ in the ternary system. As shown in **Figure 6.1N**, two major peaks were observed at 932.3 eV and 952.5 eV, corresponding to Cu $2p_{3/2}$ and Cu $2p_{1/2}$, respectively. The Cu $2p_{3/2}$ was further deconvoluted into two peaks centered 932.2 eV and 933.8 eV,

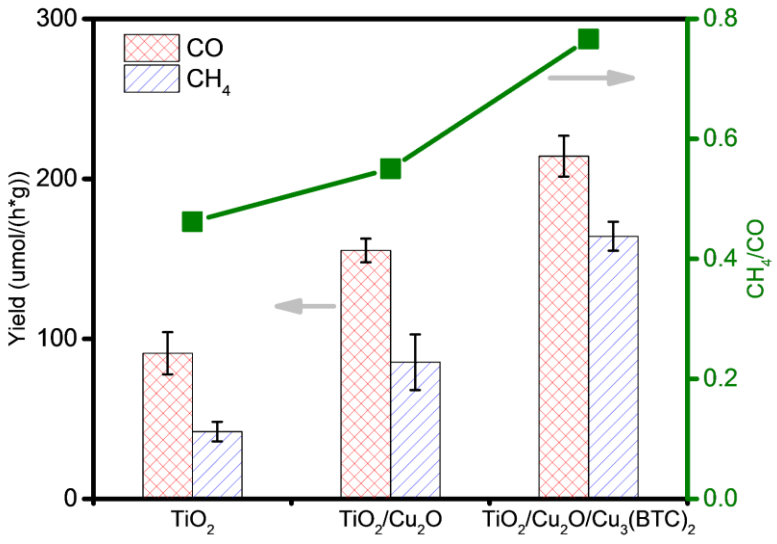

Figure 6.2 Analysis of CO_2 photoreduction product yields.

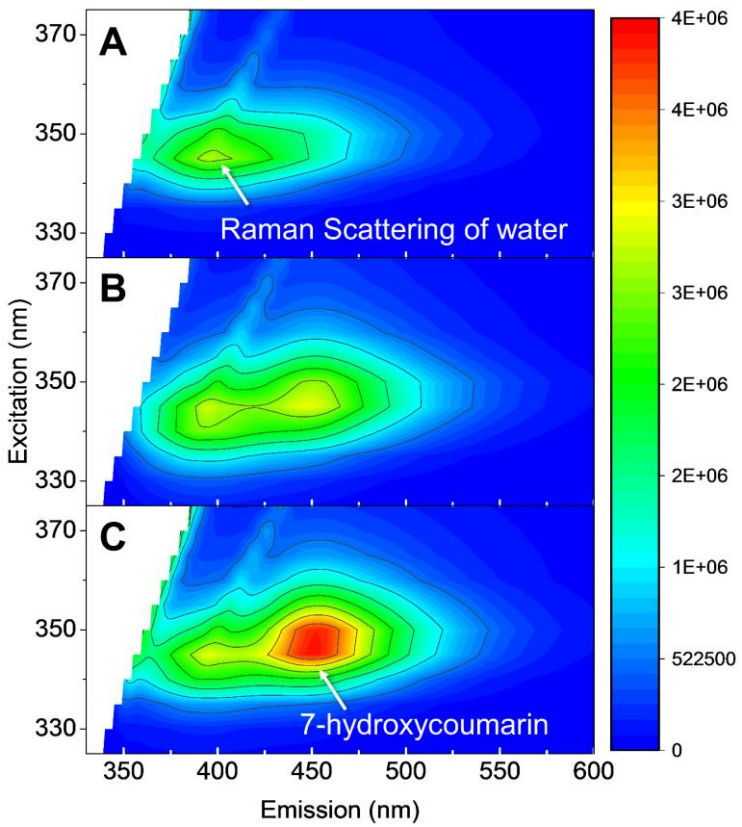

Figure 6.3 Excitation-emission matrices of 7-hydroxycoumarin washed off from catalysts after CO_2 photoreduction in the presence of coumarin: (A) as-sprayed TiO_2, (B) TiO_2/Cu_2O and (C) $TiO_2/Cu_2O/Cu_3(BTC)_2$.

originating from Cu^+ in Cu_2O and Cu^{2+} in $Cu_3(BTC)_2$, respectively.[221-222] Furthermore, based on the precursor components and the XPS data, the molar ratio of TiO_2, Cu_2O and $Cu_3(BTC)_2$ in the ternary composite was determined to be 20: 0.55: 0.45.

CO_2 Photoreduction Analysis. The CO_2 photoreduction was carried out in a continuous-flow mode. The analysis procedures were detailed in our previous studies[64, 162] and are

described briefly in the **Experimental** section. Prior to CO_2 photoreduction analysis, all samples were subjected to control measurements under helium/water atmosphere to rule out the possibilities of carbon contamination. The CO_2 photoreduction analysis results indicate that pure $Cu_3(BTC)_2$ doesn't serve as the photocatalyst for CO_2 reduction due to the unfavorable charge separation,[33, 64] while TiO_2 and the composite reduce CO_2 to carbon monoxide (CO) and methane (CH_4). Specifically, the CO and CH_4 yields of the sprayed TiO_2 were 72 and 33 μmol/(h·g), respectively (**Figure 6.2**). With the incorporation of Cu_2O, the yields increased to 155 and 85 μmol/(h·g), respectively. In the case of the ternary composite, the CO yield was increased more than 2-folds, while the CH_4 yield was almost 4 times higher than those of TiO_2. It's worth noting that, besides the overall production yields, the preferential formation of CH_4 was also enhanced along with the sample development. For example, the CH_4/CO ratio in the case of TiO_2 was only 0.46. With the incorporation of Cu_2O and $Cu_3(BTC)_2$, the CH_4/CO ratio was improved to 0.55 and 0.77, respectively (**Figure 6.2**). Moreover, the Cu valence states are relatively stable during the CO_2 photoreduction process, as evidenced by the similar Cu2p spectra of the ternary composite before and after 7-hour photocatalysis.

There are several possible reasons for the enhanced CO_2 photoreduction with the incorporation of Cu_2O and $Cu_3(BTC)_2$, including higher CO_2 uptake, enhanced charge carrier density, and improved CO_2 activation. In this study, the interference from the changes in the CO_2 uptake capacity may be negligible since the amounts of Cu_2O and

$Cu_3(BTC)_2$ in the nanocomposites were controlled at very low percentages, which ensures minimal improvement in CO_2 uptake. While, the contributions from the increased charge carrier density and facile activation of the adsorbed CO_2 molecules are discussed in detail as follows.

Analysis of Charge Carrier Density. To understand the roles of the Cu_2O and $Cu_3(BTC)_2$ in the increment of charge carrier density, quantitative measurements of charge carrier generation were carried out. In this study, a convenient and reliable photoluminescence (PL) technique using coumarin as a probe molecule to detect and quantify photoinduced holes was used.[164, 223-224] In this method, coumarin reacts with hydroxyl radicals (·OH), produced from the reaction of photoinduced holes with water molecules adsorbed on the photocatalyst surface, to form highly fluorescent 7-hydroxycoumarin (7HC), which has a characteristic PL emission peak at around 455 nm when excited at 350 nm. In the current study, all the three samples have similar water adsorption capacities, thus the amount of the hydroxyl radicals can be used to indicate the density of the holes.

As shown in **Figure 6.3A**, the as-sprayed TiO_2 demonstrates a low charge carrier density as no apparent peak at 455 nm was observed. With the incorporation of Cu_2O, the 7HC peak is prominent (**Figure 6.3B**). The strongest 7HC peak intensity was found in **Figure 6.3C**, where the ternary nanocomposite was used. Based on the calibration results, the OH generated by TiO_2, TiO_2/Cu_2O and $TiO_2/Cu_2O/Cu_3(BTC)_2$ were quantified to be 0.032, 0.067 and 0.105 μmol/(g·h), respectively, which implies that the photo-induced

holes in TiO_2/Cu_2O and $TiO_2/Cu_2O/Cu_3(BTC)_2$ were 2.09 and 3.28 times higher than those in TiO_2.

The above results indicate that the decoration of TiO_2 with Cu_2O and $Cu_3(BTC)_2$ significantly increased the charge carrier density of the catalyst, which might be attributed to several reasons, including the enhanced light absorption and promoted electron/hole separation. The light absorption properties of the three samples were assessed by the UV-Vis absorption spectra as shown in **Figure 6.4**. Specifically, TiO_2 only exhibits light absorption in the UV region (< 400 nm). With the incorporation of Cu_2O, a new absorption peak was observed from 350 to 500 nm, consistent with the yellow color of the TiO_2/Cu_2O composite. After the partial conversion of Cu_2O to $Cu_3(BTC)_2$, the ternary composite shows a broad absorption peak from 400 nm to 800 nm, suggesting the utilization of visible light for the enhanced charge carrier density.

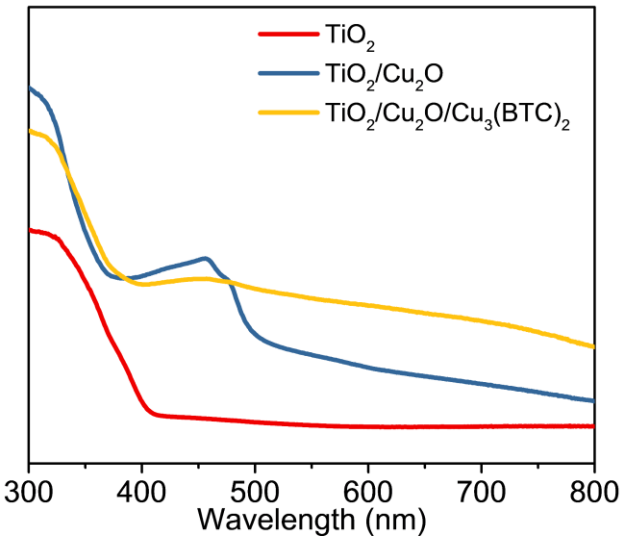

Figure 6.4 UV-Vis spectra of the samples.

In addition to the light absorption, the band alignment between TiO_2 and Cu_2O is also critical for the charge carrier density. Herein, the method proposed by Kraut *et al*[225] was applied to figure out the precise band alignment between TiO_2 and Cu_2O. Specifically, XPS measurements were conducted to acquire the core-level energy and upper edge of valence band (VB) (**Figures 6.5A-C**), meanwhile, the information from the UV-Vis analysis was used to derive the band gaps (BGs) (**Figure 6.5D**). The valence band offset, VBO, could be determined from the following equation,

$$VBO = \left(E_{Cu-core}^{bulk} - E_{Cu-valence}^{bulk}\right) - \left(E_{Ti-core}^{bulk} - E_{Ti-valence}^{bulk}\right) - (E_{Cu-core}^{composite} - E_{Ti-core}^{composite}) \quad (6.1)$$

while, the conduction band offset, CBO, could be calculated using the equation below based on the result from **Eq. 6.1**.

$$CBO = BG_{Cu_2O} + VBO - BG_{TiO_2} \quad (6.2)$$

where $E_{Cu-core}^{bulk}$ and $E_{Ti-core}^{bulk}$ are the core-level energies of pure bulk Cu_2O and TiO_2, respectively; $E_{Cu-valence}^{bulk}$ and $E_{Ti-valence}^{bulk}$ indicate the upper edges of VBs of Cu_2O and TiO_2, respectively; $E_{Cu-core}^{composite} - E_{Ti-core}^{composite}$ indicates the core-level energy differences in the TiO_2/Cu_2O composite.

With aforementioned information, the precise band alignment in the TiO_2/Cu_2O heterojunction was obtained and schematically shown in **Figure 6.5E**. With a more negative conduction band of Cu_2O, the photogenerated electrons on Cu_2O can migrate to

TiO_2 for CO_2 reduction. On the other hand, the accumulated holes flow in the opposite direction for water oxidation to release H^+ and O_2.[226] The efficient transfer of charge carriers between TiO_2 and Cu_2O highly remediates the electron-hole recombination and contributes to the higher charge carrier density.

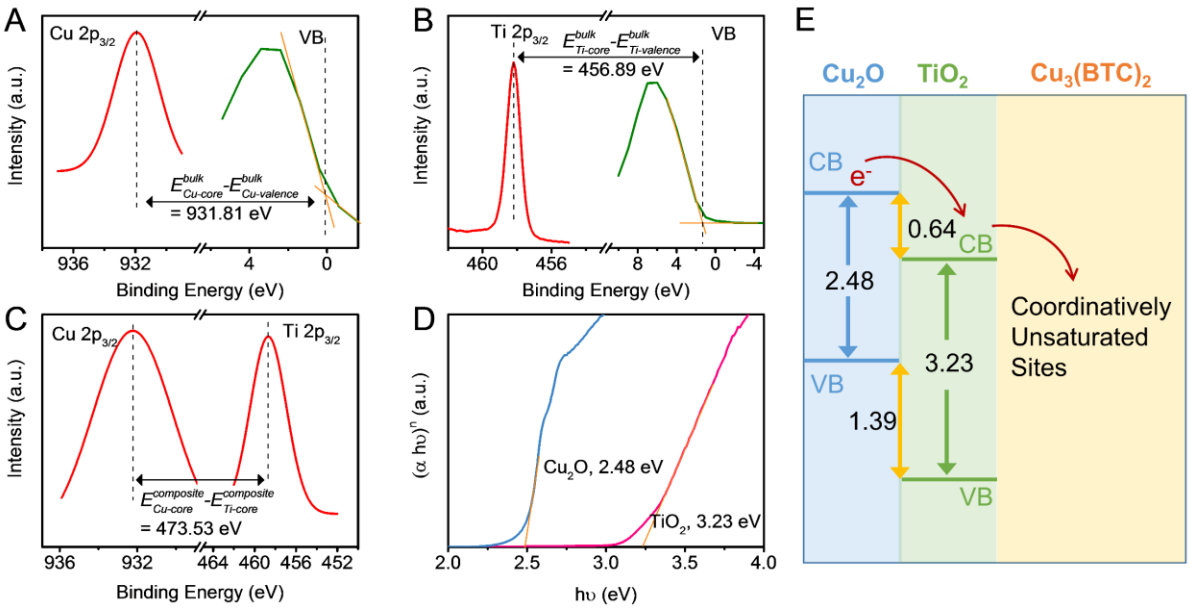

Figure 6.5 XPS valence band and core-level spectra of (A) pure bulk Cu_2O, (B) pure bulk TiO_2 and (C) TiO_2/Cu_2O composite; (D) Tauc plots of pure bulk Cu_2O and TiO_2; (E) Schematic illustration of charge transfer in $TiO_2/Cu_2O/Cu_3(BTC)_2$ (Unit: eV).

When Cu_2O was partially converted to $Cu_3(BTC)_2$, the electron-hole separation was further enhanced. In particular, $Cu_3(BTC)_2$ itself is unfavorable for charge separation as demonstrated by the ultrafast transient absorption spectroscopy analysis.[33] However, the

photoinduced electrons can effectively transfer from semiconductors to the coordinatively unsaturated copper sites in $Cu_3(BTC)_2$, suppressing the electron-hole recombination,[33] which is in agreement with experimental results of ·OH formation. The mechanism of the charge transfer between semiconductor composites and $Cu_3(BTC)_2$ is schematically shown in **Figure 6.5E**.

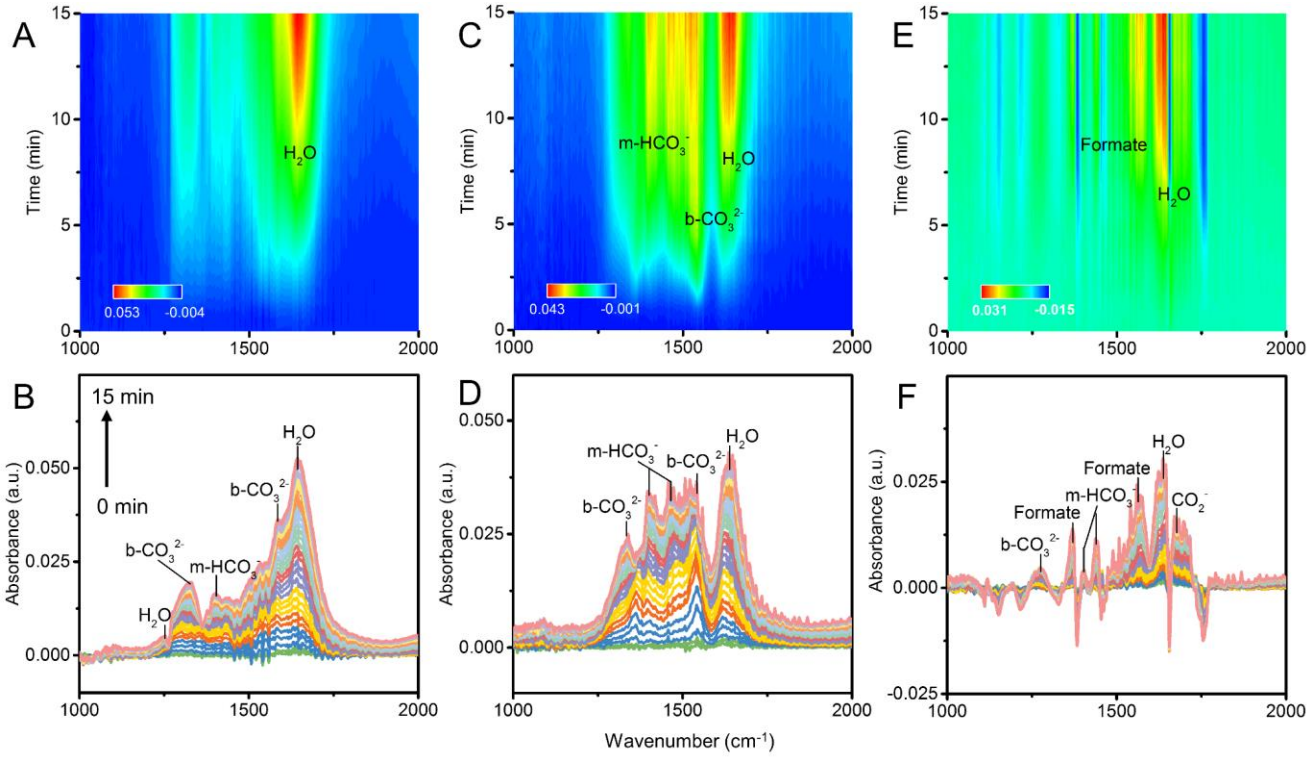

Figure 6.6 DRIFTS spectra recorded during the adsorption of CO_2/water mixture on sprayed TiO_2 (A and B), TiO_2/Cu_2O (C and D) and $TiO_2/Cu_2O/Cu_3(BTC)_2$ (E and F). Top panel: 2D view, bottom panel: the corresponding spectra.

CO_2 Molecule Activation Analysis. In addition to the enhanced charge carrier density, the CO_2 molecule activation also plays an important role in the promotion of CO_2 photoreduction efficiency of the ternary nanocomposites. In the present work, CO_2 activation is evidenced by various intermediates formed during the CO_2 adsorption process (**Figure 6.6**), which was analyzed by time-resolved *in-situ* diffuse reflectance infrared Fourier transform spectroscopy (DRIFTS). As shown in **Figure 6.6A**, the adsorbed water molecules are dominant on the pristine TiO_2 surface (1640 cm^{-1}),[227] along with small amount of bidentate carbonate (b-CO_3^{2-}, 1325 and 1585 cm^{-1})[228-229] and monodentate bicarbonate (m-HCO_3^-, 1405 cm^{-1})[230] (**Figure 6.6B**). With the incorporation of Cu_2O, the intermediates were dominated by b-CO_3^{2-} (1334 and 1543 cm^{-1})[229, 231] and monodentate HCO_3^- (1405 cm^{-1} and 1464 cm^{-1})[230, 232] (**Figures 6.6C** and **6.6D**). Compared with b-CO_3^{2-}, m-HCO_3^- is more active and can easily be converted to hydrocarbons.[233] It's worth noting that the percentage of m-HCO_3^- on TiO_2/Cu_2O is larger than that on TiO_2, indicating the enhanced activation ability of the catalyst with the incorporation of Cu_2O, which contributed to the increased CO_2 photoreduction efficiency. Furthermore, after the partial conversion of Cu_2O to $Cu_3(BTC)_2$, the intermediates were dominated by CO_2^- (1677 cm^{-1})[228] and bridging bidentate formate (1563 and 1370 cm^{-1})[234] (**Figures 6.6E** and **6.6F**). Notably, CO_2^- and formate are even more active than m-HCO_3^-, which can easily be transformed to the products upon photoirradiation.[235] The relative activities of the formed intermediates agree well with the corresponding CO_2 photoreduction performance (**Figure**

2.2), which confirms the importance of CO_2 molecule activation in the CO_2 photoreduction process in this work.

The formation of various intermediate species is related to the abundance of the coordinatively unsaturated (or open) metal sites in the catalysts. These open metal sites could induce multipole moments in CO_2 molecules and enhance the electrostatic interactions between them, resulting in the activation of CO_2 molecules.[135] The Cu_2O nanoparticles are dominated by (111) facets, where twenty-five percent of the copper ions are coordinatively unsaturated.[236] Compared with Cu_2O, $Cu_3(BTC)_2$ has more coordinatively unsaturated copper sites, arising from the unique structure of the framework.[237] Therefore, the incorporation of these two components brings extra open metal sites to the system, which significantly changes intermediate species during the CO_2 adsorption process. The formation mechanisms of two typical intermediates (i.e., m-HCO_3^- and formate) are proposed as follows and schematically shown in **Figure 6.7**.

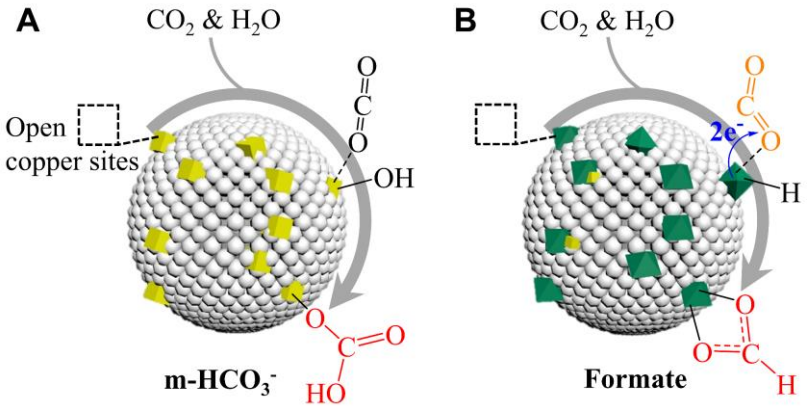

Figure 6.7 Proposed mechanisms for the formation of (A) m-HCO_3^- and (B) formate. (white spheres: TiO_2; yellow cubes: Cu_2O; green octahedrons: $Cu_3(BTC)_2$).

In general, during the co-adsorption of CO_2 and H_2O on the semiconductors, CO_2 interacts with the coordinatively unsaturated metal sites in a tilted linear configuration, while H_2O dissociates into hydroxyls. The linear CO_2 then reacts with hydroxyls to form m-HCO_3^- (**Figure 6.7A**). The incorporation of Cu_2O led to slightly increased coordinatively unsaturated metal sites, and subsequently enhanced the interaction of CO_2 with the metal sites, thus promoting the formation of m-HCO_3^- (**Figures 6.6C and 6.6D**). After partial conversion of Cu_2O to $Cu_3(BTC)_2$, the amount of coordinatively unsaturated copper sites increased significantly, leading to a bent CO_2 configuration.[135] The bent configuration makes CO_2 acting as an anionic molecule, resulting in the localization of negative charge in the carbon atom of the CO_2 molecule. The terminal oxygen then gains negative charge with the electron transferred from the coordinatively unsaturated copper sites due to the charge polarization.[214] With the electrons transferred to the lowest unoccupied molecular orbital (LUMO), the adsorbed CO_2 can then be activated to CO_2^-.[238] In the presence of protons derived from the dissociative water adsorption, the adsorbed CO_2 would be activated to formate (**Figure 6.7B**). In the meantime, the co-adsorption of water can also help to stabilize the active intermediates through hydrogen bonding.[214]

The preferential adsorption sites for CO_2 can be indirectly assessed by observing the CO_2 adsorption modes with the aid of the DRIFTS analysis (**Figure 6.8**). As shown in **Figure 6.8A**, the adsorbed CO_2 molecules have two major characteristic peaks. The peak centered at 2360 cm^{-1} is attributed to the functional group···O=C=O adducts formed by the

interaction of CO_2 with the functional groups.[67] While, the peak centered 2340 cm^{-1} with a frequency shoulder at 2330 cm^{-1} originates from the υ3 mode of CO_2 interacting with the coordinatively unsaturated metal sites.[127, 239] In addition, the peak area is associated with the amount of adsorbed CO_2. Thus, it is rational to estimate the preferential adsorption sites for the CO_2 molecules by using the area ratios of the peaks centered at 2340 cm^{-1} to those at 2360 cm^{-1}. As shown in **Figure 6.8B**, the highest peak ratios were found for the $TiO_2/Cu_2O/Cu_3(BTC)_2$ ternary nanocomposites, indicating the existence of ample coordinatively unsaturated copper sites in the structure, which contribute to the subsequent charge separation and CO_2 activation, and hence the improvement of overall CO_2 photoreduction performance.

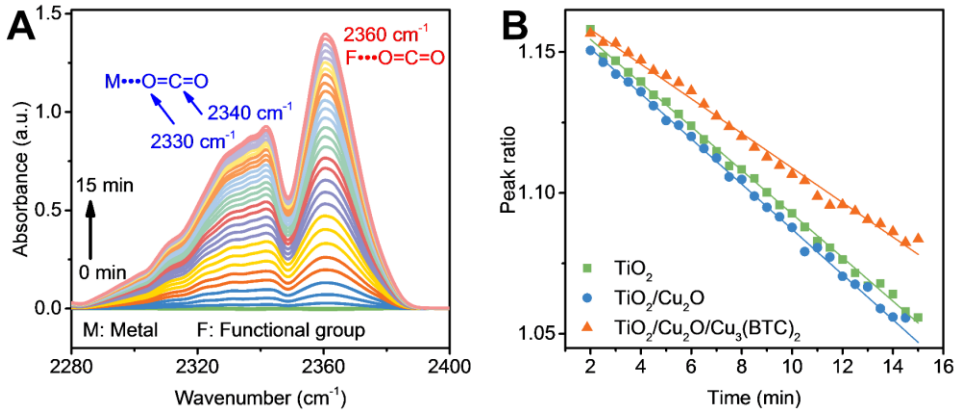

Figure 6.8 (A) DRIFTS spectra in the range of 2280 to 2400 cm^{-1} obtained during the adsorption of the CO_2/H_2O mixture on the $TiO_2/Cu_2O/Cu_3(BTC)_2$ surface; (B) Peak area ratios ($Peak_{2340}/Peak_{2360}$) of the three representative samples.

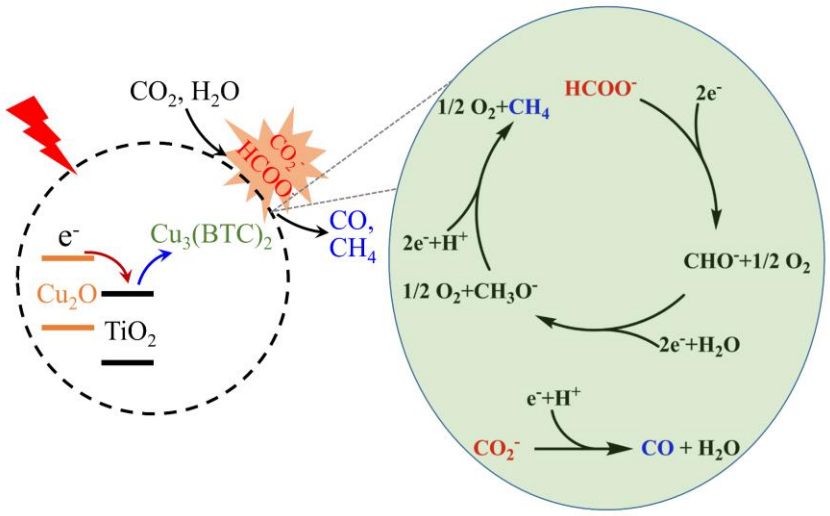

Scheme 6.2 The proposed reaction pathways in the MOF-based ternary photocatalyst system.

Taken together, a CO_2 photoreduction mechanism of using the MOF-based ternary nanocomposites is proposed in **Scheme 6.2** and descried as follows. Initially, CO_2 molecules interact with various adsorption sites, including Ti, Cu and surface functional groups. The presence of Cu_2O and $Cu_3(BTC)_2$ in the ternary system introduces abundant coordinatively unsaturated copper sites, which can activate the adsorbed CO_2 molecules to form active intermediates, including formate species and CO_2^-. Upon light irradiation, these active intermediates are converted to products with sufficient supply of electrons resulting from the enhanced light absorption and the efficient charge separation. In particular, the preferential formation of CH_4 originates from the existence of formate species, which are sequentially reduced to CHO^-, CH_3O^-, and CH_4 upon light irradiation (**Scheme 6.2**), where each step involves the transfer of two electrons.[240-241] The proposed pathway requires only six electrons, which is energetically favorable as compared to the conventional eight-

electron process of direct reduction of CO_2 to CH_4.[141, 145] On the other hand, CO is generated from CO_2^- (**Scheme 6.2**), which only requires one electron.[139-140] Another pathway where CH_4 is formed with CO being the intermediate, which usually occurs on the metal-coated photocatalysts,[162, 242-243] is unlikely in this work, since the CO evolution in the ternary system was not suppressed along with the promotion of CH_4 formation (**Figure 6.2**).

6.3 Conclusions

In summary, a MOF-based ternary composite photocatalyst (TiO_2/Cu_2O/$Cu_3(BTC)_2$) was designed towards enhanced CO_2 photoreduction by increasing the charge carrier density and facilitating CO_2 molecule activation. Systematic CO_2 photoreduction analyses were carried out to unravel the mechanisms. The results show that the incorporation of Cu_2O and $Cu_3(BTC)_2$ not only significantly improved the overall CO_2 photoconversion efficiency, but also led to the preferential formation of CH_4. The enhanced performance of the catalysts stems from the increased charge carrier density and efficient CO_2 activation by coordinatively unsaturated metal sites as verified and quantified by PL, XPS, and DRIFTS measurements. This work demonstrates a novel strategy to address low charge density and inefficient CO_2 activation issues, and meanwhile provides insights in the rational design of MOFs-based hybrid nanomaterials for CO_2 photoreduction and other applications.

Chapter 7. Highly-oriented One-dimensional MOF-semiconductor nanoarrays for Efficient Photodegradation of Antibiotics

Catalysis Science & Technology, 8(8): 2117-2123 (2018)
DOI: 10.1039/C8CY00229K

Abstract

The ineffective removal of antibiotics from the aquatic environment has raised serious problems, including chronic toxicity and antibiotic resistance. Among the numerous strategies, photocatalytic degradation appears to be one of the promising methods to remove antibiotics. Semiconductors are the most widely used photocatalysts, whereas, their efficiencies still suffer from limited light absorption and poor charge separation. Given their exceptional properties, including a superior surface area and massive active sites, MOFs are excellent candidates for the formation of hierarchical nanostructures with semiconductors to address the above issues. In this study, highly-oriented one-dimensional (1D) MIL-100(Fe)/TiO_2 nanoarrays were developed as photocatalysts for the first time (MIL = Materials Institute Lavoisier). The 1D structured TiO_2 nanoarrays not only enable the direct and enhanced charge transport, but also permit easy recycling. With the *in situ* growth of MIL-100(Fe) on the TiO_2 nanoarrays, the composite exhibits enhanced light absorption, electron/hole separation, and accessibility of active sites. As a result, up to 90.79% photodegradation efficiency of tetracycline, a representative antibiotic, by the MIL-100(Fe)/TiO_2 composite nanoarrays was achieved, which is much higher than that of pristine TiO_2 nanoarrays (35.22%). It is also worth mentioning that the composite nanoarrays demonstrate high stability and still exhibit high efficiency twice that of the pristine TiO_2 nanoarrays even in the 5th run. This study offers a new strategy for the degradation of antibiotics by using 1D MOF-based nanocomposite nanoarrays.

7.1 Introduction

Antibiotics have been extensively used for human, veterinary and agriculture purposes. However, due to the ineffectiveness of conventional wastewater treatment methods, massive antibiotics have been released to and accumulated in the aquatic environment, which can result in detrimental ecological consequences, including the occurrence and spread of antibiotic resistance and chronic toxicity to the microbial species.[244-245] Thus, the development of efficient methods is in demand for the complete elimination of these antibiotics. Several approaches have been developed to remove the antibiotics from water, including biological treatment, membrane separation, photocatalytic degradation and advanced oxidation processes (AOPs).[246] Among them, photocatalytic degradation appears to be one of the best choices because it is cost-effective and environmentally friendly.

Semiconductors, such as TiO_2, $BiVO_4$ and C_3N_4, are the most widely used photocatalysts for antibiotics degradation due to their outstanding photocatalytic ability and low cost.[247-248] However, the semiconductor-based photocatalysts have two inherent drawbacks: limited light absorption and fast electron/hole recombination. The most widely used method to solve the aforementioned issues is to create semiconductor heterojunctions, with which, not only the light absorption can be expanded, but also the electron/hole separation can be efficiently promoted.[249] For instance, Hu et al[250] constructed an all-solid-state Z-scheme photocatalytic system composed of Ag_2O, TiO_2 and reduced graphene

oxide, where Ag_2O broadens the light absorption to full spectrum and Z-scheme system of rGO-Ag_2O/TiO_2 enables efficient charge transfer. This ternary composite was reported to exhibit promoted efficiency in photodegradation of antibiotics even under near infrared light. Similarly, other heterojunctions, such as TiO_2/$Ni(OH)_2$,[251] $BiO_{1-x}Br$/$Bi_2O_2CO_3$[252] and graphene-bridged Ag_3PO_4/Ag/$BiVO_4$,[253] also showed enhanced photocatalytic ability towards the photodegradation of antibiotics. It should be noted that, the surface area and porosity of the semiconductors are generally very small, which limit the amount and accessibility of the photoactive sites to the reactants, and thus the further improvement in photocatalytic efficiency. In this sense, it would be rational to create the hierarchical nanostructures between semiconductors with porous materials.

Recently, metal-organic frameworks (MOFs) have gained much attention mainly due to their high surface area, huge porosity, and tunable structures. MOFs are composed of metal clusters and organic linkers. The metal clusters can be viewed as semiconductor quantum entities, while the organic linkers are antenna, which can enhance the light absorption and then activate the metal clusters through linker-to-metal charge transfer (LMCT).[254] In addition, the huge porosity of MOFs provides numerous reactive sites. Given all these unique properties of MOFs, efforts have been made to create semiconductor/MOF nanocomposites.[39, 64, 67, 94, 255] For example, In_2S_3@MIL-125(Ti) was synthesized by Wang et al,[39] with which antibiotics can be efficiently photodegraded, attributed to the efficient charge transfer and synergistic effect between In_2S_3 and MIL-

125(Ti). Similar synergy was also observed between C_3N_4 and ZIF-8, the composite of which can degrade 96% of the antibiotics after 1-hour sunlight exposure as a result of the efficient adsorption and rapid interfacial charge transfer.[255] Notably, most of the current semiconductor/MOFs nanocomposites are limited to powder morphologies, where the recycle of the photocatalysts could be a potential problem. In terms of this, a thin film-structured composite would be more desirable.

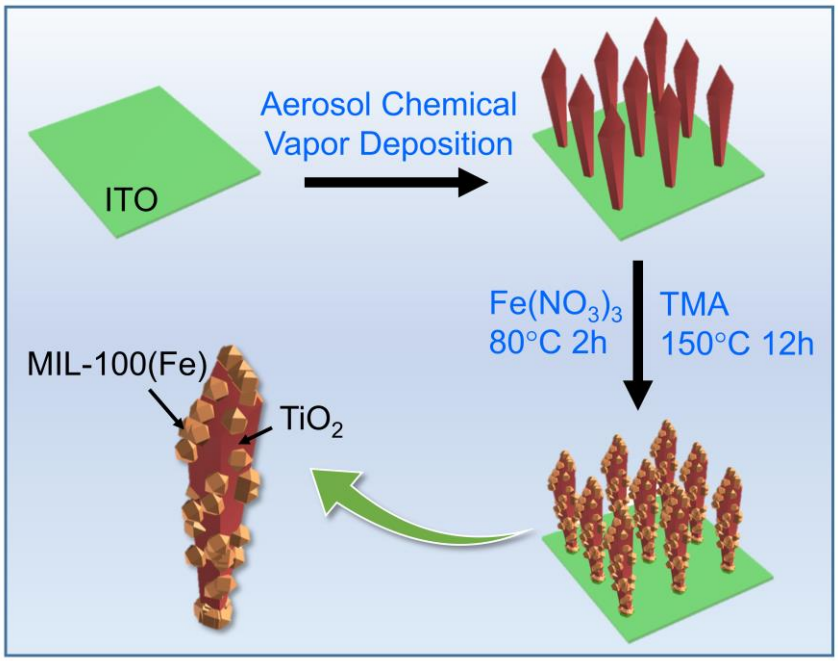

Scheme 7.1 Schematic illustration of synthetic process of 1D TiO_2/MIL-100(Fe) composite nanoarrays (TMA: Trimesic Acid).

Herein, a thin composite film composed of MIL-100(Fe) and highly-oriented TiO_2 nanoarrays was developed for the photo-degradation of antibiotics for the first time. The synthesis process is illustrated in **Scheme 7.1**. Specifically, aerosol vapor chemical deposition (ACVD) was applied to synthesize the TiO_2 nanoarrays.[256-257] In comparison to

the powder structure, the structure of nanoarrays permits easy recycle, and is also more favorable for photocatalysis owing to the direct pathway for photo-generated electrons and thus the increased electron transport rate.[257-258] As the next step, the TiO_2 nanoarrays were sequentially immersed in iron nitrate and trimesic acid (TMA) solutions for *in situ* growth of MIL-100(Fe). In this highly-oriented one dimensional (1D) composite nanostructure, the TiO_2 nanoarrays and MIL are in intimate contact, ensuring the efficient charge transfer at the interface. The properties and photocatalytic abilities of the as-prepared nanoarrays were investigated in detail. Results show that, by taking advantages of the synergy between TiO_2 nanoarrays and MIL-100(Fe), the as-prepared 1D composite nanoarrays exhibited excellent photocatalytic performance towards the degradation of tetracycline, one of the most widely used antibiotics.[259] On the basis of the results, a plausible pathway for the photodegradation of tetracycline was proposed. The outcome of this work is expected to broaden the strategies for efficient removal of antibiotics by using 1D MOFs-based photocatalysts.

7.2 Materials and Methods

Chemicals and Synthesis. Titanium (IV) isopropoxide (TTIP, Alfa Aesar), iron (III) nitrate nonahydrate ($Fe(NO_3)_3 \cdot 9H_2O$, Sigma Aldrich) and trimesic acid (TMA, Sigma Aldrich) were used as received without further purification. TiO_2 nanoarrays were synthesized on an ITO glass substrate (1.27 cm × 1.27 cm) by using TTIP as the precursor through the ACVD method.[257, 260] To remove possible organic residues and increase the crystallinity of the TiO_2 nanoarrays, the as-prepared samples were calcined at 500 °C in air for 3 hours.

Then, the TiO_2 nanoarrays were immersed into $Fe(NO_3)_3 \cdot 9H_2O$ aqueous solution (0.8 to 20 mmol/L, 10 mL) at 80 °C for 2 hours. After that, the film was taken out and washed several times with deionized (DI) water to remove residues. Subsequently, the film was put into an autoclave containing a saturated trimesic acid solution (0.3 g TMA in 4.28 mL DI water). The autoclave was then sealed and heated at 150 °C for 12 hours. After cooling down to room temperature, the MIL-100(Fe)/TiO_2 composite film was taken out and then immersed in ethanol to dissolve excess TMA, then flushed with DI water and dried in air flow. The composite films are termed hereafter T/M-0.8 (to 20) (T = TiO_2, M = MIL-100(Fe)), where the numbers indicate the concentration (unit: mmol/L) of $Fe(NO_3)_3 \cdot 9H_2O$ used in the previous step.

Material Characterization. The morphologies of the samples were analyzed by using a scanning electron microscope (SEM) equipped with energy-dispersive X-ray (EDX) spectroscopy (Su-70, Hitachi). X-ray diffraction (XRD) patterns were obtained with an X-ray diffractometer (PANalytical X'Pert Pro MPD). A UV-visible (UV-Vis) spectrophotometer (Evolution 220, ThermoFisher) was used to investigate the optical properties of the samples. The vibrational spectral analysis was carried out with a Fourier transform infrared (FT-IR) spectrometer (Nicolet iS50, Thermo Scientific). X-ray photoelectron spectroscopy (XPS) measurements were conducted with Thermo Scientific ESCALAB 250. Grazing-incidence wide-angle X-ray scattering (GIWAXS) measurements were carried out at Advanced Photon Source (APS, beamline: 8-ID-E), Argonne National

Laboratory. And the GIWAXS data was analyzed with the aid of a MATLAB toolbox, GIXSGUI.[261]

Photocatalysis Analysis. Photodegradation of tetracycline was conducted in a quartz cuvette (inner dimension: 10 mm × 10 mm) at room temperature. In a typical photocatalysis experiment, a film sample was put into the quartz cuvette with a mixture of tetracycline solution (100 mg/L, 3 mL) and hydrogen peroxide (30 wt%, 1 μL). The solution was stored in dark for 30 min, then exposed to light irradiation provided by a Xe lamp (450 W, Newport). During the photodegradation process, the concentration of the tetracycline was monitored every 10 min by using the UV-Vis spectrophotometer.

7.3 Results and Discussions

Material Characterization. The SEM images of representative samples are shown in **Figure 7.1**. The pristine TiO_2 films are composed of uniform nanoarrays (**Figures 7.1A and 3.1B**) with a thickness of ~ 1.2 μm. The surfaces of pure TiO_2 nanoarrays are clean (**Figures 7.1B**). After the growth of MIL-100(Fe), the composite retains the shape and dimensions (**Figure 7.1C**). Whereas, the surfaces of the T/M composite become rough due to the presence of MIL-100(Fe) nanocrystals (**Figure 7.1D**). **Figure 7.1E** shows the EDX spectrum of the T/M composite (T/M-1.25), where the main elements (i.e., Ti, Fe, C and O) are clearly identified. In addition, the elemental mapping of the T/M composite (**Figure 7.1F**) further reals the uniform *in situ* growth of MIL-100(Fe) crystals on the TiO_2 nanoarrays.

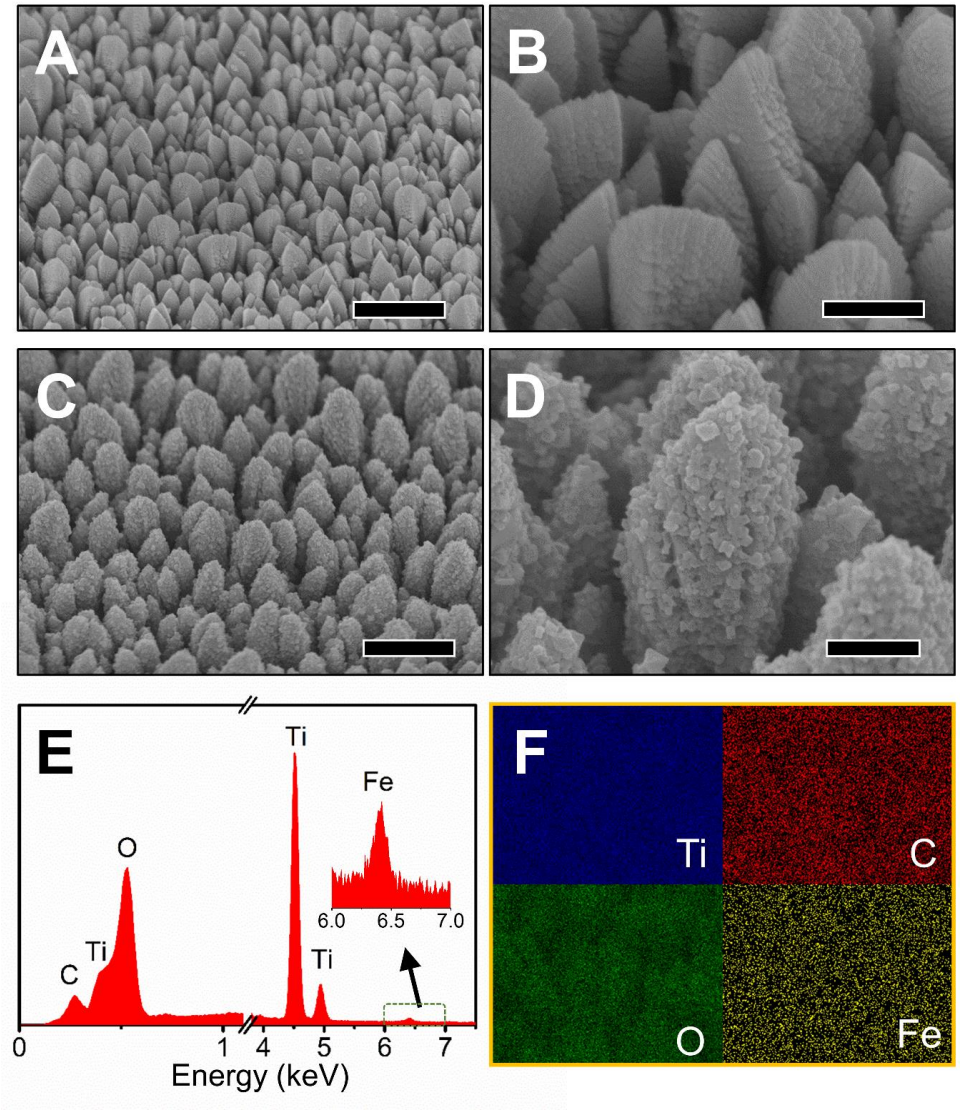

Figure 7.1 SEM images of TiO_2 nanoarrays (A and B) and T/M-1.25 (C and D); EDX spectrum (E) and element mapping (F) of T/M-1.25. Scale bars: A and C: 1 μm; B and D: 250 nm.

The crystal structures of the as-prepared samples were analyzed by XRD. As shown in **Figure 7.2A**, several diffraction peaks were observed, stemming from ITO, TiO_2 and MIL-100(Fe). In particular, the TiO_2 nanoarrays have a main diffraction peak at 70.38° and a very small diffraction peak at 25.32°, corresponding to (220) and (101) plans of anatase

(JCPDS 21–1272), respectively. The dominance of (220) diffraction peak and the absence of other peaks indicate that the TiO_2 nanoarrays are well aligned and have a preferential orientation. Moreover, the prominent (220) plane is beneficial for the photocatalytic process, as the high-index planes are generally considered to have higher catalytic ability due to the existence of massive active sites.[262-263] The incorporation of MIL-100(Fe) gave rise to new peaks at around 10°, consistent with the crystal structures of the pure MIL-100(Fe).[264] The intensities of these peaks are very low, mainly due to the small amount of MIL-100(Fe) in the composite system. The existence of the incorporated MIL-100(Fe) was also confirmed by GIWAXS measurements, where clear differences in scattering patterns between pristine TiO_2 and T/M-1.25 composite were observed. As shown in **Figure 7.2B**, for the pristine TiO_2 nanoarrays deposited on an ITO glass substrate, distinct intermittent ring-like scattering patterns with intensity modulations were observed within the q range of > 1.79 $Å^{-1}$, originating from the preferential orientation of the TiO_2 nanoarrays on the ITO glass,[265] which is consistent with the SEM and XRD results. In comparison, with the *in situ* growth of MIL-100(Fe), the T/M-1.25 exhibits new ring patterns within q range of 0 to 1.79 $Å^{-1}$ (**Figure 7.2C**), owing to the coating of the MIL nanocrystals and the porous nature of these crystals. For instance, the rings at q = 0.74 and 0.25 $Å^{-1}$ (**Figure 7.2D**) correspond to the representative pore window size (8.5 Å) and cage size (25 Å) of MIL-100(Fe), respectively.[264]

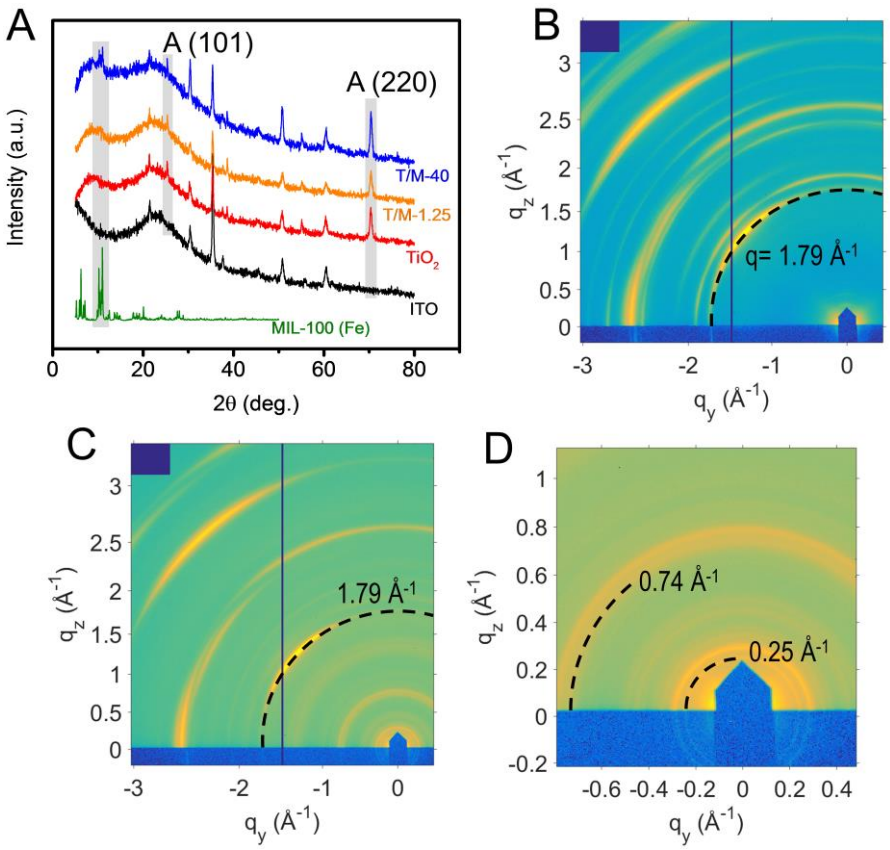

Figure 7.2 (A) XRD patterns of the as-prepared samples (A: anatase); GIWAXS profiles of TiO_2 nanoarrays (B) and T/M-1.25 composite (C and D) on ITO glass.

The UV-vis spectra obtained from the as-prepared samples were plotted in **Figure 7.3A**. As shown in **Figure 7.3A**, the pristine TiO_2 nanoarrays only absorb the UV light (< 400 nm). For the T/M-1.25 composite, the presence of small amount of MIL-100(Fe) slightly enhances the light absorption. With further increased amount of MIL-100(Fe) in the composite, the T/M composites exhibit light absorption over a wide wavelength range (< 600 nm). The enhancement in visible-light absorption by MIL-100(Fe) is attributed to

3*d*-3*d* transitions of octahedral $Fe^{III}O_6$.[266] **Figure 7.3B** shows the FT-IR spectra collected from the as-prepared pristine TiO_2 nanoarrays and T/M composites. For pristine TiO_2 nanoarrays, no discernible IR peaks were observed from 1000 cm^{-1} to 2000 cm^{-1}. Whereas, the IR spectrum of T/M-1.25 and T/M-20 shows strong peaks at 1379, 1450, 1562 and 1621 cm^{-1}, arising from the vibrations of the carboxylate groups.[267]

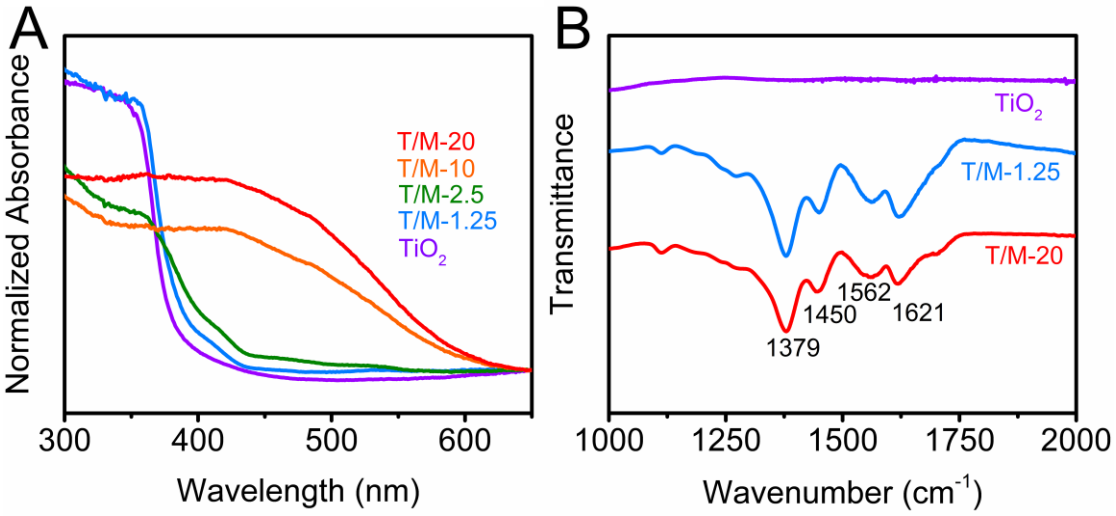

Figure 7.3 UV-Vis spectra (A) and FT-IR spectra (B) of the samples.

The amount of MIL-100(Fe) on TiO_2 nanoarrays can significantly affect the surface chemical composition. With a small amount of MIL-100(Fe), the surface of the composite is dominated by the combinations of TiO_2 and MIL-100(Fe). While, with a high loading of MIL-100(Fe), the surface of the composite is dominated by pure MIL-100(Fe) (e.g., T/M-20). The aforementioned difference in the surface configuration could affect the photocatalytic efficiency by changing the light absorption, charge carrier generation and transfer. In this sense, X-ray photoelectron spectroscopy was used to further characterize the surface chemical composition of two representative T/M composites (i.e., T/M-1.25

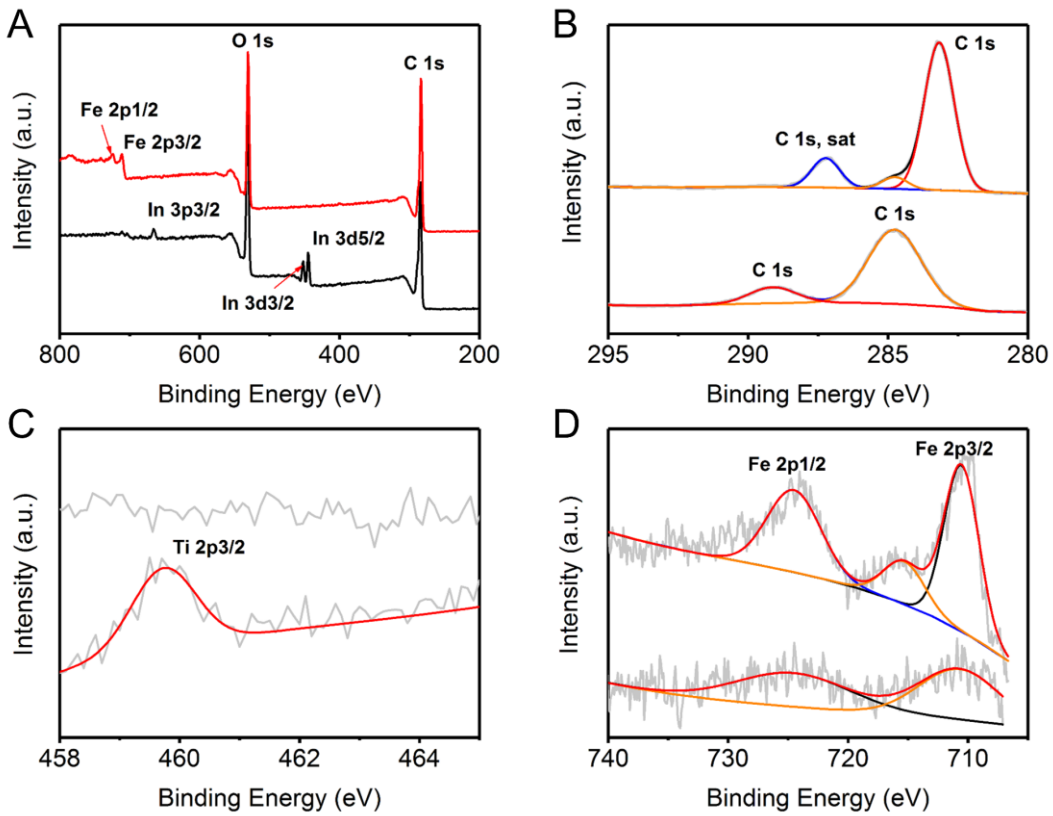

Figure 7.4 XPS spectra of T/M-1.25 (lower) and T/M-20 (upper): (A) survey scan; high-resolution spectra of (B) C 1s, (C) Ti 2p and (D) Fe 2p.

and T/M-20). The survey spectra of T/M-1.25 and T/M-20 were displayed in **Figure 7.4A**. Owing to the various coverage degrees of MIL-100(Fe), T/M-1.25 and T/M-20 exhibit different surface chemical compositions. Specifically, two prominent peaks at ~285 eV and ~532 eV were observed for both composites, corresponding to C 1s and O 1s, respectively. The T/M-1.25 shows additional characteristic binding energy of Indium (In) element, originating from the ITO glass substrate. With increased amount of MIL-100(Fe), element Fe was observed on the surface of T/M-20. **Figure 7.4B** displays the high-resolution XPS

spectra of C 1s. For T/M-1.25, there are two main peaks at 284.8 eV and 289.1 eV. In the case of T/M-20, the peak at 289.1 eV disappears, while additional two peaks emerge at 283.15 eV and 287.15 eV. The variation in C 1s spectra between T/M-1.25 and T/M-20 resulted from different MIL-100(Fe) coverages. In particular, in the case of T/M-20 where TiO_2 nanoarrays are fully covered by MIL-100(Fe) crystals, the C 1s spectrum is purely originated from MIL-100(Fe). While, the variation in C 1s for T/M-1.25 results from the chemical interaction between MIL-100(Fe) and TiO_2 nanoarrays. The Ti peak in the spectrum of T/M-1.25 was observed at 485.7 eV (**Figure 7.4C**), while no obvious distinct Ti peaks were observed for T/M-20, since the entire surface of the TiO_2 nanoarrays was covered by the thick MIL-100(Fe) layer, limiting the transmission of X-rays. For Fe, two dominated peaks were observed for both T/M-1.25 and T/M-20 at 724.65 and 710.65 eV (**Figure 7.4D**), attributed to Fe 2p1/2 and Fe 2p3/2, respectively. The difference in band energies between Fe 2p1/2 and Fe 2p3/2 is 14 eV, which is the characteristic of Fe_2O_3.[268-269] Due to increased amount of MIL-100(Fe), more information about Fe was obtained for T/M-20 with additional shoulder peak shown at 715.55 eV, corresponding to the Fe^{III} in MIL-100(Fe).[269]

The difference in the surface composition resulted from the various amount of MIL-100(Fe) plays a significant role in photocatalytic ability of the composite, as demonstrated in the following section.

Photodegradation Performance. After the detailed characterization, the MIL-100(Fe)/TiO_2 composites were applied for photodegradation of antibiotics. Tetracycline, one of the most extensively used antibiotics, was chosen as a representative antibiotic.[259] As shown in **Figure 7.5A**, tetracycline was efficiently photodegraded by the T/M composite (T/M-1.25), as evidenced by the decreased intensity of its characteristic peak (357 nm) in UV-Vis spectra. Comparison of the photocatalytic abilities of various catalysts were made (**Figure**

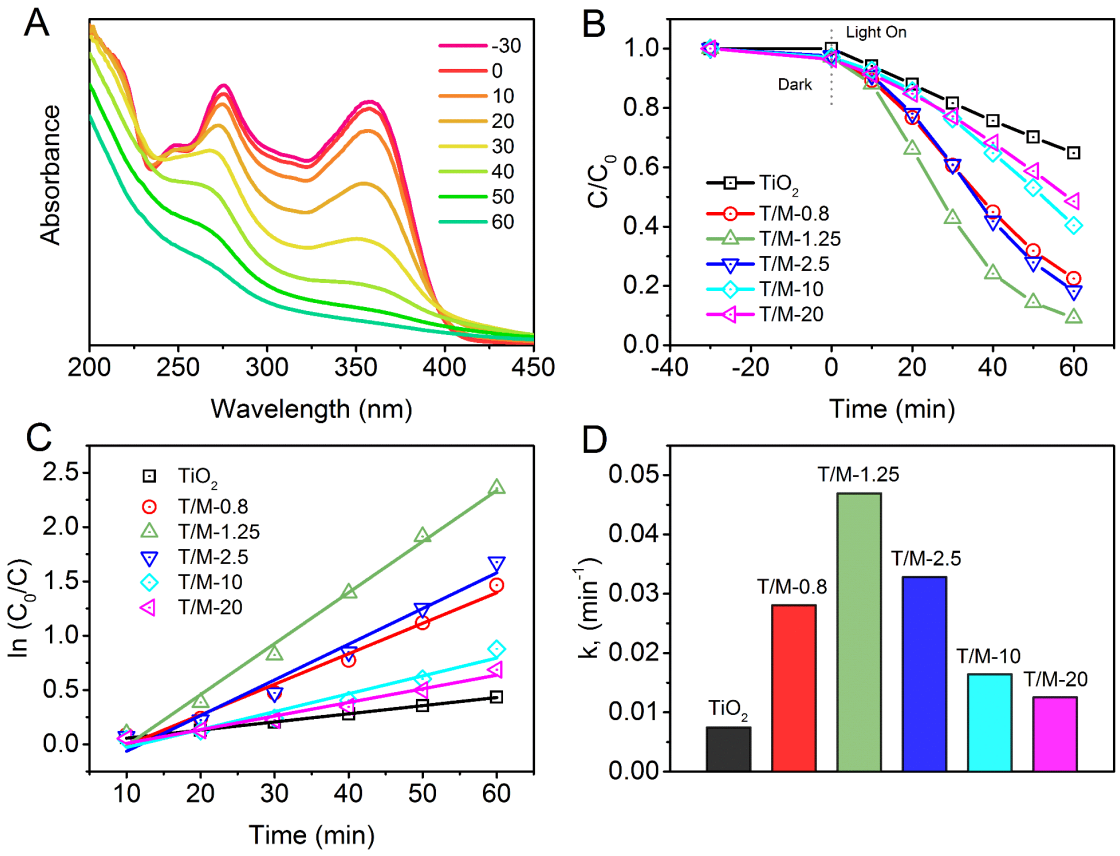

Figure 7.5 (A) UV-Vis spectra of tetracycline taken during the photocatalytic process in the presence of T/M-1.25 (unit of time: min); (B) Photodegradation of tetracycline; (C) Kinetics curves of the photodegradation of tetracycline; (D) Comparison of reaction rate constants.

7.5B). As exhibited in **Figure 7.5B**, no significant decrease in tetracycline concentration was observed after 30 min in the dark over all the catalysts, indicating the negligible adsorption of tetracycline even in the presence of MIL-100(Fe). After 60-min irradiation, the degradation efficiency of tetracycline for TiO_2 nanoarrays was about 35.22%. The incorporation of MIL-100(Fe) promotes the photo-degradation of tetracycline. And the highest efficiency was achieved in the case of T/M-1.25 with a removal efficiency of 90.79%, which is about 2.5 times higher than that of pristine TiO_2 nanoarrays. The kinetics curves shown in **Figure 7.5C** exhibit a linear relationship between $ln(C_0/C)$ and time, indicating that the photo-degradation of tetracycline follows the pseudo-first-order kinetic model, which could be described as $ln(C_0/C) = kt$, where k is the reaction rate constant (min^{-1}). The reaction rate constants for various catalysts were determined from **Figure 7.5C** by linear fitting and then summarized in **Figure 7.5D**. Specifically, the reaction rate constants for TiO_2, T/M-0.8, T/M-1.25, T/M-2.5, T/M-10 and T/M-20 are calculated to be 0.00749, 0.02808, 0.04696, 0.03283, 0.01645 and 0.01255 min^{-1}, respectively. All T/M composites exhibit higher efficiencies in photodegradation of antibiotics than the pure TiO_2, which can be attributed to the rapid charge transfer at the interface of TiO_2 and MIL-100(Fe), as verified by photoluminescence and photocurrent transient response measurements in a prior study.[270] Notably, the amount of the incorporated MIL-100(Fe) plays a significant role in photocatalytic efficiency of the T/M composite. Initially, the increased amount of MIL-100(Fe) helps to enhance interfacial charge transfer. However, if the amount of MIL-100(Fe) exceeds the optimal value, the extra MIL-100(Fe) reduces the

light absorption of TiO_2 and thus diminish the excited charge carriers and interfacial charge transfer, leading to decreased photodegradation efficiency.

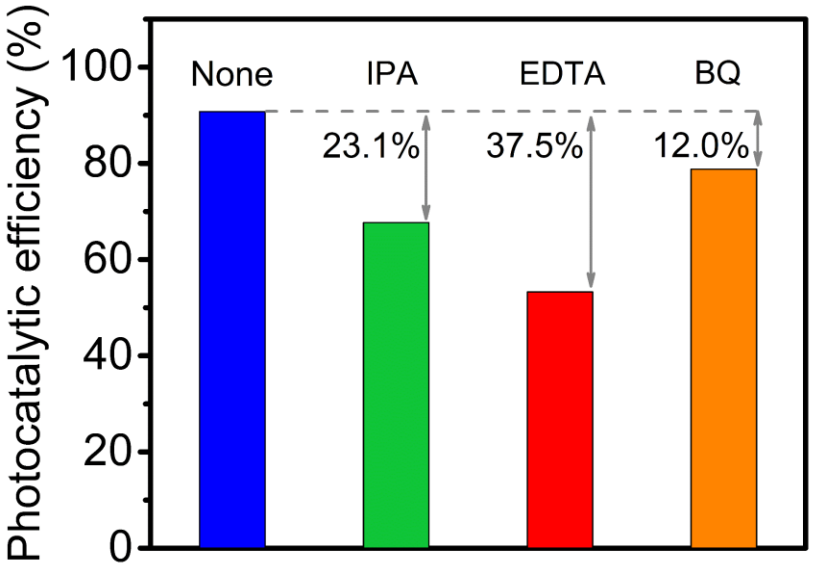

Figure 7.6 Photocatalytic degradation of tetracycline over T/M-1.25 with the addition of radical scavengers.

During the photocatalytic process, several reactive species could be generated, including electrons (e^-), holes (h^+), superoxide ions ($O_2^{\cdot-}$) and hydroxyl radicals (·OH). These species may participate in the photodegradation of tetracycline if thermodynamically favorable. In order to identify the dominant oxidative species, the photocatalytic degradation efficiency was evaluated with the addition of radical scavengers in the solution. In particular, isopropyl alcohol (IPA, 0.2 ml), ethylenediaminetetraacetic acid (EDTA, 10 mM/L) and p-benzoquinone (BQ, 33.3 μmol/L) were chosen as the scavengers of ·OH, h^+ and $O_2^{\cdot-}$, respectively.[271] As shown in **Figure 7.6**, the photocatalytic ability of T/M-1.25

was inhibited by 12.0%, 23.1% and 37.5% with the presence of BQ, IPA and EDTA, respectively, indicating the presence of the reactive species (i.e., $O_2^{\cdot-}$,·OH and h^+). Among these species, h^+ appeared to be dominated in photodegradation of tetracycline, as the addition of hole scavenger (i.e., EDTA) resulted in the most significant decrease in photocatalytic efficiency.

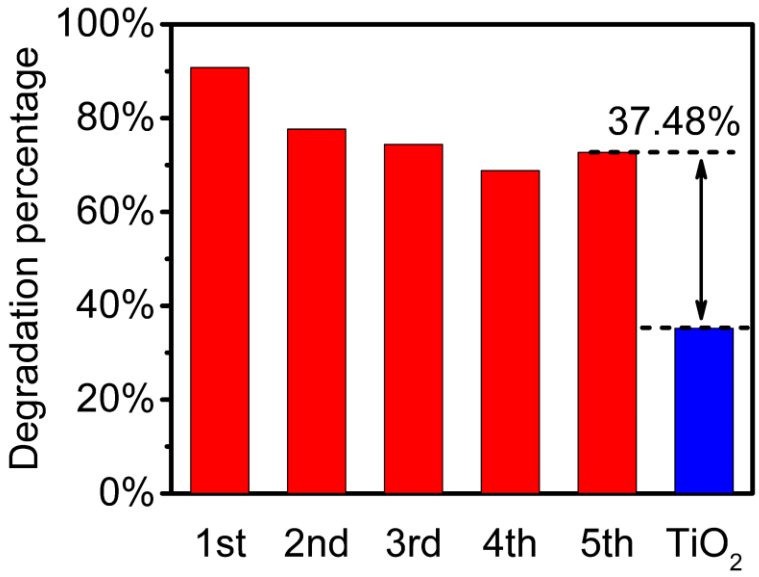

Figure 7.7 Recycling photocatalytic tests of T/M-1.25 for the degradation of tetracycline.

In addition, the MIL-100(Fe)/TiO_2 nanoarrays demonstrated excellent reusability. To be specific, the reusability of the T/M-1.25 composite was evaluated by five cycles of tetracycline photodegradation. After each cycle, the composite film was taken out from the reaction cell with a tweezer and washed with DI water to remove the residual reactants, and then dried with air flow for the next cycle. As shown in **Figure 7.7**, the degradation

percentage slightly deceased after the first cycle and then gradually stabilized at ~73 % even after 5 cycles, which is still 37.48% higher than that of the pristine TiO_2 nanoarrays.

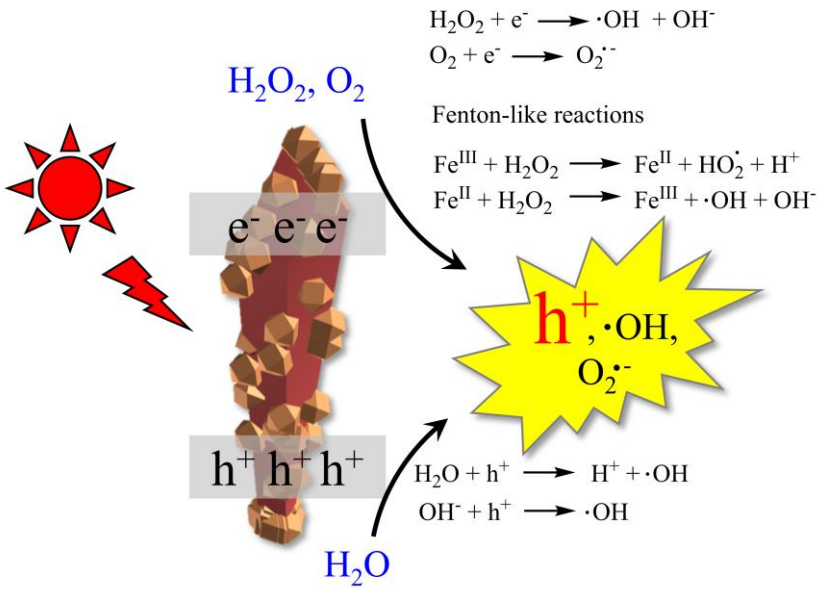

Scheme 7.2 Proposed reaction pathways.

Taken together, plausible reaction pathways are proposed in **Scheme 7.2** and described as follows. Upon irradiation, TiO_2 is activated with electrons excited from the valence band to the conduction band. On the other hand, MIL-100(Fe) is activated through ligand-to-metal charge transfer and direct excitation of Fe-O clusters.[272] It is well acknowledged that the charge transfer occurs at the interface between MIL-100(Fe) and TiO_2, due to the differences in redox potentials.[270] As a result, the electron/hole recombination was significantly suppressed, leading to abundant free electrons and holes. The porous structure of MIL-100(Fe) enables the accessibility of these electrons and holes, which subsequently react with O_2 and H_2O to form $O_2^{\cdot-}$ and ·OH, respectively (**Scheme 7.2**). The addition of H_2O_2 further facilitates the photocatalytic process by providing more

·OH through the reactions with not only photo-excited electrons but also Fe^{III} in MIL-100(Fe) to form Fenton-like reactions (**Scheme 7.2**).[273] Finally, all these reactive species, including ·OH, h^+ and $O_2^{\cdot-}$, synergistically degrade the antibiotics. And the main reactive specie responsible for the photodegradation of tetracycline has been identified to be h^+ by the radical trapping experiments.

7.4 Conclusions

In summary, highly-oriented 1D MIL-100(Fe)/TiO_2 composite nanoarrays have been synthesized for the photodegradation of tetracycline, where the incorporated MIL-100(Fe) not only enhances the light absorption but also facilitates the electron/hole separation, leading to promoted photodegradation of tetracycline. Several oxidative species, including $O_2^{\cdot-}$, ·OH and h^+, are mainly responsible for the photocatalytic process. Notably, excessive incorporated MIL-100(Fe) limits the light absorption of TiO_2, which is detrimental for the overall photocatalytic performance. This work demonstrates the use of 1D TiO_2/MIL composite for enhanced photodegradation of tetracycline, which will shed new light on photocatalysis by MOFs-based composites.

Chapter 8. Mechanistic Insight into Photocatalytic Pathways of MIL-100(Fe)/TiO_2 Composites

Abstract

The integration of metal-organic frameworks (MOFs) with semiconductors has attracted mounting attention for photocatalytic applications. However, more efforts are needed to unravel the interface structure in MOF/semiconductor composites and its role in charge transfer. Herein, a MIL-100(Fe)/TiO_2 composite was synthesized as a prototypical photocatalyst and studied systematically to explore the interface structure and unravel the charge transfer pathways during the photocatalytic processes. The composite was fabricated by growing MIL-100(Fe) crystals on TiO_2 using surface-coated FeOOH as the precursor. The as-prepared MIL-100(Fe)/TiO_2 exhibited significantly improved photocatalytic performance over pristine TiO_2, which was mainly due to the enhanced charge separation as confirmed by transient absorption spectroscopy analysis. This enhancement partially arose from the special chemical structure at the interface, where Fe-O-Ti bond was formed. As verified by density functional theory calculation, this distinct structure would create defect energy levels adjacent to the valence band maximum of TiO_2. During the photocatalytic processes, the defect energy levels serve as sinks to capture excited charge carriers and retard the recombination, which subsequently leads to the increased charge density and promoted photocatalytic efficiency. Meanwhile, the intimate interactions between MIL-100(Fe) and TiO_2 would also help to improve the charge separation by transferring photo-induced holes through ligand to Fe-O clusters. These findings would advance the fundamental understanding of the interface structure and the charge transfer pathways in MOF/semiconductor composite photocatalysts.

8.1 Introduction

Metal-organic frameworks (MOFs), an attractive class of porous crystals assembled from metal ions/clusters and organic linkers, have drawn intense interest because of their distinguished properties, including huge surface areas, tailorable chemistries, and tunable cavities.[4, 274-276] Endowed with such unique features, MOFs are promising candidates for massive applications, including sensing,[277] gas separation,[278-279] and catalysis.[280-281] In addition, the functions of MOFs can be expanded and promoted through rational integration with other components, such as metals and semiconductors.[67, 94, 96, 282]

For instance, numerous MOF-based composites have been designed and used as photocatalysts,[283] including ZIF-8/TiO_2,[32] ZIF-8/ZnO,[284] UiO-66/C_3N_4,[285] UiO-66-NH_2/$Cd_{0.2}Zn_{0.8}S$,[286] NH_2-MIL-125(Ti)/TiO_2,[287-288] MIL-125(Ti)/In_2S_3,[39] and HKUST-1/TiO_2,[33, 64] where the composites exhibit significantly improved catalytic performance as compared with the individual components. Mostly, the semiconductor serves as the major catalyst, while the MOF functions as the co-catalyst or support, which promotes the catalytic efficiency by enhancing molecule adsorption and charge transfer. For instance, CdS-embedded MIL-101 demonstrated a higher ability in hydrogen evolution as compared with either bare CdS or MIL-101.[289] The improved efficiency was primarily ascribed to the huge surface area of MIL-101, which not only allows the wide dispersion of CdS but also offers massive active sites. Recently, Panneri et al.[255] fabricated C_3N_4 anchored ZIF-8 composites with a highly stable micro-meso porous structure, which could adsorb up to 45% of tetracycline in its solution and achieve a significantly high

photodegradation efficiency. In addition to the promoted molecule adsorption, another key impetus for the enhanced photocatalytic efficiency of such MOF/semiconductor composites is the increased charge carrier density because of the distinct interface structure. For instance, Zeng et al.[32] developed a ZIF-8/TiO_2 composite by incorporating ZIF-8 on TiO_2 nanofibers. The composite showed great improvements in photodegradation of Rhodamine B mainly because of the reduced charge recombination through the N-Ti-O bonds formed at the interface between ZIF-8 and TiO_2. In addition, UiO-66/C_3N_4 heterojunction was synthesized by Wang et al.,[285] where the rate of H_2 evolution was promoted to 17 times that of pristine C_3N_4. Such a huge enhancement was also attributable to the efficient interface charge transfer, as evidenced by quenched photoluminescence (PL) emission peak and shortened PL lifetime. The interface charge transfer was also proposed to exist in MIL-100(Fe)/TiO_2[270] and ZIF-8/C_3N_4.[255] As demonstrated by these prior studies, the distinct MOF/semiconductor interface plays a vital role in enhancing the charge transfer. However, exploration of the mechanistic basis is still in its infancy. For example, the interface structures of various MOF/semiconductor composites may differ from each other, which might lead to distinctive charge transfer pathways. To further improve the photocatalytic efficiency and fully exploit the benefits of these MOF-based composites, greater efforts should be devoted to resolving the interface structure and understanding the charge transfer pathways.

Herein, a MIL-100(Fe)/TiO_2 composite was used as a prototype for the study of charge transfer by using both experimental and theoretical methods. To be specific, MIL-100(Fe) was grown on the surface of TiO_2 (i.e., P25, Degussa, Evonik) using the surface-coated FeOOH as the

precursor (**Scheme 8.1**). The composite was then subjected to systematic material characterization and photocatalytic analysis. The results show that the MIL-100(Fe)/TiO_2 composite photocatalyst exhibits significantly improved performance in both degradation of tetracycline and Cr(VI) reduction than the bare TiO_2 thanks to the enhanced charge separation. To unravel the underlying mechanism, systematic experiments and theoretical calculations were conducted. It was found that the enhanced charge separation arose from the defect energy levels existed in the TiO_2 band structure, which were created through the partial substitution of Ti by Fe during the synthesis of MIL-100(Fe) crystals on the surface of TiO_2. The outcome of this work should be able to provide new insights regarding the MOF/semiconductor interface structure and charge transfer, and ultimately to advance the fundaments in photocatalysis by using MOF/semiconductor composites.

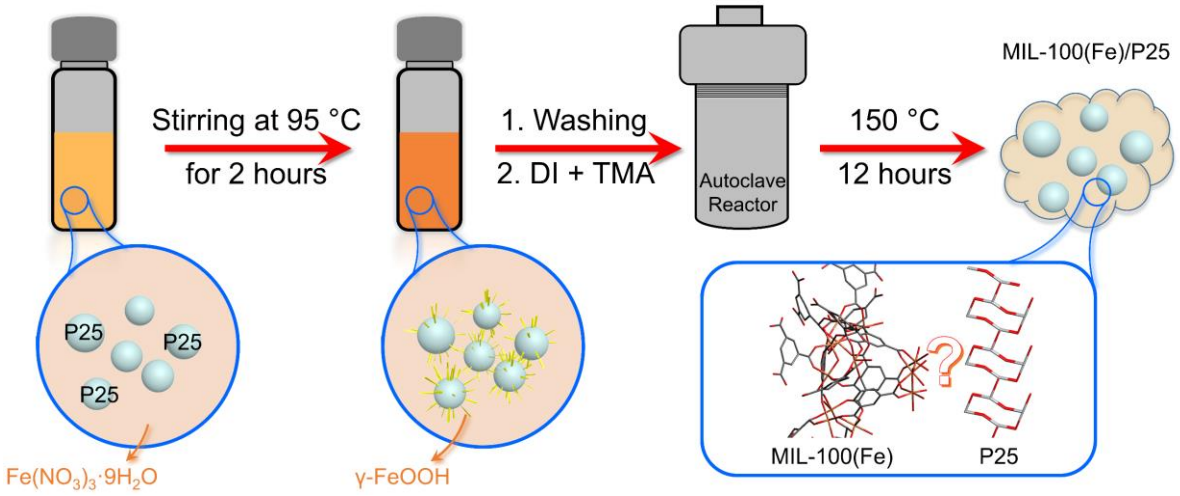

Scheme 8.1 The synthesis process of MIL-100(Fe)/P25.

8.2 Materials and Methods

Synthesis of MIL-100(Fe)/P25 Composites. In a typical synthesis procedure (**Scheme 8.1**), 0.025 g P25 (Degussa, Evonik) was firstly mixed with 5 – 40 mmol/L $Fe(NO_3)_3 \cdot 9H_2O$ aqueous solution in a glass vial. Then, the vial was heated and stirred by a hotplate stirrer at 95 °C and 1200 rpm for 2 hrs. After that, the powders were washed by deionized (DI) water through the centrifugation/re-dispersion process for five times to remove the iron residues. Subsequently, the powders were re-dispersed in 4.8 mL DI water together with 0.3 g trimesic acid (TMA). After vortex mixing, the mixtures were poured into a Teflon autoclave, which was then put in a muffle furnace at 150 °C for 12 hrs. After cooling, the composite samples were taken out from the autoclave and immersed in hot water at 80 °C for 3 hrs to remove TMA residues. Finally, the composite products were obtained after washing with DI water through the centrifugation/re-dispersion process for three times. The MIL-100(Fe)/P25 composites are hereafter termed M/P-5(to 40), where the numbers refer to the initial molar concentrations of $Fe(NO_3)_3 \cdot 9H_2O$.

Material Characterization. The morphologies and inner structures of the materials were examined by a scanning electron microscope (SEM, Su-70, Hitachi) and a transmission electron microscope (TEM, JEM 1230, JEOL), respectively. The powder X-ray diffraction (PXRD) patterns were obtained by using a PANalytical X'Pert Pro MPD X-ray diffractometer. Vibration spectral analysis was conducted by using a Fourier transform infrared (FT-IR) spectrometer (Nicolet iS50, Thermo Scientific). The UV-Vis spectra were recorded by using a spectrophotometer (Evolution 220, Thermo Fisher). X-ray photoelectron spectroscopy (XPS,

ESCALab 250, Thermo Fisher) was used to study the surface chemical composition. The wide-angle X-ray scattering (WAXS) measurements were performed at the 8-ID-E beamline, Advanced Photon Source (APS), Argonne National Laboratory, USA. The nitrogen adsorption-desorption isotherms were obtained by Autosorb iQ (Quantachrome Instruments).

Transient Absorption (TA) Spectroscopy. Femtosecond TA studies were carried out at the Center for Nanoscale Materials (CNM), Argonne National Laboratory, USA. Specifically, an amplified Ti:sapphire laser system was used, which produces 150 fs pulses centered at 800 nm with a repetition rate of 5 kHz. 90% of the output was directed to a TOPAS optical parametric amplifier to produce pump pulse at 350 nm. The beam energy was set to 2 μJ with a spot size of 150 μm diameter. The remaining 10% was used to generate probe pulse ranging from 450 nm to 700 nm by focusing into a sapphire window with a thickness of 2 mm.

Photodegradation of Tetracycline. The photocatalytic ability of the catalysts was first tested by the degradation of tetracycline with a 450 W Xe arc lamp (Newport Corporation). The experiments were conducted in a quartz beaker with continuous stirring. Specifically, 5 mg of catalyst was distributed into a 100 mL aqueous solution containing tetracycline (100 mg/L) and H_2O_2 (20 μL). Before light irradiation, the suspension was stirred for 30 min to get adsorption equilibrium. After turning the light on, 3 mL of the suspension was taken out at certain intervals and then subjected to centrifugation to remove the catalysts. Subsequently, the concentration of the tetracycline was determined from the absorbance at its characteristic wavelength (i.e., 357 nm) by using the UV-Vis spectrophotometer.

Photoreduction of Cr(VI). The experimental set-up and analysis procedures of Cr (VI) photoreduction were the same as those of the photodegradation of tetracycline, except that potassium dichromate (10 mg/L) and methanol (35 μL) were used instead of tetracycline and H_2O_2, respectively. The pH of the suspension was adjusted to 1.9 by adding sulfuric acid. After 30 min in the dark, the suspension was subjected to the light illumination, during which 1 mL of the suspension was withdrawn for test every 10 min. The Cr(VI) concentration was measured by using diphenylcarbazide method (7196A, United States Environmental Protection Agency).

Density Functional Theory (DFT) Calculations. The DFT calculations of the electronic structures of bare TiO_2 and Fe-doped TiO_2 were performed by using the VASP package.[290] The details of the calculation can be found in our prior study.[291]

8.3 Results and Discussions

Material Characterization. The morphologies and structures of the representative samples were characterized by SEM and TEM. As displayed in **Figures 8.1A and B**, pristine P25 are monodispersed nanocrystals with a diameter of ~ 25 nm. The surfaces of the pristine P25 nanoparticles are very smooth. After being suspended in $Fe(NO_3)_3 \cdot 9H_2O$ aqueous solution (10 mM) and followed by stirring on a hotplate stirrer at 95 °C for 2 hours, the P25 nanoparticles were decorated by some small FeOOH nano-sticks on the surfaces (**Figures 8.1C and D**). Further increasing the concentration of $Fe(NO_3)_3 \cdot 9H_2O$ led to the formation of more and longer FeOOH sticks (**Figure 8.1E and F**). Characterization of the P25/FeOOH composite was carried out by FT-IR, where the major bands are discovered at 1020 and 1166 cm^{-1}, corresponding to the

characteristic vibration of γ-FeOOH.[292] The PXRD pattern of the P25/FeOOH shows that all the peaks can be assigned to P25 and no apparent peaks of γ-FeOOH are observed, indicating the amorphous nature of the surface-coated FeOOH. Given this, the as-coated FeOOH could be used as a precursor for the facile growth of MIL-100(Fe) crystals. Specifically, the P25/FeOOH was put into TMA solution and subjected to hydrothermal synthesis to convert FeOOH to MIL-100(Fe) and obtain MIL-100(Fe)/P25 composite. As exhibited in **Figure 8.1G and H**, the surfaces of the MIL-100(Fe)/P25 composite turn out to be very rough owing to the presence of MIL-100(Fe) as the shell.

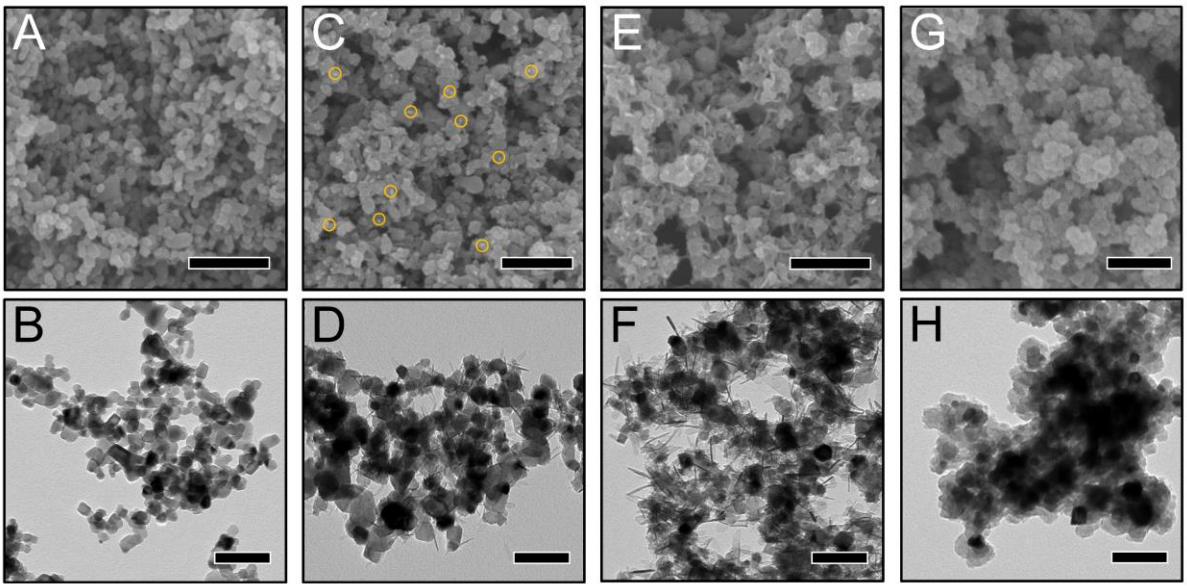

Figure 8.1 SEM and TEM images of pristine P25 (A, B), P25 modified by $Fe(NO_3)_3 \cdot 9H_2O$ with various concentrations (10 mM (C, D) and 20 mM (E, F)) and M/P-10 (G, H), Scale bars: SEM: 250 nm, TEM: 100 nm.

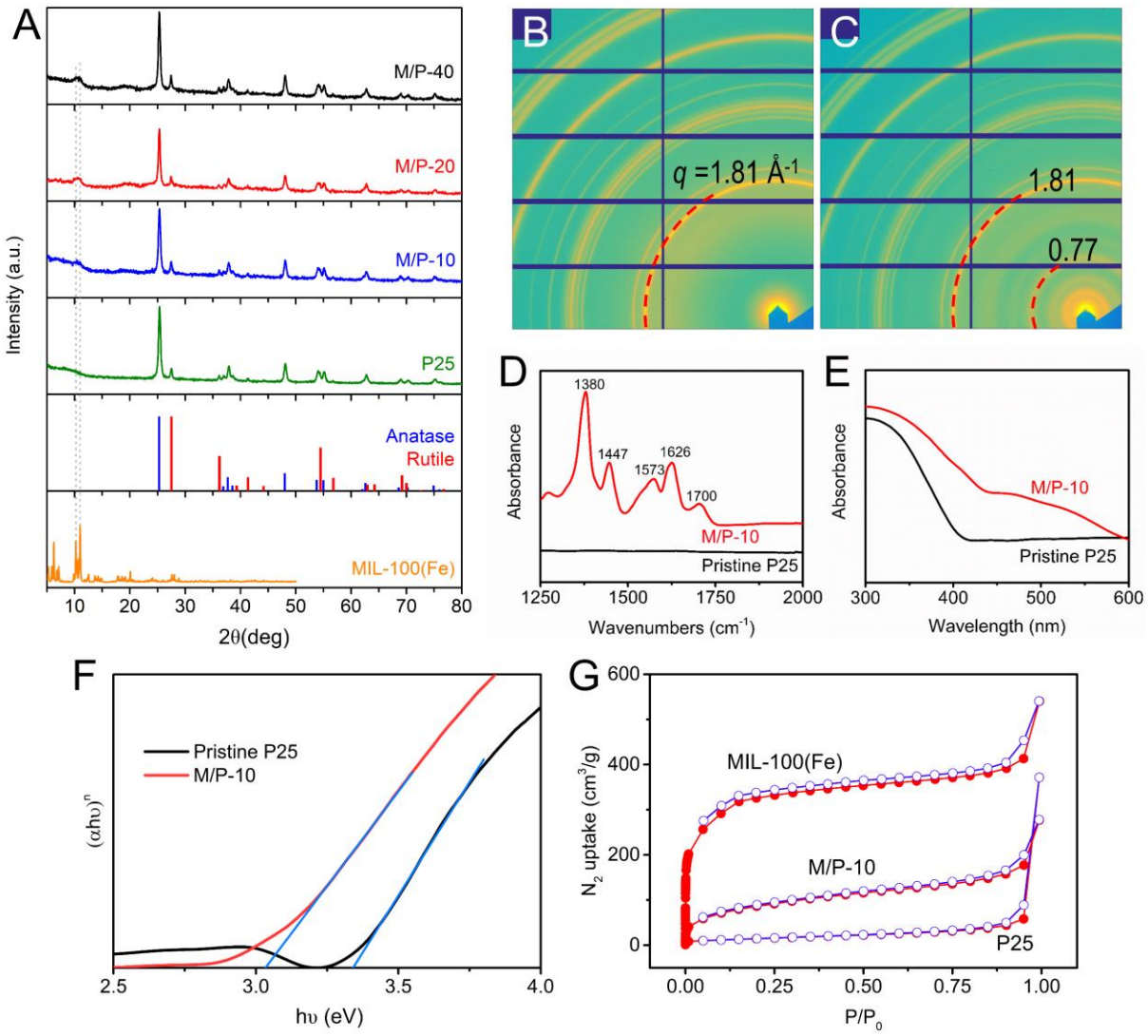

Figure 8.2 (A) PXRD patterns of the as-prepared samples; 2D WAXS patterns of (B) P25 and (C) M/P-10; FT-IR (D) and UV-Vis spectra (E) of the samples; (F) Tauc plots of pristine P25 and M/P-10. Both samples are dominated by anatase, which has an indirect band gap. Therefore, n = 2 was used for both Tauc plots; (G) Nitrogen sorption isotherms at 77 K.

The crystallinity of the MIL-100(Fe)/P25 composites was studied by PXRD measurements. As shown in **Figure 8.2A**, pristine P25 has a main anatase phase and a trace amount of rutile phase. With the incorporation of MIL-100(Fe), the crystalline structure of P25 was perfectly preserved, and a new diffraction peak shows up at ~10°, attributed to the crystal phase of MIL-100(Fe).[293] The intensity of this new diffraction peak increases with the increased amount of MIL-100(Fe) in the composite. In addition to the PXRD patterns, 2D WAXS patterns of the samples were also obtained. As shown in **Figure 8.2B**, the pristine P25 powders exhibit ring patterns with $q > 1.81$ $Å^{-1}$. With the presence of MIL-100(Fe), new ring patterns emerged with $q < 1.81$ $Å^{-1}$(**Figure 8.2C**), which originated from the crystal structure and porosity of MIL-100(Fe) crystals. For instance, the ring pattern at the position of $q = 0.77$ $Å^{-1}$ comes from the repeating structure with a dimension of 8.2 Å, which is the pore window size of the MIL-100(Fe) crystals. The MIL-100(Fe) component in the MIL-100(Fe)/P25 composite was also supported by the FT-IR results. As revealed in **Figure 8.2D**, no vibrational peaks were observed for the pristine P25 from 1250 cm^{-1} to 2000 cm^{-1}. While, for the MIL-100(Fe)/P25 composite, several peaks were observed at 1380, 1447, 1573, 1626 and 1700 cm^{-1}, which can be ascribed to carboxylate groups on the surface of MIL-100(Fe).[267] The optical properties of the samples were evaluated by the UV-vis measurements. As shown in **Figure 8.2E**, the pristine P25 exhibits absorption of UV light (< 400 nm). After the incorporation of MIL-100(Fe), the light absorption extends to the visible light range (< 600 nm), indicating the enhanced light absorption of the MIL-100(Fe)/P25 composites. Tauc plots (**Figure 8.2F**) were derived from the UV-vis spectra to calculate the band gaps. As displayed in **Figure 8.2F**, the band gaps of P25 and M/P-10 were determined to be 3.34 eV and 3.03 eV, respectively. Evidently, the incorporation

of MIL-100(Fe) narrows down the band gap, which would boost the light utilization during the photocatalytic processes. The Brunauer–Emmett–Teller (BET) surface areas were determined from the N_2 sorption isotherms (**Figure 8.2G**). More specifically, the surface area of pristine P25 was determined to be 53 m^2/g. While, for M/P-10, the surface area was improved to 307 m^2/g due to the incorporation of high-quality MIL-100(Fe) crystals (1189 m^2/g).

Photocatalytic Performance. The photocatalytic abilities of the MIL-100(Fe)/P25 composites were evaluated through both photooxidation and photoreduction experiments as detailed below. The oxidation ability of the samples was analyzed by tetracycline degradation. As shown in **Figure 8.3A**, both pristine P25 and MIL-100(Fe)/P25 composites exhibited weak adsorption abilities towards tetracycline, as the minimal decrease was observed in the concentration of tetracycline after 30-min mixing in the dark. As expected, the MIL-100(Fe)/P25 composites show better performance than the pristine P25 in the photodegradation of tetracycline. Specifically, only 30.5% of tetracycline was degraded by pristine P25 after 60-min light irradiation. While, the degradation efficiency was enhanced to 83.0%, 85.8%, 83.8% and 74.5% by M/P-5, -10, -20 and -40, respectively. Notably, the amount of MIL-100(Fe) in the composite system plays an important role in the photodegradation efficiency. Initially, the photodegradation efficiency was promoted with an increasing amount of MIL-100(Fe). The optimal composite was found to be M/P-10, which possesses the highest efficiency towards tetracycline photodegradation (85.8 %), ~ 2.8 times that of P25. Whereas, a further increased MIL-100(Fe) amount is detrimental to the photocatalytic efficiency, because the excessive MIL-100(Fe) would block P25, limiting the light absorption and

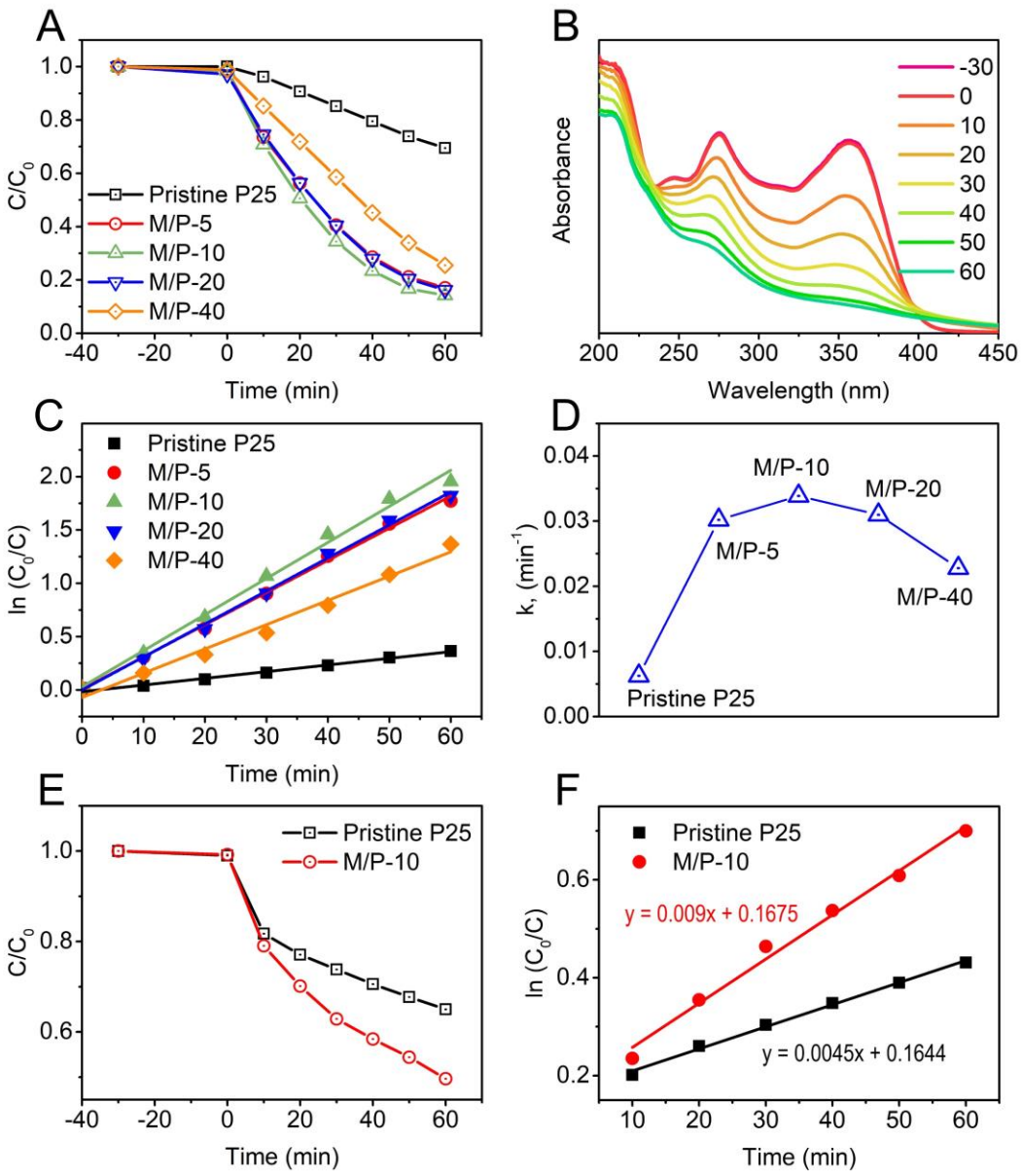

Figure 8.3 (A) Photocatalytic degradation of tetracycline by pristine P25 and as-prepared MIL-100(Fe)/P25 composites; (B) UV-Vis spectra of tetracycline degraded by M/P-10 (time unit: min); The pseudo-first-order kinetic plots (C) and corresponding reaction rate constants (D) of tetracycline degradation over various photocatalysts; (E) Cr(VI) reduction by pristine P25 and M/P-10; (F) The pseudo-first-order kinetic plots for the Cr(VI) reduction.

the accessibility of the active sites of P25. The UV-Vis spectra of tetracycline degraded by M/P-10 are presented in **Figure 8.3B**. It is obvious that the intensity of the characteristic absorbance peak of tetracycline at 357 nm gradually weakens with prolonged light illumination.

As exhibited in **Figure 8.3C**, tetracycline degradation follows pseudo-first-order kinetics:

$$\ln\left(\frac{C_0}{C}\right) = kt \tag{8.1}$$

where C_0 and C are the concentrations of tetracycline at 0 min and a given time (t), respectively; k is the apparent first-order rate constant (min^{-1}). The values of k are displayed in **Figure 8.3D**, where the largest rate constant for degradation of tetracycline obtained by M/P-10 was calculated to be 0.0339 min^{-1}, which is 5.38 times that by the pristine P25 (0.0063 min^{-1}).

In addition, the incorporation of MIL-100(Fe) with TiO_2 also facilitates photocatalytic reduction ability of the composite, as demonstrated by Cr(VI) reduction. As shown in **Figure 8.3E**, with MIL-100(Fe), the percentage of reduced Cr(VI) was improved from 35% to 50%. The photocatalytic reduction of Cr(VI) also fits the pseudo-first-order kinetic (**Figure 8.3F**), and the reaction rate constant obtained by M/P-10 (i.e., 0.009) was found to be twice of that by pristine P25 (i.e., 0.0045).

Mechanism Exploration. The pathways of the photocatalytic degradation of tetracycline and reduction of Cr(VI) have been discussed in prior literatures.[39, 294-296] In brief, there are several steps involved in the photocatalytic process, including molecule adsorption, light absorption, charge separation and transfer, and subsequent redox reactions. In the case of photodegradation of

tetracycline, the photo-generated electrons would be consumed by H_2O_2 and dissolved O_2 to generate ·OH and $O_2^{\cdot-}$, respectively. Meanwhile, holes would react with water to produce ·OH. All these oxidative species (i.e., h^+, ·OH and $O_2^{\cdot-}$) would degrade the tetracycline to fulvic acids- or humic acids-like substances, which would be ultimately mineralized into CO_2 and H_2O.[39] On the other hand, the Cr(VI) was primarily reduced to Cr(III) by the photo-induced electrons,[295] while holes were consumed by the hole scavenger (i.e., methanol). The dominating steps in the above photocatalytic processes are molecule adsorption and charge separation.[255]

Typically, the incorporated MOF would act as a co-catalyst and improve the photocatalytic performance mainly by enhancing molecule adsorption and increasing charge carrier density.[32, 270] As demonstrated in prior studies, MIL-100(Fe) crystals possess high abilities towards the adsorption of tetracycline and Cr(VI) due to the favorable pore geometry and high porosity.[297-299] In this study, the surface-coated MIL-100(Fe), however, does not improve the adsorption of either tetracycline or Cr(VI) (**Figures 8.3A and E**), which suggests that only small amount of MIL-100(Fe) was incorporated in the composite system. To quantify the composition ratios of the MIL-100(Fe)/P25 composite, Rietveld refinement was performed by using the Materials Analysis Using Diffraction (MAUD) program. The results show that the weight fractions of MIL-100(Fe), anatase and rutile in the M/P-10 are 2.8 wt%, 77.8 wt%, and 19.4 wt%, respectively. Given such a low weight fraction of MIL-100(Fe) in the composite of M/P-10, it is reasonable that the incorporation of MIL-100(Fe) exhibited minimal improvement in the adsorption of tetracycline or Cr(VI).

Based on the above discussion, the enhanced photocatalysis efficiency in the current study is mainly ascribed to the increased amount of charge carriers, which can be monitored with the aid of ultrafast transient absorption (TA) spectroscopy analysis. The TA spectra of P25 and M/P-10 composite with a delay time of 2 ps are shown in **Figure 8.4A**. With the pump pulse (350 nm), P25 produces negative TA signals in the spectral region of 450-750 nm due to the stimulated emission (SE) (**Figure 8.4C**), in accordance with the previously reported TA spectra[33, 300] and the photoluminescence spectra obtained from the bare TiO_2.[301] It should be noted that, ground-state bleach (GSB) process also contributes to the negative TA signals, which is not the case here as GSB occurs in a much bluer region.[300] A similar TA spectrum is observed for M/P-10 but with a less negative signal (**Figure 8.4A**), indicating less stimulated emission, that is, fewer electrons are coming back from excited states to ground states, or in other words, less recombination of the charge carriers. The recovery of the TA signals at 465 nm (i.e., stimulated emission) for both P25 and M/P-10 shows multiexponential decay, and M/P-10 shows a faster recovery than bare P25 (**Figure 8.4B**). The TA kinetics were further analyzed by using the global analysis,[302] expressed as follows:

$$\Delta A = \sum_{i=1}^{n} \alpha_i(\lambda) \exp(-\frac{t}{\tau_i}) \quad (8.2)$$

where $\alpha_i(\lambda)$ is the pre-exponential factor at a specific wavelength and τ_i is the corresponding lifetime. Both of $\alpha_i(\lambda)$ and τ_i are dependent on probe wavelength (λ). According to the global analysis, the excited states of both P25 and M/P-10 decayed bi-exponentially. For M/P-10, the lifetimes of the stimulated emission were determined to be 119 fs and 5.63 ps, faster

than those (176 fs and 22.90 ps) of the bare P25. As mentioned earlier, the stimulated emission mainly originates from the recombination of the charge carriers. Therefore, the short lifetime of the stimulated emission indicates less recombination of charge carriers in the case of M/P-10. The enhanced separation of the charge carriers might be owing to the generation of defect energy levels in the TiO_2 band structure after the synthesis of MIL-100(Fe). The defect energy levels would serve as trappers of charge carriers, which would prevent them from recombination, and eventually increase the charge carrier density and lead to promoted photocatalytic efficiency.

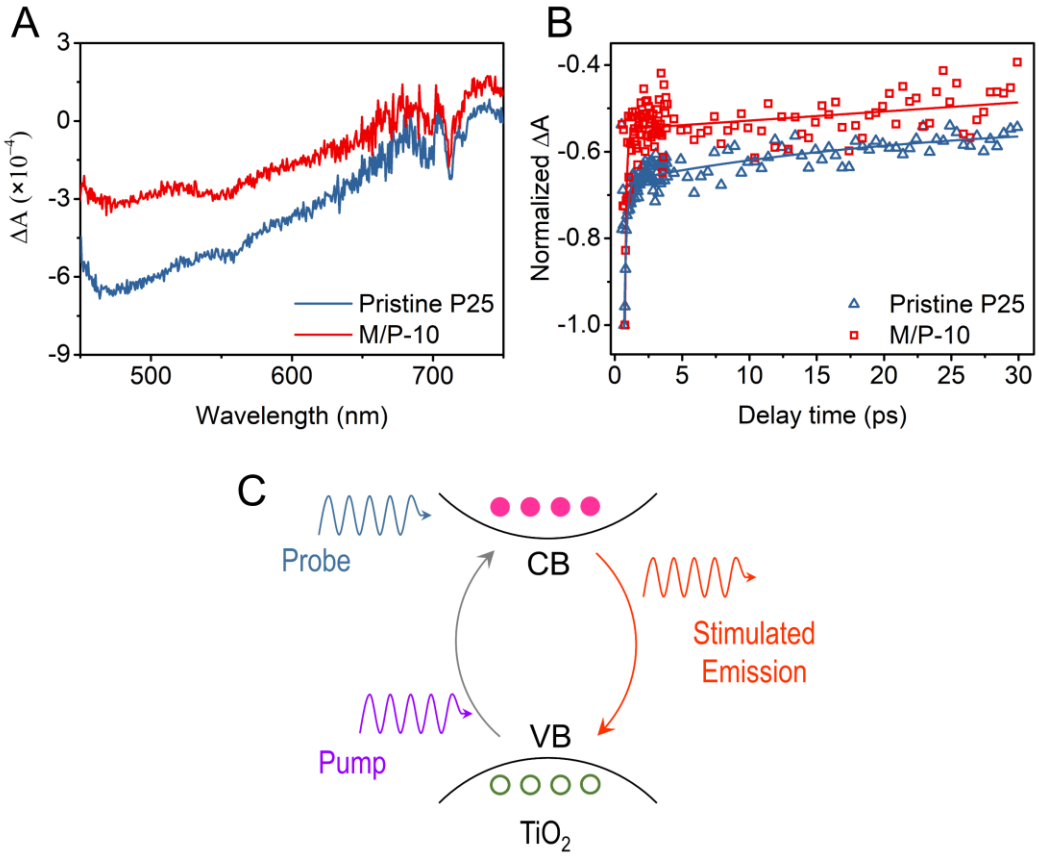

Figure 8.4 (A) Transient absorption spectra recorded 2 ps after the excitation pulse; (B) Normalized transient absorption kinetics probed at 465 nm; (C) Schematic illustration depicting the charge transfer during TAS measurements.

The formation of the defect energy levels is attributable to the distinct interface structure of MIL-100(Fe)/P25 composite, which was analyzed by XPS measurements. As displayed in **Figure 8.5A**, the XPS survey spectrum reveals that M/P-10 composite contains Fe, Ti, O and C elements. The high-resolution spectrum of O 1s (**Figure 8.5B**) consists of three component peaks at 531.4 eV, 530.4 eV, and 528.8 eV. The Fe 2p spectrum of M/P-10 is shown in **Figure 8.5C**, where two dominant peaks were found at 724.3 eV and 709.8 eV, assigned to Fe 2p1/2 and Fe 2p3/2, respectively. The satellite peak at 713.8 eV (**Figure 8.5C**) corresponds to Fe^{III} in MIL-100(Fe).[269, 303] Notably, these peaks exhibit negative shifts in comparison with the bare MIL-100(Fe) crystal (**Figure 8.5C**),[303-304] which is attributable to the formation of Fe-O-Ti bonds at the interface. Further evidence of the Fe-O-Ti bonds can be found in the Ti 2p spectrum of M/P-10 (**Figure 8.5D**). Specifically, the peaks centered at 463.6 eV and 458.5 eV are consistent with characteristic states of Ti in bare TiO_2 (**Figure 8.5D**).[305] While the extra peak at 457.6 eV is related to the Ti ions with increased outer electron cloud densities, as a sequence of the presence of Fe-O-Ti bonds.[306] The Fe-O-Ti bonds were likely formed during the growth of MIL-100(Fe) on the surface of TiO_2, where partial Ti atoms were replaced by Fe atoms. This substitution would lead to significant modification of the band structure of TiO_2 as demonstrated through the DFT calculations (**Figure 8.6**).

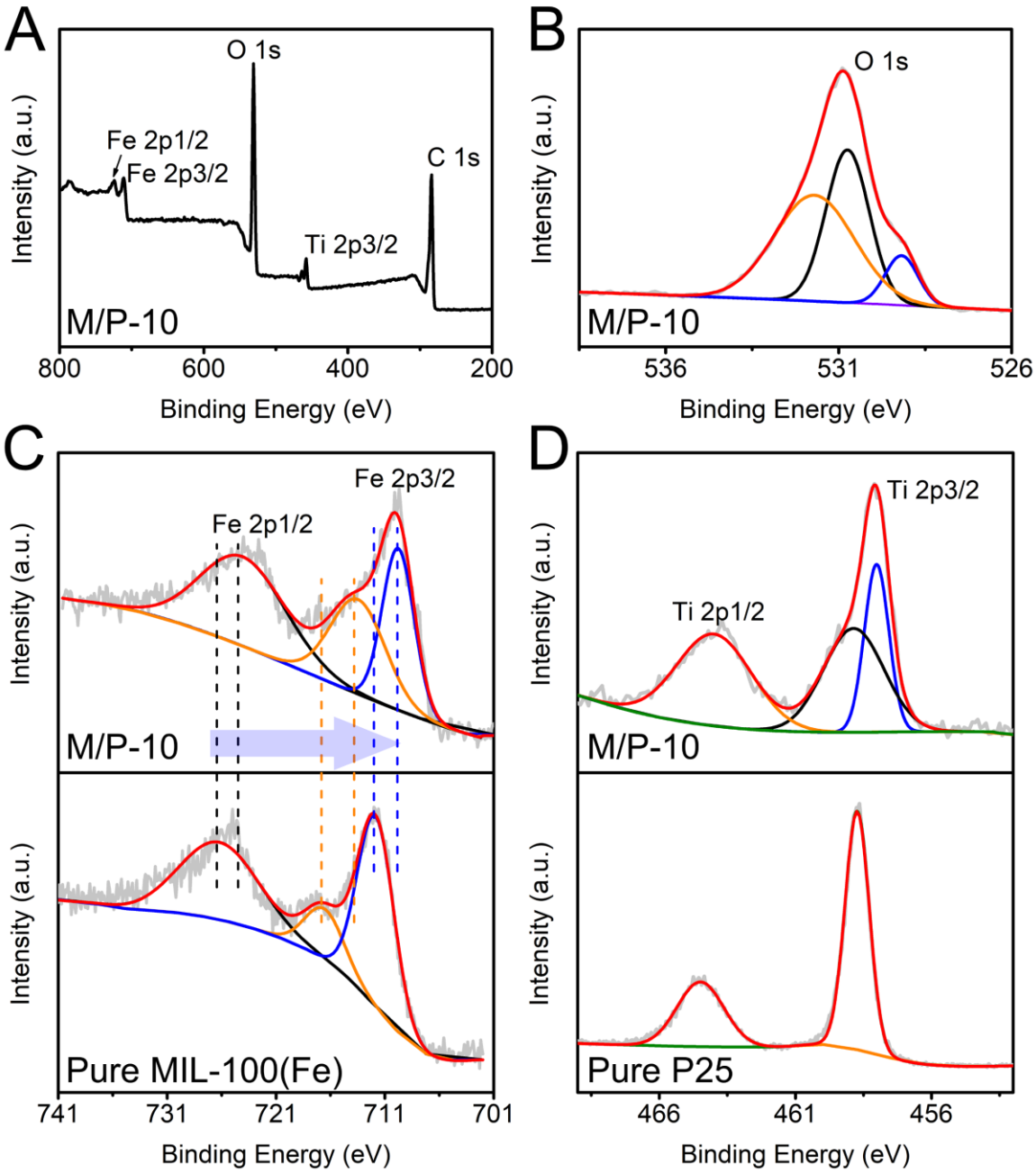

Figure 8.5 XPS spectra: (A) survey scan; high-resolution spectra of (B) O 1s, (C) Fe 2p, and (D) Ti 2p.

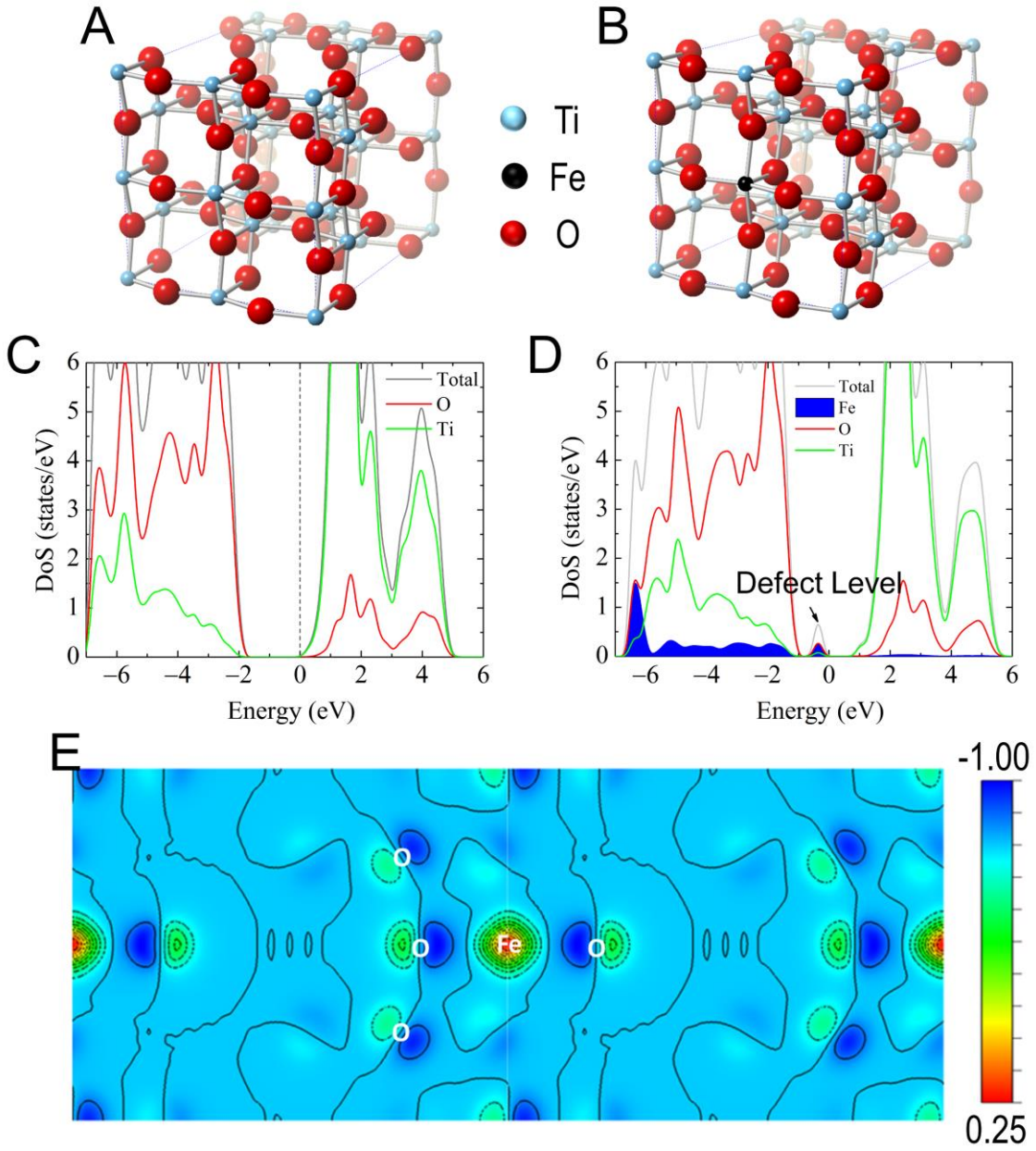

Figure 8.6 Optimized geometries of (A) TiO_2 and (B) TiO_2(Fe), with Ti in blue, Fe in black, O in red; (C) Calculated DoS of the bare TiO_2; (D) Calculated DoS of TiO_2(Fe); (E) Calculated difference charge density (e/Bohr^3) defined as the charge density of TiO_2(Fe) subtracted by the charge density of bare TiO_2. It shows that, around the doped-Fe site, the charge density is much smaller than that of the bare TiO_2, corresponding to the peak of defect levels in DoS (D).

To clarify the underlying changes in electronic properties, the electron-density distributions and electronic density of states (DoS) of bare TiO_2 (**Figure 8.6A**) and Fe doped TiO_2 (denoted TiO_2(Fe) hereafter, Fe:Ti = 1:20, **Figure 8.6B**) were calculated. As shown in **Figures 8.6C** and **D**, the DoS of bare TiO_2 and TiO_2(Fe) are dominated by Ti and O, with the same energy gap (~ 2.0 eV). The calculated energy gap is lower than the experimental energy band gap of TiO_2 (3.0-3.2 eV), which is due to the limitations of DFT calculation (i.e., lack of derivative discontinuity and self-interaction error).[307] Notably, the doping Fe creates defect energy levels, dominated by Fe and O, near the valence band (VB) maximum of TiO_2. Correspondingly, as shown in **Figure 8.6E**, the charge density around the Fe site is much lower than that of the bare TiO_2. Such a difference in charge density was achieved by subtracting the charge density of bare TiO_2 from that of TiO_2(Fe). The defect energy levels would act as trappers of charge carriers to retard the excited electrons from recombining with holes, giving rise to increased amount of charge carriers in the composite system, which agrees well with TA results (**Figure 8.4**). On the other hand, the results are also consistent with those reported in prior studies where varied Fe/Ti ratios were used for DFT calculations,[308-309] which suggest that the DoS of the Fe-doped TiO_2 would not change significantly over a reasonable range of Fe/Ti ratios. However, it should be noted that, with excessive Fe doping, the defect energy levels will work as the recombination centers and thus reduce the photocatalytic efficiency,[310] which partially explains the decreased photocatalytic efficiency with a further increased amount of MIL-100(Fe).

Proposed Mechanism. On the basis of the aforementioned results and discussions, a reasonable mechanism (**Scheme 8.2**) was proposed to explain the enhanced photocatalytic performance achieved by MIL-100(Fe)/TiO_2 composite. The growth of MIL-100(Fe) on the TiO_2 surface caused partial substitution of Ti by Fe, which led to charge deficiency at the substitution region (**Figure 8.6E**). From the perspective of the electronic band structure, the Fe doping would result in defect energy levels (**Figure 8.6D**), which would trap excited electrons and prevent the electrons from recombing with the holes (**Figure 8.4**). Accordingly, the separation of the charge carriers was greatly promoted. It should be noted that, the doped Fe would also facilitate the photocatalytic efficiency through the Fe^{3+}/Fe^{2+} redox cycle. To be specific, the doped Fe^{3+} would be reduced to Fe^{2+} by the photoinduced electron as monitored by using electron spin resonance (ESR) spectroscopy in prior studies.[311-312] Subsequently, the Fe^{2+} could not only improve the photooxidation process by providing more reactive oxygen species (**Eq. 8.3**) but also serve as a reductant to convert Cr(VI) to less toxic Cr(III) (**Eq. 8.4**).

$$Fe^{2+} + H_2O_2 \rightarrow Fe^{3+} + \cdot OH + OH^- \quad (8.3)$$

$$6Fe^{2+} + Cr_2O_7^{2-} + 14H^+ \rightarrow 6Fe^{3+} + 2Cr^{3+} + 7H_2O \quad (8.4)$$

Furthermore, the intimate interaction between MIL-100(Fe) and TiO_2 also improves the charge separation (**Scheme 8.2**). Specifically, the incorporation of MIL-100(Fe) expanded the light absorption to the visible region (**Figure 8.2E**). Upon visible light irradiation, the Fe-O clusters in MIL-100(Fe) would be excited, during which the Fe^{3+} in MIL-100(Fe) would be reduced to Fe^{2+} by accepting electrons from O^{2-}.[273] Meanwhile, due to intimate contact of MIL-100(Fe) and TiO_2,

holes in the TiO_2 valence band would migrate through ligand to Fe-O clusters and oxidize Fe^{2+} back to Fe^{3+}, which also contributes to the inhibition of charge recombination in TiO_2.

In brief, the incorporated MIL-100(Fe) could enhance the charge separation of TiO_2 by introducing defect energy levels and providing additional charge transfer pathways, which significantly increases the lifetimes of both electrons and holes. Besides, the doped Fe in TiO_2 structure would also promote the photocatalytic efficiency by offering additional reactions pathways through the Fe^{3+}/Fe^{2+} redox cycle.

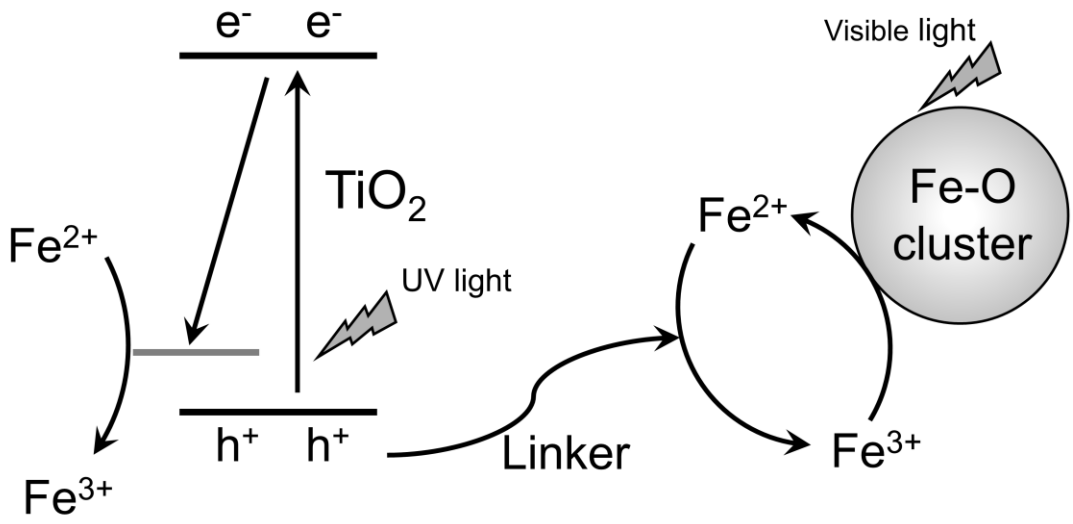

Scheme 8.2 Proposed pathways of the charge transfer inside MIL-100(Fe)/TiO_2 upon light irradiation.

8.4 Conclusions

MIL-100(Fe)/P25 composite photocatalysts were fabricated and demonstrated better photocatalytic oxidation and reduction abilities over pristine P25. As evidenced by the TA measurements, the enhanced photocatalytic performance is attributable to the promoted electron-hole separation due to the incorporation of MIL-100(Fe). In particular, partial Ti atoms were replaced with Fe atoms during the growth of MIL-100(Fe) on the TiO_2 surface, which led to changes in electron-density distribution and created defect energy levels. During the photocatalytic process, the excited electrons would be captured at the defect energy levels, which greatly restrains the recombination of charge carriers and increases the amount of charge carriers, and thus contributes to improved photocatalytic efficiency. Besides, the intimate interaction between MIL-100(Fe) and TiO_2 provided an additional pathway to further improve the charge separation. Besides the promoted charge separation, the doped Fe in the TiO_2 structure also boosted the photocatalytic efficiency through the Fe^{3+}/Fe^{2+} redox cycle. This work offers new insights into the interface structure of MOF/semiconductor and its role in charge transfer, which would contribute to the future design of innovative MOF/semiconductor composite photocatalysts.

Chapter 9. Conclusions and Future Directions

9.1 Conclusions

In this dissertation, the aerosol route was applied as the facile approach for the rapid synthesis of MOFs and MOF-based composites. Systematic analyses were carried out to unravel the formation mechanisms of MOFs in microdroplets. Further exploration of the aerosol route to tune the properties of MOFs during the synthesis process was also conducted. In addition, several MOF-based composites (i.e., HKUST-1/TiO_2, HKUST/TiO_2/Cu_2O, ZIF-8/ZnO, and MIL-100(Fe)/TiO_2) were designed as the efficient photocatalysts for energy and environmental sustainability (e.g., CO_2 photoreduction, degradation of antibiotics, and removal of heavy metal ions). Huge efforts were put into the fundamental understanding of MOFs' roles during the photocatalytic processes. The detailed conclusions from this dissertation were listed as below.

9.1.1 Mechanism for the Rapid Formation of MOFs via the Aerosol Route

As demonstrated in this dissertation, the aerosol route is a facile approach for the rapid formation of MOF crystals. The as-synthesized MOFs have comparable properties (i.e., crystallinity, porosity, and surface area) as compared with those synthesized with the conventional methods. The major impetus for the rapid formation of MOFs is attributable to the fast heat and mass transfer during the evaporation of microdroplets. In particular, the evaporation of microdroplets would induce the drastic decrease of the droplet size and subsequently increase the supersaturation ratio of MOF precursors, which finally leads to rapid nucleation and crystal growth of MOFs. Additionally, the aerosol route was also proved to be an excellent strategy for the synthesis of MOF-based composites by simply adding pre-formed nanoparticles into the MOF

precursors. As shown by the experimental results, the presence of those nanoparticles would not alter the properties of MOFs but offer additional benefits to the composite systems.

9.1.2 Regulated Synthesis of MOFs Enabled by the Aerosol Route

The synthesis of MOFs is eligible for regulation by simply adjust the operating parameters of the aerosol route, including temperature, pressure, and precursor conditions. In particular, a higher temperature would promote the evaporation of microdroplets, which would subsequently accelerate the nucleation process and creating smaller MOF crystals. Meanwhile, adjusting synthetic temperatures would also give rise to different hydration degrees of the MOF products, which corresponds to variations in the availability of coordinatively unsaturated metal sites for gas adsorption. However, the synthetic temperatures should be controlled under certain values in case of destroying the MOF structures. In terms of this, the operating pressures were demonstrated to be milder parameters to regulate the properties of MOFs. By lowering the operating pressures, the evaporation rate of the microdroplets would be enhanced, which results in higher supersaturation ratios and faster nucleation, thus leading to smaller MOF crystals. In addition to the sizes of MOF products, the operating pressure also plays a critical role in other properties, including surface area, crystalline structure, and gas adsorption abilities. Moreover, the precursor conditions can also be adjusted for the desired properties of MOFs. For example, mixed linkers can be used as the precursors with various linker ratios, which would lead to a series of products with different properties.

9.1.3 Rational Design of MOF-based Composites

The integration of MOFs and semiconductors as efficient composite photocatalysts was successfully demonstrated and illustrated in this dissertation. In addition to the aerosol route, several other techniques were also used for the facile fabrication of MOF-based composites, such as electrospinning and aerosol chemical vapor deposition. A variety of structures were presented here, including particles, nanofibers, and 2D nanoarrays.

9.1.4 Mechanistic Insights into the Photocatalytic Pathways of MOF-based Composites

Despite the poor photocatalytic ability of bare MOFs, they were demonstrated here as exceptional co-catalysts to significantly improve the efficiency of conventional semiconductor photocatalysts for energy and environmental sustainability. With systematic analyses, it was found that the incorporated MOFs mainly contributed to the enhanced adsorption, promoted molecule activation, and improved charge transfer. Particularly, the special interface structure between MOF and the semiconductor is critical for the charge separation. Taking MIL-100(Fe)/TiO_2 for an example, partial Ti atoms were replaced by Fe atoms during the *in situ* growth of MIL-100(Fe) on the surface of TiO_2. As demonstrated by the DFT calculations, the incorporated Fe atoms would create defect energy levels in the photocatalytic system, which would significantly enhance the separation of charge carriers, and thus lead to high photocatalytic efficiency.

9.2 Future Directions

Additional work is still needed in the future regarding the following aspects:

(1) Despite the successful cases presented in this dissertation, additional efforts are still needed to verify the wider applicability of the aerosol route for the synthesis of other MOFs, especially those with high-nuclearity secondary building units.

(2) In addition to the physical insights into the MOF formation via microdroplets, the chemical conversion processes from precursors to final MOF products are still vague, studies of which are necessary for better understanding of the formation mechanism.

(3) As brought out by many prior papers, the stability of MOFs during the photocatalytic processes is always a concern. Further research on the responses of MOFs to the harsh environment (e.g., high temperature, extreme pH, and aqueous environment) is of great importance.

(4) Although the examples presented here showed significantly improved efficiency for photocatalytic applications, the efficiency is still low for real-world applications. Therefore, more efficient MOF-based composites should be designed with the aid of the fundamental understanding obtained in this dissertation.

References

(1) Stassen, I.; Burtch, N.; Talin, A.; Falcaro, P.; Allendorf, M.; Ameloot, R. An updated roadmap for the integration of metal–organic frameworks with electronic devices and chemical sensors. *Chem. Soc. Rev.* **2017,** *46*, 3185-3241.

(2) Moghadam, P. Z.; Li, A.; Wiggin, S. B.; Tao, A.; Maloney, A. G. P.; Wood, P. A.; Ward, S. C.; Fairen-Jimenez, D. Development of a Cambridge Structural Database Subset: A Collection of Metal–Organic Frameworks for Past, Present, and Future. *Chem. Mater.* **2017,** *29*, 2618-2625.

(3) Allendorf, M. D.; Stavila, V. Crystal engineering, structure–function relationships, and the future of metal–organic frameworks. *CrystEngComm* **2015,** *17*, 229-246.

(4) Stock, N.; Biswas, S. Synthesis of Metal-Organic Frameworks (MOFs): Routes to Various MOF Topologies, Morphologies, and Composites. *Chem. Rev.* **2012,** *112*, 933-969.

(5) Li, J.-R.; Kuppler, R. J.; Zhou, H.-C. Selective gas adsorption and separation in metal–organic frameworks. *Chem. Soc. Rev.* **2009,** *38*, 1477-1504.

(6) Grant Glover, T.; Peterson, G. W.; Schindler, B. J.; Britt, D.; Yaghi, O. MOF-74 building unit has a direct impact on toxic gas adsorption. *Chem. Eng. Sci.* **2011,** *66*, 163-170.

(7) Tan, Y.-X.; He, Y.-P.; Zhang, J. Temperature-/Pressure-Dependent Selective Separation of CO2 or Benzene in a Chiral Metal–Organic Framework Material. *ChemSusChem* **2012,** *5*, 1597-1601.

(8) Huang, Y.-L.; Gong, Y.-N.; Jiang, L.; Lu, T.-B. A unique magnesium-based 3D MOF with nanoscale cages and temperature dependent selective gas sorption properties. *Chem. Commun.* **2013,** *49*, 1753-1755.

(9) Mon, M.; Bruno, R.; Ferrando-Soria, J.; Armentano, D.; Pardo, E. Metal–organic framework technologies for water remediation: towards a sustainable ecosystem. *J. Mater. Chem. A* **2018,** *6*, 4912-4947.

(10) Dias, E. M.; Petit, C. Towards the use of metal-organic frameworks for water reuse: a review of the recent advances in the field of organic pollutants removal and degradation and the next steps in the field. *J. Mater. Chem. A* **2015,** *3*, 22484-22506.

(11) Liu, X.; Zhou, Y.; Zhang, J.; Tang, L.; Luo, L.; Zeng, G. Iron Containing Metal–Organic Frameworks: Structure, Synthesis, and Applications in Environmental Remediation. *ACS Appl. Mater. Interfaces* **2017,** *9*, 20255-20275.

(12) Hasan, Z.; Jhung, S. H. Removal of hazardous organics from water using metal-organic frameworks (MOFs): Plausible mechanisms for selective adsorptions. *J. Hazard. Mater.* **2015,** *283*, 329-339.

(13) Jin, W.-G.; Chen, W.; Xu, P.-H.; Lin, X.-W.; Huang, X.-C.; Chen, G.-H.; Lu, F.; Chen, X.-M. An Exceptionally Water Stable Metal–Organic Framework with Amide-Functionalized Cages: Selective CO2/CH4 Uptake and Removal of Antibiotics and Dyes from Water. *Chem. - Eur. J.* **2017,** *23*, 13058-13066.

(14) Wang, B.; Lv, X.-L.; Feng, D.; Xie, L.-H.; Zhang, J.; Li, M.; Xie, Y.; Li, J.-R.; Zhou, H.-C. Highly Stable Zr(IV)-Based Metal–Organic Frameworks for the Detection and Removal of Antibiotics and Organic Explosives in Water. *J. Am. Chem. Soc.* **2016,** *138*, 6204-6216.

(15) Wu, Z.; Yuan, X.; Zhang, J.; Wang, H.; Jiang, L.; Zeng, G. Photocatalytic Decontamination of Wastewater Containing Organic Dyes by Metal–Organic Frameworks and their Derivatives. *ChemCatChem* **2017,** *9*, 41-64.
(16) Zhang, T.; Lin, W. Metal-organic frameworks for artificial photosynthesis and photocatalysis. *Chem. Soc. Rev.* **2014,** *43*, 5982-5993.
(17) Gao, J.; Miao, J.; Li, P.-Z.; Teng, W. Y.; Yang, L.; Zhao, Y.; Liu, B.; Zhang, Q. A p-type Ti(iv)-based metal–organic framework with visible-light photo-response. *Chem. Commun.* **2014,** *50*, 3786-3788.
(18) Zhao, Y.; Song, Z.; Li, X.; Sun, Q.; Cheng, N.; Lawes, S.; Sun, X. Metal organic frameworks for energy storage and conversion. *Energy Storage Materials* **2016,** *2*, 35-62.
(19) Falcaro, P.; Ricco, R.; Yazdi, A.; Imaz, I.; Furukawa, S.; Maspoch, D.; Ameloot, R.; Evans, J. D.; Doonan, C. J. Application of metal and metal oxide nanoparticles@MOFs. *Coord. Chem. Rev.* **2016,** *307, Part 2*, 237-254.
(20) Zhu, Q.-L.; Xu, Q. Metal-organic framework composites. *Chem. Soc. Rev.* **2014,** *43*, 5468-5512.
(21) Yamauchi, M.; Kobayashi, H.; Kitagawa, H. Hydrogen Storage Mediated by Pd and Pt Nanoparticles. *ChemPhysChem* **2009,** *10*, 2566-2576.
(22) Zlotea, C.; Campesi, R.; Cuevas, F.; Leroy, E.; Dibandjo, P.; Volkringer, C.; Loiseau, T.; Férey, G.; Latroche, M. Pd Nanoparticles Embedded into a Metal-Organic Framework: Synthesis, Structural Characteristics, and Hydrogen Sorption Properties. *J. Am. Chem. Soc.* **2010,** *132*, 2991-2997.
(23) Lim, D.-W.; Yoon, J. W.; Ryu, K. Y.; Suh, M. P. Magnesium Nanocrystals Embedded in a Metal–Organic Framework: Hybrid Hydrogen Storage with Synergistic Effect on Physi- and Chemisorption. *Angew. Chem. Int. Ed.* **2012,** *51*, 9814-9817.
(24) Aijaz, A.; Karkamkar, A.; Choi, Y. J.; Tsumori, N.; Rönnebro, E.; Autrey, T.; Shioyama, H.; Xu, Q. Immobilizing Highly Catalytically Active Pt Nanoparticles inside the Pores of Metal–Organic Framework: A Double Solvents Approach. *J. Am. Chem. Soc.* **2012,** *134*, 13926-13929.
(25) Leus, K.; Concepcion, P.; Vandichel, M.; Meledina, M.; Grirrane, A.; Esquivel, D.; Turner, S.; Poelman, D.; Waroquier, M.; Van Speybroeck, V.; Van Tendeloo, G.; García, H.; Van Der Voort, P. Au@UiO-66: a base free oxidation catalyst. *RSC Adv.* **2015,** *5*, 22334-22342.
(26) Xu, Z.; Yang, L.; Xu, C. Pt@UiO-66 Heterostructures for Highly Selective Detection of Hydrogen Peroxide with an Extended Linear Range. *Anal. Chem.* **2015,** *87*, 3438-3444.
(27) He, L.; Liu, Y.; Liu, J.; Xiong, Y.; Zheng, J.; Liu, Y.; Tang, Z. Core–Shell Noble-Metal@Metal-Organic-Framework Nanoparticles with Highly Selective Sensing Property. *Angew. Chem. Int. Ed.* **2013,** *52*, 3741-3745.
(28) Walton, K. S.; Millward, A. R.; Dubbeldam, D.; Frost, H.; Low, J. J.; Yaghi, O. M.; Snurr, R. Q. Understanding Inflections and Steps in Carbon Dioxide Adsorption Isotherms in Metal-Organic Frameworks. *J. Am. Chem. Soc.* **2008,** *130*, 406-407.
(29) Wang, W.; Li, Y.; Zhang, R.; He, D.; Liu, H.; Liao, S. Metal-organic framework as a host for synthesis of nanoscale Co3O4 as an active catalyst for CO oxidation. *Catal. Commun.* **2011,** *12*, 875-879.

(30) Zeng, T.; Zhang, X.; Wang, S.; Niu, H.; Cai, Y. Spatial Confinement of a Co3O4 Catalyst in Hollow Metal–Organic Frameworks as a Nanoreactor for Improved Degradation of Organic Pollutants. *Environmental Science & Technology* **2015,** *49*, 2350-2357.
(31) Wang, H.; Yu, T.; Tan, X.; Zhang, H.; Li, P.; Liu, H.; Shi, L.; Li, X.; Ye, J. Enhanced Photocatalytic Oxidation of Isopropanol by HKUST-1@TiO2 Core–Shell Structure with Ultrathin Anatase Porous Shell: Toxic Intermediate Control. *Industrial & Engineering Chemistry Research* **2016,** *55*, 8096-8103.
(32) Zeng, X.; Huang, L.; Wang, C.; Wang, J.; Li, J.; Luo, X. Sonocrystallization of ZIF-8 on Electrostatic Spinning TiO2 Nanofibers Surface with Enhanced Photocatalysis Property through Synergistic Effect. *ACS Appl. Mater. Interfaces* **2016,** *8*, 20274-20282.
(33) Li, R.; Hu, J.; Deng, M.; Wang, H.; Wang, X.; Hu, Y.; Jiang, H.-L.; Jiang, J.; Zhang, Q.; Xie, Y.; Xiong, Y. Integration of an Inorganic Semiconductor with a Metal–Organic Framework: A Platform for Enhanced Gaseous Photocatalytic Reactions. *Adv. Mater.* **2014,** *26*, 4783-4788.
(34) Hong, J.; Chen, C.; Bedoya, F. E.; Kelsall, G. H.; O'Hare, D.; Petit, C. Carbon nitride nanosheet/metal-organic framework nanocomposites with synergistic photocatalytic activities. *Catal. Sci. Technol.* **2016,** *6*, 5042-5051.
(35) Zhao, H.; Wang, X.; Feng, J.; Chen, Y.; Yang, X.; Gao, S.; Cao, R. Synthesis and characterization of Zn2GeO4/Mg-MOF-74 composites with enhanced photocatalytic activity for CO2 reduction. *Catal. Sci. Technol.* **2018,** *8*, 1288-1295.
(36) Liu, Q.; Low, Z.-X.; Li, L.; Razmjou, A.; Wang, K.; Yao, J.; Wang, H. ZIF-8/Zn2GeO4 nanorods with an enhanced CO2 adsorption property in an aqueous medium for photocatalytic synthesis of liquid fuel. *J. Mater. Chem. A* **2013,** *1*, 11563-11569.
(37) Su, Y.; Zhang, Z.; Liu, H.; Wang, Y. Cd0.2Zn0.8S@UiO-66-NH2 nanocomposites as efficient and stable visible-light-driven photocatalyst for H2 evolution and CO2 reduction. *Appl. Catal., B* **2017,** *200*, 448-457.
(38) Liu, Q.; Zhou, B.; Xu, M.; Mao, G. Integration of nanosized ZIF-8 particles onto mesoporous TiO2 nanobeads for enhanced photocatalytic activity. *RSC Adv.* **2017,** *7*, 8004-8010.
(39) Wang, H.; Yuan, X.; Wu, Y.; Zeng, G.; Dong, H.; Chen, X.; Leng, L.; Wu, Z.; Peng, L. In situ synthesis of In2S3@MIL-125(Ti) core–shell microparticle for the removal of tetracycline from wastewater by integrated adsorption and visible-light-driven photocatalysis. *Appl. Catal., B* **2016,** *186*, 19-29.
(40) Yan, S.; Ouyang, S.; Xu, H.; Zhao, M.; Zhang, X.; Ye, J. Co-ZIF-9/TiO2 nanostructure for superior CO2 photoreduction activity. *J. Mater. Chem. A* **2016,** *4*, 15126-15133.
(41) Lee, Y.-R.; Kim, J.; Ahn, W.-S. Synthesis of metal-organic frameworks: A mini review. *Korean J. Chem. Eng.* **2013,** *30*, 1667-1680.
(42) Surblé, S.; Millange, F.; Serre, C.; Férey, G.; Walton, R. I. An EXAFS study of the formation of a nanoporous metal–organic framework: evidence for the retention of secondary building units during synthesis. *Chem. Commun.* **2006**, 1518-1520.
(43) Saha, S.; Springer, S.; Schweinefuß, M. E.; Pontoni, D.; Wiebcke, M.; Huber, K. Insight into Fast Nucleation and Growth of Zeolitic Imidazolate Framework-71 by In Situ Time-Resolved Light and X-ray Scattering Experiments. *Cryst. Growth Des.* **2016,** *16*, 2002-2010.

(44) Rubio-Martinez, M.; Avci-Camur, C.; Thornton, A. W.; Imaz, I.; Maspoch, D.; Hill, M. R. New synthetic routes towards MOF production at scale. *Chem. Soc. Rev.* **2017,** *46*, 3453-3480.
(45) Jhung, S. H.; Lee, J. H.; Chang, J. S. Microwave synthesis of a nanoporous hybrid material, chromium trimesate. *Bull. Korean Chem. Soc.* **2005,** *26*, 880-881.
(46) Yuan, S.; Feng, L.; Wang, K.; Pang, J.; Bosch, M.; Lollar, C.; Sun, Y.; Qin, J.; Yang, X.; Zhang, P.; Wang, Q.; Zou, L.; Zhang, Y.; Zhang, L.; Fang, Y.; Li, J.; Zhou, H. C. Stable Metal-Organic Frameworks: Design, Synthesis, and Applications. *Adv. Mater.* **2018,** *30*, 1704303.
(47) Wang, S.; Wang, X. Multifunctional Metal–Organic Frameworks for Photocatalysis. *Small* **2015,** *11*, 3097-3112.
(48) Bunck, D. N.; Dichtel, W. R. Mixed Linker Strategies for Organic Framework Functionalization. *Chem. - Eur. J.* **2013,** *19*, 818-827.
(49) Dhakshinamoorthy, A.; Asiri, A. M.; Garcia, H. Mixed-metal or mixed-linker metal organic frameworks as heterogeneous catalysts. *Catal. Sci. Technol.* **2016,** *6*, 5238-5261.
(50) Tanasaro, T.; Adpakpang, K.; Ittisanronnachai, S.; Faungnawakij, K.; Butburee, T.; Wannapaiboon, S.; Ogawa, M.; Bureekaew, S. Control of Polymorphism of Metal–Organic Frameworks Using Mixed-Metal Approach. *Cryst. Growth Des.* **2018,** *18*, 16-21.
(51) Zhai, Z.-W.; Yang, S.-H.; Cao, M.; Li, L.-K.; Du, C.-X.; Zang, S.-Q. Rational Design of Three Two-Fold Interpenetrated Metal–Organic Frameworks: Luminescent Zn/Cd-Metal–Organic Frameworks for Detection of 2,4,6-Trinitrophenol and Nitrofurazone in the Aqueous Phase. *Cryst. Growth Des.* **2018,** *18*, 7173-7182.
(52) Rachuri, Y.; Parmar, B.; Suresh, E. Three-Dimensional Co(II)/Cd(II) Metal–Organic Frameworks: Luminescent Cd-MOF for Detection and Adsorption of 2,4,6-Trinitrophenol in the Aqueous Phase. *Cryst. Growth Des.* **2018,** *18*, 3062-3072.
(53) Lee, S. J.; Doussot, C.; Baux, A.; Liu, L.; Jameson, G. B.; Richardson, C.; Pak, J. J.; Trousselet, F.; Coudert, F.-X.; Telfer, S. G. Multicomponent Metal–Organic Frameworks as Defect-Tolerant Materials. *Chem. Mater.* **2016,** *28*, 368-375.
(54) Koh, K.; Wong-Foy, A. G.; Matzger, A. J. MOF@MOF: microporous core-shell architectures. *Chem. Commun.* **2009**, 6162-6164.
(55) Rashidi, F.; Blad, C. R.; Jones, C. W.; Nair, S. Synthesis, characterization, and tunable adsorption and diffusion properties of hybrid ZIF-7-90 frameworks. *AlChE J.* **2016,** *62*, 525-537.
(56) Burrows, A. D. Mixed-component metal-organic frameworks (MC-MOFs): enhancing functionality through solid solution formation and surface modifications. *Crystengcomm* **2011,** *13*, 3623-3642.
(57) Guo, W.; Xia, W.; Cai, K.; Wu, Y.; Qiu, B.; Liang, Z.; Qu, C.; Zou, R. Kinetic-Controlled Formation of Bimetallic Metal–Organic Framework Hybrid Structures. *Small* **2017,** *13*, 1702049.
(58) Wu, T.; Bu, X.; Zhang, J.; Feng, P. New Zeolitic Imidazolate Frameworks: From Unprecedented Assembly of Cubic Clusters to Ordered Cooperative Organization of Complementary Ligands. *Chem. Mater.* **2008,** *20*, 7377-7382.
(59) Thompson, J. A.; Blad, C. R.; Brunelli, N. A.; Lydon, M. E.; Lively, R. P.; Jones, C. W.; Nair, S. Hybrid Zeolitic Imidazolate Frameworks: Controlling Framework Porosity and Functionality by Mixed-Linker Synthesis. *Chem. Mater.* **2012,** *24*, 1930-1936.

(60) Thompson, J. A.; Brunelli, N. A.; Lively, R. P.; Johnson, J. R.; Jones, C. W.; Nair, S. Tunable CO2 Adsorbents by Mixed-Linker Synthesis and Postsynthetic Modification of Zeolitic Imidazolate Frameworks. *J. Phys. Chem. C* **2013,** *117*, 8198-8207.
(61) Eum, K.; Jayachandrababu, K. C.; Rashidi, F.; Zhang, K.; Leisen, J.; Graham, S.; Lively, R. P.; Chance, R. R.; Sholl, D. S.; Jones, C. W.; Nair, S. Highly Tunable Molecular Sieving and Adsorption Properties of Mixed-Linker Zeolitic Imidazolate Frameworks. *J. Am. Chem. Soc.* **2015,** *137*, 4191-4197.
(62) Deng, H.; Doonan, C. J.; Furukawa, H.; Ferreira, R. B.; Towne, J.; Knobler, C. B.; Wang, B.; Yaghi, O. M. Multiple Functional Groups of Varying Ratios in Metal-Organic Frameworks. *Science* **2010,** *327*, 846-850.
(63) Serre, C.; Millange, F.; Thouvenot, C.; Gardant, N.; Pellé, F.; Férey, G. Synthesis, characterisation and luminescent properties of a new three-dimensional lanthanide trimesate: M((C6H3)–(CO2)3) (M = Y, Ln) or MIL-78. *J. Mater. Chem.* **2004,** *14*, 1540-1543.
(64) He, X.; Gan, Z.; Fisenko, S.; Wang, D.; El-Kaderi, H. M.; Wang, W.-N. Rapid Formation of Metal–Organic Frameworks (MOFs) Based Nanocomposites in Microdroplets and Their Applications for CO2 Photoreduction. *Acs Appl Mater Inter* **2017,** *9*, 9688-9698.
(65) Wang, Z.; Ananias, D.; Carné-Sánchez, A.; Brites, C. D. S.; Imaz, I.; Maspoch, D.; Rocha, J.; Carlos, L. D. Lanthanide–Organic Framework Nanothermometers Prepared by Spray-Drying. *Adv. Funct. Mater.* **2015,** *25*, 2824-2830.
(66) Carné-Sánchez, A.; Imaz, I.; Cano-Sarabia, M.; Maspoch, D. A spray-drying strategy for synthesis of nanoscale metal–organic frameworks and their assembly into hollow superstructures. *Nat. Chem.* **2013,** *5*, 203-211.
(67) He, X.; Yang, C.; Wang, D.; Gilliland Iii, S. E.; Chen, D.-R.; Wang, W.-N. Facile synthesis of ZnO@ZIF core-shell nanofibers: crystal growth and gas adsorption. *CrystEngComm* **2017,** *19*, 2445-2450.
(68) Noda, I.; Ozaki, Y. *Two-dimensional correlation spectroscopy: applications in vibrational and optical spectroscopy*, John Wiley & Sons: 2005.
(69) He, X.; Wang, W.-N. Rational Design of Efficient Semiconductor-based Photocatalysts via Microdroplets: A Review. *KONA Powder Part. J.* **2019,** *36*, 201-214.
(70) Carson, C. G.; Hardcastle, K.; Schwartz, J.; Liu, X.; Hoffmann, C.; Gerhardt, R. A.; Tannenbaum, R. Synthesis and Structure Characterization of Copper Terephthalate Metal–Organic Frameworks. *Eur. J. Inorg. Chem.* **2009,** *2009*, 2338-2343.
(71) Zhang, H.; Xiao, R.; Song, M.; Shen, D.; Liu, J. Hydrogen production from bio-oil by chemical looping reforming. *J. Therm. Anal. Calorim.* **2014,** *115*, 1921-1927.
(72) Kaur, R.; Kaur, A.; Umar, A.; Anderson, W. A.; Kansal, S. K. Metal organic framework (MOF) porous octahedral nanocrystals of Cu-BTC: Synthesis, properties and enhanced adsorption properties. *Mater. Res. Bull.* **2019,** *109*, 124-133.
(73) Huang, K.; Xu, Y.; Wang, L.; Wu, D. Heterogeneous catalytic wet peroxide oxidation of simulated phenol wastewater by copper metal–organic frameworks. *RSC Adv.* **2015,** *5*, 32795-32803.

(74) Peng, L.; Wu, S.; Yang, X.; Hu, J.; Fu, X.; Li, M.; Bai, L.; Huo, Q.; Guan, J. Oxidation of benzyl alcohol over metal organic frameworks M-BTC (M = Co, Cu, Fe). *New J. Chem.* **2017,** *41*, 2891-2894.
(75) Kajita, Y.; Arii, H.; Saito, T.; Saito, Y.; Nagatomo, S.; Kitagawa, T.; Funahashi, Y.; Ozawa, T.; Masuda, H. Syntheses, Characterization, and Dioxygen Reactivities of Cu(I) Complexes with cis,cis-1,3,5-Triaminocyclohexane Derivatives: A Cu(III)2O2 Intermediate Exhibiting Higher C−H Activation. *Inorg. Chem.* **2007,** *46*, 3322-3335.
(76) Münch, A. S.; Lohse, M. S.; Hausdorf, S.; Schreiber, G.; Zacher, D.; Fischer, R. A.; Mertens, F. O. R. L. Room temperature preparation method for thin MOF-5 films on metal and fused silica surfaces using the controlled SBU approach. *Microporous Mesoporous Mater.* **2012,** *159*, 132-138.
(77) Mateo-Martí, E.; Welte, L.; Amo-Ochoa, P.; Sanz Miguel, P. J.; Gómez-Herrero, J.; Martín-Gago, J. A.; Zamora, F. Direct evidence of nanowires formation from a Cu(i) coordination polymer. *Chem. Commun.* **2008**, 945-947.
(78) Nijem, N.; Wu, H.; Canepa, P.; Marti, A.; Balkus, K. J.; Thonhauser, T.; Li, J.; Chabal, Y. J. Tuning the Gate Opening Pressure of Metal–Organic Frameworks (MOFs) for the Selective Separation of Hydrocarbons. *J. Am. Chem. Soc.* **2012,** *134*, 15201-15204.
(79) Abid, H. R.; Rada, Z. H.; Shang, J.; Wang, S. Synthesis, characterization, and CO2 adsorption of three metal-organic frameworks (MOFs): MIL-53, MIL-96, and amino-MIL-53. *Polyhedron* **2016,** *120*, 103-111.
(80) Chen, M.; Gan, N.; Zhou, Y.; Li, T.; Xu, Q.; Cao, Y.; Chen, Y. A novel aptamer- metal ions-nanoscale MOF based electrochemical biocodes for multiple antibiotics detection and signal amplification. *Sens. Actuators, B* **2017,** *242*, 1201-1209.
(81) Noda, I. Generalized Two-Dimensional Correlation Method Applicable to Infrared, Raman, and other Types of Spectroscopy. *Appl. Spectrosc.* **1993,** *47*, 1329-1336.
(82) Yu, Z.; Zhou, Z.; Huang, G.; Zheng, X.; Wu, L.; Zhao, S.; Meng, F. Two-Dimensional FTIR Spectroscopic Characterization of Functional Groups of NaOCl-Exposed Alginate: Insights into Membrane Refouling after Online Chemical Cleaning. *ACS Appl. Bio Mater.* **2018,** *1*, 593-603.
(83) Ethiraj, J.; Bonino, F.; Lamberti, C.; Bordiga, S. H2S interaction with HKUST-1 and ZIF-8 MOFs: A multitechnique study. *Microporous Mesoporous Mater.* **2015,** *207*, 90-94.
(84) Prestipino, C.; Regli, L.; Vitillo, J. G.; Bonino, F.; Damin, A.; Lamberti, C.; Zecchina, A.; Solari, P. L.; Kongshaug, K. O.; Bordiga, S. Local Structure of Framework Cu(II) in HKUST-1 Metallorganic Framework: Spectroscopic Characterization upon Activation and Interaction with Adsorbates. *Chem. Mater.* **2006,** *18*, 1337-1346.
(85) Chen, Y.; Wang, H.; Li, J.; Lockard, J. V. In situ spectroscopy studies of CO2 adsorption in a dually functionalized microporous metal–organic framework. *J. Mater. Chem. A* **2015,** *3*, 4945-4953.
(86) Bordiga, S.; Lamberti, C.; Ricchiardi, G.; Regli, L.; Bonino, F.; Damin, A.; Lillerud, K. P.; Bjorgen, M.; Zecchina, A. Electronic and vibrational properties of a MOF-5 metal–organic framework: ZnO quantum dot behaviour. *Chem. Commun.* **2004**, 2300-2301.

(87) Tan, K.; Nijem, N.; Canepa, P.; Gong, Q.; Li, J.; Thonhauser, T.; Chabal, Y. J. Stability and Hydrolyzation of Metal Organic Frameworks with Paddle-Wheel SBUs upon Hydration. *Chem. Mater.* **2012,** *24*, 3153-3167.
(88) Chaikittisilp, W.; Hu, M.; Wang, H.; Huang, H.-S.; Fujita, T.; Wu, K. C. W.; Chen, L.-C.; Yamauchi, Y.; Ariga, K. Nanoporous carbons through direct carbonization of a zeolitic imidazolate framework for supercapacitor electrodes. *Chem. Commun.* **2012,** *48*, 7259-7261.
(89) Cychosz, K. A.; Guillet-Nicolas, R.; Garcia-Martinez, J.; Thommes, M. Recent advances in the textural characterization of hierarchically structured nanoporous materials. *Chem. Soc. Rev.* **2017,** *46*, 389-414.
(90) Liu, B.; Sun, C.; Chen, G. Molecular simulation studies of separation of CH4/H2 mixture in metal-organic frameworks with interpenetration and mixed-ligand. *Chem. Eng. Sci.* **2011,** *66*, 3012-3019.
(91) Wen, L.; Cheng, P.; Lin, W. Mixed-motif interpenetration and cross-linking of high-connectivity networks led to robust and porous metal–organic frameworks with high gas uptake capacities. *Chem. Sci.* **2012,** *3*, 2288-2292.
(92) Kim, H. K.; Yun, W. S.; Kim, M.-B.; Kim, J. Y.; Bae, Y.-S.; Lee, J.; Jeong, N. C. A Chemical Route to Activation of Open Metal Sites in the Copper-Based Metal–Organic Framework Materials HKUST-1 and Cu-MOF-2. *J. Am. Chem. Soc.* **2015,** *137*, 10009-10015.
(93) Lu, J.; Luo, M.; Lei, H.; Bao, X.; Li, C. Epoxidation of Propylene on NaCl-Modified VCe1-x Cux Oxide Catalysts with Direct Molecular Oxygen as the Oxidant. *J. Catal.* **2002,** *211*, 552-555.
(94) He, X.; Wang, W.-N. MOF-based ternary nanocomposites for better CO2 photoreduction: roles of heterojunctions and coordinatively unsaturated metal sites. *J. Mater. Chem. A* **2018,** *6*, 932-940.
(95) Yaghi, O. M.; O'Keeffe, M.; Ockwig, N. W.; Chae, H. K.; Eddaoudi, M.; Kim, J. Reticular synthesis and the design of new materials. *Nature* **2003,** *423*, 705-714.
(96) Lu, G.; Li, S.; Guo, Z.; Farha, O. K.; Hauser, B. G.; Qi, X.; Wang, Y.; Wang, X.; Han, S.; Liu, X.; DuChene, J. S.; Zhang, H.; Zhang, Q.; Chen, X.; Ma, J.; Loo, S. C. J.; Wei, W. D.; Yang, Y.; Hupp, J. T.; Huo, F. Imparting functionality to a metal–organic framework material by controlled nanoparticle encapsulation. *Nat. Chem.* **2012,** *4*, 310-316.
(97) Kim, M.-K.; Kim, D.; Seo, J. Y.; Buyukcakir, O.; Coskun, A. Nanostructured ZnO as a structural template for the growth of ZIF-8 with tunable hierarchical porosity for CO2 conversion. *CrystEngComm* **2017**.
(98) Khaletskaya, K.; Turner, S.; Tu, M.; Wannapaiboon, S.; Schneemann, A.; Meyer, R.; Ludwig, A.; Van Tendeloo, G.; Fischer, R. A. Self-Directed Localization of ZIF-8 Thin Film Formation by Conversion of ZnO Nanolayers. *Adv. Funct. Mater.* **2014,** *24*, 4804-4811.
(99) Liu, Y.; Zhang, W.; Li, S.; Cui, C.; Wu, J.; Chen, H.; Huo, F. Designable Yolk–Shell Nanoparticle@MOF Petalous Heterostructures. *Chem. Mater.* **2014,** *26*, 1119-1125.
(100) Liu, T.; Liu, Y.; Xu, J.; Yao, L.; Liu, D.; Wang, C. Conversion of Cu2O nanowires into Cu2O/HKUST-1 core/sheath nanostructures and hierarchical HKUST-1 nanotubes. *RSC Adv.* **2016,** *6*, 91440-91444.

(101) Zhan, W.-w.; Kuang, Q.; Zhou, J.-z.; Kong, X.-j.; Xie, Z.-x.; Zheng, L.-s. Semiconductor@Metal–Organic Framework Core–Shell Heterostructures: A Case of ZnO@ZIF-8 Nanorods with Selective Photoelectrochemical Response. *J. Am. Chem. Soc.* **2013,** *135*, 1926-1933.
(102) Zhan, W.; He, Y.; Guo, J.; Chen, L.; Kong, X.; Zhao, H.; Kuang, Q.; Xie, Z.; Zheng, L. Probing the structural flexibility of MOFs by constructing metal oxide@MOF-based heterostructures for size-selective photoelectrochemical response. *Nanoscale* **2016,** *8*, 13181-13185.
(103) Bechelany, M.; Drobek, M.; Vallicari, C.; Abou Chaaya, A.; Julbe, A.; Miele, P. Highly crystalline MOF-based materials grown on electrospun nanofibers. *Nanoscale* **2015,** *7*, 5794-5802.
(104) Zhao, J.; Lee, D. T.; Yaga, R. W.; Hall, M. G.; Barton, H. F.; Woodward, I. R.; Oldham, C. J.; Walls, H. J.; Peterson, G. W.; Parsons, G. N. Ultra-Fast Degradation of Chemical Warfare Agents Using MOF–Nanofiber Kebabs. *Angew. Chem.* **2016,** *128*, 13418-13422.
(105) Zhao, J.; Losego, M. D.; Lemaire, P. C.; Williams, P. S.; Gong, B.; Atanasov, S. E.; Blevins, T. M.; Oldham, C. J.; Walls, H. J.; Shepherd, S. D.; Browe, M. A.; Peterson, G. W.; Parsons, G. N. Highly Adsorptive, MOF-Functionalized Nonwoven Fiber Mats for Hazardous Gas Capture Enabled by Atomic Layer Deposition. *Advanced Materials Interfaces* **2014,** *1*, n/a-n/a.
(106) Zhao, J.; Gong, B.; Nunn, W. T.; Lemaire, P. C.; Stevens, E. C.; Sidi, F. I.; Williams, P. S.; Oldham, C. J.; Walls, H. J.; Shepherd, S. D.; Browe, M. A.; Peterson, G. W.; Losego, M. D.; Parsons, G. N. Conformal and highly adsorptive metal-organic framework thin films via layer-by-layer growth on ALD-coated fiber mats. *J. Mater. Chem. A* **2015,** *3*, 1458-1464.
(107) Lemaire, P. C.; Zhao, J.; Williams, P. S.; Walls, H. J.; Shepherd, S. D.; Losego, M. D.; Peterson, G. W.; Parsons, G. N. Copper Benzenetricarboxylate Metal–Organic Framework Nucleation Mechanisms on Metal Oxide Powders and Thin Films formed by Atomic Layer Deposition. *ACS Appl. Mater. Interfaces* **2016,** *8*, 9514-9522.
(108) Zhao, J.; Nunn, W. T.; Lemaire, P. C.; Lin, Y.; Dickey, M. D.; Oldham, C. J.; Walls, H. J.; Peterson, G. W.; Losego, M. D.; Parsons, G. N. Facile Conversion of Hydroxy Double Salts to Metal–Organic Frameworks Using Metal Oxide Particles and Atomic Layer Deposition Thin-Film Templates. *J. Am. Chem. Soc.* **2015,** *137*, 13756-13759.
(109) An, D.; Li, Y.; Lian, X.; Zou, Y.; Deng, G. Synthesis of porous ZnO structure for gas sensor and photocatalytic applications. *Colloids Surf., A* **2014,** *447*, 81-87.
(110) Cravillon, J.; Nayuk, R.; Springer, S.; Feldhoff, A.; Huber, K.; Wiebcke, M. Controlling Zeolitic Imidazolate Framework Nano- and Microcrystal Formation: Insight into Crystal Growth by Time-Resolved In Situ Static Light Scattering. *Chem. Mater.* **2011,** *23*, 2130-2141.
(111) Lin, D.; Wu, H.; Zhang, R.; Pan, W. Enhanced photocatalysis of electrospun Ag− ZnO heterostructured nanofibers. *Chem. Mater.* **2009,** *21*, 3479-3484.
(112) Senthamizhan, A.; Balusamy, B.; Aytac, Z.; Uyar, T. Grain boundary engineering in electrospun ZnO nanostructures as promising photocatalysts. *CrystEngComm* **2016**.
(113) Mali, S. S.; Kim, H.; Jang, W. Y.; Park, H. S.; Patil, P. S.; Hong, C. K. Novel Synthesis and Characterization of Mesoporous ZnO Nanofibers by Electrospinning Technique. *ACS Sustainable Chemistry & Engineering* **2013,** *1*, 1207-1213.

(114) Park, K. S.; Ni, Z.; Côté, A. P.; Choi, J. Y.; Huang, R.; Uribe-Romo, F. J.; Chae, H. K.; O'Keeffe, M.; Yaghi, O. M. Exceptional chemical and thermal stability of zeolitic imidazolate frameworks. *Proceedings of the National Academy of Sciences* **2006,** *103*, 10186-10191.
(115) Özgür, Ü.; Alivov, Y. I.; Liu, C.; Teke, A.; Reshchikov, M. A.; Doğan, S.; Avrutin, V.; Cho, S. J.; Morkoç, H. A comprehensive review of ZnO materials and devices. *J Appl Phys* **2005,** *98*, 041301.
(116) Song, Y.; Hu, D.; Liu, F.; Chen, S.; Wang, L. Fabrication of fluorescent SiO2@zeolitic imidazolate framework-8 nanosensor for Cu2+ detection. *Analyst* **2015,** *140*, 623-629.
(117) Hu, Y.; Kazemian, H.; Rohani, S.; Huang, Y.; Song, Y. In situ high pressure study of ZIF-8 by FTIR spectroscopy. *Chem. Commun.* **2011,** *47*, 12694-12696.
(118) Kumar Yadav, H.; Katiyar, R. S.; Gupta, V. Temperature dependent dynamics of ZnO nanoparticles probed by Raman scattering: A big divergence in the functional areas of nanoparticles and bulk materials. *Appl Phys Lett* **2012,** *100*, 051906.
(119) Cuscó, R.; Alarcón-Lladó, E.; Ibáñez, J.; Artús, L.; Jiménez, J.; Wang, B.; Callahan, M. J. Temperature dependence of Raman scattering inZnO. *Phys Rev B* **2007,** *75*.
(120) Tanaka, S.; Fujita, K.; Miyake, Y.; Miyamoto, M.; Hasegawa, Y.; Makino, T.; Van der Perre, S.; Cousin Saint Remi, J.; Van Assche, T.; Baron, G. V.; Denayer, J. F. M. Adsorption and Diffusion Phenomena in Crystal Size Engineered ZIF-8 MOF. *J. Phys. Chem. C* **2015,** *119*, 28430-28439.
(121) Radhakrishnan, D.; Narayana, C. Guest dependent Brillouin and Raman scattering studies of zeolitic imidazolate framework-8 (ZIF-8) under external pressure. *The Journal of Chemical Physics* **2016,** *144*, 134704.
(122) Wang, F.; Liu, Z.-S.; Yang, H.; Tan, Y.-X.; Zhang, J. Hybrid Zeolitic Imidazolate Frameworks with Catalytically Active TO4 Building Blocks. *Angew. Chem. Int. Ed.* **2011,** *50*, 450-453.
(123) Srikant, V.; Clarke, D. R. On the optical band gap of zinc oxide. *J. Appl. Phys.* **1998,** *83*, 5447-5451.
(124) Yang, Q.; Liu, W.; Wang, B.; Zhang, W.; Zeng, X.; Zhang, C.; Qin, Y.; Sun, X.; Wu, T.; Liu, J.; Huo, F.; Lu, J. Regulating the spatial distribution of metal nanoparticles within metal-organic frameworks to enhance catalytic efficiency. *Nat. Commun.* **2017,** *8*, 14429.
(125) Sun, Y.; Zhang, Q.; Xu, X.; Zhang, L.; Wu, Z.; Guo, J.; Lu, G. ZnO@ZIF Core–Shell Single Crystals Formed by in Situ Conversion of ZnO Particles. *Eur. J. Inorg. Chem.* **2016,** *2016*, 3553-3558.
(126) Ban, Y.; Li, Z.; Li, Y.; Peng, Y.; Jin, H.; Jiao, W.; Guo, A.; Wang, P.; Yang, Q.; Zhong, C.; Yang, W. Confinement of Ionic Liquids in Nanocages: Tailoring the Molecular Sieving Properties of ZIF-8 for Membrane-Based CO2 Capture. *Angew. Chem. Int. Ed.* **2015,** *54*, 15483-15487.
(127) Dietzel, P. D. C.; Johnsen, R. E.; Fjellvag, H.; Bordiga, S.; Groppo, E.; Chavan, S.; Blom, R. Adsorption properties and structure of CO_2 adsorbed on open coordination sites of metal-organic framework Ni_2(dhtp) from gas adsorption, IR spectroscopy and X-ray diffraction. *Chemical Communications* **2008**, 5125-5127.

(128) Roque-Malherbe, R.; Polanco-Estrella, R.; Marquez-Linares, F. Study of the Interaction between Silica Surfaces and the Carbon Dioxide Molecule. *J. Phys. Chem. C* **2010,** *114*, 17773-17787.
(129) Serna-Guerrero, R.; Sayari, A. Modeling adsorption of CO2 on amine-functionalized mesoporous silica. 2: Kinetics and breakthrough curves. *Chem. Eng. J.* **2010,** *161*, 182-190.
(130) Cestari, A. R.; Vieira, E. F. S.; Vieira, G. S.; Almeida, L. E. The removal of anionic dyes from aqueous solutions in the presence of anionic surfactant using aminopropylsilica—A kinetic study. *J. Hazard. Mater.* **2006,** *138*, 133-141.
(131) Wang, J.; Stevens, L. A.; Drage, T. C.; Wood, J. Preparation and CO2 adsorption of amine modified Mg–Al LDH via exfoliation route. *Chem. Eng. Sci.* **2012,** *68*, 424-431.
(132) Chowdhury, S.; Parshetti, G. K.; Balasubramanian, R. Post-combustion CO2 capture using mesoporous TiO2/graphene oxide nanocomposites. *Chem. Eng. J.* **2015,** *263*, 374-384.
(133) Chizallet, C.; Lazare, S.; Bazer-Bachi, D.; Bonnier, F.; Lecocq, V.; Soyer, E.; Quoineaud, A.-A.; Bats, N. Catalysis of Transesterification by a Nonfunctionalized Metal−Organic Framework: Acido-Basicity at the External Surface of ZIF-8 Probed by FTIR and ab Initio Calculations. *J. Am. Chem. Soc.* **2010,** *132*, 12365-12377.
(134) Chizallet, C.; Bats, N. External Surface of Zeolite Imidazolate Frameworks Viewed Ab Initio: Multifunctionality at the Organic−Inorganic Interface. *The Journal of Physical Chemistry Letters* **2010,** *1*, 349-353.
(135) Wu, H.; Simmons, J. M.; Srinivas, G.; Zhou, W.; Yildirim, T. Adsorption Sites and Binding Nature of CO2 in Prototypical Metal−Organic Frameworks: A Combined Neutron Diffraction and First-Principles Study. *The Journal of Physical Chemistry Letters* **2010,** *1*, 1946-1951.
(136) Teramura, K.; Iguchi, S.; Mizuno, Y.; Shishido, T.; Tanaka, T. Photocatalytic Conversion of CO2 in Water over Layered Double Hydroxides. *Angew. Chem. Int. Ed.* **2012,** *51*, 8008-8011.
(137) Lal, R. Sequestration of atmospheric CO_2 in global carbon pools. *Energy & Environmental Science* **2008,** *1*, 86-100.
(138) D'Alessandro, D. M.; Smit, B.; Long, J. R. Carbon dioxide capture: prospects for new materials. *Angew Chem Int Edit* **2010,** *49*, 6058-6082.
(139) Usubharatana, P.; McMartin, D.; Veawab, A.; Tontiwachwuthikul, P. Photocatalytic process for CO_2 emission reduction from industrial flue gas streams. *Industrial & Engineering Chemistry Research* **2006,** *45*, 2558-2568.
(140) Indrakanti, V. P.; Kubicki, J. D.; Schobert, H. H. Photoinduced activation of CO_2 on Ti-based heterogeneous catalysts: Current state, chemical physics-based insights and outlook. *Energy & Environmental Science* **2009,** *2*, 745-758.
(141) Roy, S. C.; Varghese, O. K.; Paulose, M.; Grimes, C. A. Toward Solar Fuels: Photocatalytic Conversion of Carbon Dioxide to Hydrocarbons. *Acs Nano* **2010,** *4*, 1259-1278.
(142) Dhakshinamoorthy, A.; Navalon, S.; Corma, A.; Garcia, H. Photocatalytic CO2 reduction by TiO2 and related titanium containing solids. *Energy & Environmental Science* **2012,** *5*, 9217-9233.
(143) Kondratenko, E. V.; Mul, G.; Baltrusaitis, J.; Larrazabal, G. O.; Perez-Ramirez, J. Status and perspectives of CO_2 conversion into fuels and chemicals by catalytic, photocatalytic and electrocatalytic processes. *Energy & Environmental Science* **2013,** *6*, 3112-3135.

(144) Habisreutinger, S. N.; Schmidt-Mende, L.; Stolarczyk, J. K. Photocatalytic reduction of CO_2 on TiO_2 and other semiconductors. *Angew. Chem. Int. Edit.* **2013,** *52*, 7372-7408.
(145) White, J. L.; Baruch, M. F.; Pander, J. E.; Hu, Y.; Fortmeyer, I. C.; Park, J. E.; Zhang, T.; Liao, K.; Gu, J.; Yan, Y.; Shaw, T. W.; Abelev, E.; Bocarsly, A. B. Light-driven heterogeneous reduction of carbon dioxide: photocatalysts and photoelectrodes. *Chem Rev* **2015,** *115*, 12888-12935.
(146) Liu, Y. Y.; Yang, Y. M.; Sun, Q. L.; Wang, Z. Y.; Huang, B. B.; Dai, Y.; Qin, X. Y.; Zhang, X. Y. Chemical Adsorption Enhanced CO2 Capture and Photoreduction over a Copper Porphyrin Based Metal Organic Framework. *ACS Appl. Mater. Interfaces* **2013,** *5*, 7654-7658.
(147) Liu, L.; Zhao, C.; Xu, J.; Li, Y. Integrated CO2 capture and photocatalytic conversion by a hybrid adsorbent/photocatalyst material. *Appl. Catal., B* **2015,** *179*, 489-499.
(148) Kuppler, R. J.; Timmons, D. J.; Fang, Q. R.; Li, J. R.; Makal, T. A.; Young, M. D.; Yuan, D. Q.; Zhao, D.; Zhuang, W. J.; Zhou, H. C. Potential applications of metal-organic frameworks. *Coord. Chem. Rev.* **2009,** *253*, 3042-3066.
(149) So, M. C.; Wiederrecht, G. P.; Mondloch, J. E.; Hupp, J. T.; Farha, O. K. Metal-organic framework materials for light-harvesting and energy transfer. *Chemical Communications* **2015,** *51*, 3501-3510.
(150) Wang, C.; Xie, Z. G.; deKrafft, K. E.; Lin, W. L. Doping Metal-Organic Frameworks for Water Oxidation, Carbon Dioxide Reduction, and Organic Photocatalysis. *J. Am. Chem. Soc.* **2011,** *133*, 13445-13454.
(151) Fu, Y. H.; Sun, D. R.; Chen, Y. J.; Huang, R. K.; Ding, Z. X.; Fu, X. Z.; Li, Z. H. An Amine-Functionalized Titanium Metal-Organic Framework Photocatalyst with Visible-Light-Induced Activity for CO2 Reduction. *Angewandte Chemie-International Edition* **2012,** *51*, 3364-3367.
(152) Xu, H. Q.; Hu, J. H.; Wang, D. K.; Li, Z. H.; Zhang, Q.; Luo, Y.; Yu, S. H.; Jiang, H. L. Visible-light photoreduction of CO_2 in a metal-organic framework: Boosting electron-hole separation via electron trap states. *Journal of the American Chemical Society* **2015,** *137*, 13440-13443.
(153) Liu, Q.; Low, Z. X.; Li, L. X.; Razmjou, A.; Wang, K.; Yao, J. F.; Wang, H. T. ZIF-8/Zn_2GeO_4 nanorods with an enhanced CO_2 adsorption property in an aqueous medium for photocatalytic synthesis of liquid fuel. *Journal of Materials Chemistry A* **2013,** *1*, 11563-11569.
(154) Wang, S. B.; Wang, X. C. Photocatalytic CO_2 reduction by CdS promoted with a zeolitic imidazolate framework. *Applied Catalysis B-Environmental* **2015,** *162*, 494-500.
(155) Li, R.; Hu, J. H.; Deng, M. S.; Wang, H. L.; Wang, X. J.; Hu, Y. L.; Jiang, H. L.; Jiang, J.; Zhang, Q.; Xie, Y.; Xiong, Y. J. Integration of an inorganic semiconductor with a metal-organic framework: A platform for enhanced gaseous photocatalytic reactions. *Adv Mater* **2014,** *26*, 4783-4788.
(156) Carne-Sanchez, A.; Imaz, I.; Cano-Sarabia, M.; Maspoch, D. A spray-drying strategy for synthesis of nanoscale metal-organic frameworks and their assembly into hollow superstructures. *Nature Chemistry* **2013,** *5*, 203-211.
(157) Chui, S. S. Y.; Lo, S. M. F.; Charmant, J. P. H.; Orpen, A. G.; Williams, I. D. A chemically functionalizable nanoporous material $[Cu_3(TMA)_2(H_2O)_3]_n$. *Science* **1999,** *283*, 1148-1150.

(158) Wang, W. N.; Lenggoro, I. W.; Okuyama, K. Preparation of Nanoparticles by Spray Routes. In *Encyclopedia of Nanoscience and Nanotechnology*; Nalwa, H. S., Ed.; American Scientific Publishers: 2011; pp 435-458.
(159) Motl, N. E.; Mann, A. K. P.; Skrabalak, S. E. Aerosol-assisted synthesis and assembly of nanoscale building blocks. *Journal of Materials Chemistry A* **2013,** *1*, 5193-5202.
(160) Wang, W. N.; Jiang, Y.; Biswas, P. Evaporation-Induced Crumpling of Graphene Oxide Nanosheets in Aerosolized Droplets: Confinement Force Relationship. *J Phys Chem Lett* **2012,** *3*, 3228-3233.
(161) Wang, W. N.; Lenggoro, I. W.; Terashi, Y.; Kim, T. O.; Okuyama, K. One-step synthesis of titanium oxide nanoparticles by spray pyrolysis of organic precursors. *Mat Sci Eng B-Solid* **2005,** *123*, 194-202.
(162) Wang, W. N.; An, W. J.; Ramalingam, B.; Mukherjee, S.; Niedzwiedzki, D. M.; Gangopadhyay, S.; Biswas, P. Size and Structure Matter: Enhanced CO_2 Photoreduction Efficiency by Size-Resolved Ultrafine Pt Nanoparticles on TiO_2 Single Crystals. *J. Am. Chem. Soc.* **2012,** *134*, 11276-11281.
(163) Wang, W. N.; Wu, F.; Myung, Y.; Niedzwiedzki, D. M.; Im, H. S.; Park, J.; Banerjee, P.; Biswas, P. Surface engineered CuO nanowires with ZnO islands for CO_2 photoreduction. *Acs Appl Mater Inter* **2015,** *7*, 5685-5692.
(164) Wang, J. C.; Zhang, L.; Fang, W. X.; Ren, J.; Li, Y. Y.; Yao, H. C.; Wang, J. S.; Li, Z. J. Enhanced photoreduction CO_2 activity over direct Z-scheme alpha-Fe_2O_3/Cu_2O heterostructures under visible light irradiation. *Acs Appl Mater Inter* **2015,** *7*, 8631-8639.
(165) Yakovenko, A. A.; Reibenspies, J. H.; Bhuvanesh, N.; Zhou, H.-C. Generation and applications of structure envelopes for porous metal-organic frameworks. *J. Appl. Crystallogr.* **2013,** *46*, 346-353.
(166) Seo, Y. K.; Hundal, G.; Jang, I. T.; Hwang, Y. K.; Jun, C. H.; Chang, J. S. Microwave synthesis of hybrid inorganic-organic materials including porous $Cu_3(BTC)_2$ from Cu(II)-trimesate mixture. *Micropor Mesopor Mat* **2009,** *119*, 331-337.
(167) Bae, T. H.; Lee, J. S.; Qiu, W. L.; Koros, W. J.; Jones, C. W.; Nair, S. A High-Performance Gas-Separation Membrane Containing Submicrometer-Sized Metal-Organic Framework Crystals. *Angew Chem Int Edit* **2010,** *49*, 9863-9866.
(168) Choi, H. S.; Lee, S. J.; Bae, Y. S.; Choung, S. J.; Im, S. H.; Kim, J. Scalable continuous solvo-jet process for ZIF-8 nanoparticles. *Chem Eng J* **2015,** *266*, 56-63.
(169) Schlichte, K.; Kratzke, T.; Kaskel, S. Improved synthesis, thermal stability and catalytic properties of the metal-organic framework compound $Cu_3(BTC)_2$. *Micropor Mesopor Mat* **2004,** *73*, 81-88.
(170) Kumar, R. S.; Kumar, S. S.; Kulandainathan, M. A. Efficient electrosynthesis of highly active $Cu_3(BTC)_2$-MOF and its catalytic application to chemical reduction. *Micropor Mesopor Mat* **2013,** *168*, 57-64.
(171) Wang, F. L.; Guo, H. L.; Chai, Y. M.; Li, Y. P.; Liu, C. G. The controlled regulation of morphology and size of HKUST-1 by "coordination modulation method". *Micropor Mesopor Mat* **2013,** *173*, 181-188.

(172) Huo, J.; Brightwell, M.; El Hankari, S.; Garai, A.; Bradshaw, D. A versatile, industrially relevant, aqueous room temperature synthesis of HKUST-1 with high space-time yield. *Journal of Materials Chemistry A* **2013,** *1*, 15220-15223.
(173) Farha, O. K.; Hupp, J. T. Rational Design, Synthesis, Purification, and Activation of Metal-Organic Framework Materials. *Accounts Chem Res* **2010,** *43*, 1166-1175.
(174) Fuchs, N. A. *Evaporation and Droplet Growth in Gaseous Media*, Pergamon Press: New York, 1959.
(175) Xiong, Y.; Kodas, T. T. Droplet evaporation and solute precipitation during spray-pyrolysis. *J Aerosol Sci* **1993,** *24*, 893-908.
(176) Poling, B. E.; Prausnitz, J. M.; O'Connell, J. P. *The Properties of Gases and Liquids*, 5th ed.; McGraw-Hill: New York, 2001.
(177) Fisenko, S. P.; Wang, W. N.; Lenggoro, I. W.; Okyuama, K. Evaporative cooling of micron-sized droplets in a low-pressure aerosol reactor. *Chem Eng Sci* **2006,** *61*, 6029-6034.
(178) Wang, W.-N.; Park, J.; Biswas, P. Rapid synthesis of nanostructured Cu–TiO 2–SiO 2 composites for CO 2 photoreduction by evaporation driven self-assembly. *Catal. Sci. Technol.* **2011,** *1*, 593-600.
(179) Li, Y.; Wang, W.-N.; Zhan, Z.; Woo, M.-H.; Wu, C.-Y.; Biswas, P. Photocatalytic reduction of CO2 with H2O on mesoporous silica supported Cu/TiO2 catalysts. *Appl. Catal., B* **2010,** *100*, 386-392.
(180) Serna-Guerrero, R.; Sayari, A. Modeling adsorption of CO_2 on amine-functionalized mesoporous silica. 2: Kinetics and breakthrough curves. *Chem Eng J* **2010,** *161*, 182-190.
(181) Roque-Malherbe, R.; Polanco-Estrella, R.; Marquez-Linares, F. Study of the Interaction between Silica Surfaces and the Carbon Dioxide Molecule. *Journal of Physical Chemistry C* **2010,** *114*, 17773-17787.
(182) Bacsik, Z.; Ahlsten, N.; Ziadi, A.; Zhao, G. Y.; Garcia-Bennett, A. E.; Martin-Matute, B.; Hedin, N. Mechanisms and kinetics for sorption of CO_2 on bicontinuous mesoporous silica modified with n-propylamine. *Langmuir* **2011,** *27*, 11118-11128.
(183) Schaub, R.; Thostrup, P.; Lopez, N.; Laegsgaard, E.; Stensgaard, I.; Norskov, J. K.; Besenbacher, F. Oxygen vacancies as active sites for water dissociation on rutile TiO_2 (110). *Physical Review Letters* **2001,** *87*.
(184) Minella, M.; Faga, M. G.; Maurino, V.; Minero, C.; Pelizzetti, E.; Coluccia, S.; Martra, G. Effect of Fluorination on the Surface Properties of Titania P25 Powder: An FTIR Study. *Langmuir* **2010,** *26*, 2521-2527.
(185) Chenu, E.; Jacobs, G.; Crawford, A. C.; Keogh, R. A.; Patterson, P. M.; Sparks, D. E.; Davis, B. H. Water-gas shift: an examination of Pt promoted MgO and tetragonal and monoclinic ZrO2 by in situ drifts. *Applied Catalysis B-Environmental* **2005,** *59*, 45-56.
(186) Aboulayt, A.; Mauge, F.; Hoggan, P. E.; Lavalley, J. C. Combined FTIR, reactivity and quantum chemistry investigation of COS hydrolysis at metal oxide surfaces used to compare hydroxyl group basicity. *Catalysis Letters* **1996,** *39*, 213-218.

(187) Deiana, C.; Fois, E.; Coluccia, S.; Martra, G. Surface Structure of TiO_2 P25 Nanoparticles: Infrared Study of Hydroxy Groups on Coordinative Defect Sites. *Journal of Physical Chemistry C* **2010,** *114*, 21531-21538.
(188) Constantinou, D. A.; Fierro, J. L. G.; Efstathiou, A. M. The phenol steam reforming reaction towards H_2 production on natural calcite. *Applied Catalysis B-Environmental* **2009,** *90*, 347-359.
(189) Li, G. H.; Larsen, S. C.; Grassian, V. H. An FT-IR study of NO_2 reduction in nanocrystalline NaY zeolite: effect of zeolite crystal size and adsorbed water. *Catalysis Letters* **2005,** *103*, 23-32.
(190) Liu, L. J.; Zhao, H. L.; Andino, J. M.; Li, Y. Photocatalytic CO_2 reduction with H_2O on TiO_2 nanocrystals: Comparison of anatase, rutile, and brookite polymorphs and exploration of surface chemistry. *Acs Catal* **2012,** *2*, 1817-1828.
(191) Di Cosimo, J. I.; Díez, V. K.; Xu, M.; Iglesia, E.; Apesteguía, C. R. Structure and Surface and Catalytic Properties of Mg-Al Basic Oxides. *J. Catal.* **1998,** *178*, 499-510.
(192) Wazne, M.; Korfiatis, G. P.; Meng, X. Carbonate Effects on Hexavalent Uranium Adsorption by Iron Oxyhydroxide. *Environmental Science & Technology* **2003,** *37*, 3619-3624.
(193) Morterra, C.; Orio, L. Surface Characterization of Zirconium-Oxide .2. The Interaction with Carbon-Dioxide at Ambient-Temperature. *Materials Chemistry and Physics* **1990,** *24*, 247-268.
(194) Liu, L. J.; Zhao, C. Y.; Pitts, D.; Zhao, H. L.; Li, Y. CO2 photoreduction with H2O vapor by porous MgO-TiO2 microspheres: effects of surface MgO dispersion and CO2 adsorption-desorption dynamics. *Catal. Sci. Technol.* **2014,** *4*, 1539-1546.
(195) Heller, E. J.; Stechel, E. B.; Davis, M. J. Molecular spectra, Fermi resonances, and classical motion: Example of CO2. *The Journal of Chemical Physics* **1979,** *71*, 4759-4760.
(196) Zhang, C. B.; Liu, F. D.; Zhai, Y. P.; Ariga, H.; Yi, N.; Liu, Y. C.; Asakura, K.; Flytzani-Stephanopoulos, M.; He, H. Alkali-Metal-Promoted Pt/TiO_2 Opens a More Efficient Pathway to Formaldehyde Oxidation at Ambient Temperatures. *Angew Chem Int Edit* **2012,** *51*, 9628-9632.
(197) Guo, J. J.; Lou, H.; Mo, L. Y.; Zheng, X. M. The reactivity of surface active carbonaceous species with CO_2 and its role on hydrocarbon conversion reactions. *Journal of Molecular Catalysis a-Chemical* **2010,** *316*, 1-7.
(198) Skoulidas, A. I.; Sholl, D. S. Self-Diffusion and Transport Diffusion of Light Gases in Metal-Organic Framework Materials Assessed Using Molecular Dynamics Simulations. *The Journal of Physical Chemistry B* **2005,** *109*, 15760-15768.
(199) Chen, Z. Y.; Fang, L.; Dong, W.; Zheng, F. G.; Shen, M. R.; Wang, J. L. Inverse opal structured Ag/TiO_2 plasmonic photocatalyst prepared by pulsed current deposition and its enhanced visible light photocatalytic activity. *Journal of Materials Chemistry A* **2014,** *2*, 824-832.
(200) Kamat, P. V. Meeting the clean energy demand: Nanostructure architectures for solar energy conversion. *Journal of Physical Chemistry C* **2007,** *111*, 2834-2860.
(201) Logan, M. W.; Ayad, S.; Adamson, J. D.; Dilbeck, T.; Hanson, K.; Uribe-Romo, F. J. Systematic variation of the optical bandgap in titanium based isoreticular metal-organic frameworks for photocatalytic reduction of CO2 under blue light. *J. Mater. Chem. A* **2017,** *5*, 11854-11863.

(202) Yuan, W.; Yuan, J.; Xie, J.; Li, C. M. Polymer-Mediated Self-Assembly of TiO2@Cu2O Core–Shell Nanowire Array for Highly Efficient Photoelectrochemical Water Oxidation. *ACS Appl. Mater. Interfaces* **2016,** *8*, 6082-6092.
(203) Linsebigler, A. L.; Lu, G. Q.; Yates, J. T. Photocatalysis on TiO_2 Surfaces - Principles, Mechanisms, and Selected Results. *Chem. Rev.* **1995,** *95*, 735-758.
(204) Wang, Y. J.; Wang, Q. S.; Zhan, X. Y.; Wang, F. M.; Safdar, M.; He, J. Visible light driven type II heterostructures and their enhanced photocatalysis properties: a review. *Nanoscale* **2013,** *5*, 8326-8339.
(205) Wang, J.-C.; Zhang, L.; Fang, W.-X.; Ren, J.; Li, Y.-Y.; Yao, H.-C.; Wang, J.-S.; Li, Z.-J. Enhanced Photoreduction CO2 Activity over Direct Z-Scheme α-Fe2O3/Cu2O Heterostructures under Visible Light Irradiation. *Acs Appl Mater Inter* **2015,** *7*, 8631-8639.
(206) Li, M.; Zhang, L.; Fan, X.; Zhou, Y.; Wu, M.; Shi, J. Highly selective CO2 photoreduction to CO over g-C3N4/Bi2WO6 composites under visible light. *J. Mater. Chem. A* **2015,** *3*, 5189-5196.
(207) Wang, W.-N.; Wu, F.; Myung, Y.; Niedzwiedzki, D. M.; Im, H. S.; Park, J.; Banerjee, P.; Biswas, P. Surface Engineered CuO Nanowires with ZnO Islands for CO2 Photoreduction. *ACS Appl. Mater. Interfaces* **2015,** *7*, 5685-5692.
(208) Caballero-Briones, F.; Artes, J. M.; Diez-Perez, I.; Gorostiza, P.; Sanz, F. Direct observation of the valence band edge by *in situ* ECSTM-ECTS in *p*-type Cu_2O layers prepared by copper anodization. *Journal of Physical Chemistry C* **2009,** *113*, 1028-1036.
(209) Yang, L.; Luo, S.; Li, Y.; Xiao, Y.; Kang, Q.; Cai, Q. High Efficient Photocatalytic Degradation of p-Nitrophenol on a Unique Cu2O/TiO2 p-n Heterojunction Network Catalyst. *Environmental Science & Technology* **2010,** *44*, 7641-7646.
(210) Maina, J. W.; Pozo-Gonzalo, C.; Kong, L.; Schutz, J.; Hill, M.; Dumee, L. F. Metal organic framework based catalysts for CO2 conversion. *Mater Horiz* **2017,** *4*, 345-361.
(211) Chen, D.; Xing, H.; Wang, C.; Su, Z. Highly efficient visible-light-driven CO2 reduction to formate by a new anthracene-based zirconium MOF via dual catalytic routes. *J. Mater. Chem. A* **2016,** *4*, 2657-2662.
(212) Liu, S.; Chen, F.; Li, S.; Peng, X.; Xiong, Y. Enhanced photocatalytic conversion of greenhouse gas CO2 into solar fuels over g-C3N4 nanotubes with decorated transparent ZIF-8 nanoclusters. *Appl. Catal., B* **2017,** *211*, 1-10.
(213) Crake, A.; Christoforidis, K. C.; Kafizas, A.; Zafeiratos, S.; Petit, C. CO2 capture and photocatalytic reduction using bifunctional TiO2/MOF nanocomposites under UV–vis irradiation. *Appl. Catal., B* **2017,** *210*, 131-140.
(214) Bendavid, L. I.; Carter, E. A. CO2 Adsorption on Cu2O(111): A DFT+U and DFT-D Study. *J. Phys. Chem. C* **2013,** *117*, 26048-26059.
(215) Wang, W. N.; Park, J.; Biswas, P. Rapid synthesis of nanostructured Cu-TiO_2-SiO_2 composites for CO_2 photoreduction by evaporation driven self-assembly. *Catal. Sci. Technol.* **2011,** *1*, 593-600.
(216) Dunkle, S. S.; Helmich, R. J.; Suslick, K. S. BiVO4 as a Visible-Light Photocatalyst Prepared by Ultrasonic Spray Pyrolysis. *Journal of Physical Chemistry C* **2009,** *113*, 11980-11983.

(217) Chang, I. C.; Chen, P.-C.; Tsai, M.-C.; Chen, T.-T.; Yang, M.-H.; Chiu, H.-T.; Lee, C.-Y. Large-scale synthesis of uniform Cu2O nanocubes with tunable sizes by in-situ nucleation. *CrystEngComm* **2013,** *15*, 2363-2366.
(218) Al-Janabi, N.; Hill, P.; Torrente-Murciano, L.; Garforth, A.; Gorgojo, P.; Siperstein, F.; Fan, X. Mapping the Cu-BTC metal–organic framework (HKUST-1) stability envelope in the presence of water vapour for CO2 adsorption from flue gases. *Chem. Eng. J.* **2015,** *281*, 669-677.
(219) Loera-Serna, S.; Oliver-Tolentino, M. A.; de Lourdes López-Núñez, M.; Santana-Cruz, A.; Guzmán-Vargas, A.; Cabrera-Sierra, R.; Beltrán, H. I.; Flores, J. Electrochemical behavior of [Cu3(BTC)2] metal–organic framework: The effect of the method of synthesis. *J. Alloys Compd.* **2012,** *540*, 113-120.
(220) Maiti, S.; Pramanik, A.; Manju, U.; Mahanty, S. Cu3(1,3,5-benzenetricarboxylate)2 metal-organic framework: A promising anode material for lithium-ion battery. *Microporous Mesoporous Mater.* **2016,** *226*, 353-359.
(221) Jayaramulu, K.; Toyao, T.; Ranc, V.; Rosler, C.; Petr, M.; Zboril, R.; Horiuchi, Y.; Matsuoka, M.; Fischer, R. A. An in situ porous cuprous oxide/nitrogen-rich graphitic carbon nanocomposite derived from a metal-organic framework for visible light driven hydrogen evolution. *J. Mater. Chem. A* **2016,** *4*, 18037-18042.
(222) Peng, B.; Feng, C.; Liu, S.; Zhang, R. Synthesis of CuO catalyst derived from HKUST-1 temple for the low-temperature NH3-SCR process. *Catal. Today*.
(223) Ishibashi, K.; Fujishima, A.; Watanabe, T.; Hashimoto, K. Detection of active oxidative species in TiO2 photocatalysis using the fluorescence technique. *Electrochem Commun* **2000,** *2*, 207-210.
(224) Czili, H.; Horvath, A. Applicability of coumarin for detecting and measuring hydroxyl radicals generated by photoexcitation of TiO2 nanoparticles. *Applied Catalysis B-Environmental* **2008,** *81*, 295-302.
(225) Kraut, E. A.; Grant, R. W.; Waldrop, J. R.; Kowalczyk, S. P. Precise Determination of the Valence-Band Edge in X-Ray Photoemission Spectra: Application to Measurement of Semiconductor Interface Potentials. *Phys. Rev. Lett.* **1980,** *44*, 1620-1623.
(226) Park, S.-M.; Razzaq, A.; Park, Y. H.; Sorcar, S.; Park, Y.; Grimes, C. A.; In, S.-I. Hybrid CuxO–TiO2 Heterostructured Composites for Photocatalytic CO2 Reduction into Methane Using Solar Irradiation: Sunlight into Fuel. *ACS Omega* **2016,** *1*, 868-875.
(227) Ihli, J.; Wong, W. C.; Noel, E. H.; Kim, Y.-Y.; Kulak, A. N.; Christenson, H. K.; Duer, M. J.; Meldrum, F. C. Dehydration and crystallization of amorphous calcium carbonate in solution and in air. *Nat. Commun.* **2014,** *5*, 3169.
(228) Liu, L.; Zhao, H.; Andino, J. M.; Li, Y. Photocatalytic CO2 Reduction with H2O on TiO2 Nanocrystals: Comparison of Anatase, Rutile, and Brookite Polymorphs and Exploration of Surface Chemistry. *ACS Catalysis* **2012,** *2*, 1817-1828.
(229) Pokrovski, K.; Jung, K. T.; Bell, A. T. Investigation of CO and CO2 Adsorption on Tetragonal and Monoclinic Zirconia. *Langmuir* **2001,** *17*, 4297-4303.
(230) Khatri, R. A.; Chuang, S. S. C.; Soong, Y.; Gray, M. Thermal and Chemical Stability of Regenerable Solid Amine Sorbent for CO2 Capture. *Energy & Fuels* **2006,** *20*, 1514-1520.

(231) Liu, L.; Zhao, C.; Pitts, D.; Zhao, H.; Li, Y. CO2 photoreduction with H2O vapor by porous MgO-TiO2 microspheres: effects of surface MgO dispersion and CO2 adsorption-desorption dynamics. *Catal. Sci. Technol.* **2014,** *4*, 1539-1546.
(232) Khatri, R. A.; Chuang, S. S. C.; Soong, Y.; Gray, M. Carbon Dioxide Capture by Diamine-Grafted SBA-15: A Combined Fourier Transform Infrared and Mass Spectrometry Study. *Industrial & Engineering Chemistry Research* **2005,** *44*, 3702-3708.
(233) Liu, L.; Li, Y. Understanding the reaction mechanism of photocatalytic reduction of CO2 with H2O on TiO2-based photocatalysts: a review. *Aerosol and Air Quality Research* **2014,** *14*, 453-469.
(234) Kouva, S.; Honkala, K.; Lefferts, L.; Kanervo, J. Review: monoclinic zirconia, its surface sites and their interaction with carbon monoxide. *Catal. Sci. Technol.* **2015,** *5*, 3473-3490.
(235) Teramura, K.; Hori, K.; Terao, Y.; Huang, Z.; Iguchi, S.; Wang, Z.; Asakura, H.; Hosokawa, S.; Tanaka, T. Which is an Intermediate Species for Photocatalytic Conversion of CO2 by H2O as the Electron Donor: CO2 Molecule, Carbonic Acid, Bicarbonate, or Carbonate Ions? *J. Phys. Chem. C* **2017,** *121*, 8711-8721.
(236) Chen, S.; Cao, T.; Gao, Y.; Li, D.; Xiong, F.; Huang, W. Probing Surface Structures of CeO2, TiO2, and Cu2O Nanocrystals with CO and CO2 Chemisorption. *J. Phys. Chem. C* **2016,** *120*, 21472-21485.
(237) Chui, S. S.-Y.; Lo, S. M.-F.; Charmant, J. P.; Orpen, A. G.; Williams, I. D. A chemically functionalizable nanoporous material [Cu3 (TMA) 2 (H2O) 3] n. *Science* **1999,** *283*, 1148-1150.
(238) Liu, L.; Zhao, C.; Li, Y. Spontaneous Dissociation of CO2 to CO on Defective Surface of Cu(I)/TiO2–x Nanoparticles at Room Temperature. *J. Phys. Chem. C* **2012,** *116*, 7904-7912.
(239) Bordiga, S.; Regli, L.; Bonino, F.; Groppo, E.; Lamberti, C.; Xiao, B.; Wheatley, P. S.; Morris, R. E.; Zecchina, A. Adsorption properties of HKUST-1 toward hydrogen and other small molecules monitored by IR. *PCCP* **2007,** *9*, 2676-2685.
(240) Aurian-Blajeni, B.; Halmann, M.; Manassen, J. Photoreduction of carbon dioxide and water into formaldehyde and methanol on semiconductor materials. *Solar Energy* **1980,** *25*, 165-170.
(241) AlOtaibi, B.; Fan, S.; Wang, D.; Ye, J.; Mi, Z. Wafer-Level Artificial Photosynthesis for CO2 Reduction into CH4 and CO Using GaN Nanowires. *ACS Catalysis* **2015,** *5*, 5342-5348.
(242) Park, J. N.; McFarland, E. W. A highly dispersed Pd-Mg/SiO2 catalyst active for methanation of CO2. *Journal of Catalysis* **2009,** *266*, 92-97.
(243) Chen, Y. G.; Tomishige, K.; Yokoyama, K.; Fujimoto, K. Promoting effect of Pt, Pd and Rh noble metals to the Ni0.03Mg0.97O solid solution catalysts for the reforming of CH4 with CO2. *Applied Catalysis a-General* **1997,** *165*, 335-347.
(244) Liu, M.; Zhang, Y.; Yang, M.; Tian, Z.; Ren, L.; Zhang, S. Abundance and Distribution of Tetracycline Resistance Genes and Mobile Elements in an Oxytetracycline Production Wastewater Treatment System. *Environmental Science & Technology* **2012,** *46*, 7551-7557.
(245) Kümmerer, K. Antibiotics in the aquatic environment – A review – Part I. *Chemosphere* **2009,** *75*, 417-434.

(246) Michael, I.; Rizzo, L.; McArdell, C. S.; Manaia, C. M.; Merlin, C.; Schwartz, T.; Dagot, C.; Fatta-Kassinos, D. Urban wastewater treatment plants as hotspots for the release of antibiotics in the environment: A review. *Water Res.* **2013,** *47*, 957-995.
(247) Paul, T.; Miller, P. L.; Strathmann, T. J. Visible-Light-Mediated TiO2 Photocatalysis of Fluoroquinolone Antibacterial Agents. *Environmental Science & Technology* **2007,** *41*, 4720-4727.
(248) Chen, F.; Yang, Q.; Wang, Y.; Zhao, J.; Wang, D.; Li, X.; Guo, Z.; Wang, H.; Deng, Y.; Niu, C.; Zeng, G. Novel ternary heterojunction photcocatalyst of Ag nanoparticles and g-C3N4 nanosheets co-modified BiVO4 for wider spectrum visible-light photocatalytic degradation of refractory pollutant. *Appl. Catal., B* **2017,** *205*, 133-147.
(249) Low, J.; Yu, J.; Jaroniec, M.; Wageh, S.; Al-Ghamdi, A. A. Heterojunction Photocatalysts. *Adv. Mater.* **2017,** *29*, 1601694-n/a.
(250) Hu, X.; Liu, X.; Tian, J.; Li, Y.; Cui, H. Towards full-spectrum (UV, visible, and near-infrared) photocatalysis: achieving an all-solid-state Z-scheme between Ag2O and TiO2 using reduced graphene oxide as the electron mediator. *Catal. Sci. Technol.* **2017,** *7*, 4193-4205.
(251) Leong, S.; Li, D.; Hapgood, K.; Zhang, X.; Wang, H. Ni(OH)2 decorated rutile TiO2 for efficient removal of tetracycline from wastewater. *Appl. Catal., B* **2016,** *198*, 224-233.
(252) Ding, J.; Dai, Z.; Qin, F.; Zhao, H.; Zhao, S.; Chen, R. Z-scheme BiO1-xBr/Bi2O2CO3 photocatalyst with rich oxygen vacancy as electron mediator for highly efficient degradation of antibiotics. *Appl. Catal., B* **2017,** *205*, 281-291.
(253) Chen, F.; Yang, Q.; Li, X.; Zeng, G.; Wang, D.; Niu, C.; Zhao, J.; An, H.; Xie, T.; Deng, Y. Hierarchical assembly of graphene-bridged Ag3PO4/Ag/BiVO4 (040) Z-scheme photocatalyst: An efficient, sustainable and heterogeneous catalyst with enhanced visible-light photoactivity towards tetracycline degradation under visible light irradiation. *Appl. Catal., B* **2017,** *200*, 330-342.
(254) Wang, D.; Li, Z. Iron-based metal–organic frameworks (MOFs) for visible-light-induced photocatalysis. *Res. Chem. Intermed.* **2017,** *43*, 5169-5186.
(255) Panneri, S.; Thomas, M.; Ganguly, P.; Nair, B. N.; Mohamed, A. P.; Warrier, K. G. K.; Hareesh, U. S. C3N4 anchored ZIF 8 composites: photo-regenerable, high capacity sorbents as adsorptive photocatalysts for the effective removal of tetracycline from water. *Catal. Sci. Technol.* **2017,** *7*, 2118-2128.
(256) An, W. J.; Jiang, D. D.; Matthews, J. R.; Borrelli, N. F.; Biswas, P. Thermal conduction effects impacting morphology during synthesis of columnar nanostructured TiO2 thin films. *J. Mater. Chem.* **2011,** *21*, 7913-7921.
(257) An, W. J.; Thimsen, E.; Biswas, P. Aerosol-Chemical Vapor Deposition Method For Synthesis of Nanostructured Metal Oxide Thin Films With Controlled Morphology. *Journal of Physical Chemistry Letters* **2010,** *1*, 249-253.
(258) Liu, B.; Aydil, E. S. Growth of Oriented Single-Crystalline Rutile TiO2 Nanorods on Transparent Conducting Substrates for Dye-Sensitized Solar Cells. *J. Am. Chem. Soc.* **2009,** *131*, 3985-3990.
(259) Zhu, X.-D.; Wang, Y.-J.; Sun, R.-J.; Zhou, D.-M. Photocatalytic degradation of tetracycline in aqueous solution by nanosized TiO2. *Chemosphere* **2013,** *92*, 925-932.

(260) Wang, W.-N.; An, W.-J.; Ramalingam, B.; Mukherjee, S.; Niedzwiedzki, D. M.; Gangopadhyay, S.; Biswas, P. Size and Structure Matter: Enhanced CO2 Photoreduction Efficiency by Size-Resolved Ultrafine Pt Nanoparticles on TiO2 Single Crystals. *J. Am. Chem. Soc.* **2012,** *134*, 11276-11281.
(261) Jiang, Z. GIXSGUI: a MATLAB toolbox for grazing-incidence X-ray scattering data visualization and reduction, and indexing of buried three-dimensional periodic nanostructured films. *J. Appl. Crystallogr.* **2015,** *48*, 917-926.
(262) Jiang, H. B.; Cuan, Q.; Wen, C. Z.; Xing, J.; Wu, D.; Gong, X.-Q.; Li, C.; Yang, H. G. Anatase TiO2 Crystals with Exposed High-Index Facets. *Angew. Chem. Int. Ed.* **2011,** *50*, 3764-3768.
(263) Luan, C.; Zhou, Q.-X.; Wang, Y.; Xiao, Y.; Dai, X.; Huang, X.-L.; Zhang, X. A General Strategy Assisted with Dual Reductants and Dual Protecting Agents for Preparing Pt-Based Alloys with High-Index Facets and Excellent Electrocatalytic Performance. *Small* **2017,** *13*, 1702617-n/a.
(264) Horcajada, P.; Surble, S.; Serre, C.; Hong, D. Y.; Seo, Y. K.; Chang, J. S.; Greneche, J. M.; Margiolaki, I.; Ferey, G. Synthesis and catalytic properties of MIL-100(Fe), an iron(III) carboxylate with large pores. *Chemical Communications* **2007**, 2820-2822.
(265) Brezesinski, T.; Wang, J.; Tolbert, S. H.; Dunn, B. Ordered mesoporous alpha-MoO3 with iso-oriented nanocrystalline walls for thin-film pseudocapacitors. *Nat Mater* **2010,** *9*, 146-151.
(266) Mitchell, L.; Williamson, P.; Ehrlichová, B.; Anderson, A. E.; Seymour, V. R.; Ashbrook, S. E.; Acerbi, N.; Daniels, L. M.; Walton, R. I.; Clarke, M. L.; Wright, P. A. Mixed-Metal MIL-100(Sc,M) (M=Al, Cr, Fe) for Lewis Acid Catalysis and Tandem C□C Bond Formation and Alcohol Oxidation. *Chem. - Eur. J.* **2014,** *20*, 17185-17197.
(267) Petit, C.; Bandosz, T. J. Synthesis, Characterization, and Ammonia Adsorption Properties of Mesoporous Metal-Organic Framework (MIL(Fe))-Graphite Oxide Composites: Exploring the Limits of Materials Fabrication. *Adv. Funct. Mater.* **2011,** *21*, 2108-2117.
(268) Liang, R.; Luo, S.; Jing, F.; Shen, L.; Qin, N.; Wu, L. A simple strategy for fabrication of Pd@MIL-100(Fe) nanocomposite as a visible-light-driven photocatalyst for the treatment of pharmaceuticals and personal care products (PPCPs). *Appl. Catal., B* **2015,** *176*, 240-248.
(269) Zhao, H.; Qian, L.; Lv, H.; Wang, Y.; Zhao, G. Introduction of a Fe3O4 Core Enhances the Photocatalytic Activity of MIL-100(Fe) with Tunable Shell Thickness in the Presence of H2O2. *ChemCatChem* **2015,** *7*, 4148-4155.
(270) Liu, X.; Dang, R.; Dong, W.; Huang, X.; Tang, J.; Gao, H.; Wang, G. A sandwich-like heterostructure of TiO2 nanosheets with MIL-100(Fe): A platform for efficient visible-light-driven photocatalysis. *Appl. Catal., B* **2017,** *209*, 506-513.
(271) Yang, Z.; Xu, X.; Liang, X.; Lei, C.; Cui, Y.; Wu, W.; Yang, Y.; Zhang, Z.; Lei, Z. Construction of heterostructured MIL-125/Ag/g-C3N4 nanocomposite as an efficient bifunctional visible light photocatalyst for the organic oxidation and reduction reactions. *Appl. Catal., B* **2017,** *205*, 42-54.
(272) Sharma, V. K.; Feng, M. Water depollution using metal-organic frameworks-catalyzed advanced oxidation processes: A review. *J. Hazard. Mater.* **2017**.

(273) Wang, D.; Wang, M.; Li, Z. Fe-Based Metal–Organic Frameworks for Highly Selective Photocatalytic Benzene Hydroxylation to Phenol. *ACS Catalysis* **2015,** *5*, 6852-6857.
(274) James, S. L. Metal-organic frameworks. *Chem. Soc. Rev.* **2003,** *32*, 276-288.
(275) Drout, R. J.; Robison, L.; Farha, O. K. Catalytic applications of enzymes encapsulated in metal–organic frameworks. *Coord. Chem. Rev.* **2019,** *381*, 151-160.
(276) Islamoglu, T.; Ray, D.; Li, P.; Majewski, M. B.; Akpinar, I.; Zhang, X.; Cramer, C. J.; Gagliardi, L.; Farha, O. K. From Transition Metals to Lanthanides to Actinides: Metal-Mediated Tuning of Electronic Properties of Isostructural Metal–Organic Frameworks. *Inorg. Chem.* **2018,** *57*, 13246-13251.
(277) Lu, G.; Hupp, J. T. Metal−Organic Frameworks as Sensors: A ZIF-8 Based Fabry−Pérot Device as a Selective Sensor for Chemical Vapors and Gases. *J. Am. Chem. Soc.* **2010,** *132*, 7832-7833.
(278) Cacho-Bailo, F.; Caro, G.; Etxeberria-Benavides, M.; Karvan, O.; Tellez, C.; Coronas, J. High selectivity ZIF-93 hollow fiber membranes for gas separation. *Chem. Commun.* **2015,** *51*, 11283-11285.
(279) Altintas, C.; Avci, G.; Daglar, H.; Nemati Vesali Azar, A.; Velioglu, S.; Erucar, I.; Keskin, S. Database for CO2 Separation Performances of MOFs Based on Computational Materials Screening. *ACS Appl. Mater. Interfaces* **2018,** *10*, 17257-17268.
(280) Hwang, Y. K.; Hong, D.-Y.; Chang, J.-S.; Jhung, S. H.; Seo, Y.-K.; Kim, J.; Vimont, A.; Daturi, M.; Serre, C.; Férey, G. Amine Grafting on Coordinatively Unsaturated Metal Centers of MOFs: Consequences for Catalysis and Metal Encapsulation. *Angew. Chem. Int. Ed.* **2008,** *47*, 4144-4148.
(281) Kou, J.; Sun, L.-B. Fabrication of Metal–Organic Frameworks inside Silica Nanopores with Significantly Enhanced Hydrostability and Catalytic Activity. *ACS Appl. Mater. Interfaces* **2018,** *10*, 12051-12059.
(282) Müller, M.; Hermes, S.; Kähler, K.; van den Berg, M. W. E.; Muhler, M.; Fischer, R. A. Loading of MOF-5 with Cu and ZnO Nanoparticles by Gas-Phase Infiltration with Organometallic Precursors: Properties of Cu/ZnO@MOF-5 as Catalyst for Methanol Synthesis. *Chem. Mater.* **2008,** *20*, 4576-4587.
(283) Qiu, J.; Zhang, X.; Feng, Y.; Zhang, X.; Wang, H.; Yao, J. Modified metal-organic frameworks as photocatalysts. *Appl. Catal., B* **2018,** *231*, 317-342.
(284) Wang, X.; Liu, J.; Leong, S.; Lin, X.; Wei, J.; Kong, B.; Xu, Y.; Low, Z.-X.; Yao, J.; Wang, H. Rapid Construction of ZnO@ZIF-8 Heterostructures with Size-Selective Photocatalysis Properties. *ACS Appl. Mater. Interfaces* **2016,** *8*, 9080-9087.
(285) Wang, R.; Gu, L.; Zhou, J.; Liu, X.; Teng, F.; Li, C.; Shen, Y.; Yuan, Y. Quasi-Polymeric Metal–Organic Framework UiO-66/g-C3N4 Heterojunctions for Enhanced Photocatalytic Hydrogen Evolution under Visible Light Irradiation. *Advanced Materials Interfaces* **2015,** *2*, 1500037-n/a.
(286) Su, Y.; Zhang, Z.; Liu, H.; Wang, Y. Cd0.2Zn0.8S@UiO-66-NH2 nanocomposites as efficient and stable visible-light-driven photocatalyst for H2 evolution and CO2 reduction. *Appl. Catal., B* **2017,** *200*, 448-457.

(287) Zhao, X.; Zhang, Y.; Wen, P.; Xu, G.; Ma, D.; Qiu, P. NH2-MIL-125(Ti)/TiO2 composites as superior visible-light photocatalysts for selective oxidation of cyclohexane. *Mol. Catal.* **2018,** *452*, 175-183.
(288) Zhang, B.; Zhang, J.; Tan, X.; Shao, D.; Shi, J.; Zheng, L.; Zhang, J.; Yang, G.; Han, B. MIL-125-NH2@TiO2 Core–Shell Particles Produced by a Post-Solvothermal Route for High-Performance Photocatalytic H2 Production. *ACS Appl. Mater. Interfaces* **2018,** *10*, 16418-16423.
(289) He, J.; Yan, Z.; Wang, J.; Xie, J.; Jiang, L.; Shi, Y.; Yuan, F.; Yu, F.; Sun, Y. Significantly enhanced photocatalytic hydrogen evolution under visible light over CdS embedded on metal-organic frameworks. *Chem. Commun.* **2013,** *49*, 6761-6763.
(290) Kresse, G.; Furthmüller, J. Efficiency of ab-initio total energy calculations for metals and semiconductors using a plane-wave basis set. *Comput. Mater. Sci.* **1996,** *6*, 15-50.
(291) Fang, H.; Zhou, J.; Jena, P. Super-alkalis as building blocks of one-dimensional hierarchical electrides. *Nanoscale* **2018,** *10*, 22963-22969.
(292) Ishikawa, T.; Takeuchi, K.; Kandori, K.; Nakayama, T. Transformation of γ-FeOOH to α-FeOOH in acidic solutions containing metal ions. *Colloids Surf., A* **2005,** *266*, 155-159.
(293) Horcajada, P.; Surble, S.; Serre, C.; Hong, D.-Y.; Seo, Y.-K.; Chang, J.-S.; Greneche, J.-M.; Margiolaki, I.; Ferey, G. Synthesis and catalytic properties of MIL-100(Fe), an iron(iii) carboxylate with large pores. *Chem. Commun.* **2007**, 2820-2822.
(294) He, X.; Nguyen, V.; Jiang, Z.; Wang, D.; Zhu, Z.; Wang, W.-N. Highly-oriented one-dimensional MOF-semiconductor nanoarrays for efficient photodegradation of antibiotics. *Catal. Sci. Technol.* **2018,** *8*, 2117-2123.
(295) Wang, C.-C.; Du, X.-D.; Li, J.; Guo, X.-X.; Wang, P.; Zhang, J. Photocatalytic Cr(VI) reduction in metal-organic frameworks: A mini-review. *Appl. Catal., B* **2016,** *193*, 198-216.
(296) Shi, L.; Wang, T.; Zhang, H.; Chang, K.; Meng, X.; Liu, H.; Ye, J. An Amine-Functionalized Iron(III) Metal–Organic Framework as Efficient Visible-Light Photocatalyst for Cr(VI) Reduction. *Adv. Sci.* **2015,** *2*, 1500006-n/a.
(297) Wang, D.; Jia, F.; Wang, H.; Chen, F.; Fang, Y.; Dong, W.; Zeng, G.; Li, X.; Yang, Q.; Yuan, X. Simultaneously efficient adsorption and photocatalytic degradation of tetracycline by Fe-based MOFs. *J. Colloid Interface Sci.* **2018,** *519*, 273-284.
(298) Yang, Q.; Zhao, Q.; Ren, S.; Lu, Q.; Guo, X.; Chen, Z. Fabrication of core-shell Fe3O4@MIL-100(Fe) magnetic microspheres for the removal of Cr(VI) in aqueous solution. *J. Solid State Chem.* **2016,** *244*, 25-30.
(299) Fang, Y.; Wen, J.; Zeng, G.; Jia, F.; Zhang, S.; Peng, Z.; Zhang, H. Effect of mineralizing agents on the adsorption performance of metal–organic framework MIL-100(Fe) towards chromium(VI). *Chem. Eng. J.* **2018,** *337*, 532-540.
(300) Long, R.; Mao, K.; Gong, M.; Zhou, S.; Hu, J.; Zhi, M.; You, Y.; Bai, S.; Jiang, J.; Zhang, Q.; Wu, X.; Xiong, Y. Tunable Oxygen Activation for Catalytic Organic Oxidation: Schottky Junction versus Plasmonic Effects. *Angew. Chem.* **2014,** *126*, 3269-3273.
(301) Liu, J.; Li, J.; Sedhain, A.; Lin, J.; Jiang, H. Structure and Photoluminescence Study of TiO2 Nanoneedle Texture along Vertically Aligned Carbon Nanofiber Arrays. *J. Phys. Chem. C* **2008,** *112*, 17127-17132.

(302) Wang, L.; Wang, Z.; Wang, H.-Y.; Grinblat, G.; Huang, Y.-L.; Wang, D.; Ye, X.-H.; Li, X.-B.; Bao, Q.; Wee, A.-S.; Maier, S. A.; Chen, Q.-D.; Zhong, M.-L.; Qiu, C.-W.; Sun, H.-B. Slow cooling and efficient extraction of C-exciton hot carriers in MoS2 monolayer. *Nat. Commun.* **2017,** *8*, 13906.
(303) Zhang, F.; Shi, J.; Jin, Y.; Fu, Y.; Zhong, Y.; Zhu, W. Facile synthesis of MIL-100(Fe) under HF-free conditions and its application in the acetalization of aldehydes with diols. *Chem. Eng. J.* **2015,** *259*, 183-190.
(304) Lv, H.; Zhao, H.; Cao, T.; Qian, L.; Wang, Y.; Zhao, G. Efficient degradation of high concentration azo-dye wastewater by heterogeneous Fenton process with iron-based metal-organic framework. *J. Mol. Catal. A: Chem.* **2015,** *400*, 81-89.
(305) Cao, L.; Tang, F.; Fang, G. Preparation and characteristics of microencapsulated palmitic acid with TiO2 shell as shape-stabilized thermal energy storage materials. *Sol. Energy Mater. Sol. Cells* **2014,** *123*, 183-188.
(306) Mou, F.; Xu, L.; Ma, H.; Guan, J.; Chen, D.-r.; Wang, S. Facile preparation of magnetic [gamma]-Fe2O3/TiO2 Janus hollow bowls with efficient visible-light photocatalytic activities by asymmetric shrinkage. *Nanoscale* **2012,** *4*, 4650-4657.
(307) Geng, W.; Liu, H.; Yao, X. Enhanced photocatalytic properties of titania–graphene nanocomposites: a density functional theory study. *PCCP* **2013,** *15*, 6025-6033.
(308) Yu, J.; Xiang, Q.; Zhou, M. Preparation, characterization and visible-light-driven photocatalytic activity of Fe-doped titania nanorods and first-principles study for electronic structures. *Appl. Catal., B* **2009,** *90*, 595-602.
(309) Yen, C.-C.; Wang, D.-Y.; Chang, L.-S.; Shih, H. C. Characterization and photocatalytic activity of Fe- and N-co-deposited TiO2 and first-principles study for electronic structure. *J. Solid State Chem.* **2011,** *184*, 2053-2060.
(310) Li, Z.; Shen, W.; He, W.; Zu, X. Effect of Fe-doped TiO2 nanoparticle derived from modified hydrothermal process on the photocatalytic degradation performance on methylene blue. *J. Hazard. Mater.* **2008,** *155*, 590-594.
(311) Nishikawa, M.; Mitani, Y.; Nosaka, Y. Photocatalytic Reaction Mechanism of Fe(III)-Grafted TiO2 Studied by Means of ESR Spectroscopy and Chemiluminescence Photometry. *J. Phys. Chem. C* **2012,** *116*, 14900-14907.
(312) Ohno, T.; Miyamoto, Z.; Nishijima, K.; Kanemitsu, H.; Xueyuan, F. Sensitization of photocatalytic activity of S- or N-doped TiO2 particles by adsorbing Fe3+ cations. *Applied Catalysis A: General* **2006,** *302*, 62-68.

Xiang He

Education

Ph.D., Mechanical and Nuclear Engineering — May 2019
Virginia Commonwealth University, Richmond, USA

M.S., Environmental Engineering — 2015
Sun Yat-sen University, Guangzhou, China

B.S., Environmental Engineering — 2013
Sun Yat-sen University, Guangzhou, China

Honors and Awards

- **2018 Chinese Government Award for Outstanding Self-financed Students Abroad.** The highest honor established by the Chinese government to non-government-sponsored Chinese graduate students studying overseas for their exceptional academic achievements (top 0.1%).
- **DOE Full Financial Support to Attend 20th National School on Neutron and X-ray Scattering** Held at Argonne National Lab and Oak Ridge National Lab, 2018
  Only 60 students were selected from North American Universities.
- **Mechanical and Nuclear Engineering (MNE) Fellowship**, VCU MNE Dept., 2018
- **Outstanding Graduate Research Assistant**, VCU College of Engineering, 2018
- **National Endeavor Fellowship**, China, 2012
- **School-level Individual** (2011)**, Second-class** (2012)**, Third-class Scholarship** (2010), Sun Yat-sen University

Academic Achievements

- 19 peer-reviewed journal papers; 11 first-author papers.
  (Full Publication List: https://scholar.google.com/citations?user=zXFHqpAAAAAJ&hl=en&oi=ao)
- 6 presentations at international conferences.
- Mentored 19 undergraduate and high school students.
- Serve as a reviewer for several journals, such as *RSC Advances*.
- A graduate teaching assistant for several undergraduate courses, including *Heat transfer, Thermodynamics, HVAC.*
- A guest lecturer for a graduate course (*Advanced Characterization of Materials*).

Skills

- Nano-particles synthesis, characterization and photocatalytic application.
- Experienced in XRD, SEM, EDX, AFM, XPS, FTIR, UV-vis, GC, DRIFTS, Raman, BET, Fluorescence measurements, gas adsorption and separation, toxic gas removal, environmental pollution control, and membrane filtration.